JAERI-Review
2004-005

PROGRESS REPORT ON NEUTRON SCATTERING RESEARCH (APRIL 1, 2002-MARCH 31, 2003)

March 2004

(Eds.)Satoshi KOIZUMI, Masaaki MATSUDA and Kazuo KURIHARA

日本原子力研究所
Japan Atomic Energy Research Institute

本レポートは，日本原子力研究所が不定期に公刊している研究報告書です。
入手の問合わせは，日本原子力研究所研究情報部研究情報課（〒319-1195　茨城県那珂郡東海村）あて，お申し越しください。なお，このほかに財団法人原子力弘済会資料センター（〒319-1195　茨城県那珂郡東海村日本原子力研究所内）で複写による実費頒布をおこなっております。

This report is issued irregularly.
Inquiries about availability of the reports should be addressed to Research Information Division, Department of Intellectual Resources, Japan Atomic Energy Research Institute, Tokai-mura, Naka-gun, Ibaraki-ken, 319-1195, Japan.

編集兼発行　　日本原子力研究所

JAERI-Review 2004-005

Progress Report on Neutron Scattering Research (April 1, 2002 - March 31, 2003)

(Eds.) Satoshi KOIZUMI, Masaaki MATSUDA and Kazuo KURIHARA

Advanced Science Research Center
(Tokai site)
Japan Atomic Energy Research Institute
Tokai-mura, Naka-gun, Ibaraki-ken

(Received January 29, 2004)

This issue summarizes research progress in neutron scattering at Japan Atomic Energy Research Institute (JAERI) by utilizing the research reactor JRR-3 during the period between April 1, 2002 and March 31, 2003.

Keywords : Neutron Scattering, JRR-3

中性子散乱研究成果報告集
(2002年度次報告)

日本原子力研究所先端基礎研究センター
(編) 小泉 智・松田 雅昌・栗原 和男

(２００４年 １ 月 ２９日 受理)

本報告書は、日本原子力研究所の先端基礎研究センターに所属する中性子散乱研究グループの研究を中心に、研究用原子炉JRR-３を利用した所内の中性子散乱研究、所外との協力研究および共同研究の２００２年４月～２００３年３月の期間における成果をまとめたものである。

日本原子力研究所 (東海駐在): 〒319-1195 茨城県那珂郡東海村白方白根2-4

Contents

This is a blank page.

Research staffs for neutron scattering in JAERI
(This photo taken at 01/07/2004)

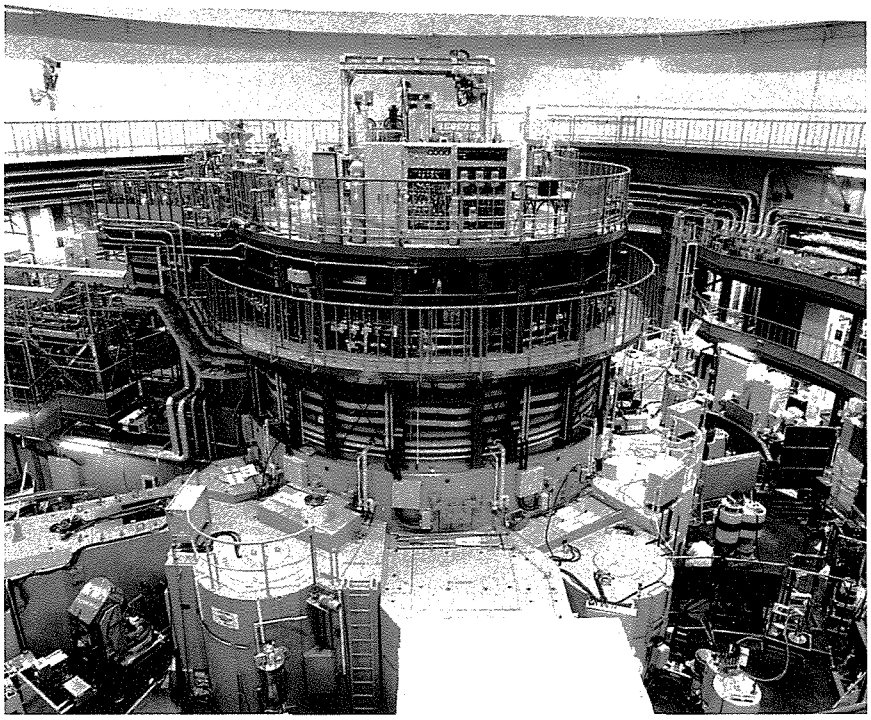

JRR-3 Reactor Hall

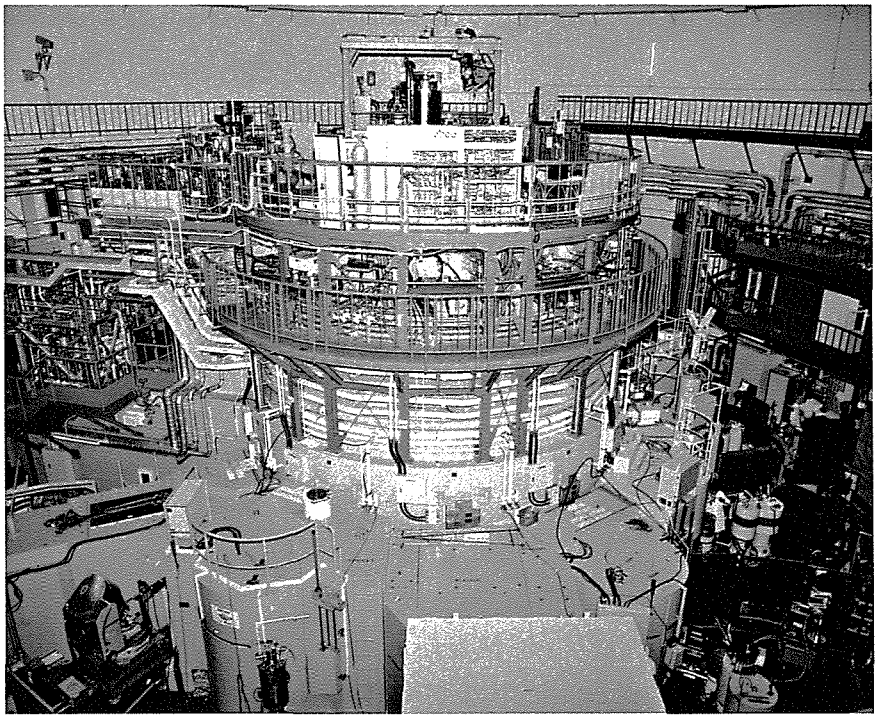

JRR-3 Guide Hall

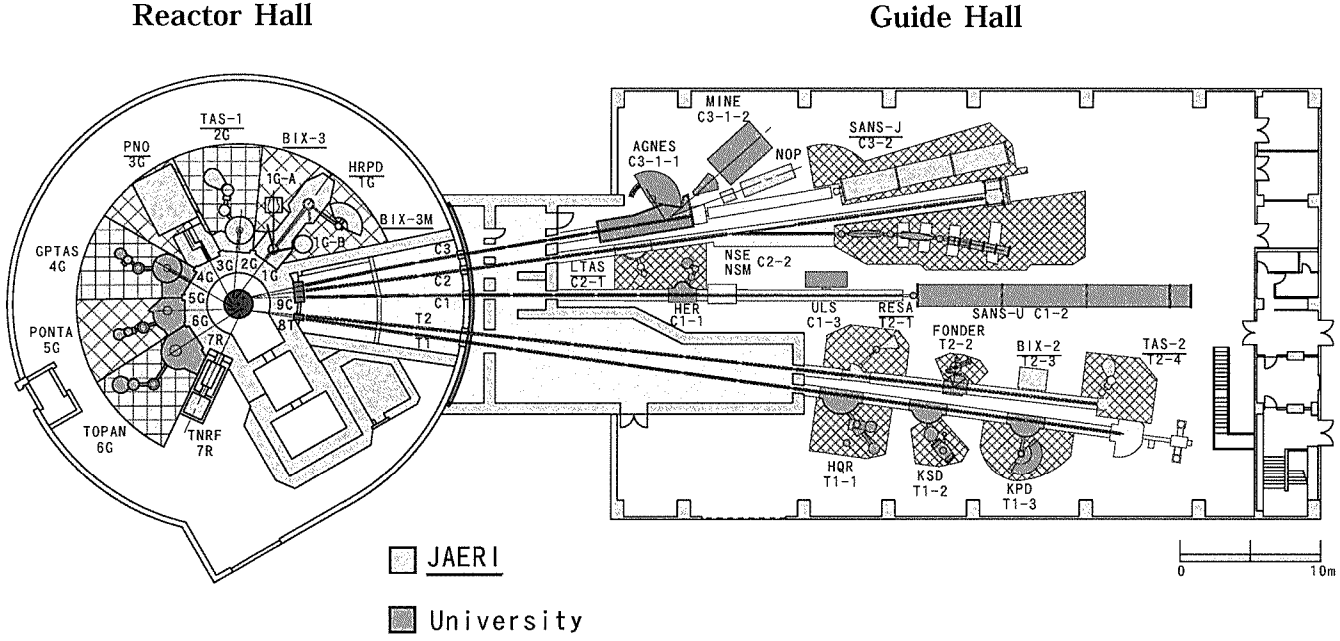

JRR-3 Beam Experimental Facilities

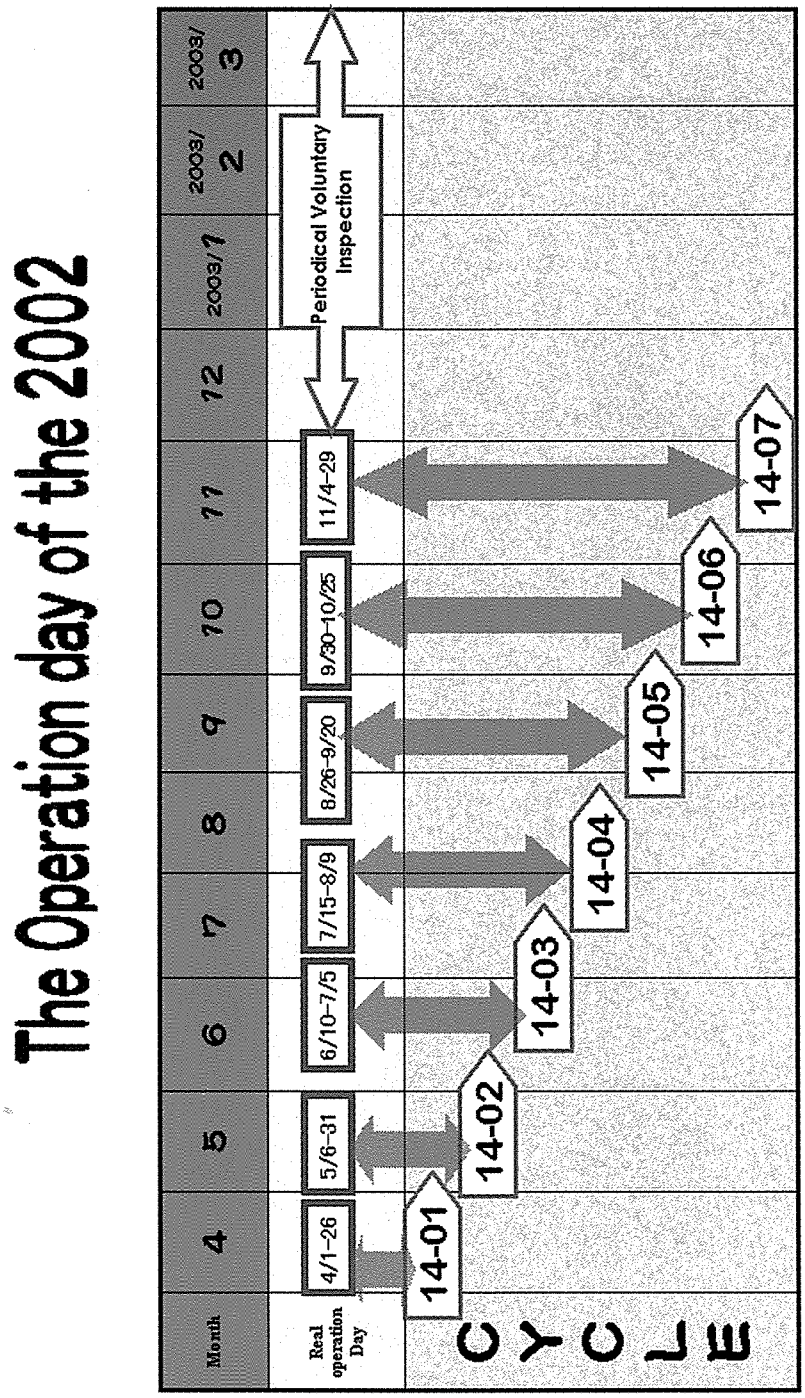
The Operation day of the 2002
Month
4
5
6
7
8
9
10
11
12
2003/1
2003/2
2003/3
Real operation Day
4/1-26
5/6-31
6/10-7/5
7/15-8/9
8/26-9/20
9/30-10/25
11/4-29
Periodical Voluntary Inspection
CYCLE
14-01
14-02
14-03
14-04
14-05
14-06
14-07

List of JAERI Instruments

A. Neutron Scattering Instruments

Beam Port	Instrument	Moderator	Instrument Staff
1G	High Resolution Powder Diffractometer (HRPD)	Thermal(H_2O)	Yoshinobu Ishii, Naoki Igawa, Yutaka Shimojo
1G-A	Diffratometer for Biological Crystallography-III (BIX-3)	Thermal(H_2O)	Ichiro Tanaka, Nobuo Niimura
1G-B	Single Crystal Diffractometer for Biological Macromolecules (BIX-3M)	Thermal(H_2O)	Kazuo Kurihara, Nobuo Niimura
2G	Triple-Axis Spectrometer (TAS-1)	Thermal(H_2O)	Kazuhisa Kakurai, Susumu Katano
3G	Apparatus for Precise Neutron Optics and Neutron Diffraction Topography (PNO)	Thermal(H_2O)	Hiroshi Tomimitsu, Kazuya Aizawa, Satoshi Koizumi
T2-1	Diffractometer for the Residual Stress Analysis (RESA)	Thermal(H_2O)	Atsushi Moriai, Yoshinobu Ishii
T2-3	Diffractometer for Biological Crystallography-II (BIX-2)	Thermal(H_2O)	Satoru Fujiwara, Nobuo Niimura
T2-4	Triple-Axis Spectrometer (TAS-2)	Thermal(H_2O)	Masaaki Matsuda
C2-1	Low energy Triple-Axis Spectrometer (LTAS)	Cold(Liquid H_2)	Naoto Metoki
C3-1-2-1	Neutron Optics (NOP)	Cold(Liquid H_2)	Jun-ichi Suzuki, Takayuki Oku
C3-2	Small-Angle Neutron Scattering Instrument (SANS-J)	Cold(Liquid H_2)	Jun-ichi Suzuki, Satoshi Koizumi

B. Special Accessories

B-1. Cryostats, Magnets and Furnaces

Accessory	Number	Performance	Instrument Staff
Dilution Refrigerator	1	T_{min}= 10mK,H_{max} = 5T (Vertical)	N. Metoki
Dilution Refrigerator (Lquid-^{4}He-Free)	2	T_{min}= 50mK	Y. Morii
10T Magnet (Liquid-^{4}He-Free)	1	T_{min}= 100mK,H_{max} =10T (Vertical)	S. Katano
^{3}HeCryostat	1	T_{min}= 0.3K,H_{max}=6T (Vertical)	N. Metoki
Orange Cryostat	1	T_{min}= 1.5K	T. Osakabe
Horizontal Magnet	1	T_{min}= 1.5K,H_{max}=5T (Horizontal)	J. Suzuki
4K Cryostat	2	T_{min}= 4K	Y. Shimojo
10K Cryostat	6	T_{min}= 10K	Y. Shimojo
Furnace for Soft Matter	1	T = 0 – 300℃	S. Koizumi
800K Displex	1	T = 5 – 800K	M. Matsuda
Furnace	2	T_{max} = 1100K	Y. Shimojo
Furnace	1	T_{max} = 1600K	Y. Ishii

B-2. Pressure Devices

McWhan Cell	3	P_{max}= 2.5GPa	T. Osakabe S. Katano
Sapphire Anvil Cell (under development)	several	P_{max}= 6GPa	T. Osakabe
Oscillatory Shear Machine	1	T=RT – 200℃, Amplitude = 0.01 - 2mm, Frequency = 0.1 - 100Hz	S. Koizumi
Tension Testing Machine	1	Tensil Speed= 0 - 0.01mm/sec, Range of Load= 50 - 1000kgf ± 1%	A. Moriai

B-3. Detectors

Neutron Imaging Plate	several	Resolution = 100 μm	N. Niimura

1. Research Activities in the JFY 2002

The research activities by neutron scattering during the 2002 JFY have been promoted by three following research groups in the avvanced science research center (ASRC) which are specialized for (i) spin-lattice correlation (group leader: Kazuhisa Kakurai), (ii) extreme environments (group leader: Yukio Morii) and (iii) structural biology (group leader: Nobuo Niimura).

1. Researches by the group for neutron scattering study on spin-lattice correlations

The aim of the project on research on spin-lattice correlations by means of neutron scattering is to focus on the role of correlation between spin degrees of freedom and other degrees of freedom as charge and orbital degrees of freedom, which are closely connected to the lattice. These spin-lattice correlations may play important roles in explaining novel phenomena in condensed matters as in high-Tc superconductors, CMR materials, magnetically low-dimensional and frustrated systems. In this project emphasis is put on the utilization of polarized neutron scattering for this purpose.

In collaboration with neutron scattering scientists from Institut Laue Langevin and CEN-Grenoble we are preparing the installation of the neutron polarimetry, a three dimensional polarization analysis method, using CRYOPAD. To reach this goal a sufficient polarized neutron flux on an existing triple axis instrument is an important prerequisite. We therefore constructed and installed a new double focusing Heusler monochromator. The neutron beam test showed the excellent performance of the new device, resulting in an average intensity gain factor of ~10 to the old device and the neutron polarization of better than 90% (see the report by Nakamura *et al.*). At the end of the fiscal year the construction of the CRYOPADUM at ILL was completed and after the successful cooling down test the device has been shipped to JAERI.

Parallel to these instrument development efforts we have continued to investigate magnetic materials where the spin-lattice correlation may play an important role. For this purpose national and international collaborations are performed to study materials including high-Tc superconducting (SC) systems, low dimensional and frustrated magnetic systems, where so far the lattice contribution to the ground state formation has not been discussed in detail and systematically, although there have been increasing number of evidences to indicate its importance. In-plane phonons of $YBa_2Cu_3O_y$ and $La_{1.48}Nd_{0.4}Sr_{0.12}CuO_4$ have been studied to extract detailed information of the effect of 'stripes'(see the report by M. Ito *et al.*). A

search for antiferromagnetic (AF) fluctuations in Bismuth-based superconductor Bi2201 has been performed(see the report by N. Kaneko *et al.*) The existence of AF spin fluctuations in electron doped SC sample has been clearly demonstrated in $Pr_{0.89}LaCe_{0.11}CuO_{4-\delta}$. However the commensurate spin fluctuations observed in both AF and SC phases are to be contrasted to the incommensurate ones observed in the hole-doped LSCO system (see the report by M. Fujita *et al.*)

Intensive studies on low dimensional and quantum spin systems have been performed. Neutron scattering studies on the impurity and pressure induced AF ordering in the spin gap system $TlCuCl_3$ have been performed(see the report by A. Oosawa *et al.*). In both cases the magnetic structures of the AF ordering have been determined for the first time. Furthermore in the pressure induced AF ordering the polarized neutron scattering investigation lead to a discovery of a novel successive phase transition involving a spin reorientation. Polarized neutron scattering technique has been also applied on the quasi-one-dimensional magnet $Ca_2Y_2Cu_5O_{10}$ and the direction of the ordered moment has been uniquely determined. This finding confirms the existence of the magnetic moments on the oxygen sites (see the report by M. Matsuda *et al.*) The spin orientation of the exotic spin-density waves in Cr(001)/Sn epitaxial films has been studied using polarized neutrons (see the report by M. Takeda *et al.*).

Spin correlations in the frustrated and/or charge ordered systems as Cs_2CuBr_4, $LuFe_2O_4$, $ZnFe_2O_4$ have been investigated. Incommensurate magnetic structure at 50mK has been observed in Cs_2CuBr_4 indicating to the frustration of the exchange interactions in the *b-c* triangular plane (see the report by T. Ono *et al.*) In the charge ordered $LuFe_2O_4$, a clear onset of the three dimensional ordering at T_N is observed and a new characteristic temperature T_f below T_N is discovered at which the magnetic intensities redistribute and the magnetic peaks acquire finite width in c^* direction (see the report by S. Nagai *et al.*). These findings are in contrast to the 2D magnetic order observed in the earlier neutron scattering experiment on a presumably less stoichiometric sample. In $ZnFe_2O_4$ the study of the diffuse scattering under applied pressure has been initiated (see the report by Y. Tsunoda *et al.*). Magnetic and charge ordering in $TbBaCo_2O_{5.5}$ has been studied and the spin state of Co^{3+} within the CoO_6 octahedra and the CoO_5 pyramids has been determined (see the report by M. Soda *et al.*).

Since the parameter 'pressure' will be important to study spin-lattice correlation a few uniaxial and hydrostatic pressure experiments, besides those already mentioned, have been performed or are being prepared. Using applied uniaxial pressure up to 2kbar the change of domain population in UGa_3 has been quantitatively analyzed using polarized neutron diffraction (see the report by M. Nakamura *et al.*). The neutron small-angle

diffraction study of the itinerant electron metamagnet MnSi under applied magnetic field has been initiated(see the report by M. Yamada *et al.*) as a preparation to study microscopically the pressure induced collapse of the Mn moment at 1.7 GPa observed in the magnetization measurement. To attack the pressure induced transition from the enhanced-paramagnetic to ferromagnetic phase in the double layered $Sr_3Ru_2O_7$ single crystal structural investigation and the development of a pressure cell for the four-circle neutron diffraction experiment have been initiated (see the report by Y. Yoshida *et al.*).

Cold neutron optical devices as magnetic and refractive lenses are being developed in the collaborative effort with RIKEN. First test of the focusing geometry SANS experiment using a MgF_2 Fresnel-type lens with large aperture has been performed and an intensity gain of ~10 over the conventional pin-hole SANS experiment has been obtained by selecting the same minimum momentum transfer condition in both cases (see the report by H. Shimizu *et al.*).

Very active polymer investigations using the small angle neutron scattering (SANS) have been carried out. In-situ observation for NIPA-block-PEG polymerization process has been carried out using the time sliced SANS measurements to investigate the structure formation and the effect of the microstructure on polymerization products in non-equilibrium condition (see the report by R. Motokawa *et al.*). Radical polymerization of polystyrene in the polymerization matrix of poly(vinyl methylether) solution with mixed solvents of ethanol and n-hexane has been studied using both U-SANS and SANS. The time-evolving q-profile over a wide q-range of 10^{-4} to 1 nm^{-1} has been obtained (see the report by S. Koizumi *et al.*). In the extended studies on polystyrene/Poly(vinyl methylether) mixture an anomalous suppression of small-angle scattering in quiescent state, competition between rheological and concentration fluctuation relaxation and shear-induced phase separation resulting into an abnormal butterfly scattering pattern have been observed (see the reports by S. Koizumi *et al.*)

2. Researches by the group for neutron scattering in extreme environments

The research group on neutron scattering in extreme environments is developing liquid-He-free instruments to provide multiple extreme environments of high pressure, low temperature, and high magnetic field, such as 8 GPa + 50 mK, 12 Tesla + 50 mK and 8 GPa + 12 Tesla, where we investigate new field of science, microscopic structure, magnetism, elementary excitations *etc.* On the other hand, extremely high temperature neutron scattering is also our subject. Furthermore the development of residual stress analysis by neutron and precise neutron optical measurements such as ultra small angle neutron scattering and neutron interferometry

are also the subjects for this instrumental research group.

The magnetic ordering of $UTGa_5$ (T : Ni, Pd, Pt), which is an iso-structural compound of the heavy fermion superconductors $CeT'In_5$ (T' : Rh, Co, Ir) and $PuCoGa_5$, has been studied. A strong quenching of orbital magnetic moment was observed in magnetic form factor measurements. A contraction ($UNiGa_5$) and expansion ($UPdGa_5$ and $UPtGa_5$) of the in-plane lattice constant below the *Néel* temperature was explained with the cross over of the magnetic interaction, controlled by the local tetragonality of UGa_3 layer. It suggests that the orbital degree-of-freedom plays a dominant role (see the report by Kaneko *et al.*).

The mystery of the unusual magnetic properties in $CeAgSb_2$ were elucidated by systematic neutron scattering study. We revealed a simple ferromagnetic order due to anisotropic interactions between 4f electrons with the $|J_z \pm 1/2>$ ground state, which is stabilized by the strong uniaxial field gradient of crystal field at the Ce site (see the report by Araki *et al.*).

The field induced antiferroquadrupolar (AFQ) order in $PrOs_4Sb_{12}$ was revealed by high field and low temperature neutron scattering study at LTAS spectrometer. The existence of the AFQ order close to the superconducting phase suggests the importance of the quadrupole interaction / fluctuation as a possible pairing mechanism. (see the report by Kohgi and Metoki *et al.*).

The sapphire anvil cell for neutron diffraction reached high pressure at 6 GPa, which is the highest record in the Japanese neutron scattering facility. The neutron focusing device with bent multiple supermirror was tested. The high efficiency of this focusing device was demonstrated by the enhancement factor 7 times as strong as the primary intensity. High pressure neutron diffraction study on Ce-monopnictides revealed the systematic change of the T-p phase diagrams. This indicates that the magnetism of Ce-monopnictides is understood by considering the strong spin-charge correlation in low carrier f-p hybridized system (see the report by Osakabe *et al.*).

An electrostatic levitation extremely high temperature furnace for neutron scattering was developed with the collaboration of JAERI and National Space Development Agency of Japan (NASDA). The sample of tiny liquid Zr sphere with 2 mm diameter was levitated by applying an electrostatic field, and heated by CO_2 laser light up to 2500 K without any sample holder, which is the key breakthrough for extremely high temperature neutron scattering experiments. Neutron diffraction experiments of liquid Zr at 2500 K was tested on the High Resolution Powder Diffractometer (HRPD) of JRR-3. This technique should accelerate neutron scattering research for high-temperature materials and liquids in the near future (see the report by Masaki and Ishii *et al.*).

The increasing number of users and widely spreading various theme for RESA spectrometer demonstrate that neutron is an essential probe for engineering use as well as material science. The residual stress of aluminum automobile engine was measured with neutron and compared with traditional strain release method by using strain gauge. The direct comparison clarified the advantage and usefulness of non-destructive neutron technique, whereas there are intrinsic, thus unavoidable difficulty and unreliability in traditional method (see the report by Minakawa *et al.*).

The mechanism of the strength in pearlite steel was established by RESA spectrometer which revealed stress partitioning into ferrite and cementite (Fe_3C). Furthermore in-situ measurements of heavily drawn pearlite wire under tensil loading present a hint to the mechanism for the ultra-high strength of heavily drawn pearlite wire. Material and lattice index selective stress measurements by neutron confirmed that the ferrite matrix itself is strengthened, where the dissolution of cementite plays a major role. The microscopic mechanism, especially the role of carbon atoms and dislocations near grain boundary, remains an open question (see the report by Tomota *et al.*).

It is noteworthy that RESA spectrometer contributes to the development of the carbon composite materials for advanced high temperature reactor and sophisticated welding technique for ITER vacuum vessels (see the report by Baba *et al.* and Nakahira *et al.*). Neutron residual stress analysis is also useful for the development of the lead-bismuth target for a spallation neutron source (see the report by Kikuchi *et al.*).

Mr. Nobuaki Minakawa, the most famous technical staff in JAERI, who made major progress and history of neutron scattering in Japan, was awarded the JSNS prize 2003 for technology by the Japanese Society for Neutron Science (JSNS) for his resent activity of RESA spectrometer and long time technical contribution to neutron scattering community.

PNO (precise neutron optics) instrument was improved by the factor 3 in primary beam intensity. The major break through is the introduction of the pre-graphite crystal. The mechanism of this beam enhancement technique is explained phenomenologically with the idea of the lattice parameter distribution in pre-graphite crystals (see the report by Tomimitsu *et al.*).

3. Researches by the group for neutron structural biology

In the research of biological macromolecules, the highlight are as follows: A large single crystal of B-DNA decamer d(CCATTAATGG) was grown in D_2O solution by using the phase diagram information, and neutron diffraction experiment of the DNA was carried out. 43 water molecules including hydrogen atoms have been identified. They form hydrogen bonding network

in minor groove and major groove, and with phosphate groups. The neutron diffraction experiments of the Dissimilatory sulfate reductase D (DsrD), which has DNA binding motif, and the cubic insulin have been performed and the analyses have been accomplished. The information of the protonation and deprotonation of two nitrogen atoms (N_π, N_τ) in imidazole ring of histidine in insulin have been obtained.

A single crystal of the water cluters, (the formation of a cluster of ten water molecules, $(H_2O)_{10}$, in a hydrophobic cavity of the self-assembled coordination cage has been discovered) was grown and its neutron diffraction experiment was performed.

Association of the amyloid protofilaments of hen egg white lysozyme has been studied by time-resolved neutron small angle scattering.

Hydrogen atoms in the crystal structure analysis of synthetic polymers by utilizing 2-dimensional neutron imaging system have been determined.

4. International collaborations

As mentioned above the JAERI-ILL collaborative effort on CRYOPAD project started in this fiscal year resulting into the successful construction and testing of the CRYOPADUM at ILL. Dr. F. Tasset from ILL visited JAERI to discuss the details of the development and Drs. M. Nakamura and M. Takeda visited ILL to attend the cooling test of the new device.

The cooperative researches with ORNL have been continued under the US-Japan cooperative program. The installation of the HB2 shielding tunnel for the thermal guides has been completed at which the WAND instrument will be installed. Efforts to develop computer control and data acquisition hard- and software for the new detector have been made by Drs. Y. Ishii, S. Katano, L. Robertson and J. Fernandez-Baca. When installed at the new HB-2 port it is expected that the combination of a taller neutron beam and a new bent Ge monochromator system will result in a neutron flux gain of 5-10 at the sample position.

2. Research Reports

2.1 Biology

2.1.1 Neutron diffraction experiment of DsrD protein

T. CHATAKE, N. MIZUNO[1], G. VOORDOUW[2], Y. HIGUCHI[3], I. TANAKA and N. NIIMURA

Neutron Science Research Center, JAERI, Tokai, Ibaraki, 319-1195
[1]Division of Chemistry, Kyoto University, Sakyo, Kyoto 606-8502
[2]Department of Biological Sciences, the University of Calgary, Alberta, T2N 1N4
[3]Department of Life Science, Himeji Institute of Technology, Kamigori, Hyogo 678-1297

It is well known that hydrogen bond networks around DNA-binding protein play important roles in DNA recognition. The protein interacts with DNA molecules by direct hydrogen bonds and water-mediated hydrogen bonds, and achieves the specific and precise recognition. However, nobody knows the details of these networks. Dissimilatory sulfite reductase D (DsrD) from the sulfate-reducing bacterium *Desulfovibrio vulgaris* has DNA-binding motif.[1)] We are trying to determine hydrogen-bond networks of this protein including hydrogen atoms by neutron crystallographic analysis, for finding hints to the mechanism of DNA recognition.

In order to get large crystals for neutron experiment, we found a proper condition by two analyses, 'crystallization phase diagram' and 'crystal-quality'. According to the results of these analyses, a largest crystal of DsrD was obtained from D_2O solution by the macro-seeding technique.A largest crystal available to us (1.7 mm^3) was sealed into a NMR sample capillary with D_2O crystallization solution for neutron experiment. Neutron diffraction data was collected at room temperature using monochromatic neutron beam (λ = 2.88 Å) with the BIX-3 [2)] in a neutron reactor JRR-3M at JAERI. 254 still diffraction patterns were recorded on a neutron imaging plate. The total time for the measurement was 30 days. The diffraction patterns were processed with the programs DENZO and SCALEPACK,[3)] which were modified for neutron experiment.

The crystal of DsrD belongs to the space group of $P2_12_12_1$, with cell dimensions of a = 60.5 Å, b = 65.1 Å, c = 46.5 Å. The diffraction patterns were processed up to 2.4 Å. A total of 5,035 independent reflections were obtained from 8,585 observed reflections with an overall R_{merge} of 11.8 %. The completeness of the data was 66.2 %. Only one data set with one rotation axis could be obtained due to the insufficient time for data collection, so the completeness of the data set is not so high. The neutron experiment for collecting reflections missed by the 'blind region' is presently scheduled. Using the present incomplete data, we are trying to solve the neutron structure of DsrD. The initial phases were determined by the molecular replacement method with the program CNS.[4)] Before the refinement, deuterium atoms in the main polypeptide chain and hydrogen atoms, whose positions could be estimated stereochemically, were added into the model. After the first refinement, R-factor was 27.5 % (R_{free} = 31.0 %).This work was supported in part by an 'Organized Research Combination System' Grant from the Ministry of Education, Culture, Sports, Science and Technology, Japan.

References

1) N. Mizuno, D.S. Hittel, G. Voordouw and Y. Higuchi : Acta Cryst. **A58** supplement (2002) C304.
2) I. Tanaka, K. Kurihara, T. Chatake and N. Niimura, : J. Appl. Cryst. **35** (2002) 35.
3) Z. Otwinowski, and W. Minor : Methods Enzymol. **276** (1997) 307.
4) A.T. Brünger, P.D. Adams, G.M. Clore, W.L. DeLano, P. Gros, R.W. Grosse-Kunstleve, J.S. Jiang, J. Kuszewski, N. Nilges, N.S. Pannu, R.J. Read, L.M. Rice, T. Simonsonand G.L. Warren, G. L. : Acta Cryst. **D54** (1998) 905.

2.1.2 Neutron crystallography of B-DNA decamer d(CCATTAATGG)

S. ARAI, T. CHATAKE, T. OHHARA, K. KURIHARA, I. TANAKA and N. NIIMURA

Research Group for Neutron Structural Biology, Neutron Science Research Center, JAERI, Tokai, Ibaraki, 319-1195

Water has long been recognized as an important determinant of nucleic acid structure; the stability, polymorphism and flexibility of the DNA double helix are all hydration-dependent. Moreover, specific hydration patterns play a role in nucleotide sequence recognition by proteins and drugs. [1] In those studies, the observed hydration structure was obtained from the network of only the oxygen atoms of water molecules since it is difficult in an X-ray crystallographic analysis to identify the hydrogen atoms. In order to more fully understand the role in nucleotide sequence recognition by proteins, the location of the hydrogen atoms in this network structure of water molecules is important.

The neutron diffraction is a very powerful method to determine the detailed structure of the biological materials including hydration and hydrogen positions. [2] We are trying to determine the structure of B-DNA duplex by using the neutron diffractmeter BIX-4 [3] with a large single crystal of B-DNA decamar d(CCATTAATGG).

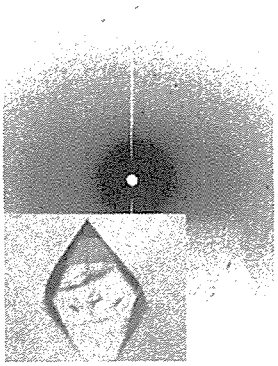

Figure 1: Neutron diffraction pattern of B-DNA decamer and the used crystal.

The DNA decamer was synthesized with a DNA synthesizer. The purity of DNA was analyzed with HPLC and the impurity arising from other macromolecule or species was less than 3.9 %. Salt impurities were removed by the reversed-phase cartridge refinement. A large single crystal was obtained by using the phase diagram information for $MgCl_2$-DNA systems [4] at 6 ℃ for 5 months, in which the size of obtained crystal was 2.8 mm^3. In a neutron diffraction experiment, in order to avoid the high background coming from the incoherent neutron scattering of hydrogen atoms, DNA crystal was grown in D_2O solution. Figure1 shows an example of the neutron diffraction pattern of DNA crystal. The exposure time of each frame was 3-6 hours

Table 1: Crystallographic and refinement statistics of B-DNA decamer d(CCATTAATGG). The values of R-factor, R-free and number of water molecules will be changed because we are refining the structure continuously.

Exposure time	3 - 6 hours /1 frame
Method	Step Scan ($\Delta\phi \sim 0.3°$)
Unit cell	a=b=32.6 Å, c=95.5 Å $\alpha = \beta = 90°$, $\gamma = 120°$
Space group	$P3_221$
Unique reflections	1422
Resolution Range	10-3.0 Å
Completeness (final shell)	63.1 % (64.7 %)
R-merge (final shell)	0.258 (0.240)
R-factor	0.271
R-free	0.359
No. of D_2O	43

and the total time for data collection was 31 days. The wavelength of the incident neutron beam was 2.60 Å. Table 1 shows the crystallographic and refinement statistics of B-DNA decamer d(CCATTAATGG). In the previous study, the 2.3 ÅX-ray structure of this B-DNA duplex has been analyzed and the positions of O atoms of 44 water molecules have been determined. [5] However, the hydrogen positions have never been reported. By the neutron diffraction experiments, we have succeeded in observing many water molecules including the deuteium positions. Several hydrogen atoms, which covalently bound to C atoms, also have been identified.

Figure 2 and Fig. 3 show the $(2|Fo| - |Fc|$ neutron density map contoured at 2.0 σ.

Figure 2 shows an example of water molecules around the phosphate group. Many D atoms of D_2O molecules bound to O atoms of the phosphate group. Moreover, the hydrogen bonds are formed between D_2O molecules. Such as this example, the phosphate groups are surrounded by many water molecules.

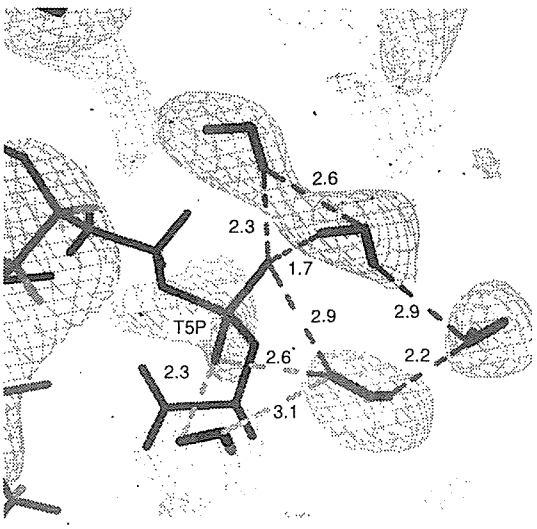

Figure 2: Water molecules near the phosphate group of THY5.

Figure 3 shows one region of the hydration structure in the minor groove. Water molecules form the network structure and connect ADE3 with GUA19. Such as this example, it can be presumed that there are several water molecules to connect the chain A with chain B.

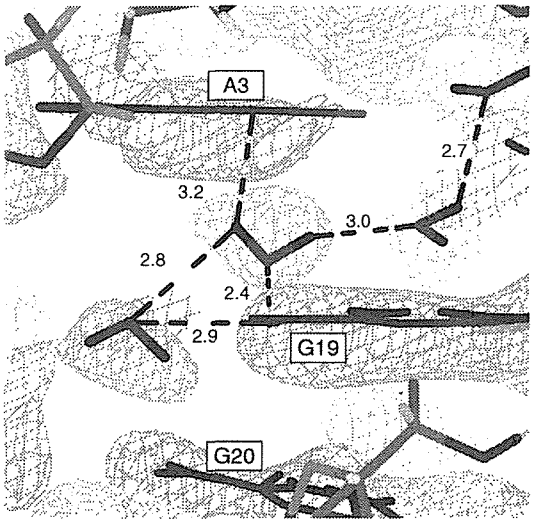

Figure 3: Network structure of the water molecules in the minor groove.

Now we are refining the structure of this DNA duplex including the locations of water molecules. This study is carried out as a part of "Development of New Structural Biology Including Hydrogen and Hydration" in ORCS promoted by Ministry of Education, Culture, Sports, Science and Technology of Japan.

References

1) Z. Owtinowski, R. W. Schevitz, R.-G. Zhang, C. L. Lawson, A. Joachimiak, R. Q. Marmorstein, B. F. Luisi, and P. B. Sigler : Nature **335** (1988) 321.
2) N. Niimura : Curr. Opin. Struct. Biol. **9** (1999) 602.
3) K. Kurihara, I. Tanaka, M. Refai Muslih, A. Ostermann, and N. Niimura : Journal of Synchrotron Radiation, in press.
4) S. Arai, T. Chatake, and N. Niimura : Acta. Cryst. D. **58** (2002) 151.
5) D.S.Goodsell, M. Kaczor-Grzeskowiak, and R.E. Dickerson : J. Mol. Biol. **239** (1994) 79.

2.1.3 Neutron diffraction experiment of cubic insulin crystal

M. MAEDA[1], T. CHATAKE[1], I. TANAKA[1], A. OSTERMANN[2] and N. NIIMURA[1,3]

[1]Neutron Science Research Center, JAERI, Tokai, Ibaraki 319-1195
[2]Physik-Department E 17 der TUM, James Frank Str., 85747 Garching, Germany
[3]Faculty of Technology, Ibaragi University, Naka-Narusawa, 4-12-1,Hitach, Ibaragi 316-8511

Hydrogen atoms and hydration water molecules surrounding protein play important roles in many physiological functions. Neutron diffraction for protein crystallography using a neutron imaging plate system has become a powerful method for locating position of hydrogen (deuterium) atoms and bound waters of protein.[1)] The cubic insulin crystal (space group $I2_13$, a=b=c=78.9Å) contains a solvent volume of 65 % and has multiple hydration layers.[2)] The first neutron protein crystallography of 2Zn insulin has been reported at 2.2 Å resolution,[3)] however, the difinite structure of hydrogen and hydration could not be obtained. On the other hand, there is no report of the cubic insulin. To elucidate hydrogen and hydration in cubic insulin crystals, a large single crystal of cubic porcine insulin for neutron protein crystallography has been grown in D_2O by using a phase diagram technique. We have succeeded in growing a large single crystal (4.0 x 4.0 x 1.3 mm^3 in volume) of cubic porcine insulin using the technique.

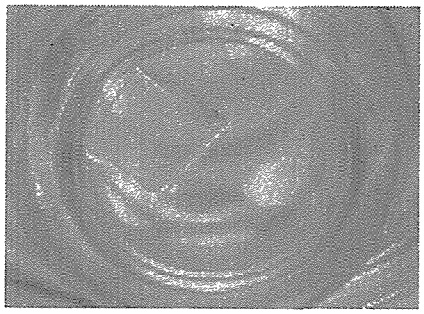

Figure 1: The photograh of cubic porcine insulin crystal grown in D_2O.

The neutron diffraction experiments were carried out with the neutron single crystal diffractometer BIX-3 installed at JRR-3 reactor in JAERI at room temperature. The crystal was sealed in quartz capillary for the measurement. The step scanning method was used for the data collection. The collection time per a frame was 55 minutes controlled by the monitor counts of direct beam in front of the crystal. The total number of 300 frames (which corresponds to 90 ° crystal rotation) was collected in the measurements.

One of the topical results is shown as follows. The protonation and deprotonation of two nitrogen atoms (Nπ, Nτ) in imidazole ring of histidine are very important information to discuss protein crystallography. This information can be given by neutron diffraction. In His 5 in B-chain, Nπ is protonated and Nτ is deprotonated. On the contrary, in His 10, both Nπ and Nτ are protonated. This means that His 5 is electrically neutral and His 10 is positively charged.

This study is supported by a grant from the Organized Research Combination System (ORCS).

References

1) N. Niimura, Y. Minezak, T. Nonaka, J-C Castanga, F. Cipriani, P. Hoghoj, M. S. Lehmann and Wilkinson: Nat Struct Biol. **4** (1997) 909.
2) J. Badger : Biophys. **61** (1993) 816.
3) A. Wlodawer, H. Savage and G. Dodson: Acta. Cryst. B. **45** (1988) 99.

2.1.4 Neutron scattering study on self-assembly of keratin molecules in water

S. NAITO, T.KARINO[1], M. FURUSAKA[1], S. FUJIWARA[2], and N. NIIMURA[2]

The Institute of Advanced Science Research, L'ORÉAL Tsukuba Center, Tsukuba, Ibaraki 300-2635
[1]High Energy Accelerator Research Organization, Tsukuba, Ibaraki 305-0801
[2] Japan Atomic Energy Research Institute, Ibaraki 319-1195

The aim of this study is to clarify structural changes of proteins in apoptosis. Once apoptotic trigger is pulled in a hair cell, the cell begins to produce enormous amount of keratin proteins. Then, SS cross-linking is induced between the molecules and keratin proteins are finally gelated [1]. Keratin is a major component of many tissues such as hair, nails, and quills. It consists of 2 types of keratin, *i.e.*, Type I 48kDa, acidic) and Type II (53kDa, basic). Wide-angle X-ray diffraction patterns of hair and other keratin fibers show an equatorial spacing of 9.8 Å, corresponding to the thickness of the α-helical coiled coil compound constructed of Type I and Type II keratins. Indeed, it is known that keratin assembles spontaneously multimer, and finally forms 10nm filaments. However, the organization process and structure of keratin in aqueous solution have not been well understood. We synthesized gene-expressed Type I and Type II keratins and the chemically modified the cysteine resides to the s-carboxymethyl alanyl disulfide ($R\text{-}S\text{-}SCH_2COO^-$, CMADK), and investigated the structure of keratin proteins in aqueous solution by small-angle neutron scattering (SANS). We confirmed the presence of keratin multimers in the buffer (10 mM Tris-HCl buffer solution, pH 7) containing a higher salt concentration, 50mM by SANS (SANS-J) measurement [2].

SANS was undertaken at SANS-J [neutron wavelength (λ= 7 Å) , sample distance (L=10m)] situated at the end of a cold-neutron guide tube from the JRR-3 reactor and at WINK [Pulsed Neutron Scattering Facility in KEK]. Figure 1 shows the scattering mixture in the buffer (10 mM Tris-HCl buffer, pH 6.2) by SANS measurements. CMADK formed the multimers without the higher concentration of salt when the pH of the solution approached to the isoelectric point (~pH 5). Double logarithmic SANS plot profiles of CMADKs in the buffer solution showed straight line which has a equimolar mixture in the buffer (10 mM Tris-HCl buffer, pH 6.2) by SANS measurements. CMADK formed the multimers without the higher concentration of salt when the pH of the solution approached to the isoelectric

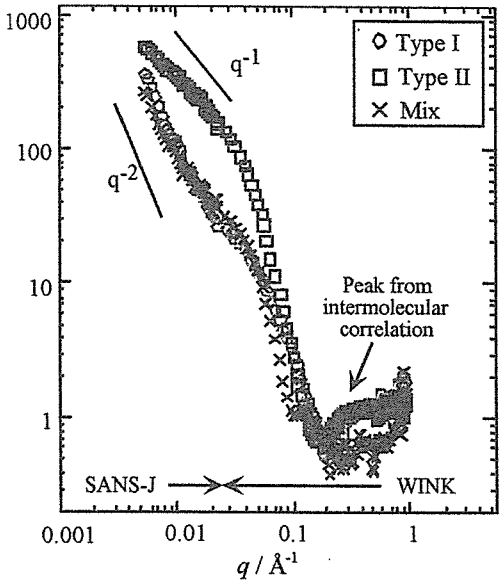

Figure 1 SANS profiles of CMADKs aq. soln. at pH 6.2.

point (~pH 5). Double logarithmic SANS plot profiles of CMADKs in the buffer solution showed straight line which has a slope of −1 (0.01<q<0.3), however, the slope increased in the lower q range. This suggests that CMADKs exist as bent rod-like molecules. The scattering function, which a cylindrical scattering function combined with Debye one was applied to fit the scattering curves from bent rod-like CMADKs. The scattering intensity $\langle I(q)\rangle$ for the bent rod-like cylindrical chain was given by the following equations.

$$I(q)=\frac{a}{V_{cyl}}\int_0^{\pi/2} f^2(q,\alpha)\sin\alpha d\alpha+\frac{b}{q^2} \quad (1)$$

$$f(q,\alpha)=2(\rho_{cyl}-\rho_{solv})V_{cyl}\,j_0(qH\cos\alpha)\frac{J_1(qr\sin\alpha)}{qr\sin\alpha} \quad (2)$$

$$V_{cyl}=\pi r^2 L \quad j_0=\frac{\sin(x)}{x}$$

where r is the radius of cylinder, $2H$ the height, ρ_{cyl} the scattering length of cylinder, ρ_{sol} the scattering length of solvent, a the volume ratio of particle

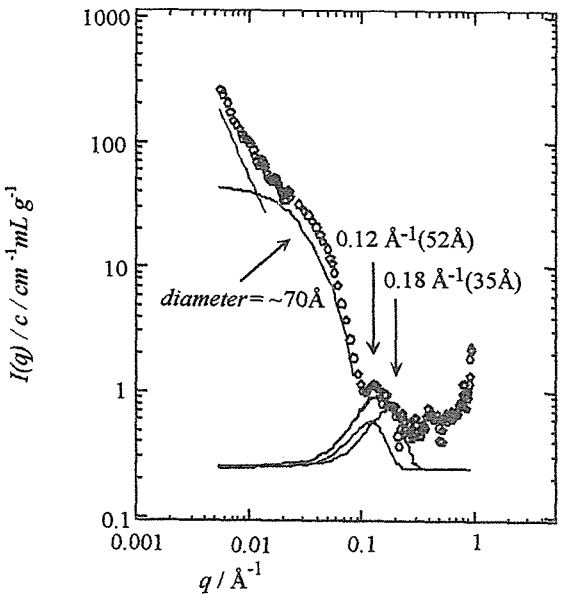

Figure 2 Modified cylindrical analysis and Gaussian fitting of SANS profiles of the eqimolar mixture consisting of Type I and Type II CMADK.

and *b* the extent of bending. Gaussian fitting was performed to the scattering profiles observed in the higher *q* ranges to determine the intermolecular correlations. Figure 2 shows typical fitting curves for the scattering profile of the equimolar mixture consisting of Type I and Type II CMADK in the buffer (pH 6.2). The diameter of the cylindrical rod-like multimer was 70Å and 2 intermolecular correlation lengths were determined from Gaussian fitting, 52Å and 35Å. On the other hand, it was found Type I and Type II CMADK was self-assembled in the buffer (pH6.2) respectively. The diameter of Type I was 38Å (4-mer) and Type II 65Å (12-mer). The minimum correlation size was 15Å and common to both types. This length suggested corresponding to the correlation between each molecule of Type I or Type II. However, the scattering intensities of the peaks from intermolecular correlation were very weak compared with those of the equimolar mixture, meaning the same type of keratin is self-assembled by very weak mutual interactions.

On the basis of the results, the schematic diagram of the assembled structure between Type I and Type II keratin in water is shown in Fig. 3. When Type I keratin is mixed with Type II at the

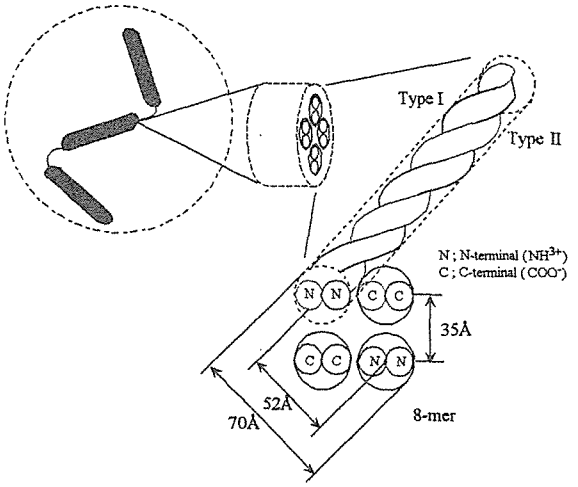

Figure 3 Schematic diagram of the assembled structure between Type I and Type II keratin in water or Type II.

same morality, two molecules form 8-mer consisting of 4 pieces of coiled-coil dimmer as a basic unit. Type I or Type II form aggregates in water respectively, however, not coiled-coil form. The interaction between the same type of keratin is considered owing to the electrostatic interaction betweenα-amino terminal and β-carboxy one. This kind of interaction is generally very weak, so the antiparallel aggregation may occur randomly. Therefore, intermolecular correlation becomes ambiguous. Whereas, the different type of keratins curiously assemble forming stable coiled-coil structure, in which N-terminal or C-terminal faces each other, that is, in parallel. We consider that both of Type I and Type II have specific sites in variable region to recognize each type just like a relation between key and keyhole. The coiled -coil formation does not begin until the molecular recognition arises between Type I and Type II keratin. However, those critical recognition sites have not cleared. The 8-mers easily assemble in axial direction one after another by electrostatic interaction since the electrical distribution at the distal end of 8-mer is well-balanced. The linking part among rod-like 8-mer corresponds to the variable region of keratin molecules, so it suggests the flexible bent rod-like molecules.

Reference

1)F. Ikkai and S. Naito: *Biomacromolecules* **3** (2001) (3) 482-487.

2) S.Naito *et al.*: JAERI-Review **2002-028** (2002) 84.

2.1.5 Neutron Diffraction Measurements of Single Crystals of Hen Egg White Lysozyme under Various Conditions

S. FUJIWARA

Neutron Science Research Center, JAERI, Tokai, Ibaraki 319-1195

Hydrogen atoms play essential roles in various aspects of functions of proteins. Moreover, hydrogen bonds between the atoms in the protein as well as hydration are important in the stability of the protein. Locating the positions of hydrogens and hydrated water is therefore important in considering the molecular mechanism of the protein function and the stability of the proteins. Neutron crystallography, which can locate the hydrogens, is one of the important methods to investigate these problems. We have started projects of exploring various aspects of hydrogens and hydrogen bonds in a protein with neutron crystallography. We used hen egg white lysozyme (HEWL) as a model protein, and measured neutron diffraction of single crystals of this protein under various conditions. In order to obtain information of the protonation state of amino acid residues in the protein at various pH, since the charge distribution of the protein, we collected the neutron diffraction data of the single crystal of HEWL grown in pH 4.9[1)2)]. and 3.4[3)], and preliminary structure analysis[4)] of these data detected the hydrogen-bond networks including the hydrated water around the active site of this enzyme.

Another ongoing project has been related to the mechanism of enzyme activity of HEWL. HEWL is an enzyme that hydrolyses a polysaccharide. To gain insight into the mechanisms of enzyme activity such as lysozyme, we performed the measurements of neutron diffraction of single crystals of the complex of HEWL and substrate-analogue, NAG_3[5)]. A solution containing 30 mg/ml HEWL in 50 mM sodium acetate (pH 4.3) in D_2O was mixed with a solution containing NAG_3 and NaCl to make 1:1 complex of HEWL and NAG_3. Crystals were formed in about two weeks, and the crystals grew only to the size of about 3 mm^3. The space group of the crystals was $P4_32_12$, and the cell parameters were $a = b = 7.91nm$, $c = 3.66nm$. Neutron diffraction patterns of the crystal were measured with BIX-2[6)]. The oscillation method of 0.4 degrees has been employed. Exposure time per one frame has been 24 hours. In addition to the data taken during the last fiscal year, the data of 30 degrees of rotation range were collected, and the data reduction and structural analysis are currently underway.

We have also been measuring neutron diffraction patterns of single crystals of HEWL in H_2O to investigate a possibility of extracting hydrogen and water positions without interferences from other atoms by difference intensities between the diffraction from HEWL in D_2O and that in H_2O. We prepared single crystals of HEWL grown in H_2O for this purpose. Crystals were grown to the size of about 10 mm^3. Neutron diffraction measurements with BIX-2 yielded clear diffraction patterns even in the crystals in H_2O. The data reduction and structural analysis are now ongoing.

References

1) S. Fujiwara et al.: JAERI Review **99-003** (1999) 13.
2) S. Fujiwara et al.: JAERI Review **2000-005** (2000) 7.
3) S. Fujiwara et al.: JAERI Review **2002-006** (2002) 19.
4) M. Maeda et al.: J. Phys. Soc. Jpn. **70** (2001) Suppl. A 403.
5) S. Fujiwara et al.: JAERI Review **2002-028** (2002) 86.
6) S. Fujiwara et al.: Physica B **241-243** (1998) 207.

2.1.6 Neutron Fiber Diffraction of the Muscle Thin Filaments

S. FUJIWARA[1], F. MATSUMOTO[1,2], and S. DESHIMARU[1,2]

[1]Neutron Science Research Center, JAERI, Tokai, Ibaraki 319-1195
[2]Laboratory for Structural Biochemistry, RIKEN Harima Institute, Hyogo 679-5148

Muscles consist of the structural units called sarcomeres that consist of mainly two kinds of filamentous structures; actin-based "thin" filaments and myosin-based "thick" filaments. We have been studying the structures of muscle and muscle proteins using neutron diffraction and scattering[1-3]. In studying such filamentous structures, measurements of the oriented samples increase the structural information obtained. It is, however, difficult to orient large amount of the samples. In order to check feasibility of neutron fiber diffraction, we oriented the purified thin filaments in quartz capillaries and measure diffraction patterns of these samples.

We put the thin filament sols purified from bovine hearts into a quartz capillary with a diameter of 3 mm. The thin filaments were then oriented in magnetic field of 19 Tesla. Length of the oriented region in the capillary was about 3 mm. The sample containing the oriented region was put on a sample holder specifically made for the capillary samples, and the regions other than the oriented region were masked with Cd plates. The sample was then illuminated with neutrons. These neutron fiber diffraction measurements were done with the Small-Angle Neutron Scattering Instrument (SANS-J) at the guide hall of the reactor JRR-3M in Japan Atomic Energy Research Institute. Neutrons with the wavelength of 6.5 Å($\Delta\lambda/\lambda$=12.98%) were employed, and the sample-to-detector distance was 1.5 m.

Figure 1 shows an example of the neutron diffraction patterns of the oriented thin filaments. Exposure time of this pattern was 20 hours. A strong intensity on the equator, actin-based layer lines at 59 Åand 51 Å, and a weak cross-pattern across the equator due to tropomyosin were observed. Moreover, at least up to 3rd layer lines of the meridional reflections due to troponin were clearly observed. This suggests a possibility of extracting the layer-line reflections of each subunit within the troponin complex by combining neutron fiber diffraction measurements with selective deuteration and the contrast-matching technique. These projects are currently underway.

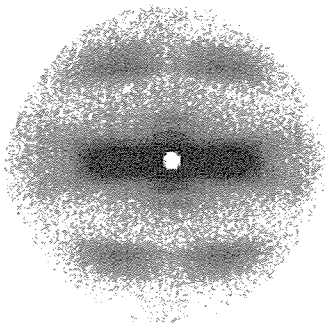

Figure 1: An example of neutron diffraction patterns of the oriented samples of the thin filaments.

Supported in part by Special Coordination Funds for Promoting Science and Technology from the Ministry of Education, Culture, Sports, Science and Technology, the Japanese Government.

References

1) S. Fujiwara *et al.*: J. Phys. Soc. Jpn. **70** (2001) Suppl. A 408.
2) S. Fujiwara *et al.*: JAERI Review **2002-028** (2002) 87.
3) F. Matsumoto *et al.*: JAERI Review **2002-028** (2002) 88.

2.1.7

Association of the Amyloid Protofilaments of Hen Egg White Lysozyme Studied by Time-Resolved Neutron Scattering

S. FUJIWARA[1], F. MATSUMOTO[1,2], and Y. YONEZAWA[3]

[1]Neutron Science Research Center, JAERI, Tokai, Ibaraki 319-1195
[2]Laboratory for Structural Biochemistry, RIKEN Harima Institute, Hyogo 679-5148
[3]Institute for Protein Research, Osaka University, Suita, Osaka 565-0871

Amyloid fibrils are filamentous protein aggregates found in a wide variety of proteins including the disease-related proteins. Understanding of the mechanism of the amyloid fibril formation is not only important for the development of therapeutic strategies against the amyloid diseases but also of considerable help to gain an insight into the generic properties of proteins related to the mechanisms of folding and stability. It was found recently that hen egg white lysozyme (HEWL) forms the amyloid fibrils in highly concentrated ethanol solution[1]. The HEWL-water-ethanol system is suitable to study the general mechanism of the amyloid fibril formation. We investigated structural states of HEWL in this model system with static small-angle X-ray and neutron scattering (SAXS and SANS) measurements[2] and proposed a pathway of the amyloid fibril formation of HEWL as the process consisting of three stages; the formation of the dimers, the formation of the protofilaments, and the formation of the amyloid fibrils *via* a lateral association of the protofilaments.

Here we performed time-resolved SANS measurements to monitor process of the formation of the amyloid fibrils[3] with SANS-J at the guide hall of the reactor JRR-3M in JAERI. The time-resolved measurements were done by successive collection of the data of 30 minutes exposure. Figure 1 shows the association process of the protofilaments of HEWL at 0.5 mM NaCl in 90% ethanol, in terms of the relative changes in the structural parameters estimated from the cross-sectional Guinier analysis of the scattering curve of each frame in the time-resolved measurements.

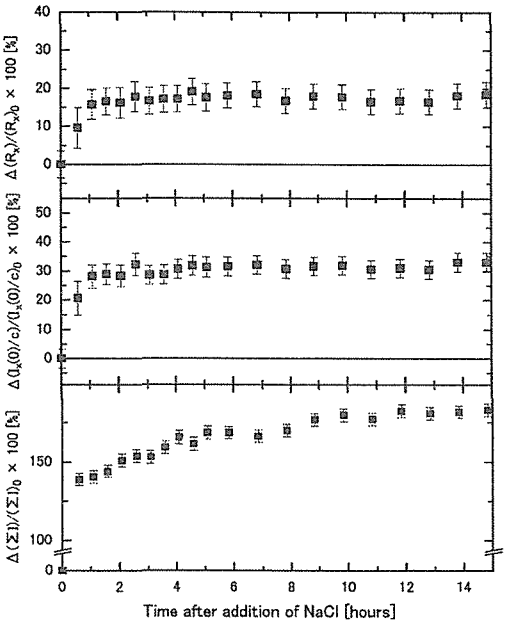

Figure 1: Time courses of the relative changes in the parameters (cross-sectional radius of gyration, $I_X(0)/c$, and integrated intensity) after addition of NaCl.

The manner in which these changes occur suggests that the association of the protofilaments of HEWL occurs *via* the lateral association of the protofilaments, followed by the cross-linking of the fibrils formed.

References

1) S. Goda et al.: Protein Sci. **9** (2000) 369.
2) Y. Yonezawa et al.: J. Mol. Biol. **323** (2002) 237.
3) S. Fujiwara et al.: J. Mol. Biol. **331** (2003) 21.

2.1.8
Small-Angle Neutron Scattering Measurements of TroponinC on the Thin Filament

F. MATSUMOTO[1,2], K. MAKINO[2], K. MAEDA[2], Y. MAEDA[2], and S. FUJIWARA[1]

[1]Neutron Science Research Center, JAERI, Tokai, Ibaraki 319-1195
[2]Laboratory for Structural Biochemistry, RIKEN Harima Institute, Hyogo 679-5148

Main components of muscles are two kinds of filaments, actin-based "thin" filaments and myosin-based "thick" filaments. Muscle contraction occurs via sliding of these filaments past each other. The molecular mechanism of the muscle contraction and its regulation is one of the most important problems in biophysics, as it is a typical example of energy transduction mechanisms of living organisms. In vertebrate skeletal and cardiac muscles, muscle contraction is regulated via the interactions between the thin filament proteins, troponin (Tn) C, TnI, TnT, tropomyosin, and actin. These interactions are triggered by binding of Ca^{2+} to TnC. We have been investigating the structure of TnC on the thin filament with and without Ca^{2+}, as a first step toward understanding the regulation mechanism of the muscle contraction.

Neutron scattering was employed to do this. Structural information of a selected component within a protein complex can be obtained with this method, when it is combined with the strategies of selective deuteration and contrast matching. We prepared the deuterated (d-) TnC by expressing the protein in *E. coli* in D_2O medium containing deuterated algal peptone. The purified d-TnC was exchanged into the native thin filaments by CDTA treatment. The native thin filaments containing d-TnC were then exposed to neutrons under the condition where the contrast of the other components of the thin filaments were matched out with 40% D_2O.

During the last fiscal year, we had measured small-angle neutron scattering patterns of these samples with and without 1.1 mM $CaCl_2$ with the Small-Angle Neutron Scattering Instrument (SANS-J) at the guide hall of the reactor JRR-3 in JAERI[1]. Experimental setting had been as follows: neutrons with the wavelength of 6.5 Å($\Delta\lambda/\lambda$=12.98%) were employed, and the sample-to-detector distance was 4 m. This year we performed similar measurements with the sample-to-detector distance of 2 m, in order to obtain the scattering curves covering wider Q-range. Figure 1 shows the merged scattering curves of d-TnC on the thin filaments with and without Ca^{2+}. Excellent agreements in the overlap Q-range between the curves with different sample-to-detector distances were observed.

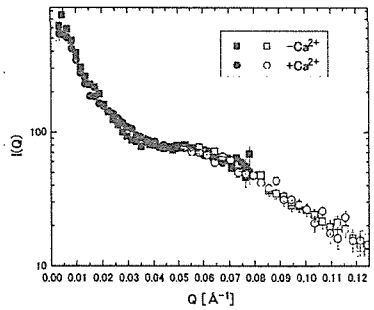

Figure 1: The merged neutron scattering curves of d-TnC on the thin filaments with and without Ca^{2+}.

Analysis of these scattering curves by model calculation is now underway. Supported by Special Coordination Funds for Promoting Science and Technology from the Ministry of Education, Culture, Sports, Science and Technology, the Japanese Government.

References

1) F. Matsumoto *et al.*: JAERI Review **2002-028** (2002) 88.

2.2 Soft Matter

2.2.1
Viscoelastic effects on the nucleation and growth in dynamically asymmetric mixtures

M. TAKENAKA[1], N. IWASE[1] and T. HASHIMOTO[1] and S. KOIZUMI[2]

[1]Department of Polymer Chemistry, Graduate School of Engineering, Kyoto University, Kyoto 606-8501
[2]Advanced Science Research Center, JAERI, Tokai, Ibaraki 319-1195

Recently, it has been found that the dynamical asymmetry between constituent components in a mixture causes the coupling between stress and diffusion during phase separation processes of the mixture due to the asymmetric stress division. This coupling is called "viscoelastic effects" and has been found to causes shear-induced phase separation in polymer solutions and non exponential decay in dynamic scattering near equilibrium. We aim to explore how the viscoelasticity affects the nucleation and growth processes in dynamically asymmetric semi-dilute polymer solutions. The strength of the effects of the viscoelastic effects is characterized by the viscoelastic length ξ_{ve} defined by

$$\xi_{ve} = \left(\frac{4D\eta_0}{3K_{OS}}\right)^{0.5},$$

where D, η_0, and K_{OS} are, respectively, the inter-diffusion coefficient, the zero-shear viscocity, and the osmotc compressibility. In order to estimate the ξ_{ve}, we need to obtain the the value of K_{OS}. Thus in this study we measured the scattering function of the solution and estimated K_{OS}. The sample used here was deutarated polystyrene (dPS, weight average molecular weight = 5.0×10^6)/Ddiethyl Moronate (DEM) =96/4 (wt.wt.). A SANS experiment of dPS/DEM was done using SANS-J. Fig.1 shows the temperature dependence of the scattered intensity S(q) of dPS/DEM. S(q) increases with decreasing temperature since dPS/DEM becomes close to the spinodal point with decreasing temperature. S(q) in the measured temperature region can be fitted with the following Ornstein-Zernike form:

$$S(q) = \frac{S(0)}{1+q^2\xi^2},$$

where ξ is the thermal correlation length. We obtained ξ and S(0) from fitting. From S(0) we estimated K_{OS}. The osmotic compressibility increases with temperature, indicating that the system has the UCST type phase diagram. We will estimate ξ_{ve} by combining the results of the dynamic light scattering experiment for the solution.

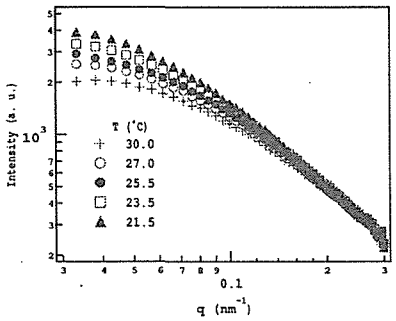

Figure 1: Fig.1 T-dependence of S(q) for dPS/DEM.

2.2.2

Small-angle Neutron Scattering Study on in-situ observation of NIPA-*block*-PEG qiasi-living polymerization

Ryuhei Motokawa, Masahiko Annaka, Takayuki Nakahira, and Satoshi Koizumi[1]

Department of Materials Technology, Chiba University, Inage-ku, Chiba 263-8522, Japan
[1]Advanced Science Research Center, Japan Atomic Energy Research Institute, Tokai-mura, Ibaraki 319-1195, Japan

The thermal sensitive diblock copolymer which is composed of poly(N-isopropylacrylamide) (NIPA) and monomethoxy-poly(ethylene glycohl) (PEG) shows immensely unique phase behavior in water. NIPA polymer is a well-known thermal sensitive polymer. It is soluble in water at room temperature but undergoes a phase separation at temperatures higher than its lower critical solution temperature (LCST) at around 32°C. An aqueous solution of NIPA-*block*-PEG indicates three distinct macroscopic phases reversibly, on varying temperature; sol, gel, and phase-separated phase, where the driving force is the coil-grobule transition due to hydrophobic interaction with NIPA block chains.

NIPA-*block*-PEG was prepared for radical polymerization by using ceric ammonium nitrate (IV) as a redox initiator in aqueous solution. A ceric ion redox system was applied for the formation of radical at the terminal carbon of PEG (-CH_2-OH). These PEG termination radicals are used for the polymerization of NIPA monomer. The polymerization method can yield the diblock copolymer with comparatively narrow molecular weight distribution ($M_w/M_n \sim$ 1.25). The cause is supeculated as follows. Performing this polymerization in water above the LCST for NIPA polymer, NIPA chains happen to aggregate with propagating reaction. Therefore, it seems that micelle like structure is organized itself, NIPA-core and PEG-corona, propagation step proceeds within the core of the micelles. Namely, the self-organized structure, which is induced by the polymerization process, has NIPA monomers consume effectively like an emulsion polymerization. We carried out in-situ observation for NIPA-*block*-PEG polymerization process using the time sliced SANS measurement in order to investigate the structure formation and the effect of the micro-structure on polymerization products in non-equilibrium condition.

The neutron scattering experiment was employed Pinhole type Small Angle Neutron Scattering with spectrometer SANS-J at JRR-3M research reactor of Japan Atomic Energy Research Institute (JAERI), Tokai, Ibaraki, Japan. In SANS, the incident neutron beam was collimated into 0.65 nm with $\Delta\lambda/\lambda = 14\%$. The scattered neutrons detected on the 2-dimensional position sensitive detector with a diameter of 0.58 m. The beam stopper size has 40 mm diameter. NIPA-d_7 substituted by isopropyl hydrogen -$CD(CD_3)_2$ was prepared ourselves, and conducted polymerization in H_2O at 32°C on account of obtaining for good contrast between NIPA and PEG-H_2O. Sample in quartz cell of 2 mm thickness was irradiated by neutron beam. The observation time slice scale was carried out 10 min in order to get sufficient statistics of scattering intensity. The sample to detector distance was 6 m ($0.06 < q = 4\pi sin\theta/\lambda < 0.5nm^{-1}$).

Figure 1 shows SANS profiles. The rise in scattering intensity was observed with proceeding polymerization. The results indicate that two effects of propagation reaction and growth of aggregation structure were reflected simultaneously. The power law behaviors of q^{-2} and q^{-4} in Figure 1 maybe make it follow that mass distribution of micelle structure and NIPA strongly aggregated domain forming a clearly sharp interface into PEG-H_2O matrix respectively. We are investigating more detail due to reveal the correlation between polymerization reaction and self-organized structure.

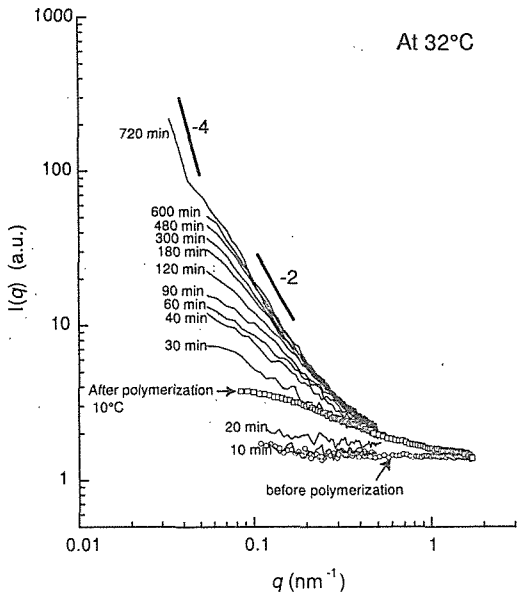

Figure 1: SANS profiles were obtaned for in-situ observation of NIPA($-d_7$)-*block*-PEG polymerization process at 32°C (solid lines), before (open circles) and after (open squares) polymerization.

2.2.3 Crystal Structure of Polymer (Cellulose)

Yasuhiro TAKAHASHI

Department of Macromolecular Science, Graduate School of Science, Osaka Univeristy
Toyonaka, Osaka 560-0043, Japan

Neutron diffraction has several advantages in comparison with X-ray diffraction for crystalline polymers.[1-7] New Information about crystal structure could be obtained differing from the X-ray work. The scattering length of an atom is independent of the atomic number. Accordingly, the hydrogen and deuterium atoms have different scattering lengths for neutron diffraction, although they have the same scattering length for X-ray diffraction. The scattering lengths of hydrogen (-3.74) and deuterium (6.67) located on the outer shell of the molecule are comparable to the scattering lengths of carbon (6.65) and oxygen (5.80). Therefore, the azimuthal angle of the molecule can be determined by neutron diffraction more accurately than by X-ray diffraction. Furthermore, the scattering lengths by neutron diffraction are independent of the scattering angle θ. The intensities of the refections with large θ values can be observed strongly and can be measured accurately. Accordingly, it can be said that neutron structure analysis gives more accurate crystal structure than X-ray structure analysis.

In the previous works, [1-7] neutron structure analyses of crystalline polymers were carried out on the equatorial reflections in the temperature range 10 -300K by using powder diffractometer. In the case of poly(vinyl alcohol),[3] the intramolecular hydrogen bond was found in the isotactic sequence of the atactic polymer. In the cases of deuterated polyethylene,[4] poly(p-phenylenebenzobisoxazole)(PBO),[5] and poly(p-phenylenebenzobisthiazole)(PBZT),[6] the more detailed structure than X-ray works could be obtained. In the case of poly(pyridobisimidazole)(PIPD),[7] the statistical structure was clarified by utilizing the difference in scattering lengths between nitrogen and carbon. However, only two-dimensional structure projected through the fiber axis can be obtained by using the powder diffractometer.

Therefore, in order to obtain the three-dimensional structure, the attempts to take the fiber diagram of crystalline polymers were made by using neutron imaging plate in the present study. Unfortunately, the fiber specimen of dueterated cellulose II was broken during the drying procedure. But the fiber diagrams of the several crystalline polymers could be taken. However, the number of observed reflections was not sufficient to analyse the crystal structure because the signal-to-noise ratio is not good. The development of the following procedure is now in progress. After summing the data of several imaging plates in order to improve the signal-to-noise ratio, the integrated intensities are estimated according to the procedures in X-ray diffraction.[8]

References

1) Y. Takahashi, "Neutron Structure Analyses of Crystalline Polymers", Recent Res. Devel. in Macromol. Res., **3** (1998) 265.
2) Y. Takahashi, "Neutron Diffraction by Crystalline Polymers", ACS Symposium Series 739, "Scattering from Polymers" edited by P. Cebe, B. S. Hsiao, and D. J. Lohse, Chapter 5 **74** (2000).
3) Y. Takahashi: J. Polymer Sci. **Part B** Polym. Phys., **35** (1997) 193.
4) Y. Takahashi: Macromolecules **31** (1998) 3868.
5) Y. Takahashi: Macromolecules **32** (1999) 4010.
6) Y. Takahashi: Macromolecules **34** (2001) 2012.
7) Y. Takahashi: Macromolecules **35** (2002) 3942.
8) Y. Takahashi and H. Sul, *to be published.*

2.2.4

Elastic incoherent scattering studies of poly(styrene) and poly(vinyl methyl ether) mixtures

H. Takeno and S. Koizumi[1]

Department of Biological and Chemical Engineering, Faculty of Engineering, Gunma University, Gunma 376-8515
[1]Japan Atomic Energy Research Institute, Tokai, Ibaraki 319-1195

In the past few decades, numerous studies have been performed on the miscibility of polymer blends. It is strongly affected by local packing of molecules such as free volume. Such local packing may affect scales of local motions such as mean square displacement of the system. We studied elastic incoherent scattering of polystyrene (PS) and poly(vinyl methyl ether) (PVME) blends with a low energy triple axis spectrometer (LTAS). Since incoherent scattering cross section of hydrogen is much larger than those of other atoms, we can obtain information about geometry of molecular motions through incoherent scattering due to hydrogen. In order to pursue the effect of the motion of each component on blending, we used two kinds of blends, deuterated PS(dPS) /PVME and protonated PS (hPS) /PVME blends (since synthesis of deuterated PVME is technically very difficult, we cannot use it), and those of pure protonated components for comparison. When the motion of the system is vibrational, the elastic incoherent scattering behavior can be described by Debye-Waller factor $I(q,\omega=0) = I_0\exp(-<u^2>q^2)$, where $<u^2>$ is the mean square displacement and $q(=(4\pi/\lambda)\sin(\theta/2))$ is the scattering vector. In fact, the scattering intensity observed for all samples had a small coherent scattering peak. Therefore, in order to eliminate the coherent effects,[1] we divided the scattering intensity at a given temperature by that at lowest temperature (ca. $T_{\min} = 10$K). Though plot of the logarithm of the divided intensity $\ln[I_T(q,\omega=0)/I_{T_{min}}(q,\omega=0)]$ against q^2 showed the linear behavior at lower temperature region than 90 or 120 K at least in the q-region covered in our measurements and it has a slight curvature at temperature region of or $T \geq 90$ or 120 K, i.e., it shows the non-Gaussian behavior. Therefore, in the latter region, we carried out the non-Gaussian analysis,

$$I(q,\omega=0) = I_0\left[\exp\left(-\alpha_T q^2 + (1/2)A_{0,T}\alpha_T^2 q^4\right)\right]$$

, where $\alpha_T = <u^2>/6$ and $A_{0,T}$ is a parameter, which characterizes non-Gaussian nature. $A_{0,T}$ may be related to dynamical heterogeneity due to different local environments. For hPS/PVME, both components involve hydrogen atoms, we analyzed it with double non-Gaussian equation, assuming additivity of non-Gaussian contribution for each component. In the fitting procedure with the double non-Gaussian equation, since we had too many adjustable parameters, we fixed the parameters for PVME by using the parameters obtained for dPS/PVME blends and obtained parameters them for hPS. The α_Ts and $A_{0,T}$s obtained thus for all the samples are shown in Figures 1 and 2, respectively. In comparison of dPS/PVME with PVME, although $A_{0,T}$ is almost the same for both samples, α_T for dPS/PVME is larger than that of PVME in the temperature region of $T \geq 120$K. The latter result indicates that spatial scale of motion of PVME in the blend is larger than that of pure components. On the other hand, as compared with the motions of PS, though α_T is hardly affected by blending, $A_{0,T}$ becomes remarkably larger relative to that of pure PS. Broadening of the distribution of local motions has been reported by Fisher et al. for a mixture of a low-molecular weight substance and polycarbonate with the same

benzene ring as PS.[2] Especially, we would like to note the behavior of α_T, which is related to the mean square displacement. By blending, the mean square displacement for PVME with small side groups became larger, while it for PS with bulky side groups did not. The result supports our "interstices model" proposed from phase diagram and glass transition temperature behavior of polymer blends, in which the small molecules go into interstices produced by another bulky molecules.[3]

References

1) T. Kanaya , T. Kawaguchi and K. Kaji: J. Chem. Phys. **104** (1996) 3841.

2) E. W. Fisher, G. P. Hellmann, H. W. Spiess, F. J. Horth, U. Ecarius and M. Wehrle: Macromol. Chem. Suppl. **12** (1985) 189.

3) M.Naoki and H. Takeno: to be submitted.

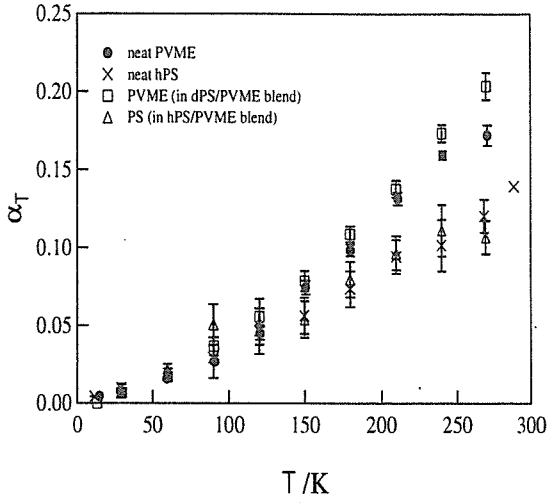

Figure 1: Temperature dependence of α_T for various samples.

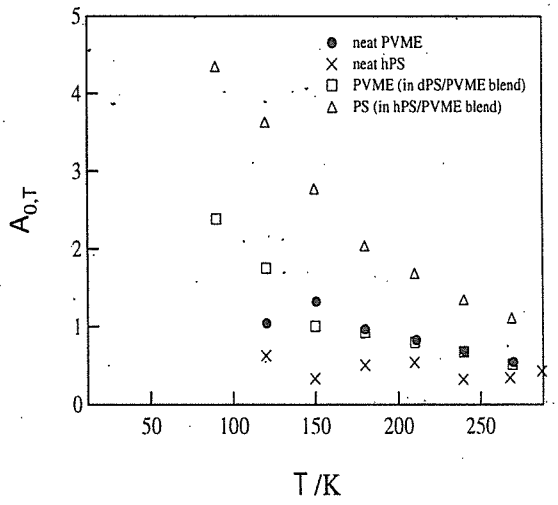

Figure 2: Temperature dependence of $A_{0,T}$ for various samples.

2.2.5

Dynamical Asymmetry Effect of Long-Chain Branching in Polyethylene Blends

T. KASAHARA, S. UTSUMI, T. SAKURAI, N. YAMAGUCHI and S. KOIZUMI[1]

Petrochemicals Research Laboratory, Sumitomo Chemical Co., Ltd.,
2-1 Kitasode Sodegaura, Chiba 299-0295, Japan
[1]Advanced Science Research Center, JAERI, Tokai, Ibaraki 319-1195, Japan

The purpose of this work is to make clear the effect of dynamical asymmetry of long-chain branchings in polyethylene blends. Samples that were mixed two kinds of hydrogenous polyethylenes (H-PEs) with a deuterated high-density polyethylene (D-HDPE) were measured small-angle neutron scattering (SANS) under shear-flow. H-PEs are linear low-density polyethylene (LLDPE) and low-density polyethylene (LDPE). The LLDPE and the LDPE are evaluated as a linear polyethylene and as a long-chain blanched polyethylene, respectivery. The effect to dynamical asymmetry of a long-chain branched polyethylene under shear-flow was compared with it of a linear polyethylene by using two-dimensional SANS patterns.

Table 1: Characteristics of materials for blend samples.
*: The number of short-chain blanchings.
**: The number of CH_3s.

		LLDPE	LDPE	D-HDPE
MFR	g/10 min	2.1	2.0	-
SR	-	1.09	1.41	-
density	g/cm^3	0.912	0.923	-
$[\eta]$	dl/g	1.48	0.88	-
Mw	-	88000	61000	493000
Mn	-	44000	19000	76000
Mz	-	146000	134000	1894000
Mw/Mn	-	2.0	3.2	6.5
SCB*	/1000C	17.8	20.7**	-

Characteristics of the D-HDPE and H-PEs that were used in this study are shown in Table 1. The D-HDPE and H-PEs were mixed by using xylene. D/H composition of blend samples were 20/80 wt%. The LLDPE (EXACT 3030) that is ethylene-hexane copolymer was purchased from ExxonMobil Chemical Company. The LDPE (SUMIKATHENE F200-0) was supplied by Sumitomo Chemical Co., Ltd.

The SANS measurements were performed with a spectrometer SANS-J at research reactor JRR-3M of JAERI. Camera length was set 10 m and scattered neutrons were detected on the Two-dimensional ^{3}He position sensitive detector. A shear cell installed in the SANS-J was Linkam Cambridge Shearing System CSS 450. Its viewing area was converted into 5mmϕ. Blend samples were once melted completely at 200 ℃ before SANS measurements. The static experiment and the shear-inducing experiment were conducted at 160 ℃ . Shear mode and shear rate of shear-inducing experiments were steady mode and 1.0 s^{-1}, respectively.

Figure 1 and 2 show the two-dimensional SANS patterns of D-HDPE/LLDPE (20/80) blend (linear blend) of static and shear rate 1 s^{-1}, respectively. Although the SANS pattern of the linear blend was isotropic before shear-inducing (Fig. 1), The pattern of the blend under shear became elliptic shape whose major axis was perpendicular to flow direction (Fig. 2). This can be interpreted that the gaussian chains of polyethylenes were extended into the flow direction.

Figure 3 and 4 show the two-dimensional SANS patterns of D-HDPE/LDPE (20/80) blend (branching blend) of static and shear rate 1 s^{-1}, respectively. The SANS pattern of the branching blend was also isotropic before shear inducing (Fig. 3). The pattern of the branching blend under shear- flow became specific SANS pattern (Fig. 4). We can see

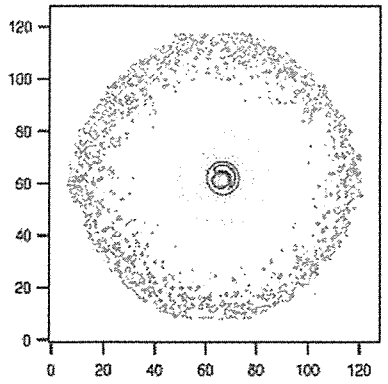

Figure 1: The two-dimensional SANS pattern of the D-HDPE/LLDPE (20/80) blend.
Befor shear-inducing.
The flow direction is the longitudinal direction.

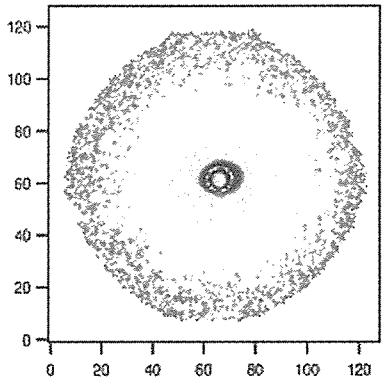

Figure 2: The two-dimensional SANS pattern of the D-HDPE/LLDPE (20/80) blend.
Shear rate is $1.0s^{-1}$.
The flow direction is the longitudinal direction.

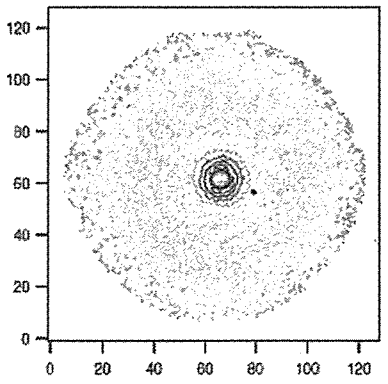

Figure 3: The two-dimensional SANS pattern of the D-HDPE/LDPE (20/80) blend.
Befor shear-inducing.
The flow direction is the longitudinal direction.

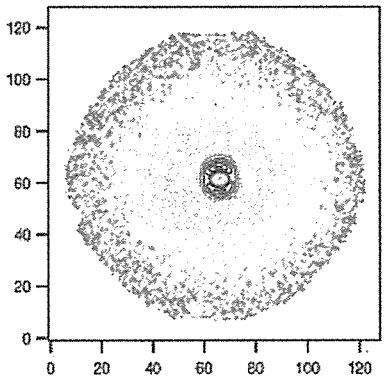

Figure 4: The two-dimensional SANS pattern of the D-HDPE/LDPE (20/80) blend.
Shear rate is $1.0s^{-1}$.
The flow direction is the longitudinal direction.

two phenomena from the specific SANS pattern. One is elliptic shape whose major axis was perpendicular to the flow direction similar to the linear blend. This showed that the gaussian chains of the blend were extended into the flow direction. The other is a abnormal butterfly pattern [1] was appeared in the parallel to the flow direction of lower q region.

Such a scattering pattern shows that phase-separation arises from different viscosity of blended polymers under shear-flow. We think that these phenomena are based on the effect of the dynamical asymmetry of long-chain blenchings in polymer melt.

References

1) Satoshi Koizumi : J. Appl. Cryst. **36** (2003) 381.

2.2.6

Small-Angle Neutron Scattering Study on Living Anionic Polymerization Process of Styrene

Kazuhiro Yamauchi, Hirokazu Hasegawa, Takeji Hashimoto and Satoshi Koizumi[1]

Graduate School of Engineering, Kyoto University, Kyoto 606-8501, Japan
[1]Advanced Science Research Center, JAERI, Tokai-mura, Ibaraki 319-1195, Japan

In addition polymerization of styrene monomers by an anionic process monomers are added to the living ends of polystyril anions and the polymer chains grow with time until all the monomer molecules are consumed. We planed the time-resolved SANS measurements of such polymerization processes. This is a report of our preliminary result.

SANS-J instrument at JAERI JRR-3M research reactor was used for this study with neutron wavelength of 0.7 nm. The polymerization of styrene monomer was performed with d_6-benzen as solvent and s-butyllithium as initiator at room temperature in a quartz cell with the sample thickness of 5 mm sealed with a 3-way cock under nitrogen gas atmosphere. Time-resolved SANS intensity profiles were obtained with 5 min interval after addition of initiator into the mixture of the monomer and the solvent. The final polymer concentration was 30% and the molecular weight of the resulting polystyrene was 5,000.

Figure 1a shows the time-resolved SANS intensity profiles. The scattering intensity increased after 5 min from the initiation. After 10 min the scattering intensity increased significantly, but it remained almost constant with time beyond this point implying that the polymerization was completed in 10 min. Figure 1b shows the change of scattering profile on addition of ethanol to kill the living anion ends of the polystyrene. It is intriguing that the scattering intensity once increased after addition of trace amount of ethanol (The orange color of living polystyrillithium disappeared and the solution underwent gelation.), but decreased again after addition of larger amount of ethanol. (The gel turned into solution.) The scattering intensity of the solution of the dead polymer is smaller than that of the living polymer suggesting the association of thechain ends for the living polymer.

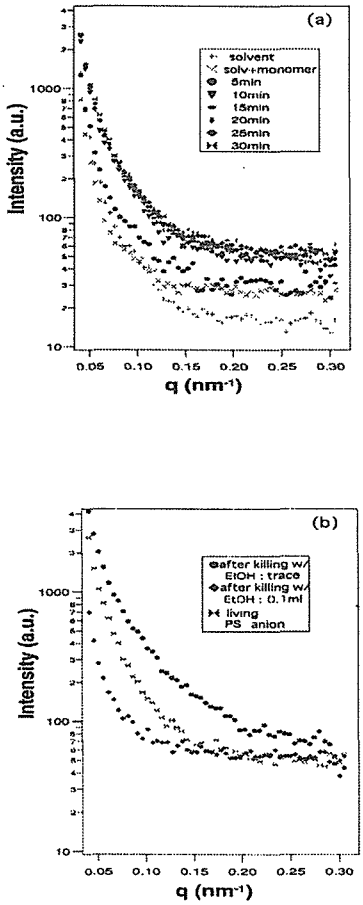

Figure 1: (a) Time dependence of SANS profiles in the anionic polymerization process of styrene in d_6-benzen. (b) Effect of adding ethanol to the solution of the living polystyril anions.

2.2.7

Small-Angle Scattering on Polystyrene/Poly (vinyl methylether) mixture I -Anomalous Suppression of Small-Angle Scattering in Quiescent State-

S. KOIZUMI and H. TAKENO[1]

Advanced Science Research Center, JAERI, Tokai-mura, Ibaraki 319-1195, Japan
[1]Faculty of engineering, Gunma University

We performed SANS measurements on polystyrene (PS)/poly (vinyl methylether) (PVME) mixture. The details of sample specimens are described in ref.1. A temperature-range is wide in a single mixed phase from above $T_{g,PS}$ to $T_{g,mix}$, where $T_{g,mix}$ is the glass transition temperature of the mixture. We found that anomalous suppression of small-angle scattering at intermediate temperature between two T_g's. We finally attributed this finding to *dynamical asymmetry enhanced by temperature change.*[1)]

In the temperature region higher than $T_{g,PS}$, the q-behavior and temperature change of SANS profiles are well reproduced by a scattering function on a basis of a mean-field random phase approximation (RPA) with an interaction parameter χ ($\sim A + B/T$). As temperature decreases below $T_{g,PS}$, however, the scattering at lower q ($< 1/\xi$ where ξ is a correlation length) decreases more than that predicted from higher temperature [2)] Simultaneously, the q-positions q_c where we observe a deviation from q-profiles calculated by RPA, shift to higher q, which means correlation lengths also decrease more than expected [2)].

These anomalous behaviors are well recognized in the forward scattering intensity $S(q = 0)$, which was determined from a small q-region according to the Ornstein-Zernike formalism. Figure 1 shows the results for the mixture of the volume fraction of PS, $\phi_{PS} =$ 0.5 and 0.8 or (50/50) and (80/20). In the high temperature region, the inverse forward scattering intensity $S(q = 0)^{-1}$ changes according to $\sim T^{-1}$. However, below about $80°C$ for the mixture of (50/50), $S(q = 0)$ is anomalously suppressed more than expected from the high temperature region. This suppression behavior becomes more pronounced as temperature decreases. For the PS-rich mixture of (80/20), in which this anomalous suppression starts from a slightly higher temperature, these trends are more obvious. Finally, at $T_{g,mix}$, $S(q = 0)$ freezes and no longer shows temperature change.

It should be noted that this anomalous suppression is a characteristic behavior only for the mixture with largely different T_g's. In the case of mixtures with similar T_g's, *e.g.*, a polybutadiene/polyisoprene (PB/PI) mixture, the scattering intensity decreases normally according to $\sim T^{-1}$ and freezes at $T_{g,mix}$ [2)].

Figure 2 shows the phase diagram of the PS/PVME mixture, where a spinodal point T_s and a cloud point T_c determined by SANS measurements are indicated.[1)] The glass transition temperature for the mixture $T_{g,mix}$ was also determined by SANS, where small-angle scattering freezes. $T_{g,mix}$ is very close to the calorimetric glass transition temperature. In Figure 2, we also show the crossover temperature T_A of anomalous suppression. From SANS measurements, we determined T_A, at which $S(q = 0)^{-1}$ deviates from a linear decrease according to T^{-1} observed in the high temperature region. The temperature T_A increases slightly as ϕ_{PS} increases.

The local segmental dynamics in the miscible mixtures of polymers with largely different T_g's is believed to be heterogeneous. Here we refer to three experimental findings obtained by rheological, spectroscopic and calorimetric measurements: (1) breakage of time-temperature superposition principle, (2) spectrum broadening and (3) T_g broadening.

These suggest heterogeneous local dynamics. The proposed interpretation is the heterogeneous cooperative motion within thermally enhanced concentration fluctuations (Kumar *et al.*,1994 & Zetsche and Fischer, 1994) or by chain connectivity (Chung *et al.*,1994, Arendt *et al.*, 1997 & Lodge and Mcleish, 2000). It is further reported that for the PS-rich mixture of $\phi_{PS} > 0.9$, PS and PVME chains move independently and the PVME chain becomes faster than pure PVME due to larger of free volume in PS-rich circumstance, which is called *"dynamical decoupling"* (Urakawa, private communication).

In the case of the PS/PVME mixture, in a temperature region above $T_{g,PS}$, PS and PVME chains are free from vitrification and there is smaller dynamical asymmetry between the two components. So far, many researchers have focused on this regime of smaller dynamical asymmetry , e.g., Schwahn et al. have shown a viscoelastic effect by determining the q-dependent Onsager coefficient $\Lambda(q)$, where the dynamical asymmetry is attributed to a large difference in molecular sizes. ($M_{w,DPS}/M_{w,PVME} \simeq 5.9$). However, as temperature decreases into an intermediate temperature region between $T_{g,PS}$ and $T_{g,mix}$, the dynamical asymmetry is enhanced by temperature. Although the concentration fluctuations become smaller at lower temperatures due to the LCST phase behavior, we expect that local contacts of PS segments in the PS-rich region tend to freeze and cause enhanced dynamical asymmetry.

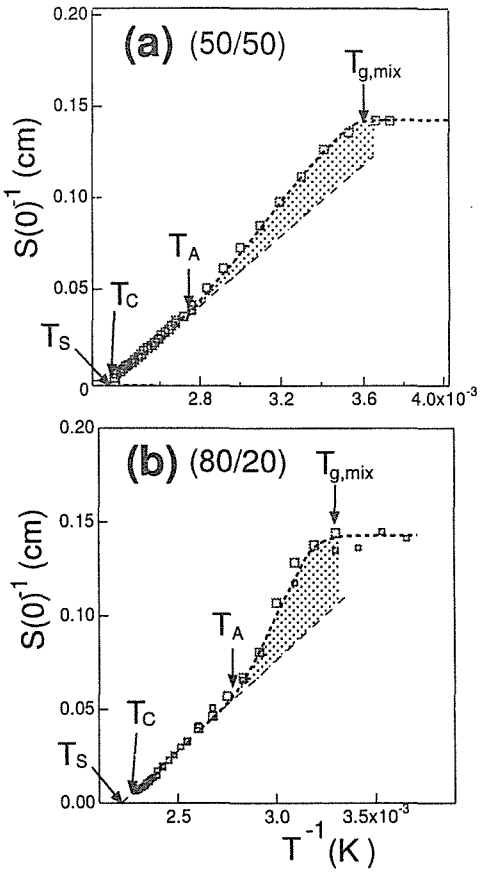

Figure 1: Forward scattering $S(q = 0)$ for d-PS/PVME (50/50) and (80/20) mixtures determined according to a Ornstein-Zernike formalism. Anomalous suppression is observed between T_A and $T_{g,mix}$.

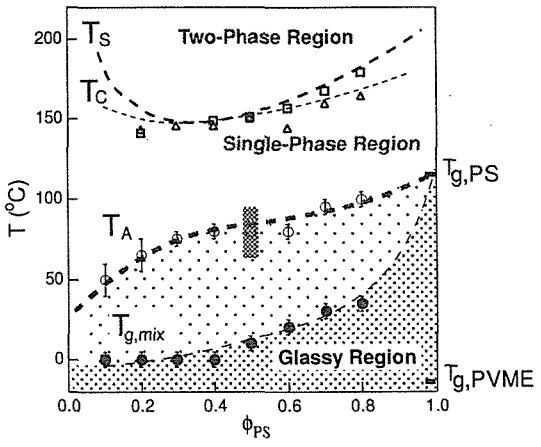

Figure 2: Phase diagram for the d-PS/PVME mixture, showing a spinodal line T_s, a binodal line T_C and glass transition temperature for the mixture T_g, mix. Crossover line for anomalous suppression is also included.

References

1) S. Koizumi *J. Appl. Cryst.* **36** (2003) 381-388.
2) H. Takeno, S. Koizumi, H. Hasegawa and T. Hashimoto *Macromolecules* **29** (1996) 2440-2448.

2.2.8

Small-Angle Scattering on Polystyrene/Poly (vinyl methylether) mixture II -Competition between Rheological and Concentration Fluctuation Relaxations-

S. KOIZUMI

Advanced Science Research Center, JAERI, Tokai-mura, Ibaraki 319-1195, Japan

Generally for polymer mixtures, there are vicous and gel-like limits, determined by a balance between stress and fluctuation relaxations. In the viscous limit, the rheological relaxation is faster than the concentration fluctuation, while in the gel-like limit where the rheological relaxation is much slower than the concentration fluctuation.

With respect to a polymer mixture of DPS/PVME (50/50) , which was studied in Part I of this report, we performed a mechanical measurement of a shear modulus in order to confirm our situation (koizumi and Inoue in preparation). We determined the rheological relaxation time as the point where the storage modulus $G'(\omega)$ and the loss modulus $G''(\omega)$ merge. For higher temperatures in the range from 120 $°C$ to 80 $°C$, we could clearly recognize this point on the spectra, while for lower temperatures below 60 $°C$, it is out of the range of our mechanical spectrometer. Therefore, we estimated the rheological relaxation time by using a shift factor a_T, although the temperature-time superposition principle is not well established for the mixture with largely different T_g's.

In Fig. 1, we show the temperature dependence of rheological relaxation time for the DPS/PVME mixture of (50/50). Additionally, we plot a relaxation time of several 10 seconds for the concentration fluctuations ($\sim 1/R(q)$) of $0.01\mathring{A}^{-1}$, which was determined by time-resolved SANS measurements after a shallow quench into a meta-stable region. Due to the LCST phase behavior, this relaxational rate $1/R(q)$ might decrease as temperature decreases (broken line). However, near $T_{g,PS}$, the kinetic coefficient $\Lambda(q)$ might be affected by $T_{g,PS}$ and may become smaller. According to the "*fast mode*" ansatz (Kausch and Tirrell, 1989) , the faster moving component of PVME governs the temperature dependence of $\Lambda(q)$. Therefore, we expect that the temperature change of $\Lambda(q)$ might be as illustrated by the shadow region in Fig. 1. Thus at around 100 $°C$, there exists a crossover from a *viscous limit* at high temperature to a *gel-like limit* at intermediate temperature.

A stress-diffusion coupling has a variety of effects depending on vicous and gel-like limits. We stress that in the viscous limit of the high temperature region, the dynamical coupling effect between stress and diffusion appears as a *viscoelastic* effect. Schwahn et al. have shown this viscoelastic effect by determining the q-dependent Onsager coefficient $\Lambda(q)$ according to q^{-2} for $q\xi_{VE} > 1$ (Schwahn *et al.*, 1992). In this study, the dynamical asymmetry is attributed to the large difference in molecular sizes of the mixture constituents (Schwahn *et al.*, 1992).

In the gel-like limit, on the other hand, we support that a long-living shear modulus G_1 starts to appear in the osmotic compressibility as a coupling effect between stress and diffusion. In other words, we expect the following modified scattering function:

$$S'(q) = \frac{1}{r_0 + Cq^2 + \frac{4}{3}\alpha^2 G_1}. \qquad (1)$$

This modified scattering function has an additional term of $4/3\alpha^2 G_1$ which disappears for the dynamically symmetric mixture with $\alpha = 0$. Eq.(1) reproduces well our observations described in Part I of this report : the suppression of the forward scattering intensity $S(0)$ and decrease of the correlation length ξ. Our experimental findings that the suppression becomes more pronounced as temper-

ature decreases suggests that the dynamical asymmetry or α is more enhanced by temperature decrease. At the same time, temperature decrease might induce a slowing down of local internal modes, and the number of local internal modes, which are responsible for the stress decaying more slowly than the concentration fluctuation, becomes larger. With a larger magnitude of G_1, the suppression becomes more pronounced. Irrespective of dynamical symmetry or asymmetry, crossover from viscous to gel-like limits generally occurs when the mixture approaches $T_{g,mix}$. In the case of a dynamically symmetric mixture, e.g., PB/PI, we could not observe any suppression of small-angle scattering. Thus, in order to observe the suppression of small-angle scattering, the dynamical asymmetry ($\alpha \neq 0$), in other words, a *one-sided stress division*, is needed. This is consistent with our hypothesis that for the PS/PVME mixture, the dynamical asymmetry is enhanced by temperature.

For elastic materials such as chemical polymer gels or metal alloys with modulus inhomogeneity, stress does not decay. For these materials, the modified structure factor $S'(q)$ can be obtained from an equilibrium argument considering free energy (Cahn, 1961, Tanaka *et al.*, 1973 & Onuki and Nishimori, 1991). In such a case, the non decaying modulus G shifts the critical point to a higher temperature. Therefore, $S(q=0)$ is apparently suppressed more than expected in the case without non decaying G or α.

However, in the case of the PS/PVME mixture, a rheological relaxation occurs with a finite relaxational time τ_R ($=\tau_1$). Here we encounter a simple question: if we wait long enough as compared to the rheological relaxational time τ_R, can we observe small-angle scattering free of the rheological relaxation or $S_0(q)$ ($\sim 1/(r_0 + Cq^2)$)? Our measurement time under each condition is of the order about 1000 seconds after changing temperature. In order to confirm this point, we performed a time-resolved measurement at 60.0 $^\circ C$, monitoring the change of intensity over a period longer than τ_R. However, we could not observe any recovery of scattering intensity and the suppression remained. This observation leads us to believe that the suppression of small-angle scattering or the concentration fluctuation results from a competition between two kinetic processes, i.e., the thermally activated concentration fluctuation of a finite wave number q and the rheological relaxation. In the gel-like limit, a long-living stress field suppresses the fast decaying concentration fluctuation of the q fourier mode. When q becomes smaller, the relaxational rate $R(q)$ becomes smaller according to q^2. Therefore, at $q=0$, τ_{CF} ($\sim 1/R(q)$) becomes infinite. In this limit, we expect to observe a viscous limit again. On the other hand, for a smaller length scale of $q\xi > 1$, corresponding to the power law regime of q^2, the small-angle scattering is not influenced by the osmotic compressibility itself (see Fig. 1 of Takeno *et al.*, 1996). Thus, this suppression behavior of small-angle scattering has upper and lower length scale limits, between which our SANS measurements were performed.

References

1) S. Koizumi *J. Appl. Cryst.* **36** (2003) 381-388.

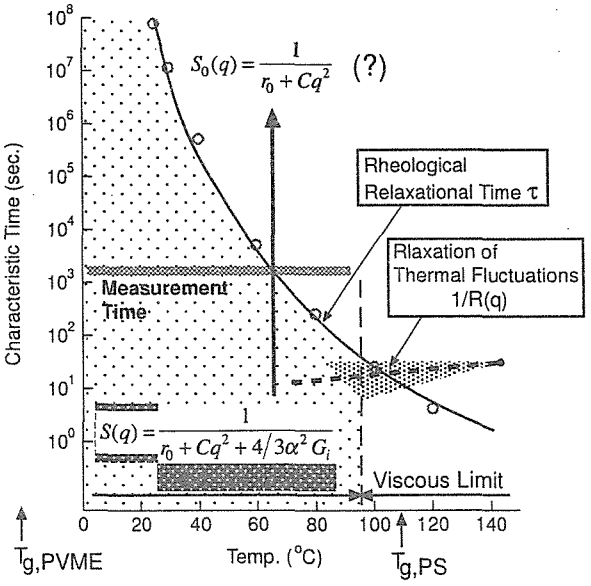

Figure 1: Schematic view for a crossover from a viscous to a gel-like limits, which happens as temperature decreases.

2.2.9

Small-Angle Scattering on Polystyrene/Poly (vinyl methylether) mixture III -Shear-induced Phase Separation-

S. KOIZUMI

Advanced Science Research Center, JAERI, Tokai-mura, Ibaraki 319-1195, Japan

We performed SANS measurements on a shared specimen of polystyrene (PS)/Poly (vinyl methylether) (PVME) mixture at intermediate temperature between $T_{g,PS}$ and $T_{g,mix}$, where $T_{g,PS}$ or $T_{g,mix}$ is the glass transition temperature of PS or the mixture, respectively. If we apply a shear field to this mixture at at intermediate temperature around T_A (see PartI in this report), the mixture shows an abnormal butterfly pattern as a result of shear-induced phase separation.[1] Figure 1 shows a 2-dimensional SANS patterns of PS/PVME (50/50) sheared at 70.0 $°C$ and quenched below $T_{g,mix}$. The shear rate and deformation rate were $\dot{\gamma} = 0.5 rad/s.$ and $\lambda > 2.0$, respectively. Before shearing, small-angle scattering is isotropic for a single mixed state. However, after shearing, we clearly recognize an abnormal butterfly pattern, i.e., enhancement of scattering intensity along the shear direction with a clear scattering maximum at q_{max}. As q increases, the 2-dimensional pattern becomes more isotropic. The sample specimen sheared at 90.0$°C$ also shows an abnormal butterfly pattern which appears at lower q but less obviously.

As a control experiment, we performed SANS measurements on the sheared mixture of DPS/HPS (50/50). Here we chose identical chain lengths of $M_n \simeq 60K$ for DPS and HPS in order to avoid dynamical asymmetry due to a difference in molecular sizes. This mixture, sheared at 150.0 $°C$ and quenched, shows an elliptical 2-dimensional scattering pattern, elongated to the direction perpendicular to shear flow. In this control experiment, shear-induced phase separation does not occur but chain deformation occurs due to shearing.

The q-profiles, which are sector-averaged over an azimuthal angle of 30° along directions parallel and perpendicular to the shear direction.[1] show two q-regions of (I) and (II). In q-region (I) at low q, we observed a shear-induced phase separation showing stronger intensity than that for the perpendicular direction and with an obvious scattering maximum at around $q = 0.006 \AA^{-1}$. The q-profile parallel to shear flow decreases, according to the Porod law q^{-4}, indicating a sharp interface between PS-rich and PVME-rich domains. The scattering maxima are predominantly in the q-Fourier mode, grown up during shearing. In the q-region (II) at high q, we observed a crossover of the scattering intensity; scattering in the perpendicular direction exceeds that in the parallel direction. The asymptotic q-behaviors for both directions are closer to q^{-2}, which is attributed to chain deformation due to shearing.

For a mixing state of the sheared mixtures, we must consider the time evolution of the concentration fluctuations under shear. The total growth rate $\Gamma(q)$ for the concentration fluctuations under shear is given by the two terms of (1) thermodynamic force and (2) imbalanced stress under shear. The imbalanced stress term can have a negative contribution relative to the first thermodynamic term which stabilizes a single mixing state when $r_0 > 0$. If $\Gamma(q)$ becomes totally negative, the corresponding q-Fourier modes can grow up during shearing. For our argument, we consider a simple case of $q_x = q_y = q$. We stress that the imbalanced stress term disappears for a vorticity direction of $q = q_z$. In this limit, $\Gamma(q)$ is given as follows (Onuki, 1997);

$$\frac{\Gamma(q)}{q^2} = \Lambda(q)(r_0 + Cq^2) - \alpha(\frac{\partial G}{\partial \phi})\dot{\gamma}$$

where Λ, α and G are an Onsager kinetic coefficient, a symmetric param ter and a shear modulus.

Figure 2(a) schematically shows the growth rate $\Gamma(q)/q^2$ where (1) the thermodynamic term and (2) the imbalanced stress term are separately drawn. The shaded region corresponds to the q-Fourier modes which give a negative relaxational rate $\Gamma(q)$. A larger contribution from the imbalanced stress is required to observe the butterfly scattering pattern by SANS, which generally covers a higher q-region of as compared to light scattering. Due to the LCST phase behavior, as temperature decreases, the thermodynamic contribution increases. As temperature decreases to intermediate temperature, the enhanced dynamical asymmetry is expected to give larger contribution of the imbalanced shear. Therefore, we successfully observed the butterfly scattering pattern by SANS at around T_A. With a higher shear rate, the shaded region expands to higher q so that the higher q-mode can respond as shear-induced phase separation. For the q-mode outside this shaded region, a shear effect appears as only chain deformation. In Fig. 2(b), we schematically draw $\Gamma(q)$, which might have a minimum at a certain q in the q-region of SANS. The dominant q-mode, which appears as a scattering maximum at q_{max}, corresponds to that where $\Gamma(a)$ is minimum. This argument is equivalent to the stability analysis for the early stage of spinodal decomposition in a quiescent state; shear rate $\dot{\gamma}$ is equivalent to a quench depth ΔT for spinodal decomposition. In this discussion, we neglected the effects of a convective flow and the first normal stress difference which are discussed in detail elsewhere (Saito *et al.*, 2001), as related to the experiment on the polystyrene solution in dioctyl phthalate (DOP).

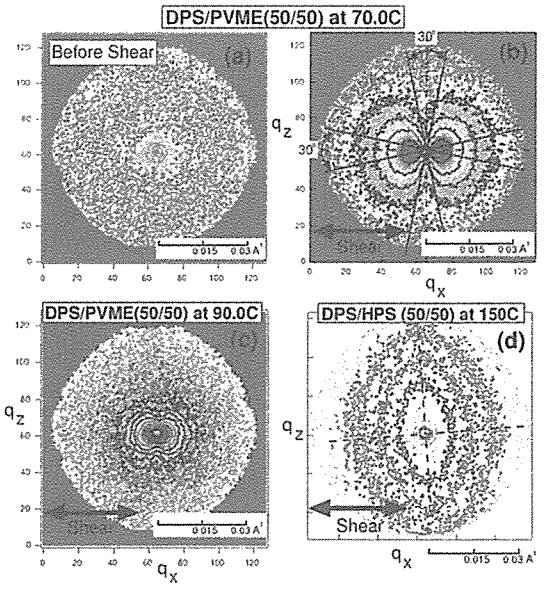

Figure 1: 2-dimensional SANS pattern for the sheared DPS/PVME mixture of (50/50), where a butterly pattern is clearly observed. As a control exeriment, the SANS pattern for DPS/HPS mixture of (50/50) shows an elliptical pattern which is elongated to a direction perpendicular to shear.

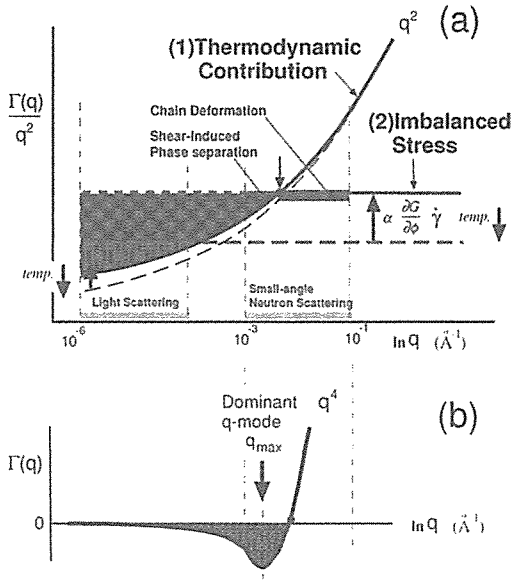

Figure 2: Schematic view for stability analysis under shear in a theoretical frame of stress-diffusion coupling.

References

1) S. Koizumi *J. Appl. Cryst.* **36** (2003) 381-388.

2.2.10

Small-angle Neutron Scatttering on Polystyrene Microsphere Formation Induced by In-situ Radical Polymerization

S. KOIZUMI, R. MOTOKAWA and M. ANNAKA[1]

Advanced Science Research Center, Japan Atomic Energy Research Institute, Tokai-mura, Ibaraki 319-1195, Japan
[1]Department of Chemistry, Faculty of Science, Kyushu University, 33 Hakozaki, Higashi-ku, Fukuoka 812-8581, Japan

By using a pin-hole and a double crystal small-angle neutron scattering spectrometers (SANS-J and PNO at JAERI), we investigated radical polymerization of polystyrene (PS) and a followed microsphere formation process which occurs in a polymerization matrix of poly(vinyl methylether) (PVME) solution with mixed solvents of ethanol and n-hexane. The polymerization matrix, composed of PVME/ethanol/n-hexane, is crucial to avoid precipitate of PS from the solution. Especially the matrix polymer PVME plays a important role to stabilize a PS microsphere in size of sub-micrometer. It is because that the matrix posesses balanced solubility with PS chains; PVME and PS are soluble each other, due to a LCST type phase diagram with a phase boundary about 120 $°C$, while ethanol and n-hexane are poor solvents for PS. In this study, we report the results obtained with the polymerization matrix; mixed solvents of ethanol/n-hexane (80/20 wt/wt) and PVME content of 8.3 $wt\%$. This condition of ethanol/n-hexane (80/20) realizes the smallest size of microspheres about 0.5 mm, which was confirmed by scanning electron micrography (SEM).[1)]

In order to have a strong scattering contrast, we prepared a reaction solution with fully deuterated styrene (d8-St) solubilized in the protonated polymerization matrix of PVME/ethanol/n-hexane. The solution was filled in a quartz cell with 1mm thickness, whose temperature was controlled at 55.0 $°C$. Radical polymerization was initiated by *2,2'-Azobisisobutyronitrile* (AIBN). For ultra small-angle scattering by PNO, we terminated radical polymerization with *1,1-Diphenyl-2-picrylhydrazyl* (DPPH), in order to observe a time-evolution of scattering profiles during radical polymerization.

Figure 1 shows scattering profiles obtained by two spectrometers of SANS-J and PNO, covering a wide range of wave number $q(= 4\pi/\lambda sin(\theta))$ from 10^{-4} nm^{-1} to 1 nm^{-1}, where λ and θ are wave length and scattering angle.

Small-angle scattering region from 0.01 to 1 nm^{-1}: For the reaction solution before starting radical polymerization, we obtained only spin incoherent scattering, which appears at the intensity level of 1 cm^{-1}. At 20 *min.* after starting radical polymerization, we observed a strong upturn of small-angle scattering in the q-region around 0.1 nm^{-1}. As a reaction-time proceeds over 60 *min*, the upturn becomes an asymptotic q-behavior close to q^{-4}, which is a so-called Porod law originating from a interface of deuterated polystyrene (DPS) microspheres dispersed in the polymerization matrix. In case when the interface has a finite thickness of t_I, we obtain a following equation in the Porod q-region;

$$\frac{d\Sigma}{d\Omega}(q) \sim (2\pi)^{1/2}\Delta B^2[\frac{S(t)}{V_0}q^{-4}]exp[-\sigma(t)^2q^2] \quad (t_I = (2\pi)^2\sigma(t), S(t) = 4\pi R(t)^2 N_s) \quad (1)$$

where $\Delta B, S, V_0, R$ are difference of scattering length between PS and the matrix, a total surface of microspheres, a sample volume and a radius of microsphere. S/V_0 is a specific interface. N_s is a number-density of PS

microspheres. By using Porod plot on a basis of eq() that is given by eq(), we analyzed time-evolution of surface structure of the PS microphere (see Fig. 2).

Figure 2 shows time-evolution of a characteristic thickness t_I and a spcific interface S/V_0 thus estimated. A specific interface S/V_0 contineuously increases, as reaction-time proceeds up to about 600 *min.* The total surface area S is given by a product surface area of a microsphere $4\pi R(t)^2$, and number density of microspheres N_s. If we assume that the number density N_s is time-independent, the increase of S/V_0 is attributed to growth of R. A characteristic interface t_I, on the other hand, is about 15 nm and seems to be time-independent.

Ultra small-angle scattering region from 10^{-4} to $10^{-2} nm^{-1}$: The ultra small-angle scattering spectrometer PNO is a Bonse-Hart type, where ultra small-angle scattering is detected by precisely rotating a channel-cut perfect crystal Si(110) with angular resolution of micro-radian order. Due to low luminecity of monochromatized incident neutron, it takes more than 10 hours in order to have a whole q-profile ranging from 10^{-4} to $10^{-2} nm^{-1}$. In order to detect time-evolution of q-profiles in ultra small-angle region, we need to terminate radical polymerization process with ***. We terminated radical reaction at different reaction-times of 60, 200, 300 and 400 *min.* and measured ultra small-angle scattering. In order to have q-profiles in a ultra small angle scattering region, we calibrated these intensities with a secondary standard of polymer films whose macrophase separated structure gives monotonous q-behavior of q^{-4} over a wide q-range from 10^{-4} to $10^{-2} nm^{-1}$ for both PNO and SANS-J spectrometers.

We plotted the q-profiles thus obtained in Fig. 1. At 60 *min.* we could not obtain enough signal to noise ratio (S/N); a noise level due to dark current and thermal diffuse scattering from a single crystals appears at about 10^4 cm^{-1} in absolute unit. For reaction-times shorter than 200 *min*, We drew speculated scattering curves as shown by broken lines. For longer reaction-times over 200 *min*, on the other hand, we obtained q-profiles which increase in its intensity as a reaction-time proceeds. The q-profiles at higher q around 0.01 nm^{-1} show the asymptotic q-behavior close to q^{-4} which would be reasonably connected to the q-profiles obtained by SANS-J at corresponding reaction-times (The broken straight lines in Figure 1 show a guide for eyes.)

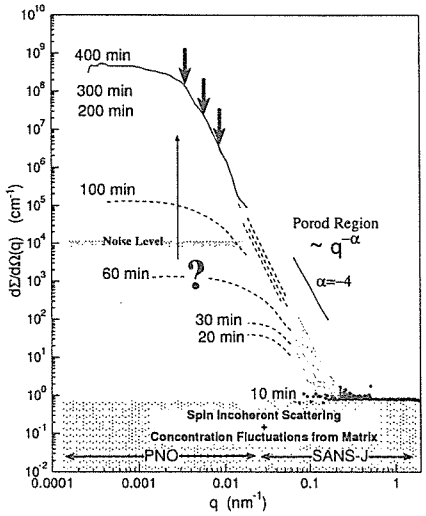

Figure 1: Time-evolving scattering profiles for microsphere formation during radical polymerization, obtained by pin-hole and double crystal small-angle neutron scattering spectrometers (SANS-J and PNO).

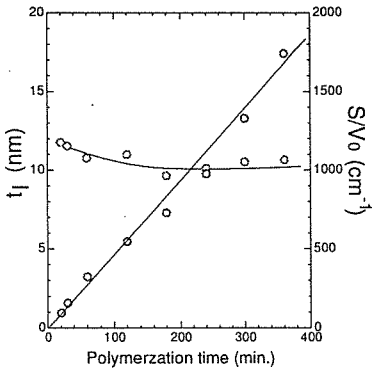

Figure 2: Time-evolution of Interfacial Structure.

References

1) Shigeki Chujo, Masayosi Rikukawa, Kohei Sanui, Noaya Ogata, Satoshi Koizumi and Takeji Hashimoto: *Polymer Journal* **Vol.33 No.1** (2001) 1-8.

2.3 Strongly Correlated Electron Systems and Superconductivity

2.3.1

Magnetic properties of perovskite manganites $L_{0.5}A_{0.5}MnO_3$ (L=Eu, Gd, Tb and Dy, A=Ca and Sr)

K. YOSHII, Y. HIRAMITSU, Y. NISHIHATA, J. MIZUKI, A. NAKAMURA[1], Y. SHIMOJO[1], Y. ISHII[1], Y. MORII[1], H. ABE[2], K. NISHIDA[2]

Synchrotron Radiation Research Center, Japan Atomic Energy Research Institute (JAERI), Mikazuki, Sayo-gun. Hyogo, 679-5148
[1]Advanced Science Research Center, JAERI, Tokai, Ibaraki, 319-1195
[2]National Institute for Materials Science, Tsukuba, Ibaraki 304-0047

Rare earth manganites with a perovskite structure have attracted considerable renewed attention in this decade, because of their intriguing properties such as colossal magnetoresistance, real-space charge-order and metal-insulator traisition. Among these oxides, $L_{0.5}A_{0.5}MnO_3$ (L=rare earth metal, A=alkaline-earth metal) is known to exhibit a wide variety of physical properties, which strongly depend on the ionic radii of the L^{3+} and A^{2+} ions.[1, 2, 3] In this work, magnetic properties were studied for this system containing the small rare earth ions of L^{3+}=Eu^{3+}, Gd^{3+}, Tb^{3+} and Dy^{3+} by means of magnetization and neutron diffraction measurements.

The samples were prepared by a solid-state reaction in air. Magnetization measurements were performed by use of a SQUID magnetometer (Quantum Design MPMS) between 4.5 and 400 K. Neutron diffraction experiments were conducted below 400 K with a high resolution powder diffractometer (HRPD) at the JRR-3 reactor to determine magnetic structures.

The magnetization measurements showed a spin-glass-like trantion around 40-50 K for $L_{0.5}Sr_{0.5}MnO_3$, while a charge-ordering transition was suggested for $L_{0.5}Ca_{0.5}MnO_3$ around room temperature. Figure 1 shows the neutron diffraction pattern for $Tb_{0.5}Sr_{0.5}MnO_3$ at 9 K. The experimental pattern at room temperature could be fitted to an orthorhombic *Pnma* structure by the Rietveld analysis (RIETAN-2000). The lattice paremeters were a=0.54191(3), b=0.76396(4), and c=0.54109(2) nm. The pattern at 9 K showed a few magnetic peaks at the low angle region, which is seen in the inset. It was found that these peaks were appreciably wider than the nuclear Bragg peaks. This result suggests that an origin of the peaks is short-range magnetic order such as either a spin-glass or a cluster-glass state, which is in accord with the result obtained from the magnetization measurements. The patterns of the isostructural $Tb_{0.5}Ca_{0.5}MnO_3$ below room temperatures could be fitted assuming a charge-ordering state of the Mn ions. The different behavior between the Sr- and Ca-systems may be explained in connenction with the randomness of magnetic interactions owing to the difference of the ionic radii of L^{3+} and A^{2+}.[2]

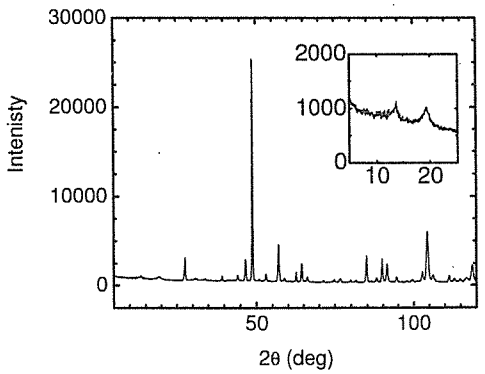

Figure 1: Neutron powder diffraction patterns of $Tb_{0.5}Sr_{0.5}MnO_3$ at 9 K. The inset shows magnetic Bragg peaks.

References

1) P. M. Woodward *et al.*: Chem. Mater. **10** (1998) 3652.
2) T. Terai *et al.*: Phys. Rev. **B61** (2000) 3488.
3) J. López *et al.*: Phys. Rev. **B66** (2002) 214402.

2.3.2

Studies on the In Plane Phonons of $YBa_2Cu_3O_y$ and $La_{1.48}Nd_{0.4}Sr_{0.12}CuO_4$

M. Ito[1], Y. Yasui[1], S. Iikubo[1], M. Soda[1], M. Sato[1] and K. Kakurai[2]

[1]Department of Physics, Nagoya University, Furo-cho, Chikusa-ku, Nagoya 464-8602
[2]Advanced Science Research Center, JAERI, Tokai, Ibaraki 319-1195

In-plane longitudinal phonons of high-T_c cuprates have been studied mainly to extract detailed information of "stripes". The suppression of the superconductivity by the "stripe" formation is known as the 1/8 anomaly in La214 systems such as $La_{2-x}Ba_xCuO_4$ and $La_{2-x-y}Nd_ySr_xCuO_4$. For these systems, even the fluctuations of the ordering or the dynamical "stripes", may have significant effects on the superconductivity. To study whether such dynamical "stripes" can play, under certain conditions, an important role on the occurrence of high-T_c superconductivity or not, we have performed the phonon measurements and tried to clarify effects of "stripes" in one of the La214 systems and in $YBa_2Cu_3O_y$ ($YBCO_y$ or YBCO).

If the ordering (or its fluctuation) of holes along the Cu-O-Cu direction exists, in-plane phonon modes are considered to be somewhat modified. Here, we have studied one of the longitudinal bond stretching branches on single crystal samples of $YBCO_y$ with several y values and on a single crystal of $La_{1.48}Nd_{0.4}Sr_{0.12}CuO_4$. Mook *et al.* [1] measured an in-plane phonon branch with the energy of ~(43~52) meV on a crystal of YBCO and reported anomalous wave vector($\boldsymbol{q}$) dependence of the phonon energy and the anomalous broadening of the observed profiles of the phonon vibrating perpendicular to the chain direction ($//\boldsymbol{b}$) at around $\boldsymbol{q}$=(2δ,0,0), where δ is the incommensurability of the magnetic excitation spectra. They suggested that these anomalies were due to effects of the dynamical "stripes". But recent research carried out by Pintschovius *et al.* [2] has shown that there is no anomaly in the peak width and the dispersion curve of the phonon branch.

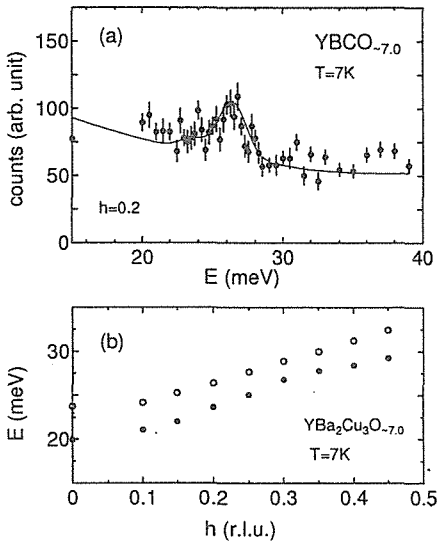

Figure 1: (a) Energy-scan profiles obtained for $YBa_2Cu_3O_{\sim 7}$ at $\boldsymbol{Q}$=(3+h,0,0) are shown (h=0.2). Solid lines show the results of the fitting with two Gaussian lines. (b) The phonon energies of the $\langle B_{2u}/B_{3u}\rangle$ modes obtained by the fittings at T=7 K for $YBa_2Cu_3O_{\sim 7}$ are plotted against h.

In our previous study, we have measured similar in-plane phonons of $YBCO_y$ (y=6.5, 6.7 and ~7) with the energy of ~(18~34) meV which are assigned as B_{2u}/B_{3u} modes at Γ point. [3] Hereafter, we just call these branches B_{2u}/B_{3u} modes. The B_{2u} and B_{3u} modes vibrate along and perpendicular to the chain direction ($//\boldsymbol{b}$), respectively, the B_{3u} mode has the significant amplitude of the chain oxygen motion. Figure 1(a) shows the phonon profile taken at T=7 K for the crystal with y ~7. We can see sharp and broad peaks in this figure. We have assigned a broad peak as B_{3u} mode. The broadening is considered to be the effect of the chain oxygen deficiency, because the broadening does not have significant temperature(T)-, $\boldsymbol{Q}$- and y-dependences. As

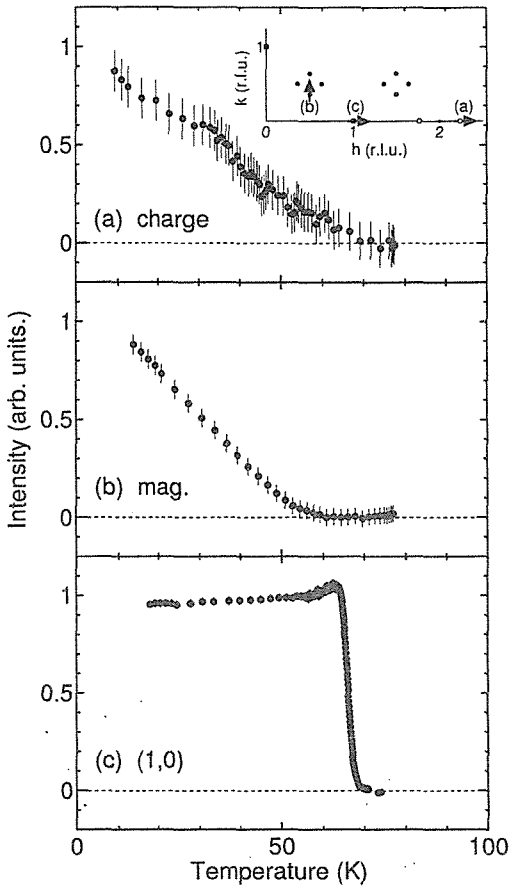

Figure 2: Temperature dependence of the peak intensities of the superlattice reflections. The data points (a) and (b) correspond to the reflections originating from the charge and magnetic ordering, respectively. The data (c) represent the reflections originating from the LTO1-LTO2 transition. In the inset of (a), the 2D reciprocal space is shown.

for the dispersion, smooth Q-dependence has been observed for all samples in the whole T-region studied here. These results are in a clear contrast to the results of Mook *et al.* [1)]

We have also adopted the $La_{1.48}Nd_{0.4}Sr_{0.12}CuO_4$ system. In Fig. 2, the T dependences of the superlattice reflection intensities originating from the structural transition and the "stripe" orderings are shown. Peaks are measured along the lines shown by arrows in the inset of Fig. 2(a). We can see that the superlattice peaks corresponding to the static "stripe" ordering begin to grow at ~69 K with decreasing T. The profiles of the bond stretching phonon,

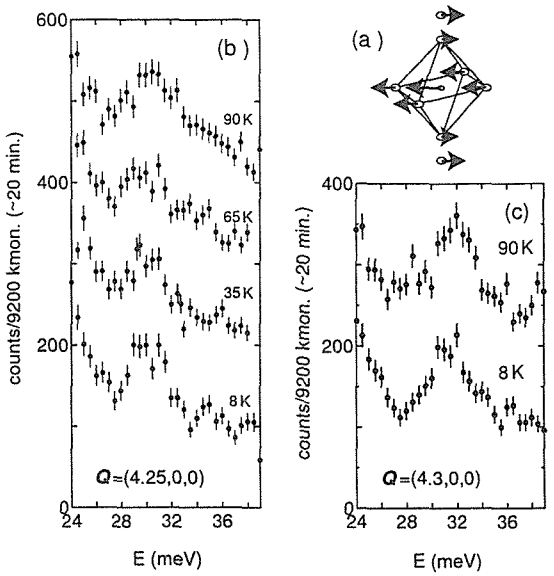

Figure 3: (a) The vibration pattern of the in-plane phonon for $La_{1.48}Nd_{0.4}Sr_{0.12}CuO_4$ at Γ point. Figures (b) and (c) show the energy-scan profiles obtained at h=0.25 and h=0.3, respectively.

whose vibration pattern at Γ point is shown in Fig. 3(a), were taken by using the triple axis spectrometer TAS-1 installed at JRR-3M of JAERI in Tokai.

The temperature dependence of the phonon profiles taken at Q=(4+h,0,0) with h=0.25 (~2δ) and 0.3 are shown in Figs. 3(b) and 3(c), respectively. We have not observed anomalous q-dependence of the peak width in the whole temperature range studied ($T \leq 90$ K). The dispersions were found to be smooth.

We have not found anomalous T-dependence of the widths of the phonon profiles at q=(0.25,0,0) and (0.3,0,0), either, on both systems of $YBCO_y$ and $La_{1.48}Nd_{0.4}Sr_{0.12}CuO_4$.

References

1) H. A. Mook and F. Dogan : Nature **401** (1999) 145.
2) L. Pintschovius, W. Reichardt, M. Klaser, T. Wolf, and H. v. Lohneysen : Phys. Rev. Lett. **89** (2002) 037001.
3) M. Ito, H. Harashina, Y. Yasui, M. Sato and K. Kakurai : Physica C **388-389** (2003) 363.

2.3.3 Successive Phase Transitions of $TbBaCo_2O_{5.5}$

M. Soda, Y. Yasui, T. Fujita, T. Miyashita, M. Ito, S. Iikubo, M. Sato and K. Kakurai[1]

Department of Physics, Nagoya University, Chikusa-ku, Nagoya 464-8602
[1]Advanced Science Research Center, JAERI, Tokai, Ibaraki 319-1195

Co^{3+} ions in Co-oxides often exhibit the spin state changes. They have the low spin (LS: S=0) ground state and the state changes to the intermediate spin (IS: S=1) state or the high spin (HS: S=2) state with increasing temperature T. This indicates that the energy difference δE between the spin states is small. Because the energy splitting between the t_{2g} and e_g orbital energies due to the crystal field generally increases with decreasing volume of the CoO_6 octahedra, δE can be controlled by the volume change of the octahedra and therefore we can seek a variety of physical behavior in the system related to the spin state change.

The perovskite oxides $R_{1-x}A_xCoO_{3-\delta}$ obtained by the substitution of R with divalent atoms A=Sr, Ba and Ca often exhibit ferromagnetic and metallic properties for small δ with increasing doping concentration x due to the double exchange interaction.[1)] When Ba and relatively small trivalent elements are chosen as A and R, respectively, the system forms the oxygen-deficient perovskite structure, in which the oxygen vacancies are ordered.[2–4)] Among such oxides, $RBaCo_2O_5$ ($\delta \sim 0.5$) exhibits transitions to the antiferromagnetic ordering and then, to the charge ordered state of Co^{2+} and Co^{3+}. $RBaCo_2O_{5.5}$ ($\delta \sim 0.25$) also exhibits several transitions. However, only restricted information is available on both the structural and the magnetic properties.

In the present work, neutron scattering studies have been carried out on a single crystal of $TbBaCo_2O_{5.5}$ to collect basic information on the spin state of Co ions and the magnetic structures. The oxygen-deficient perovskite structure of this system is formed by the linkage of alternating CoO_6 octahedra and CoO_5 pyramids along the b-axis. It has been reported that it has the orthorhombic unit cell, where Ba and Tb atoms are in different c-planes. The unit cell volume is described by $\sim a_p \times 2a_p \times 2a_p$, a_p being the lattice parameter of the cubic perovskite cell. With decreasing T, the metal-insulator (MI) transition takes place at $T_{MI} \sim 340$ K, the ferromagnetic transition occurs at $T_C \sim 280$ K, and then ferromagnetic phase suddenly changes to antiferromagnetic one at $T_N \sim 260$ K. Although transitions have been found at lower temperatures, too, in the present neutron diffraction studies, we mainly report here results of studies on the magnetic structures at 270 K and 250 K, where the spin states of Co ions within the CoO_6 octahedra and the CoO_5 pyramids are basically clarified.

Neutron measurements were carried out by using the triple axis spectrometer TAS-2 at JRR-3M. The single crystal of $TbBaCo_2O_{5.5}$ was oriented with the [100] (or [010]) axis vertical, where both $(0,k,l)$ and $(h,0,l)$ points in the reciprocal space could be observed due to the coexistence of the $\boldsymbol{a}^*$- and $\boldsymbol{b}^*$-domains. Several $0kl$ reflections can be distinguished from $h0l$ reflections by the difference between the lattice parameter a and $b/2$ (The parameter a is slightly smaller than $b/2$.).

The intensities of neutron Bragg reflections of $TbBaCo_2O_{5.5}$ have been measured in the temperature range of 7-370 K. In addition to the fundamental Bragg reflections for the unit cell with the size of $\sim a_p \times 2a_p \times 2a_p$, several superlattice reflections have been found. The points at which the reflections were observed at 7 K in the reciprocal space are shown in Fig. 1(a). ($\boldsymbol{Q}$=$(0,k,l)$ may be $(k/2,0,l)$.) The temperature dependence of the peak intensities of the typical fundamental and superlattice reflections are shown in Figs. 1(b) and 1(c), respectively. With decreasing T from

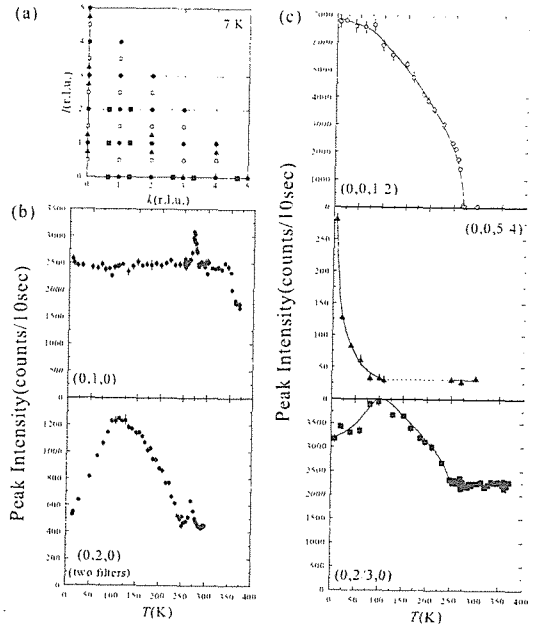

Figure 1: (a) Fundamental or superlattice points of the unit cell with the size of $\sim a_p \times 2a_p \times 2a_p$ in the reciprocal space at 7 K. (b) and (c) The peak intensities of several reflections are shown against T.

the temperature above 350 K, the intensities of several nuclear Bragg reflections change at $T_{MI} \sim 340$ K, and at $T_C \sim 280$ K additional reflections appear at several nuclear Bragg points. The additional reflections are considered to be magnetic, as is confirmed later by detailed analyses and corresponds to the appearance of the ferromagnetic moment. With further decreasing T, the additional component suddenly disappears at $T_N \sim 260$ K and the superlattice peaks corresponding to the period of $2c$ ($\sim 4a_p$) along the c-axis appear [$\boldsymbol{Q}$=(0,k,1/2), (0,k,3/2), etc.]. At $T \sim 100$ K, superlattice peaks corresponding to the period of $4c$ along the c-axis appear [$\boldsymbol{Q}$=(0,0,1±1/4), (0,0,3±1/4), (0,2,1±1/4), etc.] with decreasing T. The former group of the superlattice reflections may be magnetic, while we cannot distinguish if the latter superlattice reflections are magnetic or not. It should be also noted that the superlattice reflections corresponding to the modulation vector $\boldsymbol{q}=\boldsymbol{a}^*/3$ (the period of $\sim 3a_p$ in the real space) are observed even at temperatures higher than T_{MI}. We have not clarified detailed pattern of the modulation in the present study. Furthermore the data of Fig. 1(b) suggest the existence of structurural transitions in the present system at three temperatures, T_{MI}, ~250 K and ~100 K.

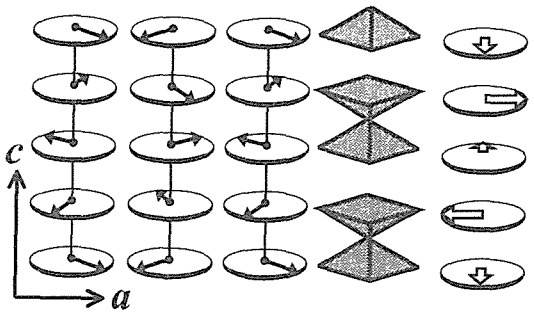

Figure 2: Schematic magnetic structure of only CoO_5 pyramids of $TbBaCo_2O_{5.5}$ at 250 K(in the antiferromagnetic phase). The open arrows drawn in the right side of the figure show the direction of the net moment of the CoO_2 layer. All Co^{3+} ions of CoO_6 octahedra are in the low spin state.

The magnetic structures have been determined at T=270 K (ferromagnetic phase) and T=250 K (antiferromagnetic one). We found that Co^{3+} ions of CoO_6 octahedra are in the low spin state (S=0) at both temperatures. Co^{3+} ions of CoO_5 pyramids are in the intermediate spin state (S=1) and their moments have the coplanar structure. At T=270 K, the Co^{3+} moments of CoO_5 pyramids have the canted structure, where the direction of the ferromagnetic moments is along the a-axis. At T=250 K, the structure changes to the helical one, where the modulation vector is along the c-axis and the net moment of each CoO_2 layer has nonzero value. This magnetic structure at T=250 K is shown in Fig. 2. We stress that the determination of the spin states of Co^{3+} within the CoO_6 octahedra and the CoO_5 pyramids has been first carried out in the present study.

References

1) H. Masuda *et al.*: J. Phys. Soc. Jpn. **72** (2003) 873.
2) A. Maignan *et al.*: J. Solid State Chem. **142** (1999) 247.
3) D. Akahoshi *et al.*: J. Solid State Chem. **156** (2001) 355.
4) H. Kusuya *et al.*: J. Phys. Soc. Jpn. **70** (2001) 3577.

2.3.4 Static Spin Correlations in Lightly-Doped $La_2CuO_{4+\delta}$

M. MATSUDA, M. FUJITA[1] and K. YAMADA[1]

Advanced Science Research Center, JAERI, Tokai, Ibaraki 319-1195
[1]Institute for Chemical Research, Kyoto University, Gokasho, Uji 610-0011

In lightly-doped $La_{2-x}Sr_xCuO_4$ ($0< x <0.02$), which shows coexistence of a three-dimensional antiferromagnetic (AF) long-range ordered phase and a spin-glass (SG) phase at low temperatures, it was reported that the SG phase in the coexistence region shows a diagonal spin modulation [1] as in the pure spin-glass phase in $La_{2-x}Sr_xCuO_4$ ($0.02\leq x \leq 0.055$). Most interestingly, electronic phase separation of the doped holes occurs so that some regions with hole concentration $c_h \sim 0.02$ and the rest with $c_h \sim 0$ are formed, which is predicted for a doped antiferromagnet theoretically. [2] Some clusters with $c_h \sim 0.02$ exhibit diagonal stripe correlations while the rest of the crystal with $c_h \sim 0$ shows 3D AF order.

As the next step, we performed neutron scattering experiments in lightly-doped $La_2CuO_{4+\delta}$. Since the hole concentration can be controlled in a very lightly-doped region in this system, it is possible to check whether the phase separation into the AF and SG phases are observable in this region. Another interesting thing is whether the hole doping by Sr substitution is equivalent to that by excess oxygen. It can be checked by measuring the properties of the diagonal spin modulation, that is, incommensurability and peak width.

The single crystal of $La_2CuO_{4+\delta}$ was grown by the traveling solvent floating zone (TSFZ) method. The dimensions of the rod shaped crystal were $\sim 5\Phi \times 30$ mm^3. The crystal has two twins, which are estimated to be equally distributed based on the ratio of the nuclear Bragg peak intensities from both twins. The crystal was first annealed in 1 bar Ar atmosphere at 900 °C for 24 h. This sample is considered to be almost stoichiometric ($\delta \sim 0$) and shows a sharp AF transition at 320 K. The crystal was also annealed in 1 bar oxygen atmosphere at 900 °C for 72 h. This sample is considered to have excess oxygen $\delta \sim 0.015$, which is estimated in the analogy of the result in Ref. [3], and shows a sharp AF transition at 270 K. This sample also shows minor superconducting phase with $T_c \sim 35$ K.

The neutron scattering experiments were carried out on the cold neutron three-axis spectrometers LTAS and the thermal neutron three-axis spectrometer TAS2.

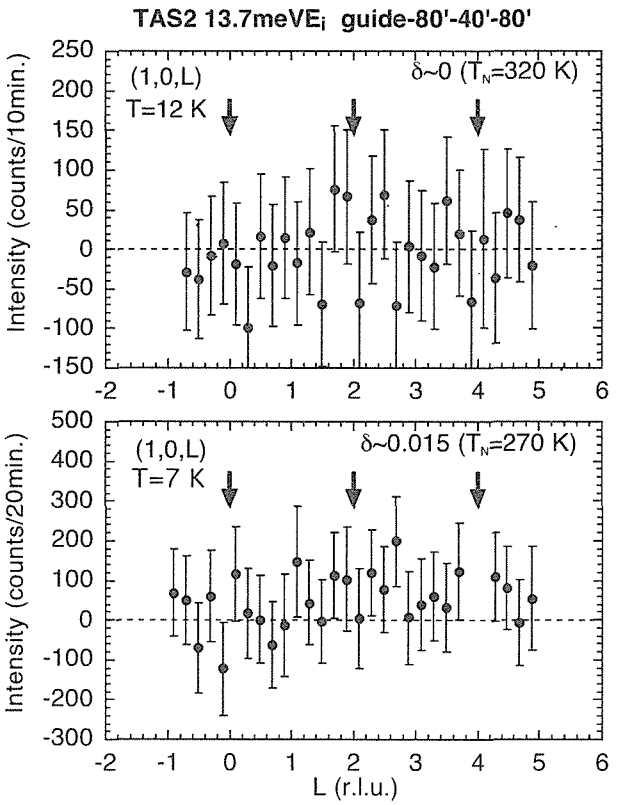

Figure 1: Elastic scans along $(1,0,L)$ at T=12 and 7 K in La_2CuO_4 and $La_2CuO_{4+\delta}$, respectively. Background intensities measured at T=50 K have been subtracted. The arrows show the positions where broad magnetic peaks originating from the SG phase are expected.

Figure 1 shows elastic scans along $(1,0,L)$ perpendicular to the CuO_2 planes in La_2CuO_4 and $La_2CuO_{4+\delta}$. As shown in Ref. [1], if the SG phase appears at low temperatures, broad magnetic peak should be observed at (1,0,even). Magnetic signal is not appreciable in both samples, indicating that the volume fraction of the SG phase is negligibly small even in the sample with $La_2CuO_{4+\delta}$.

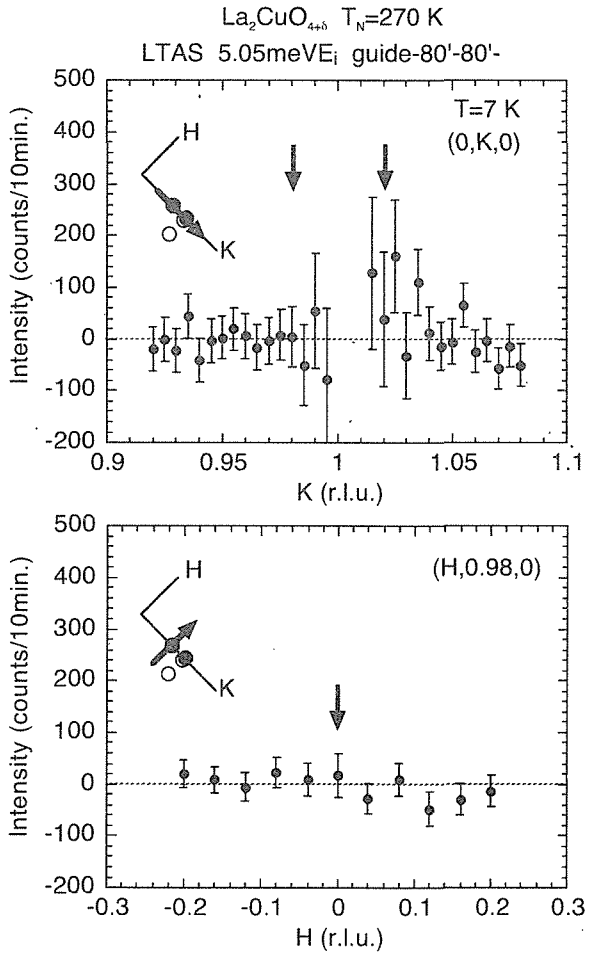

Figure 2: Elastic scans along $(0,K,0)$ and $(H,0.98,0)$ at T=7 K in $La_2CuO_{4+\delta}$ (T_N=270 K). The data measured at T=50 K are subtracted as background intensities. The arrows show the positions where broad magnetic peaks originating from the SG phase are expected.

In order to confirm absence of the magnetic signal originating from the SG phase, we also performed neutron scattering experiments in the $(HK0)$ scattering zone. Figure 2 shows elastic scans along $(0,K,0)$ and $(H,0.98,0)$ in $La_2CuO_{4+\delta}$. The error bar is large around (0,1.01,0) because a tail of the intense magnetic Bragg peak exists at this position. The magnetic peak originating from the SG phase is expected around (0,0.98,0) and (0,1.02,0). As in the results in the $(H0L)$ scattering zone, there is no sign of magnetic peaks originating from the SG phase.

Since $La_{1.99}Sr_{0.01}CuO_4$ shows a Néel temperature of 240 K, [1] the effective hole concentration in $La_2CuO_{4+\delta}$ (T_N=270 K) is estimated to be ~0.005, which is just between La_2CuO_4 and $La_{1.99}Sr_{0.01}CuO_4$. If the volume fraction of the SG phase is proportional to the hole concentration, ~25% of the total volume should be in the SG phase in $La_2CuO_{4+\delta}$ at low temperatures. From the data shown above, an upper limit for the volume fraction of the SG phase is estimated to be ~1%, suggesting that there may exist a threshold to realize the phase separation into the AF and SG phases.

In $La_2CuO_{4+\delta}$ system with $0.01 < \delta < 0.055$, the samples phase separates into hole-poor phase (0.01) and hole-rich phase (0.055) [4] so that samples with the hole concentration range cannot be available at low temperatures. Therefore, it is not possible to check whether the hole doping by Sr substitution is equivalent to that by excess oxygen. $La_{2-x}Bi_xCuO_{4+\delta}$ system, which does not show macroscopic phase separation and hole concentration at low temperatures gradually changes, [3] is appropriate to study the magnetic properties in the hole concentration range. We plan to perform neutron scattering experiments in the system in future.

References

1) M. Matsuda, M. Fujita, K. Yamada, R. J. Birgeneau, Y. Endoh andG. Shirane: Phys. Rev. B **65** (2002) 134515.
2) S. A. Kivelson and V. J. Emery: *Proceedings of the Los Alamos Symposium – 1993 : Strongly Correlated Electronic Materials*, ed K. S. Bedell *et al.* (Addison-Wele 1994), p. 619.
3) S. Wakimoto, C.-H. Lee, K. Yamada, Y. Endoh and S. Hosoya: J. Phys. Soc. Jpn. **65** (1996) 581.
4) B. O. Wells, Y. S. Lee, M. A. Kastner, R. J. Christianson R. J. Birgeneau, K. Yamada, Y. Endoh and G. Shirane: Science **277** (1997) 1067.

2.3.5

Magnetic-Field-Induced Quadrupolar Ordering in the Heavy-Fermion Superconductor $PrOs_4Sb_{12}$

M. KOHGI, K. IWASA, M. NAKAJIMA, N. METOKI[1], S. ARAKI[1], N. BERNHOEFT[2], H. SATO, Y. AOKI and H. SUGAWARA

Department of Physics, Tokyo Metropolitan University, Tokyo 192-0397
[1]Advanced Science Research Center, Japan Atomic Energy Research Institute, Ibaraki 319-1195
[2]DRFMC, SPSMS, CEA-Grenoble, 38054 Grenoble, France

$PrOs_4Sb_{12}$ is a filled-Skutterudite compound. It belongs to the space group $Im\bar{3}$ (T_h^5, #204). Maple et al. [1] and Bauer et al. [2] reported that the compound shows superconductivity below T_C = 1.85 K and electrons with a large effective mass of about 50 m_0 are responsible for the superconductivity from the value of specific heat jump at T_C. They suggested that the interaction of the quadrupole moments of Pr ions with conduction electrons is responsible for the heavy-fermion superconducting state in the material. Another interesting experimental fact is the appearance of a new phase found by specific heat and resistivity measurements under a magnetic field above approximately 5 T at low temperatures. [3]

In order to clarify the nature of ordering in this field-induced ordered phase (FIOP), a neutron diffraction experiment on a single-crystal sample of this material was performed. A single-crystal sample of about 4 g was used in the experiment. It is actually an aggregate of smaller cubes of about 1 mm average size with sharing (100) crystal planes. The half-height width of rocking curves of the sample was about 1.1 degrees in the experimental condition described below. The neutron diffraction experiment was carried out on the cold neutron triple axes spectrometer LTAS at JAERI. A pyrolytic graphite (002) monochromator and analyzer were used with a neutron wave-vector of k = 1.5Å^{-1}. The collimation of the neutron beam was open-80'-80' in the beam paths between monochromator and sample, sample and analyzer, and analyzer and detector. A cooled Be filter was inserted before the sample to eliminate higher order contaminations from the monochromator. The sample was set in a dilution refrigerator, which is inserted into the center bore of the Helmholtz-type superconducting magnet, with its [001] direction vertical.

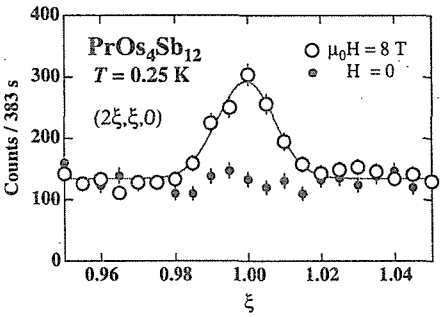

Figure 1: Scattering patterns of 210 superlattice reflection at 0.25 K with (8 T) and without magnetic field.

Scans in the reciprocal lattice plane (h,k,0) revealed resolution-limited peaks at superlattice positions characterized by the wave vectors q = [1, 0, 0] and [0,1,0] in the FIOP. Figure 1, for example, shows the observed 210 superlattice reflection at 0.25 K and 8 T together with the data at zero magnetic field. Figure 2 shows the magnetic field dependence of the peak intensity of the 210 superlattice reflection as well as that of 110 Bragg reflection where field-induced ferromagnetic Bragg scattering is superimposed. The 210 reflection starts to develop at about 5 T in accordance with the start of the FIOP at low tem-

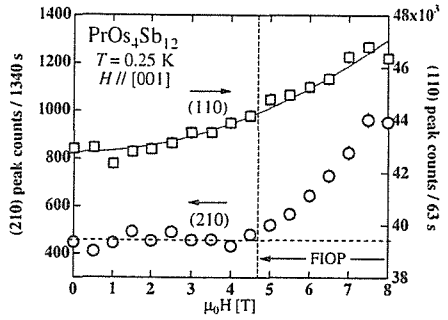

Figure 2: Magnetic field dependence of the peak intensities of the 210 and 110 reflections.

peratures. On the other hand, the intensity of the 110 reflection increases gradually with increasing field, indicating that the induced ferromagnetic moment is approximately proportional to the applied field. The superlattice peak intensities at 6 and 8 T decrease with increasing temperature, and disappear at the background level at about 0.8 and 1 K, respectively. These temperatures are also in accordance with the reported boundaries of the FIOP. Several superlattice reflections at 0.25 K and 8 T were measured in the (h,k,0) plane in order to see their origin. It was found that the integrated intensities of the observed peaks after correction of the dependence of magnetic form factor of Pr^{3+} are highly proportional to $\sin^2\alpha$ within experimental error where α is the angle between the scattering vector and the direction of the [010] axis. This fact clearly indicates that the observed superlattice reflections are due to magnetic Bragg scattering originating from antiferromagnetic moments on Pr ions parallel to the [010] direction. From the data, we can estimate the value of the antiferromagnetic moment μ_{AF} by comparing it with the integrated intensity of the 110 nuclear Bragg reflection measured at a zero magnetic field. The value of the induced ferromagnetic moment μ_F is also estimated from the integrated intensity of the field-induced component of 110 Bragg reflection. They are $\mu_{AF} = 0.025 \pm 0.006\mu_B$ and $\mu_F = 0.354 \pm 0.006\mu_B$, respectively, per Pr ion at 0.25 K and at 8 T. The antiferromagnetic component is only 8% of the induced ferromagnetic moment.

The present experimental result is reasonably explained by a model that the observed antiferromagnetic moment is due to the ordering of 4-f electron orbit such that the the magnetic field applied along the [001] direction (z-direction) gives rise to the induced magnetic moment whose component along the [010] direction (y-direction) changes sign from the corner site to the body center site of the *bcc* lattice. This type of ordering is actually realized by the ordering of the O_{yz}-type quadrupolar moment. This model is supported by the molecular field calculation based on the crystal field level scheme in which the ground state is the singlet Γ_1 and triplet ${\Gamma_4}^{(1)}$ is the first excited state at about 8 K [4]. The quadrupolar ordering is induced by the applied magnetic field due to formation of a pseudo-doublet by the Zeeman effect.

The present experiment revealed that there exists rather strong quadrupolar interaction than the magnetic interaction in $PrOs_4Sb_{12}$. This fact suggests that the unusual superconductivity in the compound may be mediated by the degrees of freedom of the quadrupolar moment in the system. A report of the present work has been published elsewhere [4].

References

1) M. B. Maple, P.-C. Ho, V. S. Zapf, N. A. Frederick, E. D. Bauer, W. M. Yuhasz, F. M. Woodward and J. W. Lynn: J. Phys. Soc. Jpn. **71** (2002) Suppl., 23.
2) E. D. Bauer, N. A. Frederick, P.-C. Ho, V. S. Zapf and M. B. Maple: Phys. Rev. B **65** (2002) 100506(R).
3) Y. Aoki, T. Namiki, S. Ohsaki, S.R. Saha, H. Sugawara and H. Sato: J. Phys. Soc. Jpn. **71** (2002) 2098.
4) M. Kohgi, K. Iwasa, M. Nakajima, N. Metoki[1], S. Araki[1], N. Bernhoeft[2],J.-M. Mignot., A. Gukasov, H. Sato, Y. Aoki and H. Sugawara: J. Phys. Soc. Jpn. **72** (2003) 1002.

2.3.6 Ferromagnetism in CeP under High Pressure

D. Kawana, T. Osakabe[1], A. Hannan, M. Kohgi

Department of Physics, Tokyo Metropolitan University, Hachioji, Tokyo 192-0397
[1]Advanced Science Research Center, JAERI, Tokai, Ibaraki 319-1195

CeP, with the simple NaCl-type crystal structure, shows dense-Kondo-like behavior in the transport properties in spite that its carrier number is very low (0.01/f.u.).[1)] It shows also unusual magnetic properties especially under high pressures, where double layers of ferromagnetic Ce(001)-plane with a large moment value of $\sim 2\mu_B$ appear periodically among the type-I antiferromagnetic structure of Γ_7 Ce ions. The period of the structure decreases one by one from 9 to 4 with increasing pressure up to 1.7GPa. It is remarkable that some of the magnetic structures around 2 GPa are similar to ones of CeSb and CeBi at ambient pressure.[2)] We have systematically investigated the magnetic strctures and complex phase diagram of this compound by neutron scattering.

Our previous work shows that, in the pressure range between 2.5 and 2.8GPa, a ferromagnetic phase appears at low temperatures below around 30 K. Above this temperature another phase 3* (↑↑○↓↓○; the arrow and circle represent ferromagnetic and paramagnetic Ce(001)-planes, respectively) appears. Interpolating phase boundaries, we expect that only ferromagnetic phase exists at the pressure above about 3.1GPa.[3)] In order to confirm this point, we performed an experiment at the triple-axis-spectrometer TAS-1(2G) installed at JRR-3 reactor, JAERI. To apply a pressure on the sample, we used a sapphire anvil cell. The sample of $0.3 \times 0.2 \times 0.15$ mm^3 was set in a hole of phosphorous bronze gasket, with a little ruby powder for pressure calibration and Daphne7373 as pressure transmitting medium. We achieved a pressure value of 3.2GPa.

Figure 1 shows the temperature dependences of peak intensities at (2 0 0) and (2 −1/3 0). With decreasing temperature, the former begins to increase at 41 K, but the latter does not show any clear change below 50 K. The experimental result clearly indicates that there is only one ordered-state, which is ferromagnetic, at 3.2GPa.

From the measurement of electric resistance, the critical temperature T_c of the ferromagnetic phase will decrease with increasing pressure and disappear at about 6 GPa.[4)] The process is quite interesting because a drastic change of $4f$-electron state of Ce atom is brought about by applying pressure. The present work is a part of the study of this phenomenon.

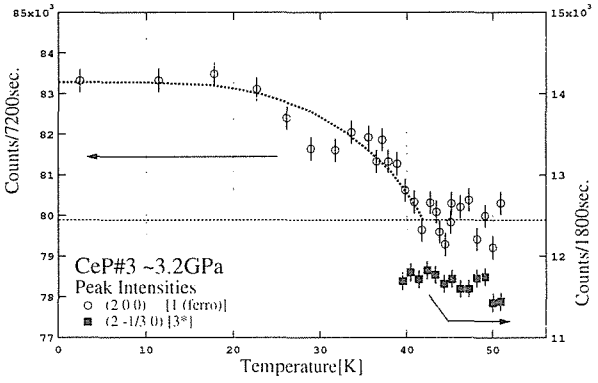

Figure 1: Temperature dependencies of peak intensities at (2 0 0) and (2 -1/3 0) on CeP in 3.2GPa.

References

1) T. Suzuki: Physica B, **186-188** (1993) 347.
2) M. Kohgi *et al.*: Physica B, **281-282** (2000) 417.
3) A. Hannan *et al.*: Applied Phys A, **74** (2002) S565.
4) N. Môri *et al.*: *Physcal Properties of Actinde and Rare Earth Compounds* JJAP Series **8** (1993) 182.

2.3.7

Structure refinements for single crystalline $Sr_3Ru_2O_7$ under magnetic field

Y. YOSHIDA[1,2], S. KATANO[3] , N. ASO[4], S.I. IKEDA[1], N. SHIRAKAWA[1] , M. NISHI[4], and Y. UWATOKO[4]

[1]NeRI, AIST, Tsukuba, Ibaraki 305-8568, Japan
[2]JSPS, Chiyoda, Tokyo 102-8471, Japan
[3]JAERI, Tokai, Ibaraki 319-1195, Japan
[4]ISSP, University of Tokyo, Kashiwa, Chiba 277-8581, Japan

Relation between magnetism and structural distortions due to oxygen displacements in transition metal oxides is a crucial issue to understand such materials microscopically. High critical- temperature cuprate superconductors, for instance, have been investigated based on such a perspective. Recently, strontium ruthenates with the layered perovskite crystal structure were found intriguing. Single layered Sr_2RuO_4 (tetragonal structure with the $I4/mmm$ symmetry) shows spin-triplet superconductivity [1] and double layered $Sr_3Ru_2O_7$ reveals magnetic field induced quantum criticality at around metamagnetic field of 7 tesla [2]. Particular instability of the crystal structure with rotations of RuO_6 octahedra along the c-axis (normal to the RuO_2 plane) subsists in $Sr_3Ru_2O_7$ (nearly tetragonal : orthorhombic with the $Bbcb$ symmetry) [3,4]. Indeed, from the results of magnetization measurements under hydrostatic and uniaxial pressure, it is suggested that uniaxial pressure along the c-axis, normal to the two-dimensional RuO_2 plane, causes an outstanding transition from the enhanced-paramagnetic to ferromagnetic phase [5–7]. Although neutron scattering study for structural refinements under uniaxial pressure is under progress, it is appropriate to assume that the structural instability of the RuO_6 octahedron plays an important role in magnetic property of $Sr_3Ru_2O_7$.

In order to clarify whether the crystal structure changes at the metamagnetic field, we have tried to refine its structure for single crystalline $Sr_3Ru_2O_7$ under magnetic field at TAS-2 in JRR-3, JAERI. Single crystalline samples of $Sr_3Ru_2O_7$ were grown by a self-flux floating-zone technique using an image furnace. The dimension of the samples is $5 \sim 6$ mm in diameter and $10 \sim 15$mm in length.

According to Shaked *et al.*, superlattice reflections corresponding to the rotation of the RuO_6 octahedron are observed [8].As the first step, we tried a structural analysis under a zero field at several temperatures. In this study, we employed the [HHL] zone, and tried to find out some intensity changes of reflections in this plane with decreasing temperature . There we could not observe clear evidence of the expected intensity change associated with the greater rotation angle which was already reported on powder samples [3]. To investigate the superlattice reflections described above directly, we are now performing four-circle neutron diffraction experiments on single crystalline $Sr_3Ru_2O_7$ at FONDER to check whether the superlattice reflections are strong enough to be observed at the JRR-3 neutron source. After that, the measurements under magnetic fields will be examined.

References

1) Y.Maeno, T.M. Rice and M. Sigrist, Physics Today **54** (2001) 42.
2) S.A. Grigera *et al.*, Science **294**(2001) 329 .
3) H. Shaked *et al.*, Phys. Rev. B **62** (2000) 8725.
4) Q. Huang *et al.*, Phys. Rev. B **58** (1998) 8515 .
5) S.I. Ikeda *et al.*, Phys. Rev. B **62** (2000) R6089 .
6) S.I. Ikeda *et al.*, Physica C **364-365** (2001) 376 .
7) S.I. Ikeda *et al.*, preprint.
8) H. Shaked *et al.*,J. Solid State Chem. **154** (2000) 361.

2.3.8 Magnetic excitations in Ni-substituted $La_{2-x}Sr_xCuO_4$

H. HIRAKA, T. CHUREI[1], Y. ENDOH, K. YAMADA[1] and M. MATSUDA[2]

Institute for Materials Research, Tohoku University, Sendai 980-8577
[1]Institute for Chemical Research, Kyoto University, Uji 611-0011
[2]Advanced Science Research Center, JAERI, Tokai, Ibaraki 319-1195

Impurity doping of 3*d*-metal Zn or Ni upon high-T_c superconductors gives an invaluable information how magnetic spins concern the novel high-T_c superconductivity, because non-magnetic Zn^{2+} ($S = 0$) or magnetic Ni^{2+} ($S = 1$) directly substitutes for Cu^{2+} ($S = 1/2$) in CuO_2 planes. Although effects of Zn doping are intensively studied from experimental and theoretical aspects, there are few studies for Ni impurity, particularly through neutron scattering. Recently, Kimura *et al.* performed a systematic study on spin dynamics for Zn-substituted $La_{1.85}Sr_{0.15}CuO_4$. [1] They insist that Zn substitution induces an in-gap state and fills the spin gap structure of impurity-free system. [2] Therefore, it is also interesting to investigate how Ni impurity modifies the spin gap excitations.

We have grown a single crystal of $La_{1.85}Sr_{0.15}Cu_{0.98}Ni_{0.02}O_4$ by means of TSFZ techniques. After an annealing process under oxygen-gas flow, the onset T_c was determined to be 28 K with a somewhat broad transition. The neutron scattering experiments were carried out on thermal-neutron triple-axis spectrometers TAS-1 and TAS-2, and a cold-neutron triple-axis spectrometer HER at JRR-3M. The incident or final energy of thermal (cold) neutrons was fixed at 14.7 or 13.5 meV (5.0 meV). The sample with a total volume $v \simeq 1.7$ cc and an effective mosaic $\eta \simeq 40'$, was set in the tetragonal (h, k, 0) scattering plane.

In contrast to pure $La_{1.85}Sr_{0.15}CuO_4$, magnetic scattering below 3 meV is clearly observable in the Ni-doped compound even at well below T_c. Furthermore, Fig. 1 demonstrates that $\chi''(q_{1C}, \omega)$ strikingly increases at about 1 meV, associated with a sharpening of peak width as seen in κ in the inset. Substitution on Ni smears and fills the spin-gap structure like Zn does. However, judging from the less clear static component in the Ni-substituted system compared to Zn, [3] spin fluctuations are considered to slow down gradually around Ni in the wide space but never quench. This behavior seems to be consistent with the broad superconducting transition appeared in the shielding effect, if both T_c and spin-fluctuation energy vary locally in space with an intimate relation. The magnetic-impurity effects should be qualitatively different from non-magnetic Zn.

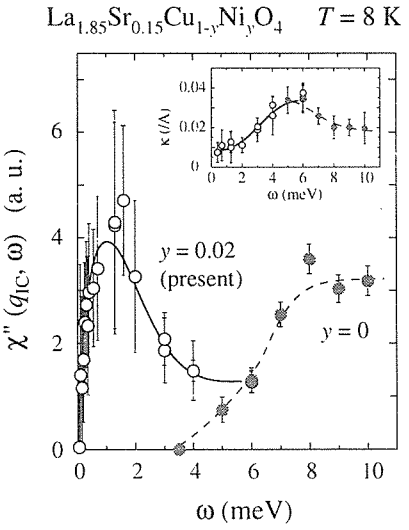

Figure 1: The dynamical susceptibility $\chi''(q_{1C}, \omega)$ and the inverse coherent length κ (inset) at 8 K. The open and solid circles represent data from Ni 2%-doped and Ni-free $La_{1.85}Sr_{0.15}CuO_4$ ($T_c = 38$ K) [2], respectively. The lines are drawn as a guide to the eyes.

References

1) H. Kimura *et al.*: cond-mat/0209428.
2) K. Yamada *et al.*: Phys. Rev. Lett. **75** (1995) 1626.
3) T. Churei *et al.*: submitted to Physica C (2003).

2.3.9 Neutron scattering study of spin correlations in electron-doped $Pr_{0.89}LaCe_{0.11}CuO_{4+\delta}$ single crystals

M.FUJITA[1], S.KUROSHIMA[1], T.UEFUJI, M.MATSUDA[2], K.KAKURAI[2] and K.YAMADA[1]

[1]Institute for Chemical Research, Kyoto university, Uji 611-0011
[2]Advanced Science Research Center, JAERI, Tokai, Ibaraki 319-1195

Mechanism of high-T_c superconductivity mediated by spin fluctuations is one of the central topics in highly correlated electron systems. Studies of spin correlations in the hole-doped high-T_c cuprates such as $La_{2-x}Sr_xCuO_4$ (LSCO) have intensively been carried out by neutron scattering experiments, and show an intimate relation between incommensurate spin correlations and superconductivity.[1)] However, comprehensive study on the electron-doped system is lacking due to the difficulties in growing single crystal and post-anneal treatment for inducing superconductivity.

Quite recently, neutron-scattering study on the electron-doped $Nd_{1.85}Ce_{0.15}CuO_4$ (NCCO) first revealed that *commensurate* spin fluctuations exist in the superconducting (SC) phase as seen in the antiferromagnetic (AF) phase.[2)] This is crucial result for understanding the common role of the spin correlations for the mechanism of high-T_c superconductivity irrespective of carrier type. However, to investigate the universal nature in the electron-doped system further study using other electron-doped cuprates is important. Especially sample with negligible effects from large rare-earth moment is highly required since such as Nd^{3+} moment would impede the detailed study of inherent nature of Cu^{2+} spins that will play important role for superconductivity.

We therefore performed systematic susceptibility and neutron scattering measurements on the $Pr_{0.89}LaCe_{0.11}CuO_{4+\delta}$ (PLCCO) system in which the effect of rare-earth moment is much reduced compared with that in NCCO.[3)] By controlling the relative oxygen contents per unit formula δ during the annealed procedure, we study the change in the static and dynamical spin correlations and in the superconducting property in the PLCCO system. Note that as-grown sample is assumed to be stoichiometric (δ=0) and the values for annealed sample were determined by measuring the weight loss of the sample after the heat treatment. Neutron-scattering measurements were carried out at thermal neutron triple-axis spectrometers, TAS-1 and TAS-2.

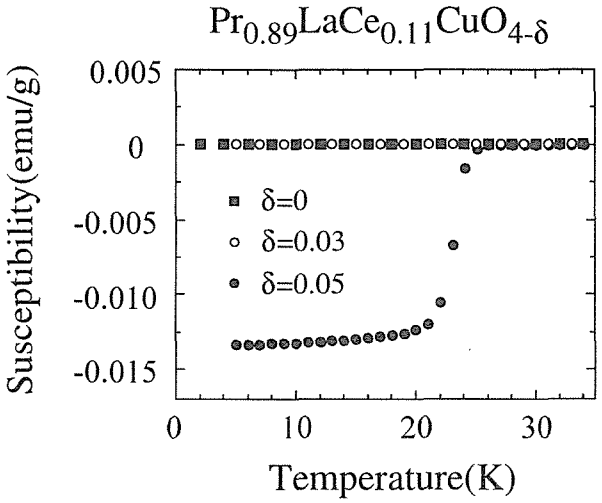

Figure 1: Magnetic susceptibility measured at 10 Oe for single crystal samples of $Pr_{0.89}LaCe_{0.11}CuO_{4+\delta}$ with (a) δ=0, (b) 0.03 and (c) 0.05 after the zero-field-cooling process.

Figure 1 shows magnetic susceptibility for x=0.11 samples with different δ. The as-grown (δ=0) and slightly oxygen-reduced (δ=0.03) samples do not show the superconductivity. However, in the sample with δ=0.05, bulk superconductivity appears at the onset temperature of 25.5 K. These results clearly demonstrate that there exists a critical value of oxygen loss, δ_c, for the appearance of

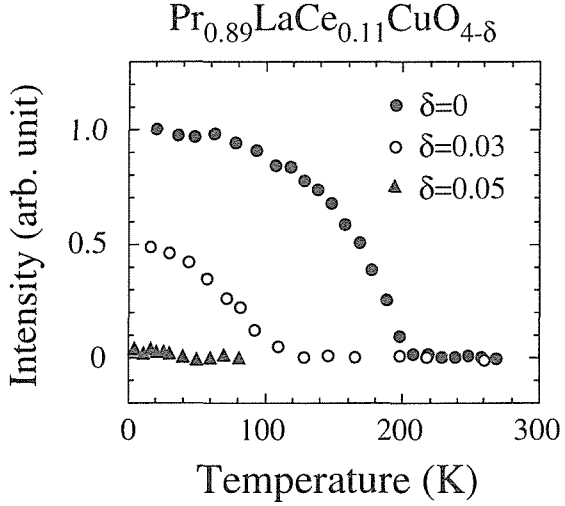

Figure 2: Temperature dependence of volume corrected peak intensity of (1 2 0) magnetic Bragg position measured for $Pr_{0.89}LaCe_{0.11}CuO_{4+\delta}$ with δ=0, 0.03 and 0.05.

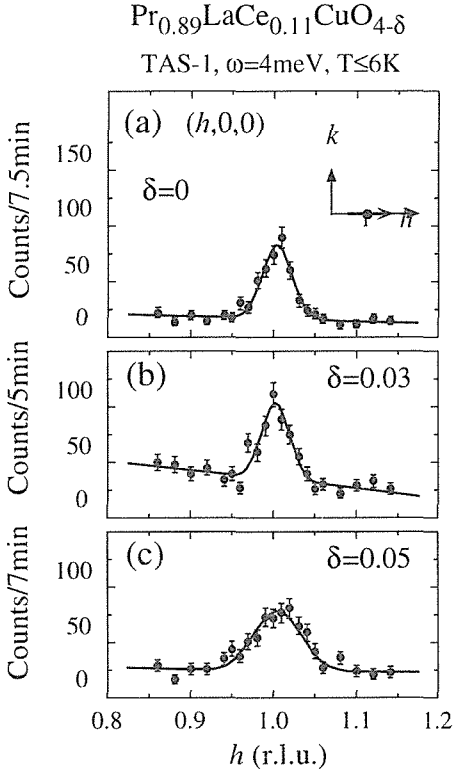

Figure 3: Constant-energy profiles at ω=4meV though (1 0 0) AF zone center for $Pr_{0.89}LaCe_{0.11}CuO_{4+\delta}$ with (a) δ=0, (b) 0.03 and (c) 0.05. Scan trajectory is shown in the upper panel. Solid lines are results fitted with a single Gaussian function by convoluting the experimental resolution.

superconductivity in the sample with a given Ce concentration.

We next investigated the magnetic properties in these samples. Temperature dependence of magnetic peak intensity at orthorhombic (1 2 0) reciprocal position are shown in Fig. 2. Intensities for three samples are measured under the identical experimental setups and normalized by the effective sample volume after subtracting the background. Comparing to the results for δ=0 and 0.03, it is obvious that both peak-intensity and T_N decreases with increasing δ. No clear evidence of magnetic order was observed in the superconducting sample with δ=0.05. Therefore, the AF order is degraded by the oxygen-reduction with decreasing ordered moment and/or region and T_N with increasing δ. Upon further oxygen-reduction, SC phase concomitantly appears with the disappearance of AF phase, suggesting the competitive relation between superconductivity and magnetic order.

On the other hand, spin fluctuations were observed even in the SC sample. Therefore, well-correlated spin fluctuations exist in the SC phase irrespective of the types of doped carrier, supporting a common role of the spin fluctuations for the high-T_c superconductivity. However, commensurate spin fluctuations observed in both AF and SC phases are contrastive to the incommensurate ones in the hole-doped LSCO system in which the spin density modulation changes from being diagonal to parallel to the Cu-O bond direction on crossing the insulator-superconductor phase boundary.[4)]

These similarities and differences in the spin correlation between the electron- and hole-doped system would provide important clues for understanding common mechanism of the high-T_c superconductivity.

References

1) K. Yamada *et al.* : Phys. Rev. B. **57** (1998) 6165.
2) K. Yamada *et al.* : Phys. Rev. Lett. **90** (2003) 137004.
3) M. Fujita *et al.* : Phys. Rev. B. **67** (2003) 014514.
4) M. Fujita *et al.* : Phys. Rev. B. **65** (2002) 064505.

2.3.10

Search for Antiferromagnetic Fluctuations in Bismuth-Based Superconductors

N. Kaneko, M. Matsuda[1], K. Kakurai[1], and M. Greven

Laboratory for Advanced Materials, Stanford University, Stanford CA 94305, USA
[1]Advanced Science Research Center, JAERI, Tokai, Ibaraki 319-1195, Japan

It is widely believed that antiferromagnetic fluctuations play an important role in the physics of high-temperature superconductivity. The undoped parent compounds, such as La_2CuO_4, are antiferromagnetic insulators. Upon doping the CuO_2 sheets with a few percent of holes, these materials become metallic and superconducting, with "strange" metallic behavior in the normal state. Neutron scattering studies have demonstrated that dynamic antiferromagnetic correlations are a robust feature of both superconducting and normal states[1-6].

$La_{2-x}Sr_xCuO_4$ (LSCO) has been the only single-layer hole-doped high-temperature superconductor that has been studied systematically via neutron scattering, since it is relatively straightforward to grow the required large single crystals. Detailed studies have revealed many interesting properties, such as an incommensurate magnetic response[1,2,7,8]. The only other high-Tc family of materials for which sizeable crystals over a wide range of hole-doping have been available for neutron scattering studies is the structurally more complicated bi-layer system $YBa_2Cu_3O_{6+\delta}$ (YBCO)[3-6,9]. The magnetic response of YBCO appears to be rather different from that of LSCO. In particular, it was found that the magnetic response is gapped and incommensurate only at high energies, and that there exists a magnetic resonance (at 41meV for optimally doped YBCO) in the superconducting state.

To better understand the connection between antiferromagnetic correlations and high-temperature superconductivity, it will be necessary to study additional materials. Neutron scattering experiments require sizeable samples, a fact that has presented a significant obstacle toward this end. We have succeeded with the growth of sizeable crystals of the single-layer and double-layer Bi-based superconductor $Bi_{2-y}Pb_ySr_{2-x}La_xCuO_{6+\delta}$ (Bi2201). The sample shown in Fig. 1 consists of 6 co-aligned single crystals with total volume of 1.1 cm^3. Initial crystal checks demonstrated the single-grain nature of the individual crystals. Small pieces from these crystals show excellent superconducting properties, with an onset of $T_c \sim 36$ K, which compares well with the highest values achieved in LSCO.

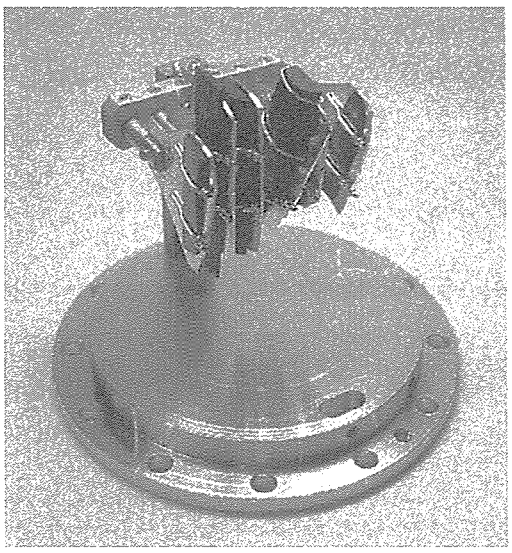

Figure 1: A set of $Bi_{1.7}Pb_{0.3}Sr_{1.6}La_{0.4}CuO_{6+\delta}$ crystals mounted on a sample holder in the (H0L) zone.

In light of the differences observed for LSCO and YBCO, a study of the magnetic response of Bi2201 should yield valuable new information about the connection between superconductivity and antiferromagnetic order and fluctuations. We have continued to pursue neutron scattering measurements to search

for antiferromagnetic fluctuations in Bi2201. Specifically, we carried out inelastic neutron scattering measurements on the TAS-1 and TAS-2 triple-axis instruments at the JAERI JRR-3M research reactor. Previously we had conducted measurements in the (HK0) scattering plane in the range 3-12 meV. Our most recent measurements extended the search of inelastic magnetic features to the (H0L) zone and examined energy transfers up to 30 meV. Consistent with our previous results, these measurements reveal no obvious features. A possible (incommensurate) low-energy magnetic response may be harder to discern, perhaps because it is intrinsically broader than in LSCO. We note, that the experiment is made difficult by the fact that the scattering in Bi2201 results in a very high "background," in large part due to significant low-energy phonon scattering, a result of the complex crystal structure of Bi2201.

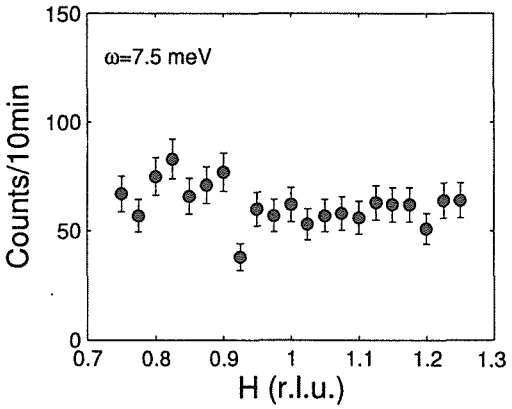

Figure 2: Data taken around (1,0,3.5) for Bi-2201 at an energy transfer of 7.5 meV just above the superconducting transition at T=40 K. The spectrometer configuration is Open-Sapphire-80-S-PG-80-80, E_f=14.7 meV.

In optimizing the crystal growth, it was very helpful to aim for a sample composition that resulted in the highest possible superconducting transition temperature and in very sharp transition widths. On the other hand, underdoped Bi2201 should exhibit more prominent antiferromagnetic fluctuations. While it has not been possible so far to obtain single crystals at half-filling (i.e., undoped CuO_2 sheets), we have managed to grow samples that are very underdoped and non-superconducting. Our goal for the near future is to continue our search for antiferromagnetic correlations in underdoped Bi2201.

References

1) M.A. Kastner, R.J. Birgeneau, G. Shirane and Y. Endoh, Rev. Mod. Phys. **70**, 897 (1998).
2) G. Aeppli *et al.*, Physica C **318**, 9 (1999).
3) H.F. Fong *et al.*, Phys. Rev. Lett. **78**,713 (1997).
4) H.F. Fong *et al.*, Phys. Rev. B **61**, 14773 (2000).
5) M. Arai *et al.*, Phys. Rev. B **83**, 608 (1999).
6) Y. Sidis *et al.*, Science **288**, 1234 (2000).
7) H. Kimura *et al.*, Phys. Rev. B **59**, 6517 (1999).
8) M. Matsuda *et al.*, Phys. Rev. B **65**, 134515 (2002).
9) P. Dai *et al.*, Phys. Rev. B **63**, 054525 (2001).

2.3.11

Crystal Field Excitation in rare earth Er-based antiferromagnet $ErAg_2$

I. Umehara[1], K. Sato[2], N. Metoki[3,4]

[1] Department of Physics, Faculty of Engineering, Yokohama National University, Tokiwadai, Yokohama 240-8501
[2] Department of Physics, Faculty of Science, Toyama University, Toyama 930-8555
[3]Advanced Science Research Center, JAERI, Tokai, Naka, Ibaraki 319-1195
[4] Department of Physics, Tohoku University, Aoba, Sendai, 980-8578

$ErAg_2$ is a rare earth compound with a body centered tetragonal $MoSi_2$-type (space group: I4/mmm) structure.[1-3] It has been reported that the magnetic moments on Er atoms order antiferromagnetically below the Néel temperature $T_N = 5.2$ K, and exhibit a magnetic structural change at $T = 3.5$ K. A previous neutron powder diffraction study[1] revealed a complicated incommensurate sinusoidal moduration at high temperature phase, while a commensurate antiferromagnetic ordering was observed below $T = 3.5$ K. On the other hand, our specific heat measurement on a single crystalline sample of $ErAg_2$ reported a new transition at $T = 4.0$ K[4]. Furthermore multi-step magnetization process has been observed in this compound, indicating the existence of a complicated magnetic H-T phase diagram. Recently the pressure effect of these transtions were also studied. In order to understand the origin of the successive magnetic transitions and the metamagnetic transitions, we tried to measure the crystal field excitation of $ErAg_2$.

The inelastic scattering profile was measured using triple-axis spectrometer TAS-2 with fixed E_f at 14.7 meV. The collimation was 40'-40'-80'. A polycrystalline sample was cooled by using a close cicle refregerator down to 10 K.

Figure 1 summarizes the result of the inelastic scattering profile of $ErAg_2$. We observed a clear excitation around 5.5 meV and 8.5 meV at $T = 10$ K. The intensity of these peaks decreased with elevating temperature at $T = 100$ K. Therefore we concluded that these peak were crystal field excitations. The excitation energy of these peaks were more or less consistent with CEF level scheme which explains susceptibility data, where the excitation energy would be 34 K, 77 K, and 85 K for the first, second, and third excitation level, respectively. On the other hand, the excitation observed below 3 meV at 100 K is considered as phonon.

References

1) M. Atoji: J. Chem. Phys. **57** (1972) 851.
2) S. Miura, T. Kaneko and M. Ohashi: J. Phys. Soc. Japan **37** (1974) 1464.
3) M. Ohasi, T. Kaneko and S. Miura: J. Phys. Soc. Japan **37** (1975) 588.
4) I. Umehara, Y. Takamo, M. Endo, F. Ishikawa, M. Yamaguchi and K. Sato: Physica **B281&282** (2000) 169.

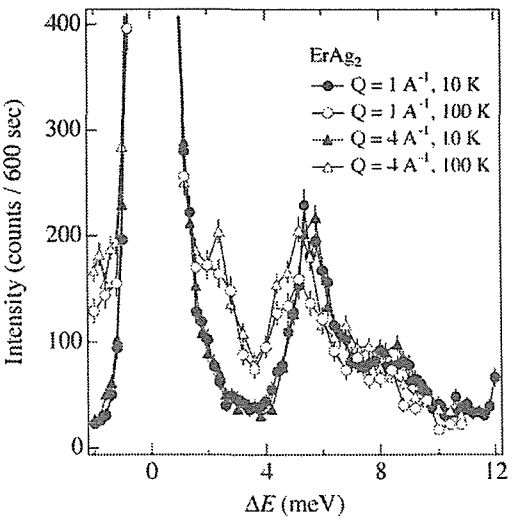

Figure 1: The inelastic scattering profile of $ErAg_2$.

2.3.12 Magnetic and Crystal Structure of $CeAgSb_2$

S. ARAKI[1], N. METOKI[1,2] A. THAMIZHAVEL[3] and Y. ŌNUKI[1,3]

[1]Advanced Science Research Center, JAERI, Tokai, Ibaraki 319-1195
[2]Department of Physics, Tohoku University, Aoba, Sendai 980-8578
[3]Graduate School of Science, Osaka University, Toyonaka, Osaka 560-0043

$CeAgSb_2$ with tetragonal crystal structure orders at T_c = 9.6 K with a small net ferromagnetic component of $0.33\mu_B$/Ce parallel to the c-axis [1]. The in-plain magnetization below T_c increases linearly with magnetic field and reached about $1.2\mu_B$ at 3 T [2]. This induced moment is much larger than the spontaneous moment along the c-axis. Therefore, the antiferromagnetic (AFM) and/or complex magnetic structure was suggested to be the origin of the unusual magnetic properties. However, no AFM peak has been reported from neutron diffraction experiment [1]. The purpose of this study is to clarify the crystal and magnetic structure in $CeAgSb_2$.

The neutron diffraction experiments were carried out using TAS-1 and HRPD. A large amount of polycrystalline sample, 30 g, and single crystal with 0.85 g were used.

$CeAgSb_2$ crystallizes in the tetragonal structure with space group P4/nmm. Two controversial models have been proposed so far for the crystal structure of $CeAgSb_2$. Sologub *et al.* [3] and Brylak *et al.* [4] reported that $CeAgSb_2$ has the $ZrCuSi_2$-type structure, where Ce, Ag and Sb atoms occupy the crystallographical 2c (Ce), 2b (Ag), 2a (Sb1), and 2c (Sb2) sites. On the other hand, André *et al.* [1] attributed their neutron powder diffraction data to the same type of structure, but assumed different site occupations, namely, 2a (Ag) and 2b (Sb1) sites. This controversy is due to the weak contrast between Ag and Sb atoms both for X-rays and neutrons. Figure 1 shows the high-resolution neutron powder diffraction data of $CeAgSb_2$ measured at room temperature in the paramagnetic state. This powder diffraction data can be explained by both Sologub- and André-type structures, although reliable parameters for Sologub's model are slightly better than the ones for André's model. In order to clarify the crystal structure of $CeAgSb_2$, the weak (001), (002), (003), and (005) reflections from a large polycrystalline sample (30 g) and a high-quality single-crystalline sample were measured with very good statistics on the TAS-1 spectrometer. The observed integrated intensities are plotted in the inset of Fig. 1. The agreement of the experimental data with the calculated intensity for Sologub's model (solid line) is clearly better than that of André's model denoted by the dashed line. Therefore we conclude that Sologub's model describes the crystal structure of $CeAgSb_2$. The high-resolution neutron powder diffraction pattern in Fig. 1 was analyzed by means of Rietveld refinement with RIETAN-2000 [5] assuming Sologub's model. The fit of the data is satisfactory. The obtained structural parameters are listed in Ta-

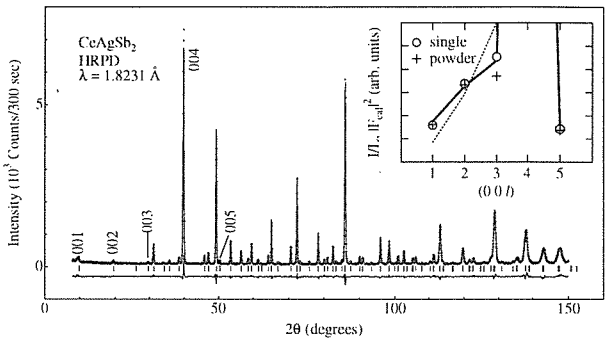

Figure 1: Neutron powder diffraction pattern at room temperature in $CeAgSb_2$. The inset shows the integrated intensities of the $(00l)$ reflections at 12 K. The bold line and dashed line denote the square of the structure factor calculated based on the Sologub-type structure and André-type structure, respectively.

ble 1.

Figure 2 shows the neutron powder diffraction pattern at $T = 4$ K and 12 K, which are below and above the Curie temperature $T_c = 9.6$ K, respectively. The low-temperature data after subtracting the high-temperature data are also plotted in Fig. 2. The clear ferromagnetic scattering from Ce moments were superposed on the (101) and (110) nuclear peaks. The ferromagnetic scattering on the (103) and (112) may also be observed, however, which are masked by the large nuclear scattering. Some small cusp-like structure, e.g., 2θ=36°, seen in Fig. 2 were investigated again with higher statics, however, these peak structures were not reproducible. Therefore, we conclude that no antiferromagnetic scattering was observed in our neutron powder diffraction experiment. The inset of Fig. 2 shows the integrated intensity divided by the Lorentz factor. The observed data can be explained by the ferromagnetic component of $0.41(3)\mu_B$ parallel to the c-axis. This is consistent with previous neutron scattering and magnetization studies. [1, 2] Although the statistical error of our neutron powder diffraction data is much smaller than that in the previous study [1], we could observe no trace of antiferromagnetic or incommensurate magnetic satellite peaks within the accuracy range of the order of $0.09\mu_B$/Ce. This value is much smaller than the in-plane antiferromagnetic component on the order of $1\mu_B$ expected from the magnetization measurements. An antiferromagnetic peak was also searched for in

Table 1: Crystallographic data in $CeAgSb_2$ obtained by Rietveld refinement of neutron powder diffraction data in Fig. 1.

a=4.3675(4) Å, c=10.708(1) Å				
Atom	site	x	y	z
Ce	2c	1/4	1/4	0.2388(2)
Ag	2b	3/4	1/4	1/2
Sb1	2a	3/4	1/4	0
Sb2	2c	1/4	1/4	0.6734(3)

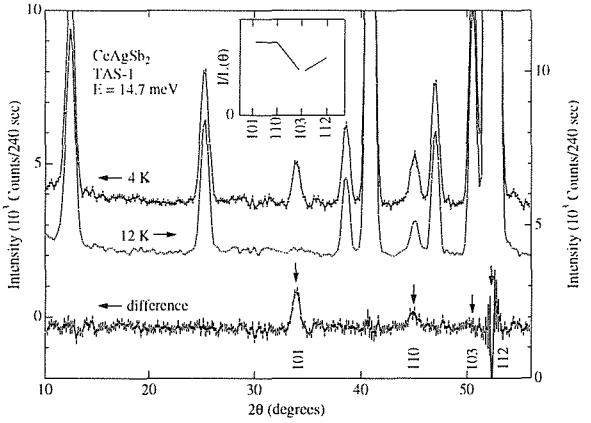

Figure 2: Neutron powder diffraction patterns below (4 K) and above (12 K) $T_c = 9.6$ K in $CeAgSb_2$. The magnetic diffraction pattern, which is obtained as the difference of patterns between 4 K and 12 K, is also plotted. The inset shows the integrated intensity of the magnetic scattering.

the case of the single-crystalline sample. Although the diffraction experiments with a single crystal presents a much higher sensitivity with low background, no trace of the antiferromagnetic peak was observed in the accuracy range of 3×10^{-3} of the (101) ferromagnetic peak along some high symmetry axes on the (hhl), $(h0l)$, and $(hk0)$ scattering planes. We also performed a mesh scan on the $(h0l)$ scattering plane. However no antiferromagnetic or SDW peak was detected.

We conclude that $CeAgSb_2$ has a simple ferromagnetic ground state with the ordered moment of $0.41\mu_B$ along the c-axis.

References

1) G. André, F. Bourée, M. Kolenda, B. Leśniewska, A. Oleś and A. Szytuła: Physica B **292** (2000) 176.
2) K.D. Myers, S.L. Bud'ko, I.R. Fisher, Z. Islam, H. Kleinke, A.H. Lacerda and P.C. Canfield: J. Magn. Magn. Mater. **205** (1999) 27.
3) O. Sologub, H. Noël, A. Leithe-Jasper, P. Rogl and O.I. Bodak, J. Solid State Chem. **115** (1995) 441.
4) M. Brylak, M. H. Möller and W. Jeitschko, J. Solid State Chem. **115** (1995) 305.
5) F. Izumi and T. Ikeda, Mater. Sci. Forum, **321-324** (2000) 198.

2.3.13 Magnetic Excitations in $CeAgSb_2$

S. ARAKI[1], N. METOKI[1,2] A. THAMIZHAVEL[3] and Y. ŌNUKI[1,3]

[1]Advanced Science Research Center, JAERI, Tokai, Ibaraki 319-1195
[2]Department of Physics, Tohoku University, Aoba, Sendai 980-8578
[3]Graduate School of Science, Osaka University, Toyonaka, Osaka 560-0043

$CeAgSb_2$ with tetragonal crystal structure orders at $T_c = 9.6$ K with a small net ferromagnetic component of $0.33\mu_B$/Ce parallel to the c-axis [1]. The in-plain magnetization below T_c increases linearly with magnetic field and reached about $1.2\mu_B$ at 3 T [2]. This induced moment is much larger than the spontaneous moment along the c-axis. Therefore, the antiferromagnetic (AFM) and/or complex magnetic structure was suggested to be the origin of the unusual magnetic properties. However, no AFM peak has been reported from neutron diffraction experiment [1]. Our recent experiment also revealed that $CeAgSb_2$ has a simple ferromagnetic ground state [4]. The purpose of this neutron scattering study is to reveal the origin of the unusual magnetization curve.

The neutron scattering experiments were carried out using TAS-1 at $E_f = 14.7$ meV and LTAS at $E_f = 4.0$ meV. A large amount of polycrystalline sample, 30 g, and single crystal with 0.85 g were used. The neutron diffraction experiment under magnetic fields was performed using TAS-2 and 5 T horizontal superconducting magnet.

Figure 1 shows the neutron inelastic scattering spectra on the polycrystalline sample of $CeAgSb_2$. At $T = 4$ K, we observed conspicuous excitation peaks at $\Delta E = 1.9$ and 5.9 meV, respectively. The q dependence of the intensity of these peaks is consistent with the square of the $4f$ magnetic form factor in the Ce^{3+} ion. This means that these inelastic peaks are due to magnetic excitations. On elevating the sample temperature to $T = 12$ K, just above $T_c = 9.6$ K, the excitation peak at 1.9 meV disappeared. This means that this peak is due to the spin wave excitation.

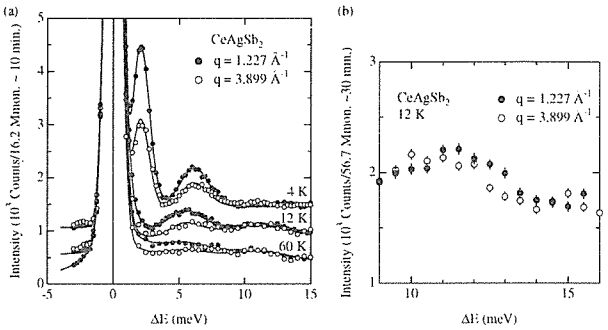

Figure 1: Inelastic neutron scattering spectra measured for a polycrystalline sample of $CeAgSb_2$.

The 5.2 meV peak, which corresponds to the 5.9 meV excitation at 4 K, survived in the paramagnetic state, although the peak became weak and broad. At a much higher temperature, $T = 60$ K, the excitation peak spread out in a wide energy range. From the q and temperature dependence, we concluded that the 5.2 meV peak is due to crystalline electric field (CEF) excitation. In addition to these clear excitation peaks, a very weak CEF excitation at $\Delta E = 12.5$ meV was also observed at 12 K, as shown in Fig. 1 (b). Recently, these two CEF excitations were also observed by Adroja *et al.* on a HET spectrometer at ISIS, independent of our work [3]. In CEF with tetragonal symmetry, the J multiplet of the Ce^{3+} ion splits into three doublets. Therefore the observation of two CEF excitation peaks is reasonably understood in terms of the excitation between the ground state and the two excited levels. We concluded that the ground state is $|\pm\frac{1}{2}\rangle$, the first and the second level are dominated by $|\pm\frac{3}{2}\rangle$ and $|\pm\frac{5}{2}\rangle$, respectively. The magnetic moment of the ground state, $g_J\mu_B J_z = 0.428\mu_B$, is in good agreement

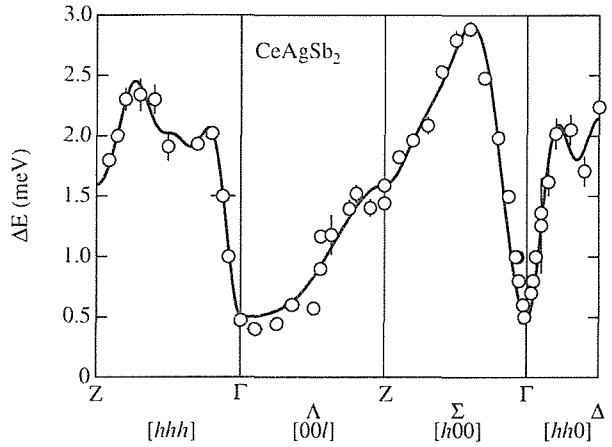

Figure 2: Spin wave dispersion in $CeAgSb_2$.

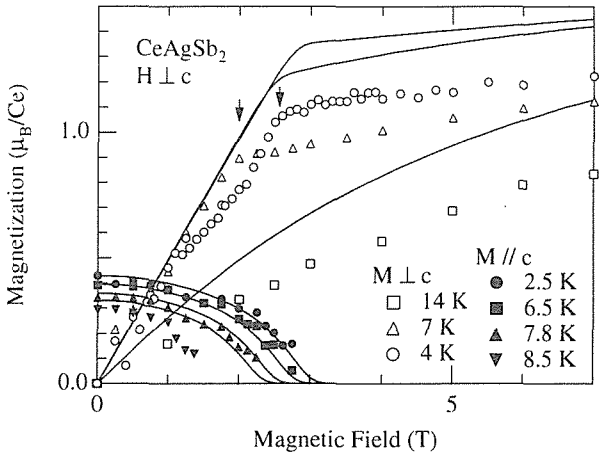

Figure 3: In-plane magnetization ($M \perp c$, open marks) and the ferromagnetic moment ($M \parallel c$, solid marks) are plotted as a function of magnetic field perpendicular to [001].

with the observed ferromagnetic moment of $0.41\mu_B$ [4]. The CEF level scheme determined by the present neutron scattering study is very similar to the result of the recent thermal expansion study by Takeuchi *et al.* [5]

The dispersion of the spin wave excitation has been measured with the use of a single-crystalline sample. Figure 2 is the dispersion relation of the spin wave excitation.The anisotropic exchange interaction between $4f$-moments in the $|\pm\frac{1}{2}\rangle$ ground state for the ferromagnet is introduced to account for the dispersion [4]. The solid line in Fig. 2 is the result of the calculated dispersion relation.The obtained interaction coefficient for the z component of J is about 10 times larger than that for the in-plane component of J, indicating the existence of ising like exchange interaction.

The CEF splitting and ising-like interaction, determined in this study, well account for the 'unusual' magnetic properties. The open marks in Fig. 3 show the in-plane magnetization measured from the neutron diffraction. The kink, denoted by arrows, appears below T_c. On the other hand, the closed marks in Fig. 3 show the ferromagnetic moment along the c-axis with the magnetic field parallel to [110] measured from the neutron diffraction intensity at the (110) peak position. With this configuration, the in-plane magnetization does not contribute to any magnetic scattering, because the induced in-plane magnetic moment is parallel to the scattering vector q. Therefore only the ferromagnetic component along [001] was observed. The ferromagnetic component along [001] exhibits a gradual decrease with increasing in-plane magnetic field, and disappears at the critical field H_c where the in-plane magnetic moment shows a kink behavior. Our data indicate that H_c is the field where the ferromagnetic moment switches its direction from parallel to perpendicular relative to [001]. This feature is well reproduced by the calculation based on the CEF and ising like exchange interaction, as shown in Fig. 3.

References

1) G. André, F. Bourée, M. Kolenda, B. Leśniewska, A. Oleś and A. Szytuła: Physica B **292** (2000) 176.
2) K.D. Myers, S.L. Bud'ko, I.R. Fisher, Z. Islam, H. Kleinke, A.H. Lacerda and P.C. Canfield: J. Magn. Magn. Mater. **205** (1999) 27.
3) D.T. Adroja, P.C. Riedi, J.G.M. Armitage and D. Fort Acta Phys. Pol. B **34** (2003) 945.
4) S. Araki, N. Metoki, A. Galatanu, E. Yamamoto, A. Thamizhavel and Y. Ōnuki: Phys. Rev. B, to be published.
5) T. Takeuchi, A. Thamizhavel, T. Okubo, M. Yamada, N. Nakamura, T. Yamamoto, Y. Inada, K. Sugiyama, A. Galatanu, E. Yamamoto, K. Kindo, T. Ebihara and Y. Ōnuki, Phys. Rev. B **67** (2003) 064403.

2.3.14

Magnetic order of UGa_3 investigated by neutron scattering under uniaxial pressure

M. NAKAMURA[1], T. D. MATSUDA[1], K. KAKURAI[1], G. H. LANDER[1,2], S. KAWARAZAKI[3] and Y. ŌNUKI[1,3]

[1]Advanced Science Research Center, JAERI, Tokai, Ibaraki 319-1195, Japan
[2]European Commission, JRC, Institute for Transuranium Elements, Postfach 2340, D-76125 Karlsruhe, Germany
[3]Graduate School of Science, Osaka University, Toyonaka, Osaka 560-0043

The uranium intermetallic compounds UX_3 demonstrate a wide variety of magnetic properties[1]. Among the UX_3 compounds, special attention was paid to UGa_3 because experiments and band structure calculations strongly suggested an itinerant nature for the magnetism of UGa_3. UGa_3 orders below $T_N = 67$ K with a type-II antiferromagnetic structure in which alternate (111) ferromagnetic planes of U moments are coupled antiferromagnetically[2,3]. The ordered moment is $\sim 0.6\ \mu_B$ per U atom. UX_3 systems crystallize in high symmetric structure, that is cubic $AuCu_3$ type. Therefore, the neutron diffraction measurement usually gives no conclusive information on the total magnetic moment orientation for UX_3 compounds because of their multidomain structures. In this study, we apply the weak uniaxial pressure to single crystalline UGa_3 so as to induce the anisotropic domain structure, which should bring a clue to the magnetic moment orientation of UGa_3. We demonstrate that the combination of uniaxial pressure and polarization analysis enables us to quantitatively estimate the domain population.

Experiments were carried out on triple axis spectrometer TAS-1 installed at the research reactor JRR-3M in JAERI. The scans were performed in (h, l, l) plane and the uniaxial pressure was applied along the $[01\bar{1}]$ axis up to 2 kbar, which is perpendicular to the scattering plane. Both polarized and unpolarized beam experiments were performed with an incident energy $E_i = 14.7$ meV. For polarized beam experiment, the incident neutron beam polarization was perpendicular to the scattering plane, that is vertical field geometry (VF). In this configuration all the magnetic components in the scattering plane (hereafter referred to as in-plane components) are detected in spin-flip (SF) channel and the magnetic components perpendicular to the scattering plane (out-of-plane components) are probed

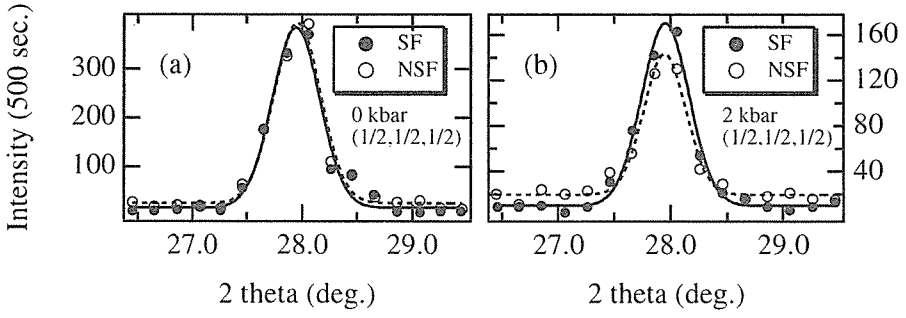

Figure 1: Polarization analysis of the (1/2, 1/2, 1/2) magnetic reflection at (a) 0 kbar and (b) 2 kbar. Measurements were performed at 8 K.

in the non-spin-flip (NSF) channel.

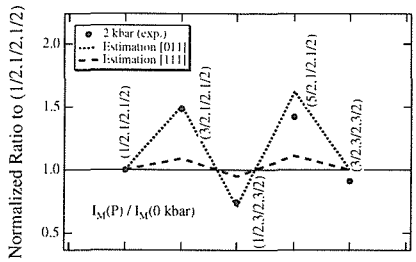

Figure 2: The ratio of intensities at 2 kbar to those at 0 kbar obtained by unpolarized measurements at 8 K. The estimated angle factors are also plotted for $\mu \parallel [011]$ (dotted line) and $\mu \parallel [111]$ (dashed line) . All of the data are normalized to the intensity at (1/2,1/2,1/2).

Uniaxial pressure dependences of the polarization analysis for (1/2,1/2,1/2) magnetic reflection are shown in Fig.1. At 0 kbar the NSF intensity is almost equal to the SF intensity. At ambient pressure the ratio of in-plane and out-of-plane component is expected to be unity due to the isotropic domain distribution. On the other hand, the difference of the integrated intensities between NSF and SF becomes obvious at 2 kbar. The intensity ratio NSF/SF is estimated to be 0.61±0.07 and indicates the deviation from the isotropic distribution.

We now show, that the determination of the in-plane and out-of-plane component by means of polarized neutrons as described above, can be used to actually determine the domain population. Previously, we reported a method of estimating the magnetic moment orientation of UGa_3 from the pressure dependent behaviors of several magnetic reflections[4]. The same method is also applied to the magnetic intensities measured by unpolarized experiments under the 2 kbar uniaxial pressure as plotted in Fig.2. The y-axis represents the normalized *angle factors* to the value of (1/2,1/2,1/2). The angle factor is related to an angle between the magnetic moment vector and scattering vector. If the multidomain structure remains under uniaxial pressure, the values for each magnetic reflection must be unity in this figure. Therefore, the non-flat behavior in Fig. 2 confirms the induction of anisotropic domain structure by uniaxial pressure. In addition, this behavior tells us that an easy axis of ordered magnetic moment in UGa_3 is by no means along the [100] axis, because the calculated results for [100] axis[4] show opposite behaviors to the results for the present experiment.

We discuss the possibility that the total magnetic moment of UGa_3 is along the [011] or [111] axis. From the ratio of NSF/SF, we can analytically determine the domain population for both cases. The normalized angle factors calculated from domain populations are also plotted in Fig.2. The results of [011] direction successfully reproduce the experimental result. The domain population under 2 kbar uniaxial pressure is quantitatively solved, [011] direction occupies 25/42($\sim$ 60%) and [01$\bar{1}$] direction 5/42 ($\sim$ 12%). The other equivalent axes along [110] ,[101] ,[10$\bar{1}$] ,[1$\bar{1}$0] occupy 3/42 ($\sim$ 7%). The finding of the [011] direction is consistent with that reported under hydrostatic pressure[4].

In summary, we have succeeded in determining the magnetic moment orientation of UGa_3 by polarized and unpolarized neutron beam experiments under uniaxial pressure. We found that the magnetic moment of UGa_3 is parallel to [011]. We consider that the determination of domain population by VF polarized beam experiments should serve us to obtain the *correct* form factor under hydrostatic pressure which includes the information on the orbital moment quenching[5], because the hydrostatic pressure contains the residual uniaxial component and may develop the anisotropic domain structure[4].

References

1) D. D. Koelling *et al.* : Phys. Rev. B **31** (1985) 4966.
2) A. Murasik *et al.* : Phys. Stat. Sol. A **23** (1974) K147.
3) P. Dervenagas *et al.* : Physica B **269** (1999) 368.
4) M. Nakamura *et al.* : J. Phys. Chem. Solids **63** (2002) 1193.
5) A. Hiess *et al.* : Europhys. Lett. **55** (2001) 267.

2.3.15

Structural study of itinerant 5f antiferromagnet $UTGa_5$ (T: Ni, Pd, Pt) by neutron diffraction

K. KANEKO[1], N. METOKI[1,2], N. BERNHOEFT[3], G. H. LANDER[1,4], Y. ISHII[1], Y. TOKIWA[1], S. IKEDA[1], Y. HAGA[1] and Y. ŌNUKI[1,5]

[1]Advanced Science Research Center, JAERI, Tokai, Ibaraki 319-1195
[2]Department of Physics, Tohoku University, Aoba, Sendai 980-8578
[3]DRFMC-CEA, 38054 Grenoble, France
[4]EC-JRC, Institute for Transuranium Elements, Postfach 2340, D-76125 Karlsruhe, Germany
[5]Graduate School of Science, Osaka University, Toyonaka, Osaka 560-0043

$UTGa_5$ with T=Ni, Pd and Pt exhibit itinerant antiferromagnetic ordering below the Néel temperature, T_N=86, 30 and 26K.[1-3] Our recent neutron scattering study revealed that the magnetic structures are different significantly between the iso-electronic compounds $UNiGa_5$ and $UPtGa_5$[4]. It has been suggested that the orbital degree of freedom may play an important role on the stability of the magnetic structure. To address this issue, we studied crystal structure and its thermal evolution together with the magneto-striction.

The neutron powder diffraction data were measured on HRPD installed at JRR-3 in JAERI. The obtained diffraction patterns were analysed by the Rietveld method using RIETAN-2000[5]. The details of sample preparation were published elsewhere[2,3].

The structural and reliable parameters obtained in this work are summarized in Table I. The crystal structure of $UTGa_5$ consists of a UGa_3 block and an intercalating transition metal sheet stacking along the c axis, as shown in Fig. 1. The value of a, c and z_{Ga} gives the information on the tetragonality of the local UGa_3 block, $t = 1 - (2cz_{Ga}/a)$, where t =1 corresponds to the cubic UGa_3 with $AuCu_3$ type structure. We find that the tetragonality t of UGa_3 block in $UTGa_5$ increases markedly with changing the transition element. At room temperature, the local UGa_3 block with t=1.55% in $UNiGa_5$ is very close to cubic UGa_3, whereas t=7.02% in $UPtGa_5$ indicates the uniaxially compressed UGa_3 block along the c-axis.

Figure 2 shows the lattice constants a and c in $UTGa_5$ as a function of temperature. It is clear that there is magneto-striction in the $UTGa_5$ compounds. At base temperature, $UNiGa_5$ exhibits a relative increase in a of about 0.1% and decrease in c about 0.04% compared with their respective values at T_N. The lattice parameter a in $UPdGa_5$ exhibits a quasi-invar like plateau below T_N, indicating that a magneto-elastic interaction essentially compensates the paramagnetic thermal contraction in the basal plane, whereas the c-axis exhibits a monotonous decrease with decreasing temperature. The lattice constants in $UPtGa_5$ increase by $\sim$ 0.013 % at base temperature relative to their value at T_N in both a- and c-directions. The lattice contraction of a in $UPtGa_5$ was opposite from the lattice expansion in $UNiGa_5$, whilst the intermediate

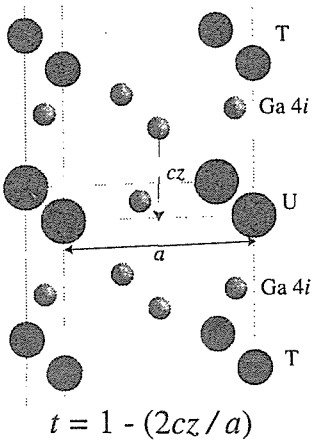

Figure 1: Crystal structure of $UTGa_5$.

Table 1: Structural parameters and conventional reliability factors obtained for $UTGa_5$ (T: Ni, Pd, Pt).

	T (K)	a (Å)	c(Å)	z_{Ga}	t (%)	R_{wp}	S	R_B
$UNiGa_5$	300	4.2380(1)	6.7864(1)	0.3074(1)	1.55	9.65	1.33	3.56
$UPdGa_5$	300	4.3218(1)	6.8637(1)	0.2987(1)	5.12	7.32	1.79	2.13
$UPtGa_5$	300	4.3386(1)	6.8054(1)	0.2964(1)	7.02	5.61	1.16	2.15

behavior was found in $UPdGa_5$.

The change in the sign of the basal plane contribution to the thermal expansion between $UNiGa_5$ and $UPtGa_5$ may reflect the different basal plane coupling: antiferromagnetic in $UNiGa_5$ whereas ferromagnetic in $UPtGa_5$.[4] This situation suggests the presence of a critical separation ε_0, where the effective U-U basal plane interaction changes its sign. On the other hand, the antiferromagnetic coupling as well as the negative thermal expansion for c-axis is common to $UNiGa_5$ and $UPtGa_5$. After subtracting the thermal contraction, a in $UPdGa_5$ also exhibit the lattice expansion due to the magnetic ordering. This fact suggests that the magnetic structure of $UPdGa_5$ may be the same as in $UPtGa_5$.

One possibility for the sign change of the nearest neighbor interaction is that a concurrent orbital ordering takes place in $UTGa_5$ and affects on the change of basal plane magnetic configuration. The present study clarifies the difference in the tetragonality of local UGa_3 block and the relevant lattice distortion corresponding to the different magnetic structure between $UNiGa_5$ and $UPtGa_5$. It is noteworthy that recent NMR [6] and resonant x-ray scattering [7] work on UGa_3 do suggest strong $5f$-$4p$ hybridisation and the possibility of some form of orbital ordering. Resonant x-ray scattering experiment on $UTGa_5$ is now in progress.

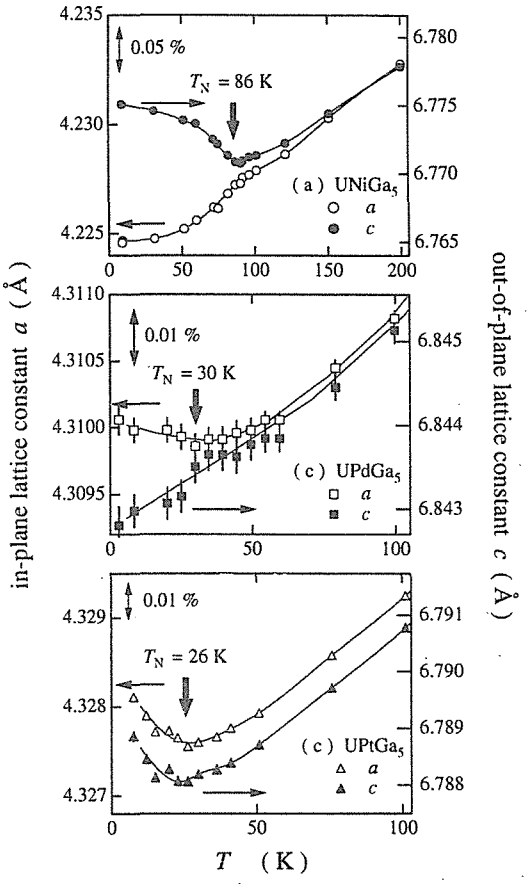

Figure 2: Temperature dependence of lattice constants, a(open circle) and c(closed circle) in $UTGa_5$.

References

1) Yu. N. Grin, P. Rogl, K. Hiebl, J. Less-Common Met. **121** (1986) 497.
2) Y. Tokiwa, Y. Haga, E. Yamamoto, D. Aoki, N. Watanabe, R. Settai, T. Inoue, K. Kindo, H. Harima, Y. Ōnuki, J. Phys. Soc. Jpn. **70** (2001) 1744.
3) Y. Tokiwa, S. Ikeda, Y. Haga, T. Okubo, T. Iizuka, K. Sugiyama, A. Nakamura, Y. Ōnuki, J. Phys. Soc. Jpn. **71** (2002) 845.
4) Y. Tokiwa, Y. Haga, N. Metoki, Y. Ishii, Y. Ōnuki, J. Phys. Soc. Jpn. **71** (2002) 725.
5) F. Izumi and T. Ikeda, Mater. Sci. Forum **321-324** (2001) 538.
6) S. Kambe, H. Kato, H. Sakai, R. E. Walstedt, D. Aoki, Y. Haga and Y. Ōnuki, Phys. Rev. B **66** (2002) 220403.
7) D. Mannix, A. Stunault, N. Bernhoeft, L. Paolasini, G. H. Lander, C. Vettier, F. de Bergevin, D. Kaczorowski and A. Czopnik, Phys. Rev. Lett. **86** (2001) 4128.

2.3.16 Magnetic form factors of $5f$ itinerant antiferromagnetic compound $UTGa_5$ (T: Ni, Pt)

K. KANEKO[1], N. METOKI[1,2], N. BERNHOEFT[3], G. H. LANDER[1,4], Y. ISHII[1], Y. TOKIWA[1], S. IKEDA[1], Y. HAGA[1] and Y. ŌNUKI[1,5]

[1]Advanced Science Research Center, JAERI, Tokai, Ibaraki 319-1195
[2]Department of Physics, Tohoku University, Aoba, Sendai 980-8578
[3]DRFMC-CEA, 38054 Grenoble, France
[4]EC-JRC, Institute for Transuranium Elements, Postfach 2340, D-76125 Karlsruhe, Germany
[5]Graduate School of Science, Osaka University, Toyonaka, Osaka 560-0043

The f electron systems attract much interest because of the unconventional superconductivity and the coexistence with the magnetic ordering around the quantum critical point. Recent studies reported a new series of heavy fermion superconductor $CeTIn_5$ (T:Rh, Co, Ir)[1-3], which is followed by the discovery of high-T_C heavy fermion superconductor $PuCoGa_5$ and $PuRhGa_5$[4,5]. On the other hand, the iso-structural compounds $UT'Ga_5$ exhibit strong itinerant character of $5f$ electrons. $UT'Ga_5$ with T'=Ni, Pd and Pt exhibit antiferromagnetic ordering at T_N=86, 31 and 26 K, respectively[6]. Our recent neutron scattering study revealed the significant difference in the magnetic structures between the iso-electronic compound $UNiGa_5$ and $UPtGa_5$; the nearest neighbor interaction is antiferromagnetic in $UNiGa_5$ whereas ferromagnetic in $UPtGa_5$[7]. The difference in the magnetic structure of these iso-electronic compounds were discussed in terms of the orbital ordering. In the present study we report on the magnetic form factor in $UNiGa_5$ and $UPtGa_5$ to shed light on the nature of the itinerant antiferromagnetism with uranium $5f$ electrons[8].

The magnetic form factors were measured on single crystals by the triple-axis spectrometers TAS-1 and TAS-2, installed at research reactor JRR-3 in JAERI. All collimation, except that in front of the monochromator, was removed and the background scattering from the sample cell and the cryostat was eliminated by a pair of beam slits. The magnetic contribution was extracted by subtracting the harmonic contaminations, measured at $T > T_N$, where T_N is the Néel temperature, and put on an absolute scale by calibration against selected nuclear peaks. The details of sample preparation were published

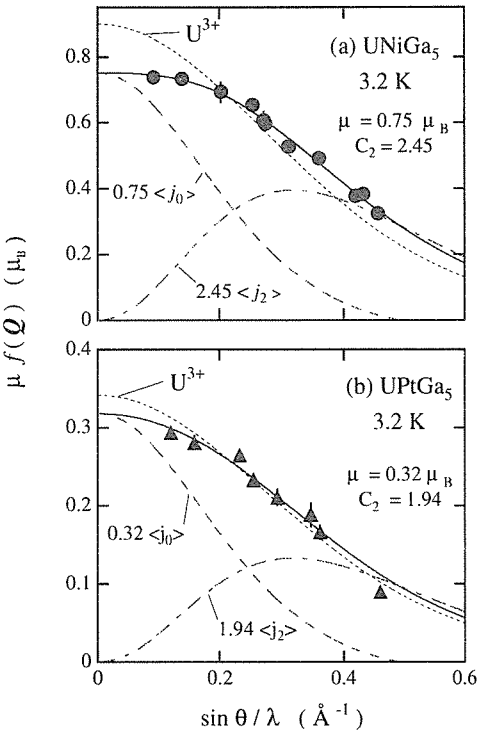

Figure 1: The experimentally obtained magnetic form factors for (a) $UNiGa_5$ and (b) $UPtGa_5$ denoted by circles and triangles, respectively. The solid lines are the best fit of the calculated form factors using Eq. (1) with μ and C_2 as fitting parameters. The dotted line indicates the magnetic form factor for U^{3+} free ion. The dashed line and dash-dot line show the calculated curves for $\langle j_0 \rangle$ and $\langle j_2 \rangle$ terms, respectively.

elsewhere[9,10].

Figure 1 shows the magnetic form factor observed in (a) $UNiGa_5$ and (b) $UPtGa_5$. Within the dipole approximation, $\mu f(\boldsymbol{Q})$ can be described by the sum of Bessel's function,

$$\begin{aligned} \mu f(Q) &= \mu(\langle j_0\rangle + C_2\langle j_2\rangle) \qquad (1)\\ \text{where } C_2 &= \mu_L/\mu \\ \mu_L/\mu_S &= C_2/(1-C_2) \end{aligned}$$

where μ is the total magnetic moment and $\boldsymbol{Q}$ is the momentum transfer. The experimental form factors, given in Fig. 1, have been decomposed using Eq. (1). The result of a least square fitting to the moment μ and C_2 coefficient is denoted by the solid curves and values of μ, μ_L, μ_S and C_2 for $UNiGa_5$ and $UPtGa_5$ are listed in Table 1.

The most remarkable thing is the large orbital contribution, which is characteristic to the uranium intermetallic compounds based on itinerant $5f$ electrons. However, we found that the contribution of the orbital moments μ_L/μ_S is strongly suppressed in $UTGa_5$ from the value for U^{3+} free ion. For comparison the values of C_2 and μ_L/μ_S for U^{3+} with f^3 configuration are also described in Table 1. The $|\mu_L/\mu_S| = 1.68$ for $UNiGa_5$ is much smaller than the value of U^{3+} free ion, $|\mu_L/\mu_S| = 2.56$. The $|\mu_L/\mu_S| = 2.10$ for $UPtGa_5$ is smaller than that of U^{3+} free ion as well. The suppression of μ_L can be recognized in the large contribution of $\langle j_2\rangle$ term denoted by dash-dot lines in Fig. 1. The dotted lines in Fig. 1 is the magnetic form factor for U^{3+} free ion, which is obviously deviates from the experimental data, especially for $UNiGa_5$.

Large orbital contribution and the suppression of the magnetic orbital moment has been reported in UGa_3[11]. The results of UGa_3 are summarized in Table 1 for comparison. Note that the C_2 as well as μ_L/μ_S in $UNiGa_5$ are very similar to those for UGa_3. Besides, $UNiGa_5$ and UGa_3 show a very flat magnetic susceptibility for T> T_N, while a weak Curie-Weiss behavior with a small effective moment μ_{eff}=1.8 μ_B was observed in $UPtGa_5$. It roughly means that the strength of the hybridization in $UNiGa_5$ might be comparable with UGa_3 but stronger than that in $UPtGa_5$. Therefore, we conclude that the quenching of the orbital moment is correlated with the itinerancy of $5f$ electrons.

Table 1: Fitting results of total magnetic moment μ, orbital and spin magnetic moment μ_L and μ_S, $|\mu_L/\mu_S|$ and C_2 for U^{3+}, $UPtGa_5$, $UNiGa_5$, and UGa_3[11].

	μ (μ_B)	μ_L (μ_B)	μ_S (μ_B)	$\lvert\mu_L/\mu_S\rvert$	C_2
U^{3+}				2.56	1.64
$UPtGa_5$	0.32(5)	0.62(7)	-0.30(7)	2.10(20)	1.94(17)
$UNiGa_5$	0.75(5)	1.84(7)	-1.09(7)	1.68(4)	2.45(7)
UGa_3[11]	0.63(5)	1.5(1)	-0.9(1)	1.66(5)	2.52(5)

References

1) R. Movshovich, M. Jaime, J. D. Thompson, C. Petrovic, Z. Fisk, P. G. Pagliuso, and J. L. Sarrao, Phys. Rev. Lett. **86** (2001) 5152.
2) H. Hegger, C. Petrovic, E. G. Moshopoulou, M. F. Hundley, J. L. Sarrao, Z. Fisk and J. D. Thompson, Phys. Rev. Lett. **84** (2000) 4986.
3) C. Petrovic, R. Movshovich, M. Jaime, P. G. Pagliuso, M. F. Hundley, J. L. Sarrao, Z. Fisk and J. D. Thompson, Europhys. Lett. **53** (2001) 354.
4) J. L. Sarrao, L. A. Morales, J. D. Thompson, B. L. Scott, G. R. Stewart, F. Wastin, J. Rebizant, P. Boulet, E. Colineau and G. H. Lander, Nature **420** (2002) 297.
5) F. Wastin, P. Boulet, J. Rebizant, E. Colineau and G. H. Lander, J. Phys.: Condens. Matter **15** (2003) S2279 .
6) Yu. N. Grin, P. Rogl, K. Hiebl, J. Less-Common Met. **121** (1986) 497.
7) Y. Tokiwa, Y. Haga, N. Metoki, Y. Ishii, Y. Ōnuki, J. Phys. Soc. Jpn. **71** (2002) 725.
8) K. Kaneko, N. Metoki, N. Bernhoeft, G. H. Lander, Y. Ishii, Y. Tokiwa, S. Ikeda, Y. Haga anad Y. Ōnuki, submitted to Phys. Rev. B.
9) Y. Tokiwa, Y. Haga, E. Yamamoto, D. Aoki, N. Watanabe, R. Settai, T. Inoue, K. Kindo, H. Harima, Y. Ōnuki, J. Phys. Soc. Jpn. **70** (2001) 1744.
10) Y. Tokiwa, S. Ikeda, Y. Haga, T. Okubo, T. Iizuka, K. Sugiyama, A. Nakamura, Y. Ōnuki, J. Phys. Soc. Jpn. **71** (2002) 845.
11) A. Hiess, F. Boudarot, S. Coad, P. J. Brown, P. Burlet, G. H. Lander, M. S. S. Brooks, D. Kaczorowski, A. Czopnik, R. Troc, Europhys. Lett. **55** (2001) 267.

2.4 Magnetism and Low Temperature Physics

2.4.1

Spin Structure of the Impurity-induced Antiferromagnetic Ordered Phase in the Doped Spin Gap System $Tl(Cu_{1-x}Mg_x)Cl_3$

A. OOSAWA, M. FUJISAWA[1], K. KAKURAI and H. TANAKA[2]

Advanced Science Research Center, JAERI, Tokai, Ibaraki 319-1195
[1]Dep. of Phys., Tokyo Inst. of Tech., Oh-okayama, Meguro-ku, Tokyo 152-8551
[2]Res.Cent.for Low Temp.Phys.,Tokyo Inst. of Tech.,Oh-okayama,Meguro-ku,Tokyo 152-8551

The spin gap in quantum spin systems is the macroscopic quantum phenomenon and has been attracting considerable attention theoretically and experimentally [1]. When nonmagnetic ions are substituted for magnetic ions in a spin gap system, the singlet ground state is disturbed so that staggered moments are induced around the impurities. If the induced moments interact through effective exchange interactions, which are mediated by intermediate singlet spins, three-dimensional (3D) long-range order can arise. Such impurity-induced antiferromagnetic ordering was first observed in the well-known inorganic spin-Peierls system $CuGeO_3$ [2]. More recently, we performed the magnetization measurements in the Mg-doped spin gap system $Tl(Cu_{1-x}Mg_x)Cl_3$, and observed the novel ordering [3]. In order to investigate the spin structure of the impurity-induced antiferromagnetic ordered phase in the doped spin gap system $Tl(Cu_{1-x}Mg_x)Cl_3$, we carried out the neutron elastic scattering measurements in $Tl(Cu_{0.97}Mg_{0.03})Cl_3$.

The parent compound $TlCuCl_3$ has the monoclinic structure (space group $P2_1/c$). The crystal structure is composed of planar dimers of Cu_2Cl_6, in which Cu^{2+} ions have spin-$\frac{1}{2}$. The dimers are stacked on top of one another to form infinite double chains parallel to the a-axis. These double chains are located at the corners and center of the unit cell in the $b-c$ plane, and are separated by Tl^+ ions. The magnetic ground state of $TlCuCl_3$ is the spin singlet with the excitation gap $\Delta = 7.7$ K [4]. From the results of analyses of the dispersion relations obtained by neutron inelastic scattering, it was found that $TlCuCl_3$ can be characterized as the 3D strongly coupled antiferromagnetic dimer system [5].

The preparation of the single crystal of $Tl(Cu_{1-x}Mg_x)Cl_3$ has been reported in ref. 3. Neutron elastic scattering measurements were performed using the JAERI-TAS1. The constant-k_i mode was taken with a fixed incident neutron energy E_i of 14.7 meV and collimations were set as open-40'-80'-80'. A PG filter was placed to suppress the higher order contaminations. We used a sample with a volume of approximately 1 cm^3. The sample was mounted in an ILL-type orange cryostat with its a^*- and c^*-axes in the scattering plane.

The inset of Fig. 1 shows the $\theta-2\theta$ scans for $Q = (1, 0, -3)$ reflection measured at $T = 1.4$ and 4.2 K in $Tl(Cu_{0.97}Mg_{0.03})Cl_3$. The resolution limited additional intensity at $T = 1.4$ K can be clearly seen. Figure 1 shows the temperature dependence of the peak intensity at $Q = (1, 0, -3)$. The rapid increase of the intensity below $T_N = 3.45$ K is observed. This transition temperature is in agreement with the phase diagram of this doped sample obtained from the magnetization measurements [3]. We thus infer that the additional intensity at low T is of magnetic origin. In order to determine the spin structure of the impurity-induced antiferromagnetic ordered phase in $Tl(Cu_{0.97}Mg_{0.03})Cl_3$, we measured the integrated intensities of nine magnetic Bragg reflections at $Q = (h, 0, l)$ with integer h and odd l. The results are summalized in Table 1. The intensities of nuclear Bragg reflections were also measured at $Q = (h, 0, l)$ with even l in order to estimate the magnitude of the effective magnetic moment averaged per site. To refine the magnetic structure, we

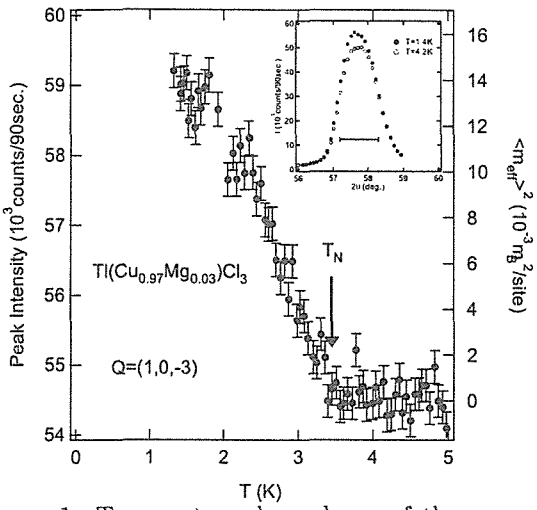

Figure 1: Temperature dependence of the magnetic Bragg peak intensity for $Q = (1, 0, -3)$ reflection in $Tl(Cu_{0.97}Mg_{0.03})Cl_3$. The square of the effective magnetic moment averaged per site $\langle m_{\rm eff}\rangle^2$ is shown on the right abscissa. The inset shows the $\theta - 2\theta$ scans for $Q = (1, 0, -3)$ reflection measured at $T = 1.4$ and 4.2 K in $Tl(Cu_{0.97}Mg_{0.03})Cl_3$. The horizontal bar indicates the calculated instrumental resolution widths.

(h, k, l)	$I_{\rm obs}$	$I_{\rm cal}$
$(0, 0, 1)_{\rm M}$	1 ± 0.021	1
$(0, 0, 3)_{\rm M}$	0.006 ± 0.001	0.014
$(0, 0, 5)_{\rm M}$	0.058 ± 0.010	0.106
$(1, 0, 1)_{\rm M}$	0.039 ± 0.011	0.002
$(1, 0, -1)_{\rm M}$	0.059 ± 0.002	0.100
$(1, 0, 3)_{\rm M}$	0.024 ± 0.007	0.033
$(1, 0, -3)_{\rm M}$	0.352 ± 0.006	0.332
$(2, 0, 1)_{\rm M}$	0.017 ± 0.005	0.007
$(2, 0, -1)_{\rm M}$	0.065 ± 0.013	0.075
R	0.11	

Table 1: Integrated Intensities of the magnetic Bragg reflections at $T = 1.4$ K in $Tl(Cu_{0.97}Mg_{0.03})Cl_3$. The intensities are normalized to the $(0, 0, 1)_{\rm M}$ reflection. R is the reliability factor given by $R = \sum_{h,k,l} |I_{\rm cal} - I_{\rm obs}| / \sum_{h,k,l} I_{\rm obs}$.

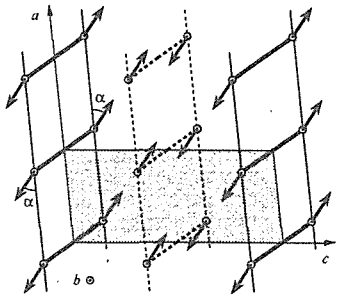

Figure 2: The spin structure observed in the impurity-induced ordered phase of $Tl(Cu_{0.97}Mg_{0.03})Cl_3$. The double chains located at the corner and the center of the chemical unit cell in the $b-c$ plane are represented by solid and dashed lines, respectively. The shaded area is the chemical unit cell in the $a-c$ plane. The angle α between the spins and the a-axis in the ordered phase is expressed in the text.

used the atomic coordinates of $TlCuCl_3$ [6] and the nuclear scattering lengths $b_{\rm Tl} = 0.878$, $b_{\rm Cu} = 0.772$ and $b_{\rm Cl} = 0.958$ in the unit of 10^{-12} cm. The magnetic form factors of Cu^{2+} were taken from ref. 7. The extinction effect was evaluated by comparing observed and calculated intensities for various nuclear Bragg reflections.

As a result, the spin structure, as shown in Fig. 2, with $\alpha = 34.4° \pm 4.4°$ were obtained. Although scans in the reciprocal plane including the b^*-axis were not performed, the spin structure shown in Fig. 2 is uniquely determined within the present measurements. The obtained angle α is consistent with the magnetization measurements of $Tl(Cu_{1-x}Mg_x)Cl_3$ [3], and is the same as that in the spin structure of the field-induced ordered phase of $TlCuCl_3$ in error bars [6]. Hence we conclude that the spin structure of the impurity-induced antiferromagnetic ordered phase on average in $Tl(Cu_{0.97}Mg_{0.03})Cl_3$ is the same as that of the field-induced magnetic ordered phase for $H \parallel b$ in the parent compound $TlCuCl_3$ ("on average" means that the magnitude of the ordered moments in the impurity-induced antiferromagnetic ordered phase may be not uniform.). The magnitude of the effective magnetic moment averaged per site at $T = 1.4$ K was evaluated as $\langle m_{\rm eff}\rangle = g\mu_{\rm B}\langle S_{\rm eff}\rangle = 0.12(1)$ $\mu_{\rm B}$. This value is much smaller than 1 $\mu_{\rm B}$, which is the full moment of Cu^{2+}.

References

1) E. Dagotto *et al.*: Science **271** (1996) 618.
2) T. Masuda *et al.*: Phys. Rev. Lett. **80** (1998) 4566.
3) A. Oosawa *et al.*: Phys. Rev. B **66** (2002) 020405(R).
4) A. Oosawa *et al.*: J. Phys. : Condens. Matter **11** (1999) 265.
5) A. Oosawa *et al.*: Phys. Rev. B **65** (2002) 094426.
6) H. Tanaka *et al.*: J. Phys. Soc. Jpn. **70** (2001) 939.
7) P. J. Brown: *International Tables for Crystallography*, vol. C, ed. A. J. C. Wilson (Kluwer, Dordrecht, 1992) p. 391.

2.4.2

Magnetic Excitations in the Impurity-induced Antiferromagnetic Ordered Phase of the Doped Spin Gap System $Tl(Cu_{1-x}Mg_x)Cl_3$

A. OOSAWA, M. FUJISAWA[1], K. KAKURAI and H. TANAKA[2]

Advanced Science Research Center, JAERI, Tokai, Ibaraki 319-1195
[1]Dep. of Phys., Tokyo Inst. of Tech., Oh-okayama, Meguro-ku, Tokyo 152-8551
[2]Res.Cent.for Low Temp.Phys.,Tokyo Inst. of Tech.,Oh-okayama,Meguro-ku,Tokyo 152-8551

The magnetic excitations in the spin gap systems are new subject in magnetism, and the information on the magnetic excitation is necessary to elucidate the microscopic mechanism leading to the novel impurity-induced antiferromagnetic ordering in the spin gap systems. In order to investigate the magnetic excitations in the impurity-induced antiferromagnetic ordered phase of the doped spin gap system $Tl(Cu_{1-x}Mg_x)Cl_3$, we performed neutron inelastic scattering measurements in $Tl(Cu_{0.97}Mg_{0.03})Cl_3$.

The parent compound $TlCuCl_3$ has the monoclinic structure (space group $P2_1/c$). The crystal structure is composed of planar dimers of Cu_2Cl_6, in which Cu^{2+} ions have spin-$\frac{1}{2}$. The dimers are stacked on top of one another to form infinite double chains parallel to the a-axis. These double chains are located at the corners and center of the unit cell in the $b-c$ plane, and are separated by Tl^+ ions. The magnetic ground state of $TlCuCl_3$ is the spin singlet with the excitation gap $\Delta = 7.7$ K [1]. From the results of analyses of the dispersion relations obtained by neutron inelastic scattering, it was found that the origin of the spin gap in $TlCuCl_3$ is the strong antiferromagnetic interaction in the chemical dimer Cu_2Cl_6, and that the neighboring dimers couple via the strong three-dimensional interdimer interactions along the double chain and in the $(1, 0, -2)$ plane, in which the hole orbitals of Cu^{2+} spread [2]. Using the cluster series expansion, the intradimer and the important individual interdimer exchange interactions were obtained [2]. The notation of the exchange interactions is given in Fig. 1. The main intradimer interaction is denoted as J, and then the exchange interaction per bond between spins in dimers separated by a lattice vector $l\boldsymbol{a}+m\boldsymbol{b}+n\boldsymbol{c}$ is denoted as the exchange energy J_{lmn} for pairs of spins at equivalent positions in their respective dimer and as J'_{lmn} for spins at inequivalent positions.

The preparation of the single crystal of $Tl(Cu_{1-x}Mg_x)Cl_3$ has been reported in ref. 3. Neutron inelastic scattering measurements were performed using the JAERI-TAS1. The constant-$\boldsymbol{k}_f$ mode was taken with a fixed final neutron energy E_f of 14.7 meV and collimations were set as open-80'-80'-80'. A PG filter was placed to suppress the higher order contaminations. We used a sample with a volume of approximately 1 cm^3. The sample was mounted in an ILL-type orange cryostat with its a^*- and c^*-axes in the scattering plane.

Constant-$\boldsymbol{Q}$ energy scan profiles were measured along $(h, 0, 1)$, $(0, 0, l)$, $(h, 0, 2h + 1)$ and $(h, 0, -2h + 1.4)$ with $0 \leq h \leq 0.5$ and $1 \leq l \leq 2$ at $T = 1.5$ K, which is lower than $T_N = 3.45$ K in $Tl(Cu_{0.97}Mg_{0.03})Cl_3$. Figure 2 (a) shows the representative scan profiles for $\boldsymbol{Q} = (h, 0, 2h+1)$, in which the magnetic excitation is most dispersive. A well-defined single excitation can be observed in almost all scans. The scan profiles were fitted with a Gaussian function to evaluate the excitation energy, as shown by the solid lines in Fig. 2 (a). The obtained scan profiles in $Tl(Cu_{0.97}Mg_{0.03})Cl_3$ were almost the same as those obtained in the parent compound $TlCuCl_3$ [2], and we confirmed that the origin of the observed excitation is magnetic from the temperature dependence. Hence we can expect that the observed excitation is the triplet magnetic excitation in the impurity-induced ordered state. The

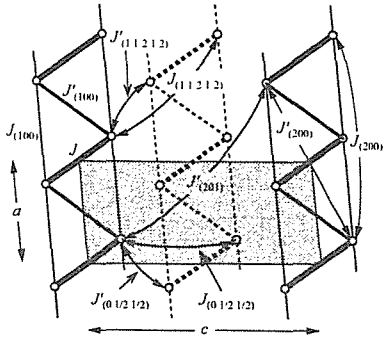

Figure 1: The exchange interactions of $Tl(Cu_{0.97}Mg_{0.03})Cl_3$. The double chains located at the corner and the center of chemical unit cell in the b-c plane are represented by solid and dashed lines, respectively. The shaded area is chemical unit cell in the a-c plane.

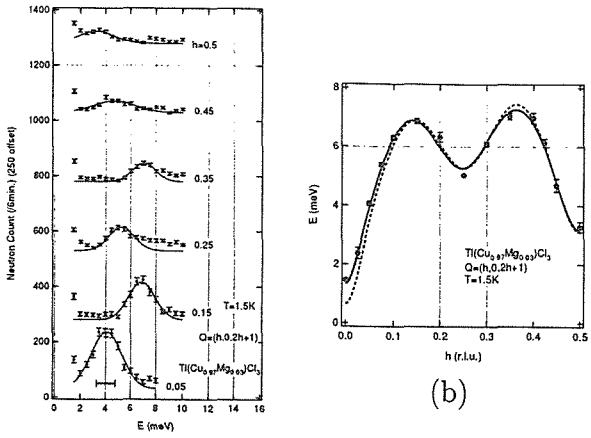

Figure 2: (a) Profiles of the constant-Q energy scans and (b) dispersion relation in $Tl(Cu_{0.97}Mg_{0.03})Cl_3$ for Q along $(h, 0, 2h+1)$ with $0 \leq h \leq 0.5$ at $T = 1.5$ K. The solid lines in (a) are fits using a Gaussian function. The horizontal bar in (a) indicates the calculated instrumental resolution width. Solid line in (b) is the dispersion curve calculated by RPA approximation using eq. (1). Dashed line in (b) is the dispersion curve of the triplet excitation in $TlCuCl_3$ [2].

dispersion relation $\omega(Q)$ of the excitation for $Q = (h, 0, 2h+1)$ at $T = 1.5$ K is shown in Fig. 2 (b). The dispersion curve of the triplet excitation in $TlCuCl_3$ [2] is also depicted in Fig. 2 (b) by the dashed line. As shown in Fig. 2 (b), there is not much difference between the dispersion relations of $Tl(Cu_{0.97}Mg_{0.03})Cl_3$ and those of $TlCuCl_3$, except in the vicinity of the lowest excitation at $Q = (0, 0, 1)$ corresponding to the spin gap.

We fit the obtained dispersion relations by the following equation obtained from the RPA approximation, which is applied to $TlCuCl_3$ [2]

$$\omega_{\pm}(Q) = \sqrt{J^2 + 2J\delta\omega_{\pm}(Q)}\ , \qquad (1)$$

where

$$\begin{aligned}\delta\omega_{\pm}(Q) &= [J^{\rm eff}_{(100)}\cos(2\pi h) + J^{\rm eff}_{(200)}\cos(4\pi h) \\ &+ J^{\rm eff}_{(201)}\cos\{2\pi(2h+l)\}] \pm 2[J^{\rm eff}_{(1\frac{1}{2}\frac{1}{2})}\cos\{\pi \\ &(2h+l)\}\cos(\pi k) + J^{\rm eff}_{(0\frac{1}{2}\frac{1}{2})}\cos(\pi k)\cos(\pi l)]. \qquad (2)\end{aligned}$$

In the equations, J denotes the main intradimer exchange interaction, and $J^{\rm eff}_{(lmn)}$ denote the effective interactions between dimers separated by a lattice vector $la + mb + nc$ and are expressed as

$$\begin{aligned}&J^{\rm eff}_{(100)} = \frac{1}{2}(2J_{(100)} - J'_{(100)})\ , \quad J^{\rm eff}_{(200)} = \frac{1}{2}(2J_{(200)} - J'_{(200)}) \\ &J^{\rm eff}_{(1\frac{1}{2}\frac{1}{2})} = \frac{1}{2}(J_{(1\frac{1}{2}\frac{1}{2})} - J'_{(1\frac{1}{2}\frac{1}{2})})\ , \quad J^{\rm eff}_{(0\frac{1}{2}\frac{1}{2})} = \frac{1}{2}(J_{(0\frac{1}{2}\frac{1}{2})} - J'_{(0\frac{1}{2}\frac{1}{2})})\ , \\ &J^{\rm eff}_{(201)} = -\frac{1}{2}J'_{(201)}\ , \qquad (3)\end{aligned}$$

where J_{lmn} and J'_{lmn} are shown in Fig. 1. Under the present experimental condition, *i.e.*, Q in the a^*-c^* plane, the $\omega_+(Q)$ branch gives the only nonvanishing contribution. The solid line in Fig. 2 (b) indicates the calculated results with the exchange parameters, as shown in Table 1. The experimental dispersion curves can be reproduced well by the fitting. Compared to the parent compound $TlCuCl_3$, the magnitude of the intradimer interaction J becomes slightly larger, while that of the important effective interdimer interactions $J^{\rm eff}_{(100)}$, $J^{\rm eff}_{(1\frac{1}{2}\frac{1}{2})}$ and $J^{\rm eff}_{(201)}$ become slightly smaller.

	$TlCuCl_3$ [2]	$Tl(Cu_{0.97}Mg_{0.03})Cl_3$
J	5.68	5.74
$J^{\rm eff}_{(100)}$	−0.46	−0.41
$J^{\rm eff}_{(200)}$	0.05	−0.03
$J^{\rm eff}_{(1\frac{1}{2}\frac{1}{2})}$	0.49	0.46
$J^{\rm eff}_{(0\frac{1}{2}\frac{1}{2})}$	−0.06	−0.03
$J^{\rm eff}_{(201)}$	−1.53	−1.41

Table 1: The intradimer interaction J and the effective interdimer interactions $J^{\rm eff}_{(lmn)}$ in $TlCuCl_3$ [2] and $Tl(Cu_{0.97}Mg_{0.03})Cl_3$. All energies are in units of meV.

No antiferromagnetic spin-wave excitation could be observed. This may be due to the large incoherent scattering by chlorines near the zone center $Q = (0, 0, 1)$ and the rapid broadening of spectra far from $Q = (0, 0, 1)$.

References

1) A. Oosawa *et al.*:J. Phys.:Cond. Mat. **11**(1999)265.
2) A. Oosawa *et al.*: Phys. Rev. B **65** (2002) 094426.
3) A. Oosawa *et al.*: Phys. Rev. B **66** (2002) 020405(R).

2.4.3

Coexistence of the Spin Gap and the Magnetic Ordering in the Impurity-induced Antiferromagnetic Ordered Phase of the Doped Spin Gap System $Tl(Cu_{1-x}Mg_x)Cl_3$

A. OOSAWA, M. FUJISAWA[1], K. KAKURAI and H. TANAKA[2]

Advanced Science Research Center, JAERI, Tokai, Ibaraki 319-1195
[1]Dep. of Phys., Tokyo Inst. of Tech., Oh-okayama, Meguro-ku, Tokyo 152-8551
[2]Res.Cent.for Low Temp.Phys.,Tokyo Inst. of Tech.,Oh-okayama,Meguro-ku,Tokyo 152-8551

The impurity-induced antiferromagnetic ordering in spin gap systems is the novel quantum phenomenon and attracted much interest and thus led to a large number of vivid experimental and theoretical investigations. Especially, the coexistence of the spin gap and the magnetic ordering in the impurity-induced antiferromagnetic ordered phase has been observed by neutron scattering experiments in $(Cu_{1-x}Zn_x)GeO_3$ and $Cu(Ge_{1-x}Si_x)O_3$ with low x [1, 2], and the coexistence of the mutually exclusive phenomena at first glance is still argued vigorously by many theorists and experimenters. In order to investigate whether the coexistence occurs in the impurity-induced antiferromagnetic ordered phase of the doped spin gap system $Tl(Cu_{1-x}Mg_x)Cl_3$, we performed neutron scattering measurements in $Tl(Cu_{0.97}Mg_{0.03})Cl_3$.

The parent compound $TlCuCl_3$ has the monoclinic structure (space group $P2_1/c$). The crystal structure is composed of planar dimers of Cu_2Cl_6, in which Cu^{2+} ions have spin-$\frac{1}{2}$. The dimers are stacked on top of one another to form infinite double chains parallel to the crystallographic a-axis. These double chains are located at the corners and center of the unit cell in the $b-c$ plane, and are separated by Tl^+ ions. The magnetic ground state of $TlCuCl_3$ is the spin singlet with the excitation gap $\Delta = 7.7$ K [3]. From the results of analyses of the dispersion relations obtained by neutron inelastic scattering, it was found that the origin of the spin gap in $TlCuCl_3$ is the strong antiferromagnetic interaction in the chemical dimer Cu_2Cl_6, and that the neighboring dimers couple via the strong three-dimensional interdimer interactions along the double chain and in the $(1, 0, -2)$ plane, in which the hole orbitals of Cu^{2+} spread [4, 5, 6].

The preparation of the single crystal of $Tl(Cu_{1-x}Mg_x)Cl_3$ has been reported in ref. 7. Neutron inelastic scattering measurements were performed using the JAERI-LTAS. The constant-k_f mode was taken with a fixed final neutron energy E_f of 5.0 meV and collimations were set as 24'-80'-80'-80'. We used a sample with a volume of approximately 1 cm^3. The sample was mounted in an ILL-type orange cryostat with its a^*- and c^*-axes in the scattering plane.

Figure 1 shows the constant-Q energy scan profiles in $Tl(Cu_{0.97}Mg_{0.03})Cl_3$ for $Q = (0, 0, 1)$, where the lowest triplet excitation corresponding to the spin gap occurs in the parent compound $TlCuCl_3$, at various temperatures. A well-defined single excitation can be seen at all temperatures. Hence it is confirmed that the spin gap remains even in the impurity-induced ordered phase. Because the excitation was also observed at $T = 5.2$ K, which is higher than $T_N = 3.45$ K, the excitation is not spin-wave excitation by the antiferromagnetic ordering, but the triplet excitation from the ground state. The horizontal bar in Fig. 1 denotes the calculated instrumental resolution width. The broadening of the spectra can be seen. The solid lines in Fig. 1 are fits to the dispersion relations convoluted with the instrumental resolution. A Lorentzian function for the magnetic excitation is used. The free parameters are I, Γ and $E_{(0,0,1)}$, which are the integrated intensity, the Lorentzian width and the spin gap, respec-

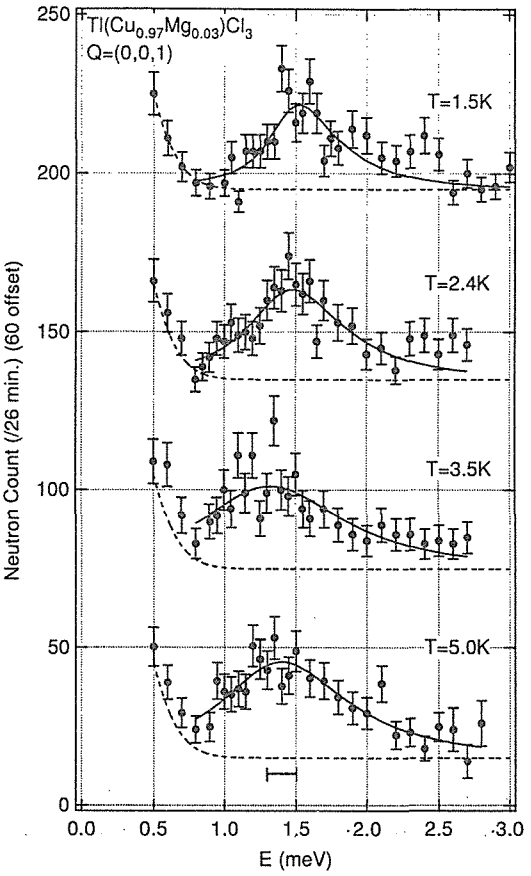

Figure 1: Constant-Q energy scan profiles in $Tl(Cu_{0.97}Mg_{0.03})Cl_3$ at $Q = (0, 0, 1)$ for various temperatures. The solid lines are fits to the dispersion relations convoluted with the instrumental resolution. The horizontal error bar indicates the calculated instrumental resolution widths. Dashed lines denote the background with the Bragg reflection at $Q = (0, 0, 1)$.

tively. The shape of the dispersion relation in the vicinity of Q=(0, 0, 1) was fixed to that obtained from the RPA approximation. The temperature dependence of the energy of the triplet excitation at $Q = (0, 0, 1)$ is shown in Fig. 2. The rapid increase of the excitation energy can be clearly seen below $T_N = 3.45$ K. The triplet excitation depends on temperature due to the temperature dependence of the occupation difference between the singlet and triplet states [8]. However, the increase of temperature causes to flatten the dispersion relation due to the suppression of the interdimer correlations by the decrease of the occupation difference, namely the energy of the lowest excitation corresponding to the spin gap should rather decrease upon decreasing temperature. Hence, we can expect that the rapid increase of the spin gap is caused by the impurity-induced antiferromagnetic ordering and can conclude that the impurity-induced antiferromagnetic ordering coexists with the spin gap in $Tl(Cu_{0.97}Mg_{0.03})Cl_3$. The energy of the lowest excitation is $E = 1.3$ meV at $T = 5.2$ K, which is higher than T_N, and is a little larger than that of $0.65 \sim 0.8$ meV estimated for the pure $TlCuCl_3$ [4, 5, 6]. This indicates that the spin gap is also enhanced by the Mg doping, irrespective of the ordering. The temperature dependence of Γ is also shown in inset of Fig. 2. No significant variation of Γ can be seen.

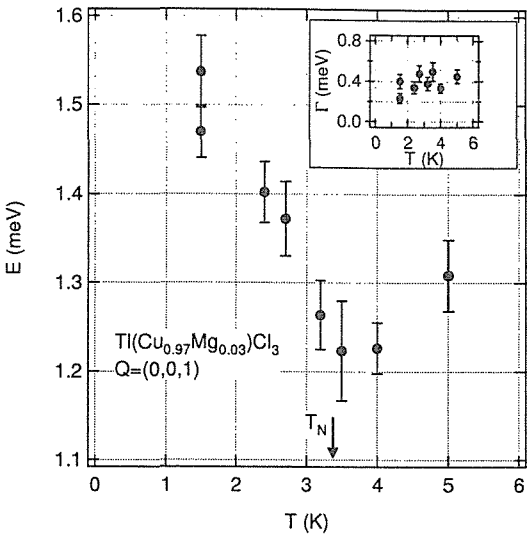

Figure 2: Temperature dependence of the energy of the magnetic excitation at $Q = (0, 0, 1)$. The inset shows the temperature dependence of the Lorentzian width Γ.

References

1) M. C. Martin *et al.*: Phys. Rev. B **56** (1997) 3173.
2) L. P. Regnault *et al.*: Europhys. Lett. **32** (1995) 579.
3) A. Oosawa *et al.*: J. Phys.: Condens. Matter **11** (1999) 265.
4) A. Oosawa *et al.*: Phys. Rev. B **65** (2002) 094426.
5) A. Oosawa *et al.*: J. Phys. Soc. Jpn. Suppl. A **70** (2001) 166.
6) N. Cavadini *et al.*: Phys. Rev. B **63** (2001) 172414.
7) A. Oosawa *et al.*: Phys. Rev. B **66** (2002) 020405(R).
8) N. Cavadini *et al.*: Eur. Phys. J. B **18** (2000) 565.

2.4.4

Spin Structure of the Pressure-induced Magnetic Ordered Phase in the Spin Gap System $TlCuCl_3$

A. OOSAWA, M. FUJISAWA[1], T. OSAKABE, K. KAKURAI and H. TANAKA[2]

Advanced Science Research Center, JAERI, Tokai, Ibaraki 319-1195
[1]Dep. of Phys., Tokyo Inst. of Tech., Oh-okayama, Meguro-ku, Tokyo 152-8551
[2]Res.Cent.for Low Temp.Phys.,Tokyo Inst. of Tech.,Oh-okayama,Meguro-ku,Tokyo 152-8551

Recently, the novel magnetic orderings induced by the magnetic field, the impurity ions and the pressure in spin gap systems have been energetically investigated. Quite recently, magnetization measurements were performed under hydrostatic pressures in the spin gap system $TlCuCl_3$, and the antiferromagnetic ordering was observed at zero field [1]. In order to investigate the spin structure of the pressure-induced magnetic ordered phase and the mechanism leading to the ordering, we performed neutron elastic scattering experiments under a high hydrostatic pressure.

The magnetic ground state of $TlCuCl_3$ is the spin singlet with the excitation gap $\Delta = 7.7$ K [2] and this system can be characterized as the three-dimensional strongly coupled antiferromagnetic dimer system [3].

The preparation of the single crystal of $TlCuCl_3$ has been reported in ref. 2. The sample with 0.2 cm^3 was set in the McWhan-type high-pressure cell (HPCNS-MCW®, Oval Co., Ltd.) [4]. As the pressure transmitting medium, a mixture of Fluorinert FC70 and FC77 was used. The applied hydrostatic pressure of $P = 1.48$ GPa at low temperature was determined from the pressure dependence of the lattice constants of a NaCl crystal in the sample space. Neutron elastic scattering measurements were performed using the JAERI-TAS1. The constant-k_i mode was taken with a fixed incident neutron energy E_i of 14.7 meV. Because the size of the sample has to be small due to the small sample space, collimations were set as open-80'-80'-80' in order to gain intensity. Sapphire and PG filters were placed to suppress the background by high energy neutrons, and higher order contaminations, respectively. The sample was mounted in the cryostat with its a^*- and c^*-axes in the scattering plane. The crystallographic parameters were determined as $a^* = 1.6402$ Å^{-1}, $c^* = 0.72843$ Å^{-1} and $\cos\beta^* = 0.0861$ at helium temperatures and $P = 1.48$ GPa. The lattice constants a and c become shorter by 1.5% and the angle β becomes closer to 90° than those at ambient pressure [3].

The inset of Fig. 1 shows the $\theta - 2\theta$ scans for the $Q = (1, 0, -3)$ reflection measured at $T = 4.0$, 12.2 and 28.2 K for $P = 1.48$ GPa in $TlCuCl_3$. With decreasing temperature, the increase in the intensity of the reflection with a resolution limited width can be clearly seen. Figure 1 shows the temperature dependence of the Bragg peak intensity at the $Q = (1, 0, -3)$ reflection for $P = 1.48$ GPa in $TlCuCl_3$. The rapid increase in the intensity with no pronounced diffuse scattering is observed below $T_N = 16.9$ K. Because it has already been observed that the pressure-induced magnetic ordering occurs at $T_N \approx 11$ K for $P \approx 0.8$ GPa in $TlCuCl_3$ [1], we can conclude that the $Q = (1, 0, -3)$ reflection is the magnetic Bragg reflection indicative of the pressure-induced magnetic ordering. The magnetic Bragg reflections were observed at $Q = (h, 0, l)$ with integer h and odd l. These reciprocal points are equivalent to those with the lowest magnetic excitation energy at ambient pressure [3]. This indicates that the spin gap corresponding to the lowest magnetic excitation energy closes under an applied pressure.

In order to determine the spin structure of the pressure-induced magnetic ordered phase in $TlCuCl_3$, we measured the integrated in-

Table 1: Observed and calculated magnetic Bragg peak intensities at $T = 12.2$ and 4.0 K for $P = 1.48$ GPa in $TlCuCl_3$. The intensities are normalized to the $(0, 0, 1)_M$ reflection. R is the reliability factor given by $R = \sum_{h,k,l} |I_{cal} - I_{obs}| / \sum_{h,k,l} I_{obs}$.

	$T = 12.2$ K		$T = 4.0$ K	
(h, k, l)	I_{obs}	I_{cal}	I_{obs}	I_{cal}
$(0, 0, 1)_M$	1 ± 0.051	1	1 ± 0.051	1
$(0, 0, 3)_M$	0.018 ± 0.004	0.014	0.007 ± 0.003	0.014
$(0, 0, 5)_M$	0.085 ± 0.007	0.103	0.075 ± 0.006	0.103
$(1, 0, 1)_M$	0.014 ± 0.006	0.021	0.104 ± 0.009	0.113
$(1, 0, -1)_M$	0.127 ± 0.014	0.153	0.135 ± 0.016	0.165
$(1, 0, 3)_M$	0.037 ± 0.009	0.014	0.083 ± 0.004	0.085
$(1, 0, -3)_M$	0.448 ± 0.009	0.413	0.371 ± 0.007	0.375
$(2, 0, 1)_M$	0.006 ± 0.003	0.021	0.057 ± 0.005	0.051
$(2, 0, -1)_M$	0.114 ± 0.007	0.127	0.191 ± 0.008	0.157
R		0.08		0.06

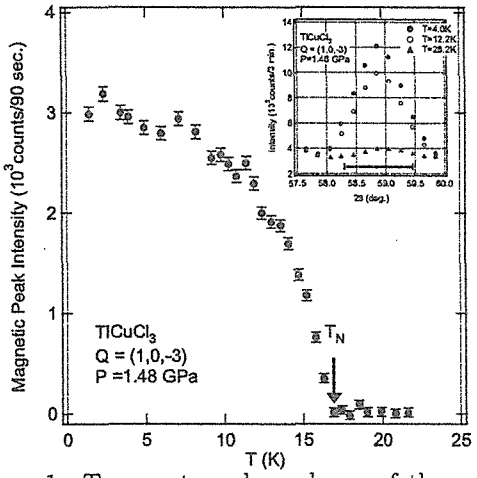

Figure 1: Temperature dependence of the magnetic Bragg peak intensity for $Q = (1, 0, -3)$ reflection measured at $P = 1.48$ GPa in $TlCuCl_3$. The inset shows $\theta - 2\theta$ scans for $Q = (1, 0, -3)$ reflection measured at $T = 4.0$, 12.2 and 28.2 K at $P = 1.48$ GPa in $TlCuCl_3$. The horizontal bar in the inset denotes the calculated instrumental resolution width.

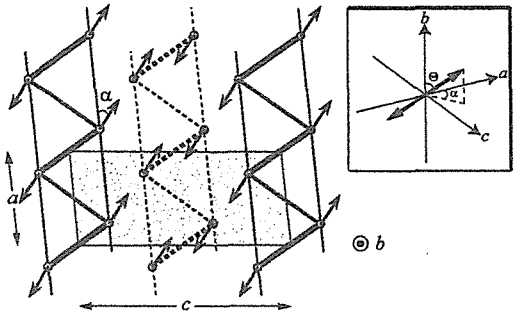

Figure 2: Projection of the spin structure observed in the pressure-induced magnetic ordered phase for $P = 1.48$ GPa in $TlCuCl_3$ onto the $a - c$ plane. The double chains located at the corner and the center of the chemical unit cell in the $b-c$ plane are represented by solid and dashed lines, respectively. The shaded area is the chemical unit cell in the $a - c$ plane. The inset shows the inclination of the ordered spin toward the b-axis. The angle α denotes the angle between the a-axis and the spin component projected onto the $a-c$ plane. The angle Θ is the angle between the spin and the b-axis.

tensities of nine Bragg reflections at $T = 4.0$, 12.2 and 28.2 K. The results are summarized in Table 1 together with the calculated intensities. To refine the magnetic structure, we carried out the same analyses as those of the field-induced magnetic ordered phase in $TlCuCl_3$ [5]. As a result, the spin structure shown in Fig. 2 with $\alpha = 42.6° \pm 1.4°$ and $\Theta = 90.0° \pm 9.0°$ for $T = 12.2$ K, and that with $\alpha = 49.5° \pm 2.4°$ and $\Theta = 58.0° \pm 3.4°$ for $T = 4.0$ K were obtained. This result means that the ordered moments lie in the $a-c$ plane just below T_N, and that they incline toward the b-axis with decreasing temperature. In the temperature dependence of the magnetic Bragg peak intensity shown in Fig. 1, there is no apparent anomaly indicative of an additional phase transition, at which the ordered moments start to incline toward the b-axis.

Comparing magnetic Bragg intensities with those of nuclear reflections, the magnitude of the ordered moment was evaluated as $\langle m \rangle = g\mu_B \langle S \rangle = 0.64(4)\ \mu_B$ at $T = 4.0$ K and $\langle m \rangle = 0.51(3)\ \mu_B$ at $T = 12.2$ K.

References

1) H. Tanaka *et al.*: Physica B **329-333** (2003) 697.
2) A. Oosawa *et al.*:J.Phys.: Cond. Mat. **11**(1999)265.
3) A. Oosawa *et al.*: Phys. Rev. B **65** (2002) 094426.
4) D. B. McWhan *et al.*:Phys.Rev.B **20** (1979) 4612.
5) H. Tanaka *et al.*: J.Phys.Soc.Jpn. **70** (2001) 939.

2.4.5

Pressure-induced Successive Magnetic Phase Transitions in the Spin Gap System $TlCuCl_3$: Polarized Neutron Scattering Study

A. OOSAWA, K. KAKURAI, T. OSAKABE, M. NAKAMURA, M. TAKEDA, Y. SHIMOJO and H. TANAKA[1]

Advanced Science Research Center, JAERI, Tokai, Ibaraki 319-1195
[1]Res.Cent.for Low Temp.Phys.,Tokyo Inst. of Tech.,Oh-okayama,Meguro-ku,Tokyo 152-8551

Recently, unpolarized neutron diffraction measurements under the hydrostatic pressure $P = 1.48$ GPa were carried out in the spin gap system $TlCuCl_3$, and then we observed that the ordered moments lying in the $a-c$ plane just below $T_N = 16.9$ K incline toward the b-axis at lower temperatures [1]. Such inclination is directly observable using the polarized neutron scattering technique, because the spin components in and out of a scattering plane can be separated. With this motivation, we performed the polarized neutron scattering measurements under the pressure in $TlCuCl_3$.

The preparation of the single crystal of $TlCuCl_3$ has been reported in ref. 1. We used again the sample in the McWhan-type high-pressure cell [2] used in the previous unpolarized measurements [1]. Uniaxial polarized neutron elastic scattering measurements [3] were performed using the JAERI-TAS1. Heusler(111)-Heusler(111) monochromator-analyser configuration was used. The sample was mounted in the cryostat with its a^*- and c^*-axes in the scattering plane. The guide field was applied perpendicular to the scattering $a-c$ plane, *i.e.* , Vertical Field (VF) configuration. The polarization was measured on the nuclear Bragg reflection and was determined to be around 71 %. This value is considerably worse than the polarization of almost 90 % realized in the standard polarization analysis set-up on JAERI-TAS1. This is due to the ferromagnetic components of the high-pressure cell. We checked that the polarization does not change in the experimental temperature range, *i.e.*, independent of the high-pressure cell temperature. Other instrumental conditions were the same as those in previous unpolarized measurements [1].

The inset of Fig. 1 shows the magnetic Bragg intensities for the Spin-Flip (SF) scattering at $Q = (0,0,1)$ measured at $T = 3.5$ K and 10.0 K for $P = 1.48$ GPa in $TlCuCl_3$. The intensities are corrected for the background measured above T_N. For $T = 3.5$ K and 10.0 K, which are lower than $T_N = 16.9$ K, the Bragg intensity attributed to the magnetic ordering can be clearly seen. It should be noted that the magnetic Bragg intensity at $T = 10.0$ K is larger than that at $T = 3.5$ K. This indicates that the additional change in spin structure occurs at low temperatures in the ordered phase. The Bragg reflection retains resolution limited width at these temperatures. Figure 1 shows the temperature dependence of the magnetic Bragg peak intensities of SF and Non-Spin-Flip (NSF) scatterings, and of the total magnetic Bragg peak intensity of the both scatterings for $Q = (0,0,1)$ reflection measured at $P = 1.48$ GPa. As shown in Fig. 1, the peak intensity of the SF scattering increases, while that of the NSF scattering retains the background level just below T_N upon decreasing temperature. However, at $T_{SR} = 10.0$ K, the peak intensity of the SF scattering has a maximum, and then decreases. On the other hand, the peak intensity of the NSF scattering begins to increase below T_{SR}. Because all the observed intensity at $Q = (0,0,1)$ below T_N can be safely assigned to be of the magnetic origin, the intensity of the SF and NSF scattering in the present experiment are proportional to the square of the spin component perpendicular to the scattering vector Q in the scattering $a-c$ plane $\langle S_\perp^{ac} \rangle^2$ and that parallel to the b-axis $\langle S^b \rangle^2$, respec-

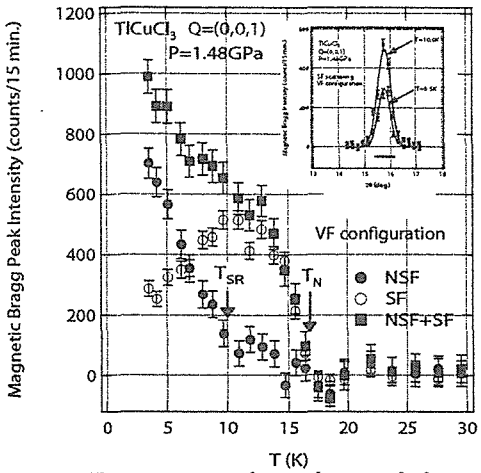

Figure 1: Temperature dependence of the magnetic Bragg peak intensities of SF and NSF scatterings, and of the total magnetic Bragg peak intensity of the both scatterings for $Q = (0, 0, 1)$ reflection measured at $P = 1.48$ GPa in $TlCuCl_3$. The inset shows the magnetic Bragg intensities for the SF scattering at $Q = (0, 0, 1)$ measured at $T = 3.5$ K and 10.0 K for $P = 1.48$ GPa in $TlCuCl_3$. The horizontal bar in the inset denotes the calculated instrumental resolution width.

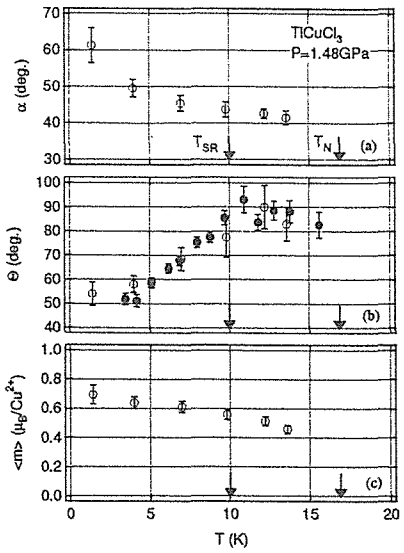

Figure 2: Temperature dependence of the angles (a) α, (b) Θ and (c) the magnitude of the ordered moment $\langle m \rangle$ at $P = 1.48$ GPa. The angle α denotes the angle between the a-axis and the spin component projected onto the $a - c$ plane, and the angle Θ is the angle between the spin and the b-axis [1]. The closed circles denote the angles Θ determined from the ratio of SF and NSF magnetic Bragg peak intensities at $Q = (0, 0, 1)$ corrected for the guide field tilt angle. The open circles denote the values estimated from the unpolarized experiments.

tively. Hence this result concludes that the ordered moments which lie in the $a - c$ plane just below T_N begin to incline toward the b-axis below T_{SR}. Because the peak intensity of the NSF scattering shows the rapid increase at T_{SR}, we can deduce that the inclination arises from a phase transition.

The angle Θ can be evaluated as $34.7° \pm 3.1°$ from the ratio of SF and NSF magnetic Bragg peak intensities for $Q = (0, 0, 1)$ at $T = 4.0$ K, as shown in Fig. 1. The discrepancy between this value and $\Theta = 58.0° \pm 3.4°$ estimated from previous unpolarized experiments [1] indicates that the applied guide field is tilted slightly from the b-axis due to the ferromagnetic components of the high-pressure cell. Assuming $\Theta = 58.0°$, the tilting angles of the guide field ψ and ϕ could be determined as 21° and 29° using the ratio of SF and NSF magnetic Bragg intensities for $Q = (0, 0, 1)$ and $Q = (1, 0, -3)$, in which ψ and ϕ are the angle between the guide field and the b-axis, and that between the a-axis and the guide field projected onto the a-c plane, respectively. The temperature dependence of angle Θ determined from the ratio of SF and NSF magnetic Bragg peak intensities at $Q = (0, 0, 1)$ corrected for the guide field tilt angle is shown in Fig. 2 (b). We can clearly see that the angle Θ which is 90° just below T_N begin to decrease gradually below T_{SR}. It is noted that the angle α is fixed to 45° in this calculation because the angle α is almost independent in this temperature range, *i.e.* $T \geq 4$ K. The values estimated in *un*polarized measurements at a few temperatures are also shown in Fig. 2. As shown in Fig. 2, the temperature dependence of angle Θ obtained in the unpolarized experiments is consistent with that obtained in the polarized experiments, and the temperature dependence of the magnitude of the ordered moment $\langle m \rangle$ shows no anomaly at T_{SR} and increases monotonically with decreasing temperature.

References

1) A. Oosawa *et al.*:J.Phys.Soc.Jpn. **72** (2003) 1026.
2) D. B. McWhan *et al.*:Phys.Rev.B **20** (1979) 4612.
3) R. M. Moon *et al.*: Phys. Rev. **181** (1969) 920.

2.4.6 Polarized Neutron Scattering Study of the Edge-Sharing CuO_2 Chains in $Ca_2Y_2Cu_5O_{10}$

M. MATSUDA, M. NAKAMURA, M. TAKEDA, K. KAKURAI, H. YAMAGUCHI[1], T. ITO[1] and K. OKA[1]

Advanced Science Research Center, JAERI, Tokai, Ibaraki 319-1195
[1]National Institute of Advanced Industrial Science and Technology, Tsukuba, Ibaraki 305-8568

In the edge-sharing CuO_2 chain in which the Cu ions are coupled by the nearly 90° Cu-O-Cu bond, large magnetic moments can be induced at oxygen sites because of the strong hybridization between Cu d and O p orbitals. An existence of the magnetic moments in the CuO_2 chains is predicted theoretically in Li_2CuO_2. [1)] and observed experimentally in $La_9Ca_5Cu_{24}O_{41}$ [2)] and in Li_2CuO_2 [3)].

$Ca_2Y_2Cu_5O_{10}$ is a quasi-one-dimensional magnet, which consists of the edge-sharing CuO_2 chains. This compound shows an antiferromagnetic long-range ordering below T_N=29.5 K with ferromagnetic coupling along the chain [4, 5)]. It is worth while studying the magnetic moment at the oxygen sites in this compound in order to check whether the phenomenon is universal. Previous magnetic structural analysis using unpolarized neutrons suggests that the magnetic moments are not localized at the Cu sites but some of the moments also exist at the oxygen sites [4, 6)]. However, without considering the oxygen moments, there is a slight possibility that the Cu moments are just tilted from the b axis perpendicular to the CuO_2 plane. This study using polarized neutrons confirms that the magnetic moments point along the b axis, strongly supporting the existence of the moments at the oxygen sites.

The neutron scattering experiments were carried out on the 3-axis spectrometer TAS-1. Heusler alloy (111) was used as monochromator and analyzer. A flipping ratio of ~20 was measured on some nuclear Bragg peaks. The horizontal collimator sequence was open-80'-S-80'-open. The incident neutron energy was fixed at E_i=32.4 meV. The single crystal of $Ca_2Y_2Cu_5O_{10}$ was grown using a traveling solvent floating zone method in air [7)]. The crystal structure is orthorhombic and the lattice constants are a=2.810 Å (chain direction), b=6.190 Å, and c=10.613 Å at room temperature. The crystal, which is oriented in the (hhl) scattering plane, was mounted in a closed cycle refrigerator. The $(00L)$ and $(11L)$ (L: integer) magnetic Bragg reflections were measured.

Figure 1 shows the typical data obtained from the polarized neutron measurements in the vertical field. The non-spin-flip (NSF) and spin-flip (SF) mode experiments give magnetic scattering caused by spin component parallel to the field direction [1,-1,0] and perpendicular to it, respectively. A correction originating from imperfect polarization of the neutron beam was made. The tail of the Bragg peaks probably comes from the poor mosaicity of the crystal and/or the the Heusler monochromator and analyzer. The $(00L)$ intensities originate from the spin component perpendicular to the c axis. From the ratio of the NSF and SF reflection in the $(00L)$ reflections ~5, as shown in Figs. 1(a) and 1(b), the angle between the field and the spin directions projected in the ab plane is estimated to be ~25°. This direction almost corresponds to the b axis. From the $(11L)$ intensities the spin component along the c axis can be estimated. Since the SF $(11L)$ intensities are weak, as shown in Figs. 1(c) and 1(d), the c component should be very small even if it exists. The broken lines in Fig. 1 represent the estimated values with the spin structure model in which the moments point along the b axis. [6)] The estimated intensities reproduce

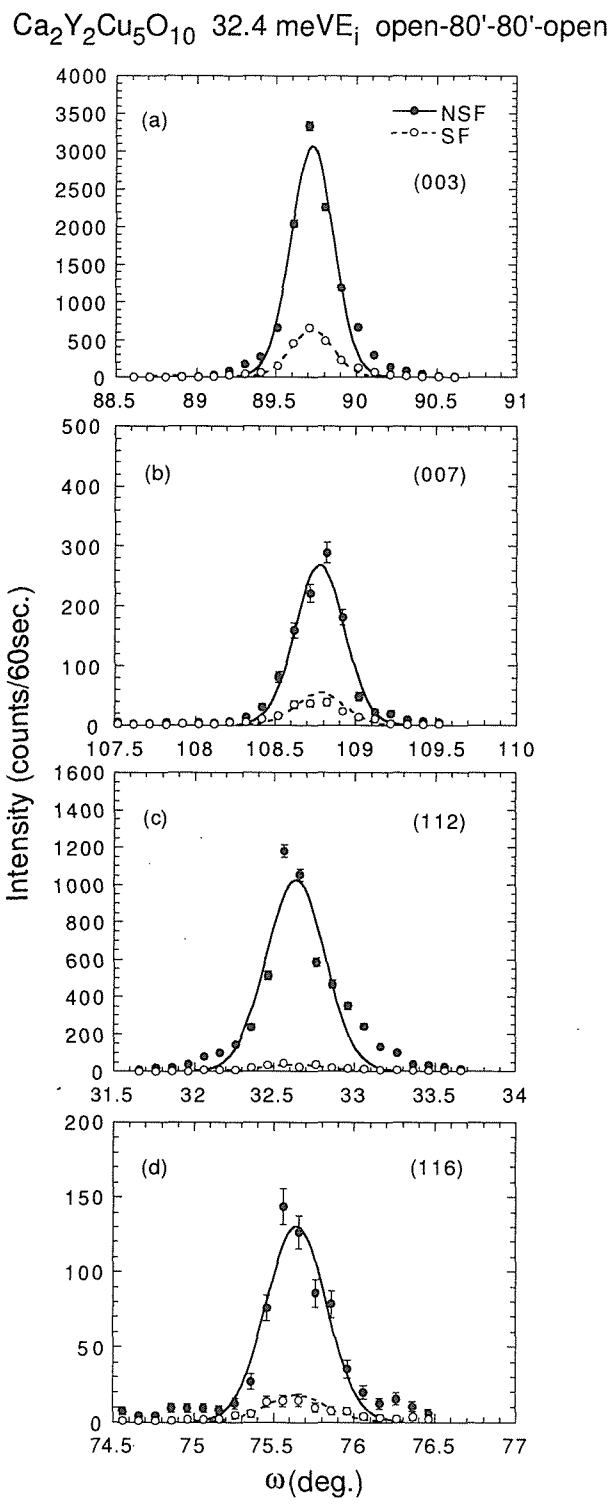

Figure 1: $Ca_2Y_2Cu_5O_{10}$ at (0,0,3), (0,0,7), (1,1,2), and (1,1,6) measured at T=15 K with polarized neutrons in the vertical field spin-flip (SF) and non-spin-flip (NSF) mode. A correction originating from imperfect polarization of the neutron beam was made. The solid lines represent the results of fits to a Gaussian. The broken lines show the intensities estimated for the SF mode.

the observed ones reasonably well. From these results, it can be concluded that the moments point along the b axis.

The previous neutron scattering measurements using unpolarized neutrons shows that a simple model that assumes magnetic moments only at the Cu sites does not describe the magnetic Bragg intensities, especially those of the $(11L)$ reflections [6]. Then, assuming that the moments point along the b axis, it is suggested that the magnetic moments are not localized at the Cu sites but extend to the oxygen sites. Since the present study confirms that the moments point along the b axis, it is clearly concluded that some fraction of the magnetic moments in the CuO_2 unit (~22%) exists at the oxygen sites.

References

1) R. Weht and W. E. Pickett: Phys. Rev. Lett. **81** (1998) 2502.
2) M. Matsuda, K. M. Kojima, Y. J. Uemura, J. L. Zarestky, K. Nakajima, K. Kakurai, T. Yokoo, S. M. Shapiro and G. Shirane: Phys. Rev. B **57** (1998) 11467.
3) U. Staub, B. Roessli and A. Amato: Physica B **289-290** (2000) 299.
4) M. Matsuda, K. Ohoyama and M. Ohashi: J. Phys. Soc. Jpn. **68** (1999) 269.
5) H. F. Fong, B. Keimer, J. W. Lynn, A. Hayashi and R. J. Cava: Phys. Rev. B **59** (1999) 6873.
6) M. Matsuda, K. Kakurai, H. Yamaguchi, T. Ito, C. H. Lee and K. Oka, Appl. Phys. A **74** (2002) 637.
7) H. Yamaguchi, K. Oka and T. Ito: Physica C **320** (1999) 167.

2.4.7 Diffuse Scattering of $ZnFe_2O_4$ Under High Pressure

Y. Tsunoda, K. Kamazawa and S. Katano[1]

School of Science and Engineering, Waseda University, Shinjuku, Tokyo 169-8555
[1] Advanced Science Research Center, JAERI, Tokai, Ibaraki 319-1195

As pointed out by P. W. Anderson, [1)] if only the B-site of normal spinel structure has magnetic moment and the nearest neighbor spin coupling is anti-parallel, there is no definite magnetic ground state. This is a so-called 3-D geometrical spin frustration. In $ZnFe_2O_4$ and $CdFe_2O_4$, since Zn and Cd ions occupy the A-site and both ions have no magnetic moments but all of magnetic ions Fe^{3+} occupy the B-site, these systems satisfy Anderson ' s condition. Actually, in recent neutron scattering measurements using $ZnFe_2O_4$ and $CdFe_2O_4$ single crystal specimens,[2, 3)] only strong diffuse scattering was observed without magnetic Bragg peaks at low temperature, indicating that both $ZnFe_2O_4$ and $CdFe_2O_4$ are the 3-D geometrical spin frustration systems. However, the locations of the diffuse peak positions in the reciprocal lattice space (RLS) for these systems are completely different; for the $ZnFe_2O_4$, the diffuse peak intensities are located slightly inside of the 1-st Brillouin zone boundary (BZB) of the fcc structure and for the $CdFe_2O_4$, slightly outside of the 2-nd BZB of the RLS, suggesting that the spin couplings for these substances are different although the atomic configurations of magnetic ions (Fe^{3+}) are the same for both systems. Only the difference between them is the atomic volumes of Zn^{2+} and Cd^{2+} ions. The Cd^{2+} has a larger volume than the Zn^{2+}. Then, due to the large volume of the A-site atom in $CdFe_2O_4$, the tetrahedron configuration of the B-site is slightly deformed and the angle of super-exchange coupling between Fe^{3+} spins deviates from the right angle, resulting in a big change of the spin coupling. Thus, if we apply the high pressure to $ZnFe_2O_4$ and deform the tetrahedron configuration of Fe^{3+} ions, then, the situations similar to the $CdFe_2O_4$ is expected to occur for $ZnFe_2O_4$ and the diffuse scattering peak position for the $ZnFe_2O_4$ would shift towards those for the $CdFe_2O_4$. This is a motivation of the present investigations.

Using a $ZnFe_2O_4$ single crystal specimen, measurements were performed at the TAS-1 spectrometer installed in JRR-3, Tokai, under the pressure of 1.8 GPa at 15 K and the data were compared with those under the atmospheric condition. A CuBe pressure cell was used for the present measurements.

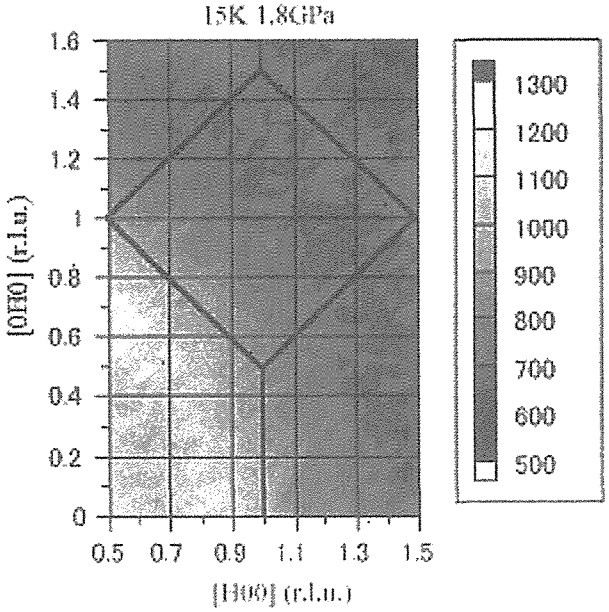

Figure 1: The elastic diffuse scattering intensity contour map studied at 15K under the pressure of 1.8Gpa. The solid lines indicate the Brillouin zone boundaries of the fcc structure.

In order to study the distribution of diffuse scattering extending in a wide area of the RLS, scattering intensity contour map was measured in the (0 0 1) scattering plane. Scattering intensity contour map obtained at 15

K under the pressure of 1.8GPa is given in Fig. 1. In this figure, heavy lines indicate the Brillouin zone boundary of fcc structure. Strong intensities distributing slightly inside of the 1-st Brillouin zone boundary are diffuse scattering due to the spin correlations in $ZnFe_2O_4$. Broad circle along the 2-nd zone boundary is a diffraction line from the pressure transmitting medium 3M Fluorinert. At the first glance, the intensity contour map obtained under the 1.8GPa looked no difference from that obtained at the atmospheric condition. However, if we take the difference of the intensities between both maps, the effects of high pressure become appreciable. The subtracted data I(1.8GPa)- I(0GPa) are mapped in Fig. 2.

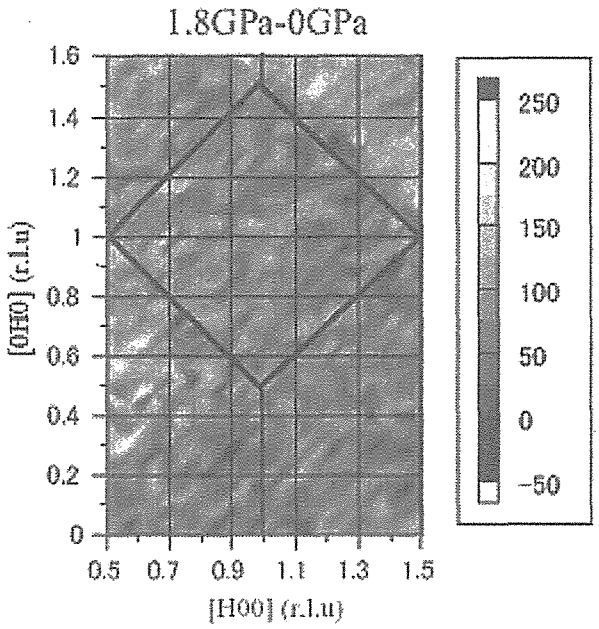

Figure 2: The subtracted intensity contour map I(1.8GPa)- I(0GPa) studied at 3.5K. The solid lines indicate the Brillouin zone boundaries of the fcc structure.

We can observe strong intensities slightly outside of the 2-nd zone boundary and weak intensities inside of the 1-st zone boundary. Since for the $CdFe_2O_4$, diffuse scattering appears slightly outside of the 2-nd zone boundary, experimental data indicate that the $ZnFe_2O_4$-type spin correlations were suppressed and the $CdFe_2O_4$-type spin correlations increased by applied high pressure. This is consistent with our first expectation. However, in order to obtain the persuasive results, further experiments for the data with better statistics are required.

References

1) P. W. Anderson: Phys. Rev. **102** (1956) 1008.
2) K. Kamazawa *et. al.*, *to be appeared in* Phys Rev. B.
3) K. Kamazawa *et. al.*, submitted to the Phys. Rev. Letters.

2.4.8

Spin Structure and Magnetic Excitation of $S = 1/2$ Quasi Two-dimensional Triangular Antiferromagnet Cs_2CuBr_4

T. ONO, H. TANAKA[1], A. OOSAWA[2], Y. KOIKE[2] and K. KAKURAI[2]

Department of Physics, Tokyo Institute of Technology, Tokyo 152-8551
[1]Low Temperature Center, Tokyo Institute of Technology, Tokyo 152-8551
[2]Advanced Science Research Center, JAERI, Tokai, Naka, Ibaraki 319-1195

Cs_2CuBr_4 has the orthorhombic crystal structure with the space group *Pnma*, and magnetic Cu^{2+}-ions form a distorted triangular lattice within the *bc*-plane. For the

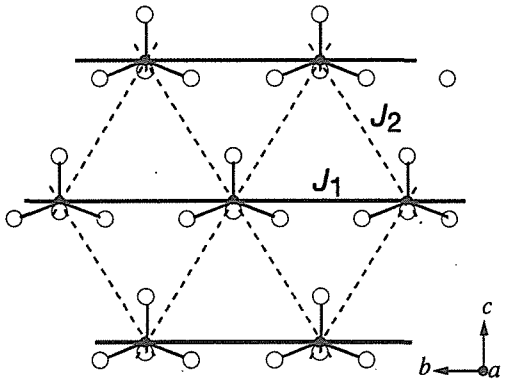

Figure 1: Arrangement of the magnetic Cu^{2+}-ions and the antiferromagnetic interactions J_1 and J_2 within the *bc*-plane.

isostructural compound Cs_2CuCl_4, the magnetic properties were well investigated by the neutron scattering experiments [1,2]. The magnetic properties of Cs_2CuCl_4 is well described by the quasi two dimensional antiferromagnetic model which has two different exchange coupling shown in Fig. 1 with weak Dzyaloshinskii-Moriya terms. Since Cs_2CuBr_4 has the same crystal structure, it is expected that the magnetic behavior of Cs_2CuBr_4 should be qualitatively described by the same hamiltonian which was determined for Cs_2CuCl_4 [2]. Although, the difference of the quantitative ratio between the exchange interactions J_1 and J_2 should give rise to the striking changes of the spin ordering in the magnetic field, since this system is fully frustrated.

This compound undergoes magnetic phase transition at Néel temperature $T_N = 1.4$ K. In the temperature region below T_N, a magnetization plateau appears at 1/3 of the saturation magnetization [3] for the field within the *bc*-plane.

In this report, we report the preliminary results of the inelastic neutron scattering experiments.

Measurements were performed at LTAS triple axis spectrometer installed at JRR-3M, JAERI Tokai. A single crystal with 3 cm^3 in volume was mounted on the sample stage of the dilution refrigerator. Measurements were performed for the *bc* scattering plane. Reflected neutron wave length was fixed at $\lambda_f = 4.045$ Å, and the collimation sequence was chosen as monochromator-80'-sample-80'-analyser-80'-detector. Figure 2 shows the typical scan of the magnetic Bragg peak along the b^*-axis at $T = 50$ mK. Magnetic Bragg reflec-

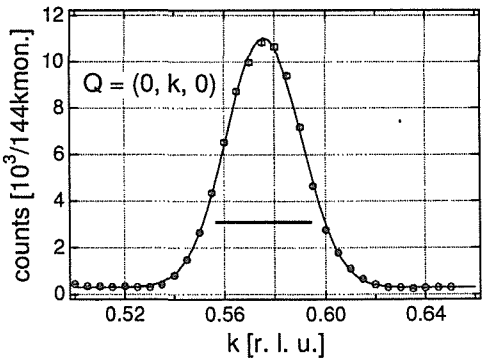

Figure 2: A typical scattering profile scanned along the b^*-direction measured around $T = 100$ mK. Solid straight line below the magnetic Bragg peak indicates the instrumental resolution.

tion appears at $Q_0 = (0, 0.576, 0)$. This result indicates the magnetic structure is incommensurate with the lattice along the b-axis. This incommensuration originates from the frustration among the antiferromagnetic interactions J_1 and J_2 within the bc-plane. For isostructural Cs_2CuCl_4, magnetic Bragg reflection appears at $Q = (0, 0.528, 0)$ [1]. Since the ordering vector is given by the ratio of J_1 and J_2 as $\cos(\pi Q_0) = -J_2/2J_1$ in view of classical spin model, we can obtain $J_2/J_1 = 0.467$ for Cs_2CuBr_4 and 0.175 for Cs_2CuCl_4. This result implies that Cs_2CuBr_4 is more frustrated than Cs_2CuCl_4.

In order to determine the magnitude of the exchange interactions experimentally, we have studied the magnetic excitation along the primary b-axis. Figure 3 shows the energy scan profiles along the b^*-axis. Solid lines are the fit

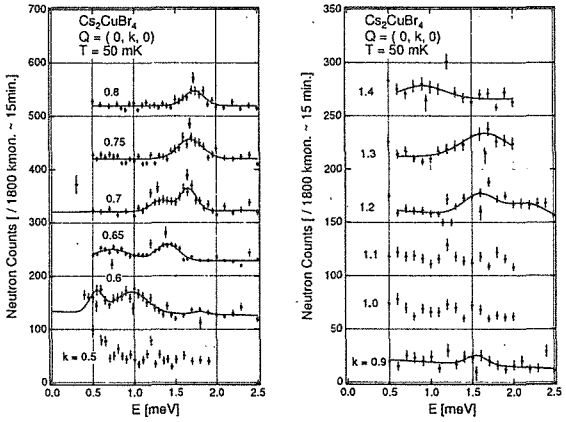

Figure 3: Energy scan profiles along the b^*-axis measured at 50 mK. Solid lines indicate the Gaussian fits to the experimental data.

to the Gaussian function(s). The energy scan profiles show the several excitation peaks at the energy indicated by the arrows. The observed peaks are summarized in Fig. 4. In this plot, the length of the vertical error bar are determined only from the fitting error. The solid line indicates the spin-wave mode [4]

$$\omega(k) = \sqrt{(J_k - J_{Q_0})\left[(J_{k+Q_0} + J_{k-Q_0})/2 - J_{Q_0}\right]}$$

of the Hamiltonian

$$\mathcal{H} = J_1 \sum_{\langle i,i' \rangle} S_i \cdot S_{i'} + J_2 \sum_{\langle i,j \rangle} S_i \cdot S_j$$

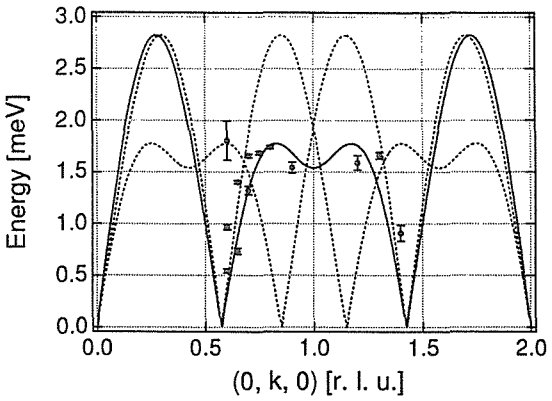

Figure 4: Plot of the dispersion of the magnetic excitations along the b^*-direction. The solid line indicates the linear spin wave dispersion described in the text.

, where J_k denotes the Fourier transformation of the exchange interaction $J_k = J_1 \cos(2\pi k) + 2J_2 \cos(\pi k)\cos(\pi \ell)$. The mode of the solid line indicates the spin wave which polarize out of the spin plane (bc-plane). In Fig. 4, the coupling constant J_2 is fixed as $J_2 = -2J_1 \cos(\pi Q_0)$, and the primary interaction J_1 is scaled as $J_1 = 2.15$ meV. The dashed lines indicate the secondary spin waves $\omega^{\pm}(k) = \omega(k \pm Q_0)$ which polarize within the spin plane [4]. In this model, Dzyaloshinskii-Moriya interactions and the inter-plane interactions are neglected. It is not clear whether this model corresponds to the experimental results because of the insufficiency of the data points. Precise measurements of the inelastic scattering are in progress in order to determine the detailed dispersion relation.

References

1) R. Coldea *et al.*: J. Phys.: Condens. Matter **8** (1996) 7473.
2) R. Coldea *et al.*: Phys. Rev. Lett. **88** (2002) 137203.
3) T. Ono *et al.*: Phys. Rev. B **67** (2003) 104431.
4) R. Coldea *et al.*: Phys. Rev. Lett. **86** (2001) 1335.

2.4.9 Magnetic ordering process in the charge ordered $LuFe_2O_4$

S. NAGAI*, M. MATSUDA, Y. ISHII, K. KAKURAI, H. KITO[1], N. IKEDA[2] and Y. YAMADA[3]

ASRC, JAERI, Tokai, 319-1195
[1]NRIM, Tsukuba, 305-0047
[2]JASRI, Hyogo, 679-5198
[3]ARCSE, Waseda Univ., Tokyo, 169-0072
*Present address: NSL, ISSP, Univ. of Tokyo, Tokai, 319-1106

$LuFe_2O_4$ belongs to a class of materials expressed by RFe_2O_4, R being rare-earth metals.[1)] The crystals of these materials belong to the rhombohedral system. The Fe ions are arranged to form the hexagonal double layers and stack in the sequence of (AB), (CA), (BC),... along the rhombohedral unique axis. The average valence of the Fe ions is expected to be $Fe^{+2.5}$ in these materials and hence a mixed valence state of Fe^{2+} and Fe^{3+} ions occupying the equivalent Fe sites on the hexagonal plane with equal probability is expected. An earlier neutron scattering experiment on this compound by J. Iida *et al.* [2)] reports the observation of 2-D magnetic correlation even at lowest temperature (T=10K) in their single crystal sample. From their high temperature data (at RT) one can also deduce that there is no well developed 3-D charge ordering in their sample. Recently Y. Yamada *et al.*[3)] reported the sequential charge ordering observed by means of X-ray scattering in a $LuFe_2O_4$ single crystal grown by H. Kito. The charge ordering is characterized by an 3-D incommensurate charge-density wave state in the lowest temperature phase for T$\leq$320K. It is of great interest to study the low temperature magnetic behavior in this charge ordered sample of $LuFe_2O_4$ to look for a correlation between the charge and spin ordering. We thus performed neutron scattering experiments on TAS-1 and TAS-2 in the temperature range of RT to 7K.

Figure 1 shows the purely magnetic scattering along (1/3, 1/3, L) at 270K and 7K measured by polarization analysis. At 270K 2-D scattering along c*-direction can be clearly seen and at T=7K 3-D like ordering can be observed. The insets indicate the temperature dependence of the peak intensities at Q=(1/3, 1/3, 1) and (1/3, 1/3, 2). One can clearly recognize the onset of the 3-D magnetic ordering at T_N=242K, but at the same time the temperature dependence of (1/3, 1/3, 1) and (1/3, 1/3, 2) indicates the existence of the second characteristic temperature T_f=177K. The hysteresis associated with T_f is remarkable. Figure 2 shows the detailed spectra at around this characteristic temperature along (1/3, 1/3, L) taken with better resolution (17'-20'-10'-20' collimations were used). The existence of both resolution limited peaks and broad peaks at 186K can be seen, while be-

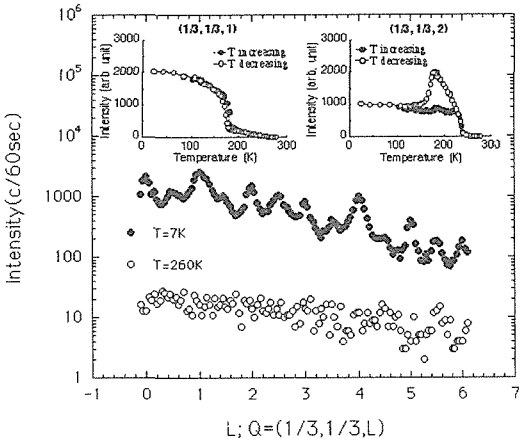

Figure 1: Purely magnetic intensity along Q=(1/3, 1/3, L) as obtained from the polarization analysis experiment at T=260K and 7K. Inset: T-dependence of the peak intensities at Q=(1/3, 1/3, 1) and (1/3, 1/3, 2).

low the characteristic temperature at T=161K the broad peaks considerably gain in intensities and at the same time the resolution limited peaks acquire finite widths resulting into the apparent diffuse contribution observed at lowest temperature. Figure 3 depicts the ferrimagnetic component showing up at Q=(1, 0, L), L=-6.5, -3.5, -0.5, 2.5. They also show the strong hysteretic behaviour as the (1/3, 1/3, 2) antiferromagnetic peak, as indicated in the inset.

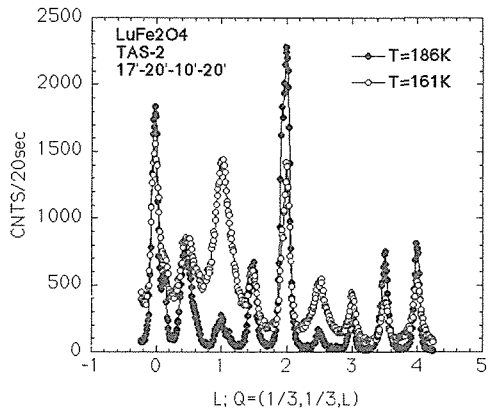

Figure 2: Magnetic scattering above and below T_f along Q=(1/3, 1/3, L) measured with tight collimations.

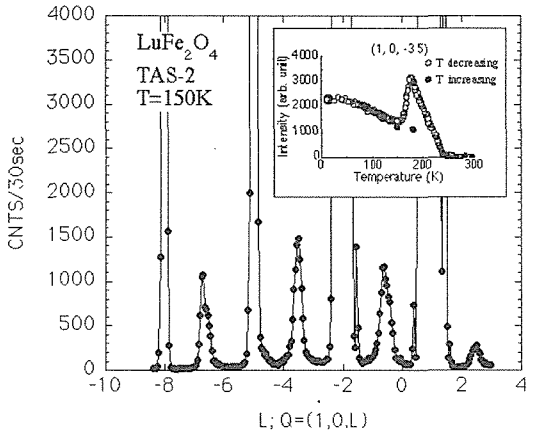

Figure 3: Scan along Q=(1, 0, L) at T=150K probing the ferrimagnetic component at L=-6.5, -3.5, -0.5 and 2.5. Inset: T-dependence of the peak intensity at Q=(1, 0, -3.5).

To summarize the following extraordinary magnetic ordering characteristics in $LuFe_2O_4$ were observed.

1) In contrast to the non-charge ordered sample a clear sign of 3-D magnetic ordering at T_N=242K is observed. Despite the triangular configuration a strong 2-D antiferromagnetic correlation with ferrimagnetic component in the double layer in the hexagonal plane develops to a 3-D order along the c-axis at this temperature.

2) At around 177K there is another characteristic temperature T_f, where new type of broad magnetic peaks start to grow and at the same time the magnetic peaks developing below T_N also acquire finite line width, including the peaks due to the ferrimagnetic component.

3) There is a strong hysteresis observed at T_f.

4) Due to the second 'transition' at T_f the low temperature magnetic peaks have a finite width along the c* direction causing the broad diffuse-like intensity distribution. The high energy resolution experiment using thermal neutron spin echo (see Activity Report on Neutron Scattering Research 2003 of NSL, ISSP) demonstrated that these diffuse intensities are of static nature within the resolution of 1μeV.

The surprisingly different charge and magnetic behaviour in the new sample may be explained by the difference in the oxygen stoichiometry, as has been already pointed out for YFe_2O_4 sample.[4] These results anyhow indicate that the charge ordering process strongly influences the low temperature magnetic ordering and that the subtle balance between charge frustration and spin frustration may cause the peculiar short range freezing of the spins in the ground state.

References

1) N. Kimizuka, E. Muromachi and K. Shiratori in *Handbook on the Physics and Chmistry of Rare Earths*, ed K.A. Gschneidner, Jr. and L. Eyring (Elsevier, Amsterdam, 1990) **Vol.13** p.283ff.
2) J. Iida *et al.* : J. Phys. Soc. Jpn. **62** (1993) 1723.
3) Y. Yamada *et al.* : Phys. Rev. B**62** (2000) 12167.
4) S. Funahashi *et al.* : J. Phys. Soc. Jpn. **53** (1984) 2688.

2.4.10 Magnetic structure of GeV_4S_8 with V_4 tetrahedral clusters

H. NAKAMURA, H. CHUDO[1], Y. SHIMOJO[2], Y. ISHII[2] and K. KAKURAI[2]

Graduate School of Science, Himeji Institute of Technology, Kamigori, Ako-gun, Hyogo 678-1297
[1]Department of Chemistry, Kyoto University, Kyoto 606-8502
[2]Advanced Science Research Center, JAERI, Tokai, Ibaraki 319-1195

Critical phenomena of tetrahedral lattices such as Pyrochlore lattice attracts much attention recently. We are investigating compounds with tetrahedral clusters, which have (molecular-orbital like) direct mixing among d electrons, (1) in order to distinguish anomalies of an infinite lattice and an isolated tetrahedron, and (2) as miniatures of the itinerant-electron frustrated system. Johrendt [1] first synthesized GeV_4S_8 and reported its basic magnetic and transport properties. The crystal structure is characterized as $(V_4S_4)^{4+}$ cubane-type clusters are implanted in a cubic lattice, where V atoms form tetrahedral clusters. It is expected that a V_4 tetrahedron has 2 unpaired d electrons ($S = 1$ per V_4). So far, we determined an antiferromagnetic-like transition at $T_N = 18$ K, being consistent with [1], and also a small structural deformation from cubic to monoclinic at $T_S = 33$ K [2]. NMR measurements revealed that there exists 3 different internal field at V sites in the ground state; absolute values of the internal fields are 1.9, 4.9 and 5.9 T [2].

In order to determine the magnetic structure at low temperature and to know the reason why there exist 3 internal fields, we performed powder neutron diffraction experiments with use of HRPD at JAERI (wave length $\lambda = 1.823$ Å). Figure 1 shows the difference profile between 4 K and 25 K (i.e., magnetic scattering). Magnetic Bragg reflections are explained assuming a propagation vector $\mathbf{Q} = [\frac{1}{2}\frac{1}{2}0]$, suggesting that the compound has a relatively simple spin structure. Intensity analyses indicate that moments are parallel or antiparallel to $[1\bar{1}0]$, and that the magnitude is unique of 0.5 μ_B per V atom. The spin arrangement in the cluster is of interest, which is ferrimagnetic-like as $\uparrow\uparrow\uparrow\downarrow$, and the antiferromagnetism is satisfied as a whole magnetic unit cell. It should be noted that the moment magnitude is unique, indicating that the considerably different internal fields at V sites can not be attributed to simple separation of moment values but due to unconventional hyperfine coupling inherent to the tetrahedral cluster. On the basis of the proposed spin structure and assuming a large anisotropy in the hyperfine field and a large transferred field from neighboring V atoms within the cluster, we expect 3 different magnetic sites of V, which is in good accordance with the NMR observation. Hence we suggest that the internal field in this compound is dominated by the direction of moments rather than the magnitude of moments.

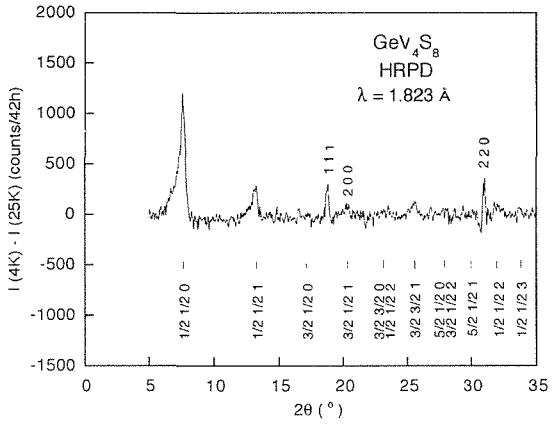

Figure 1: Magnetic scattering of GeV_4S_8.

References

1) D. Johrendt: Z. Anorg. Alleg. Chem. **642** (1998) 952.
2) H. Nakamura and H. Chudo: unpublished.

2.4.11

Spin Orientation of Exotic Spin-Density Waves in Cr(001)/Sn Epitaxial films

M. TAKEDA[1,2], K. MIBU[3], J. SUZUKI[1], M. NAKAMURA[1], M. MATSUDA[1], K. KAKURAI[1] and Y. ENDOH[4]

[1]Advanced Science Research Center, JAERI, Tokai, Ibaraki 319-1195
[2]Physics Department, Graduate School of Science, Tohoku University, Sendai 980-8578
[3]Research Center for Low Temperature and Materials Sciences, Kyoto University, Uji, Kyoto 611-0011, Japan
[4]Institute for Material Research, Tohoku University, Katahira Sendai 980-8577

A variety of mysterious phenomena observed in metal Chromium (Cr) have attracted a lot of researchers for a long time. Among them most famous one is the spin-density wave (SDW) formed in bulk Cr below the Néel temperature of 311 K [1]. The SDW itself is now well known to condensed matter physicists, however, it is hard to say that the nesting model of Fermi surface can completely explain all magnetic behaviors of Cr. The SDW strongly depends on circumstances like impurities, temperature, internal stress and so on which affects the Fermi surface. The Fermi surface in Cr multilayers is expected to be effectively modified by the interfaces. By changing the counterpart of Cr multilayers we can have a variety of Fermi surface of Cr. This is a useful approach to elucidate all the details of the mechanism of the SDW which is governed by the nature of Fermi surface.

Recently we synthesized epitaxial Cr(001) / Sn multilayers in which monatomic Sn layers are periodically inserted in the Cr(001) epitaxial films and investigated the magnetic structures by complementary use of neutron and Mössbauer spectroscopies[2–5]. We have found that in the multilayers SDWs with complicated waveform were stabilized at low temperatures. The most exotic feature of the SDWs is that the artificial periodicity, Λ introduced by the embedded Sn monatomic layers, governs the wavelength of the SDWs, which is believed to be defined by the nesting vector in pure bulk Cr. In this brief report we focus on the Λ dependence of spin orientation: another prominent influence of the embedded Sn monatomic layers on the SDW state.

In the multilayers stacked bilayers of [Cr(t_{Cr})/Sn(0.2 nm)] (t_{Cr} = 4.0, 8.0, 10, 12 and 16 nm) were epitaxially deposited on MgO(001) substrates with a 5-nm-thick Cr buffer. The MgO[001] and bct Cr[001] directions are normal to the sample plane, and MgO[110] and Cr[010] are parallel each other. The stacking number of the bilayer in each sample, M, was determined to make the accumulated thickness of Cr 240 nm ($t_{Cr} \times M$ = 240 nm). According to the t_{Cr}, the samples are called as CS4, CS8, CS10, CS12, CS14 and CS16, respectively. In X-ray diffraction profiles, the satellite peaks stemming from Λ were clearly observed up to the 4th order in all these samples, which indicated that the multilayer structures were well established.

Figure 1 shows the Λ dependence of in-plane and out-of-plane lattice parameters measured by TAS-1, TAS-2 and a conventional X-ray diffractometer at ambient temperatures where all of the sample have a commensurate antiferromagnetic structure [5]. Both in-plane (010) and out-of-plane (001) lattice constants were expanded in comparison with bulk Cr, however, they gradually approached the bulk value with increasing Λ. The in-plane lattice constants were larger than the out-of-plane one. The Λ dependence and the anisotropy leads to different internal stress in each sample. We performed scans along [001] and [010] through the (010) and (001) reciprocal points of the bct structure at 290 K. Single magnetic peaks at (010) and (001)

Table 1: The designed artificial period, Λ, the volume fraction of each S (spin direction) domains in the case of multi-S domain state, the easy axis of Cr moments in the case of single domain state and the magnitude of Cr magnetic moments at 300 K. The magnitude is common in both domain states.

	multi-S domain		single domain	
	in-plane	out-of-plane		
Λ (nm)	components (%)	component (%)	easy axis	M(300K) (μ_B)
4.2	37	63	[112]	0.57 ± 0.19
8.2	51	49	[223]	0.44 ± 0.10
10.2	68	32	[111]	0.38 ± 0.08
12.2	32	68	[112]	0.43 ± 0.16
14.2	32	68	[112]	0.44 ± 0.08
16.2	47	53	[223]	0.39 ± 0.10

appeared in the scan profiles of all samples, which indicates that the commensurate antiferromagnetic structure forms in the multilayers. Integrated intensities of those peaks were normalized by the intensity of Cr(020) and (002) nuclear peaks. The integrated intensities of the (001) and (010) are not identical even after the normalization. The degree of the unbalance indicates the direction of averaged Cr magnetic moments and the directions are consistent with the previous report on polarized neutron experiments [6].

If the sample is a single magnetic domain, the intensity of (010) peak is proportional to the summation of squared in-plane [010] and out-of-plane [001] components of Cr spins, and that of (001) to the summation of two squared in-plane components. In the case of multi-S domain state, in which domains with the easy axis of Cr moments being either [100] ([010]) or [001] coexist, the (010) intensity is proportional to sum of the volume of in-plane [100] and out-of-plane [001] S domains, and the (001) to that of two in-plane S domains.

When the single domain is assumed, the intensity ratio gives the spin orientation. Possible easy axes deduced from the intensity ratios are summarized in Table 1. This table also shows the volume fraction of each S domains in case of multi-S domain and the magnitude of averaged Cr magnetic moments. It is known that the easy axes of the SDW in bulk Cr are bcc principle axes. The hard axis of bulk Cr like [111] is unlikely to be the easy axes of these multilayers. At the moment we can not conclude either of domains is realized in each multilayers. CRYOPAD, which is now developed by our group, is going to give clear conclusion on this ambiguity [7].

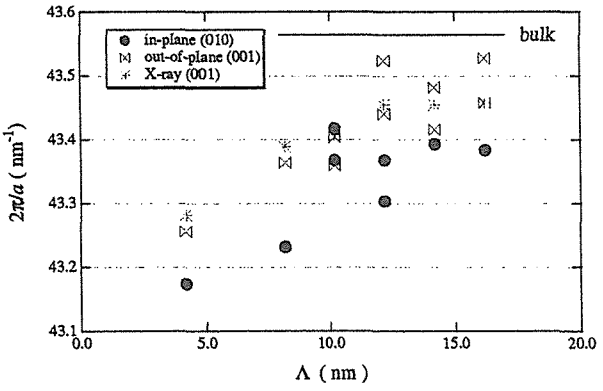

Figure 1: The artificial periodicity, Λ, dependence of in-plane and out-of plane lattice parameters of Cr/Sn(001) multilayers.

References

1) E. Fawcett, Rev. Mod. Phys. **60,** 209 (1988).
2) K. Mibu, S. Tanaka and T. Shinjo, J. Phys. Soc. Jpn. **67,** 2633 (1998).
3) M. Takeda, K. Mibu, K. Takanashi, K. Himi, Y. Endoh, T. Shinjo and H. Fujimori, J. Phys. Soc. Jpn. **69,** (2000) 1590.
4) K. Mibu, M. Takeda, J. Suzuki, A. Nakanishi, T. Kobayashi, Y. Endoh and T. Shinjo, Phys. Rev. Lett. **89** (2002) 287202.
5) M. Takeda, K. Mibu, T. Shinjo, J. Suzuki and Y. Endoh, App. Phys. **74** (2002) s1554.
6) M. Takeda, K. Mibu, J. Suzuki, M. Nakamura, M. Matsuda, K. Kakurai and Y. Endoh, JAERI-Review. **2002-028** (2002) 51.
7) M. Nakamura, M. Takeda, Y. Shimojo and K. Kakurai, see in this review.

2.4.12 Neutron Diffraction Study on β-MnCoZn Alloys

T. HORI, H. SHIRAISHI and Y. ISHII[1]

Shibaura Institute of Technology, Saitama-city 337-8570
[1]Advanced Science Research Center, JAERI, Tokai, Ibaraki 319-1195

Pure β-Mn has a complicated cubic structure, so-called β-Mn structure, which contains 20 atoms distributed between two nonequivalents 8c and 12d sites.[1)] It is considered that this metal remains in paramagnetic state down to 1.4 K.[2)] β-Mn alloys containing some impurities show an antiferromagnetic behavior at low temperature. Two decades ago, we have made magnetization measurements and neutron diffraction experiments at KUR for β-Mn alloys containing Cobalt. The susceptibility for alloys with around 40 at. % Co has a maximum value at 80 K which must be the antiferromagnetic Néel temperature.[3)] However, this alloy has no applicable long range magnetic order structure.[3)]

On the other hand, β-CoZn alloy has a also β-Mn structure, and shows a typical ferromagnetism with the Curie temperature T_C = 460K.

We have found that wide solid solution from pure β-Mn to β-CoZn exist in ternary Mn–Co–Zn alloy system, so we have made X-ray and neutron diffraction experiments and magnetization measurements for ternary β-MnCoZn alloys.

Figure 1 shows magnetization in a field of 8.0 kOe versus temperature curves for β-CoZn alloy which shows a typical ferromagnetism with the Curie β-$Mn_{0.24}Co_{0.36}Zn_{0.40}$ alloys and show a temperature T_C = 460 K. Another alloy, β-$Mn_{0.24}Co_{0.36}Zn_{0.40}$, shows also a ferromagnetism with T_C = 200 K. However, more Mn rich alloy, β-$Mn_{0.42}Co_{0.28}Zn_{0.30}$, shows an antiferromagnetic behavior below around 70 K as shown in Fig. 1.

We have made neutron diffraction experiments for β-CoZn, β-$Mn_{0.24}Co_{0.36}Zn_{0.40}$ and β-$Mn_{0.42}Co_{0.28}Zn_{0.30}$ using HRPD.

Figure 2 shows observed and calculated neutron diffraction patterns for β-CoZn alloy at 7 K. The alloy shows a typical β-Mn structure with a = 4.000 Å. The site occupation and magnetic moment μ are as follows: Co on 8c, residual Co and Zn on 12d and $\mu = 1.3\mu_B$/ Co atom. The detailed analysis for other alloys is now in progress.

References

1) P. Villars and L. D. Calvet: *Pearson Handbook of Crystallographic Datafor Intermetallic Phases.* **Vol. 4** (1999) 4321.
2) T. Kohara and K. Asayama: J. Phys. Soc jpn. **37** (1974) 401.
3) T. Hori: J. Phys. Soc. jpn. **38** (1975) 1738.

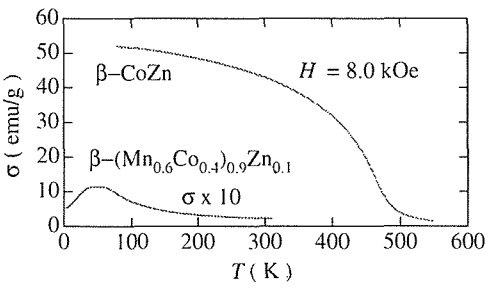

Figure 1: agnetization in a field versus temperature curves for β-CoZn and β-$Mn_{0.42}Co_{0.28}Zn_{0.30}$ alloys.

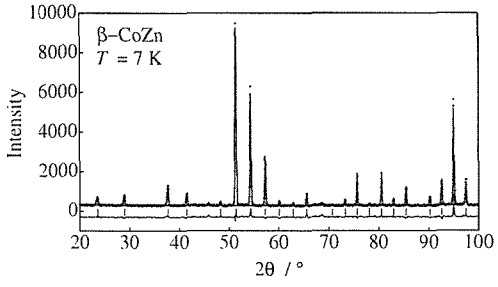

Figure 2: Observed (+) and calculated (a line) neutron diffraction patterns for β-CoZn alloy at 7 K. The difference between the observed and calculated intensities is shown by the lower curve.

2.4.13 Unusual antiferromagnetic properties affected by antiferroquadrupolar interaction in TbB_2C_2

K. KANEKO[1], N. METOKI[1,2], K. OHOYAMA[3], H. ONODERA[3] and Y. YAMAGUCHI[3]

[1]Advanced Science Research Center, JAERI, Tokai, Ibaraki 319-1195
[2]Department of Physics, Tohoku University, Aoba, Sendai 980-8578
[3]Institute for Materials Research, Tohoku University, Sendai 980-8577

In f-electron systems, there is an upsurge of interest on the role of orbital degree of freedom , i.e., quadrupolar interactions in their magnetic properties. The existence of the strong antiferroquadrupolar (AFQ) interaction is a characteristic feature in the tetragonal RB_2C_2 (R=rare earth) compounds. DyB_2C_2 shows an AFQ ordering at T_Q = 24.7 K above an antiferromagnetic (AFM) transition at T_N = 15.3 K [1]. An AFQ order in HoB_2C_2 coexists with an AFM order below T_Q=4.5 K [2]. The present report focus on another isostructural compound TbB_2C_2, which shows an AFM order at T_N=21.7 K under H=0. [3] In TbB_2C_2 the effect of AFQ interaction becomes prominent by applying external magnetic fields. Magnetic fields stabilize a characteristic commensurate magnetic structure involving a slight distortion which are basically the same as those of the AFQ+AFM ordered phase in DyB_2C_2 and HoB_2C_2 [4].

Under H=0, the magnetic structure in the AFM ordered state of TbB_2C_2 has an incommensurate component of $\boldsymbol{k}_L$=(1±δ, ±δ,0) (δ=0.13) in addition to the dominant $\boldsymbol{k}_2$=(1 0 1/2) and $\boldsymbol{k}_4$=(0 0 1/2) components. Furthermore, the magnetic diffuse scattering exists around the satellite peak corresponding to $\boldsymbol{k}_L$. It should be pointed out that the existence of the diffuse scattering around satellites is common to the AFM ordered state in HoB_2C_2 [5,6]. In the present work, we provide details of the satellite and diffuse scattering in TbB_2C_2 studied by neutron scattering under high energy resolution, which reveal the unusual antiferromagnetic ordering in TbB_2C_2.

For sample preparation, the stoichiometric amounts of constituents, Tb, ^{11}B and C

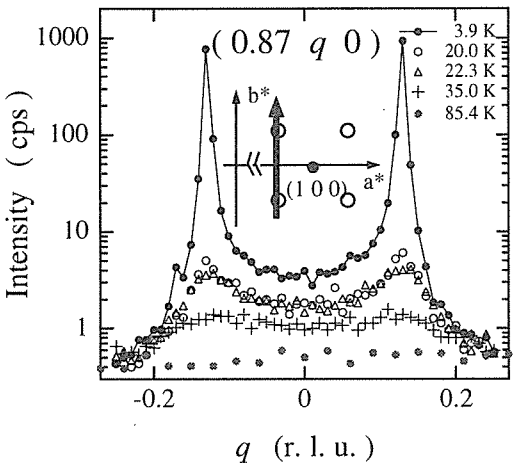

Figure 1: Line scan along (1-δ q 0) measured at various temperatures. Note that the vertical axis is displayed in the logarithmic scale. The schematic scan trajectory in the reciprocal space around (1 0 0) is given in the inset where the open circles correspond to the positions of the satellite peaks.

were synthesized through the argon arc melting. Single-crystalline sample of $Tb^{11}B_2C_2$ was grown by the Czochralski pulling method using a tetra-arc furnace. Neutron scattering experiments were carried out on the cold neutron triple-axis spectrometer, LTAS, installed at JRR-3M in Japan Atomic Energy Research Institute, Tokai. Pyrolytic graphite (PG) monochromator and analyser crystals were used with a Be filter to reduce the higher order contamination. The horizontal collimation of 80'-sample-80'-80' giving energy resolution of less than 0.15 meV was employed.

Figure 1 shows the line scan along (1−δ q 0) obtained at various temperature. The inset gives the schematic scan trajectory around the (1 0 0) reciprocal lattice point. Note that the vertical scale is displayed in the logarithmic

scale. At 3.9 K, the sharp and intense satellite peaks were observed at $q = \pm 0.13$. In addition, there exists the peculiar shape of weak and broad diffuse scattering between the satellites as well. The energy width of both the satellite and diffuse scattering corresponds to resolution limit at least in 3.9 K.

With increasing temperature, we observed the unusual temperature dependence in the scattering intensity. It is notable that only the sharp satellite peaks disappeared clearly below T_N of 20 K, whereas the broad diffuse scattering exists even above T_N. The diffuse scattering intensity decreases unevenly in q-space with increasing temperature and becomes almost flat between $q = \pm 0.15$ at 35.0 K. No trace of diffuse scattering can be seen at 85.4 K.

Figure 2 shows the detailed temperature dependence of the relative magnetic peak intensity of all components, 1 0 1/2 (·), 0 0 1/2(○), satellite at (1-δ δ 0)(+), and diffuse scattering at (1 0 0)(▲). The temperature dependence of these peak intensities is quite diversified. In particular, the satellite peaks exhibit unusual behavior among them. It becomes clear that the intensity of satellite peak disappears far below T_N of ~13 K, in other words, the incommensurate structure is not realized at T_N. On the other hand, the diffuse scattering, having almost the same q as satellites, shows no anomaly in its intensity around 13 K where satellites vanished. The intensity of diffuse scattering forms a small peak at T_N. The diffuse scattering survives even above T_N and exhibits monotonous decrease with increasing temperature. Finally around 60 K(~$3T_N$), the intensity reaches almost the background level. These behavior makes clear contrast to the 0 0 1/2 and intense 1 0 1/2 reflections, disappearing just at T_N.

It is quite interesting that no anomaly was observed in the specific heat, magnetic susceptibility and electrical resistivity around 13 K where the satellite peak disappeared. Furthermore, the present disappearance temperature of 13 K is different from the previous one of 18 K obtained under lower energy resolution of

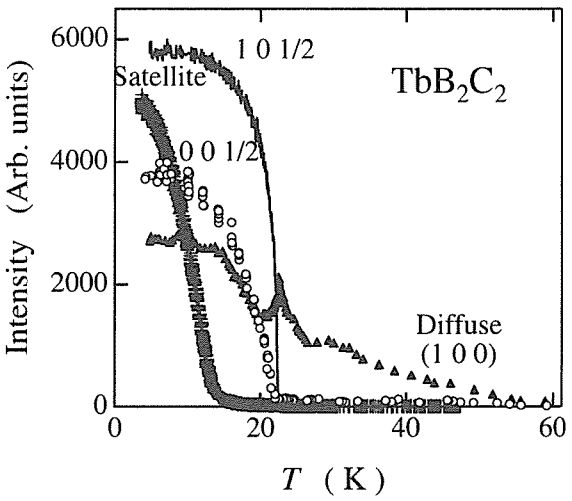

Figure 2: Peak intensities of the antiferromagnetic reflections 1 0 1/2(·), 0 0 1/2(○), satellite at (1-δ δ 0)(+), and diffuse scattering at (1 0 0)(▲) as a function of temperature.

0.9 meV, whereas the diffuse scattering as well as the $\boldsymbol{k}_2$=(1 0 1/2) and $\boldsymbol{k}_4$=(0 0 1/2) components exhibits the almost same temperature dependence in both experiments. This energy resolution dependence suggests the existence of dynamical effect on the development of incommensurate structure.

Unfortunately, we have no clear explanation for these unusual behavior of satellite and diffuse scattering at present. In order to clarify the origin of the diffuse scattering and incommensurate structure,further neutron scattering experiments are in progress.

References

1) H. Yamauchi, H. Onodera, K. Ohoyama, T. Onimaru, M. Kosaka, M. Ohashi and Y. Yamaguchi, J. Phys. Soc. Jpn. **68** (1999) 2057.
2) H. Onodera, H. Yamauchi and Y. Yamaguchi, J. Phys. Soc. Jpn. **68** (1999) 2526.
3) K. Kaneko, H. Onodera, H. Yamauchi, K. Ohoyama, A. Tobo and Y. Yamaguchi, J. Phys. Soc. Jpn. **70** (2001) 3112.
4) K. Kaneko, S. Katano, M. Matsuda, K. Ohoyama, H. Onodera and Y. Yamaguchi, Appl. Phys. A**74** (2002) S1749.
5) A. Tobo, T. Ohmori, T. Matsumura, K. Hirota, N. Oumi, H. Yamauchi, K. Ohoyama H. Onodera and Y. Yamaguchi, Physica B **312-313** (2002) 853.
6) K. Kaneko, K. Ohoyama, S. Katano, M. Matsuda, H. Onodera and Y. Yamaguchi, J. Phys. Soc. Jpn. **71** (2002) 3024.

2.4.14 The neutron small-angle diffraction study of an itinerant electron metamagnet MnSi

M. Yamada, T. Goto, J. Suzuki[1], M. Takeda[1] and K. Kakurai[1]

ISSP, University of Tokyo, 5-1-5 Kashiwanoha, Kashiwa 277-8581
[1]Advanced Science Research Center, JAERI, Tokai, Ibaraki 319-1195

The intermetallic MnSi compound has the cubic B20-type crystal structure and exhibits a helical magnetic ordering with a long wavelength of $\lambda = 180$ Å in the [111] direction [1]. The helical ordering originates from the Dzyaloshinsky-Moriya interaction. By applying magnetic fields, the magnetic state changes from the helical state to a conical one and then into a forced ferromagnetic one at about $B_f = 0.6$ T. When the pressure is applied, the magnetic order vanishes at $P_c = 1.5$ GPa [2,3]. The magnetic transition at T_C is of second-order at $0 < P < P_t$, but becomes first-order transition at $P_t < P < P_c$, where $P_t = 1.2$ GPa. From AC susceptibility measurements, a broad maximum of the susceptibility is observed at $P > P_t$ [2]. These results are typical characteristics of the Itinerant Electron Metamagnet (IEM). From DC magnetization measurements, a hysteresis of the metamagnetic transition is observed above P_t [4]. We have revealed the metamagnetic properties of MnSi and determined the phase diagram. The obtained diagram corresponds to the theoretical one [5] very well. It is very interesting to investigate the metamagnetic transition by the neutron diffractions under the multiple extreme conditions, high fields, low temperatures and high pressures. In this report, the obtained results under ambient pressure measurements are shown.

A single crystal was prepared by Czochralski method. The cylindrical crystal 60 mm in diameter and 60mm in length with [001] long axis was used in this experiment. We have carried out a neutron small-angle diffraction study at JAERI (SANS-J). All reflections around the (000) reciprocal point in the (110) reciprocal plane were measured simul-

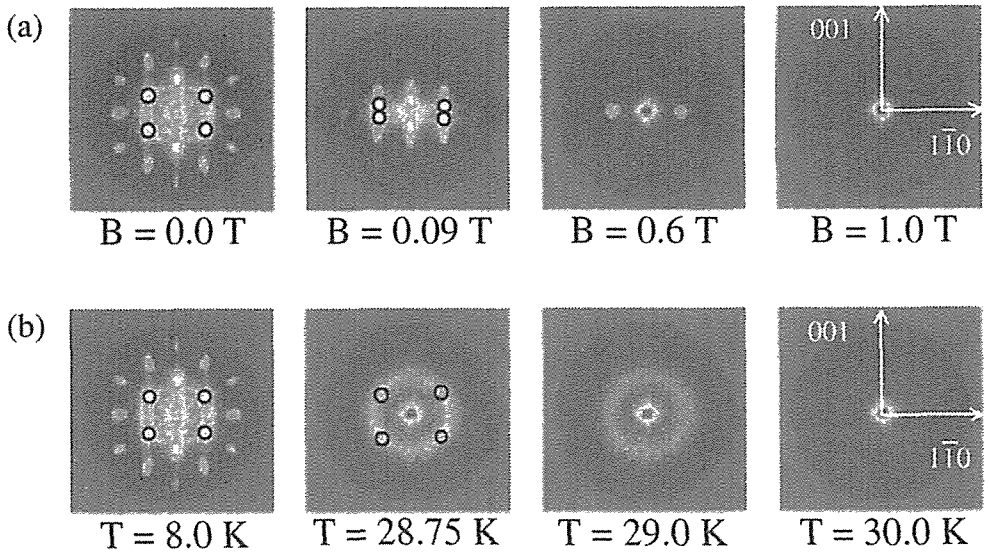

Figure 1: (a) The field and (b) temperature dependence of the satellite spots. The ⟨111⟩ satellites are emphasized by open circles at $B = 0$ T.

taneously with the two dimensional multi-counters. For ambient pressure, the neutron diffraction study was carried out at 8 K $< T <$ 30 K without pressure cell. Magnetic field B is applied in the $[1\bar{1}0]$ direction.

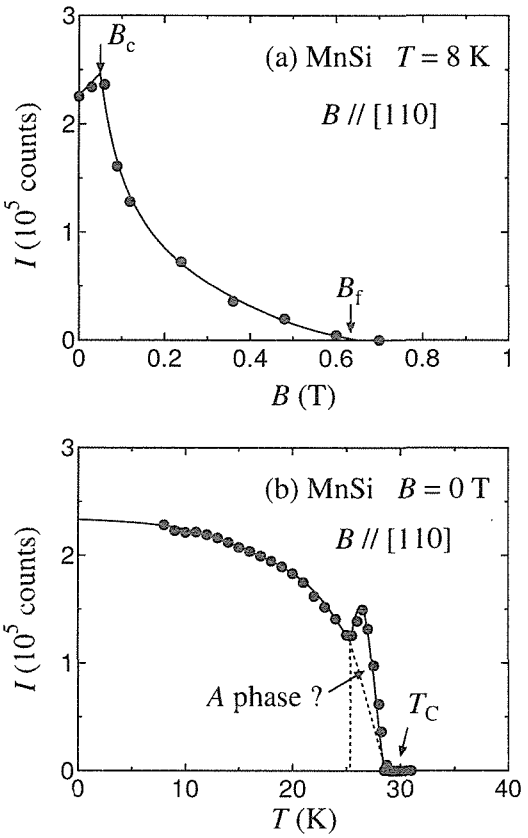

Figure 2: (a) The field dependence of the integrated intensity I of [111] satellites at T = 8 K. (b) The temperature dependence of I at B = 0 T.

Figure 1 (a) shows the magnetic field dependence of satellites spots at T = 8 K, observed by the neuton diffraction measurements. At B = 0 T, the main four satellite appears in the $\langle 111 \rangle$ direction. At $B > 0.06$ T, the satellites begin to rotate from [111] to $[1\bar{1}0]$ direction. From magnetization measurements [4], the spin structure changes from helical to conical one at $B_c = 0.04$ T. It has been confirmed that the helical state changes into conical one at $B = B_c$ by the present neutron diffraction measurements. With increasing field, these satellite spots are gathered along $[1\bar{1}0]$ direction. Finally, $B > B_f \sim 0.6$ T, no spots are observed, as the forced ferromagnetic state is stabilized. These results are consistent with the magnetization measurements [4]. On the other hand, these [111] satellites change with increasing temperature as shown in Fig. 1 (b) at zero field. The intensity of the [111] satellites decreases with increasing temperature. At just $T_C = 29$ K, the four spots vanish completely, while a ring, which comes from fluctuation of magnetic moments, is observed. Since this ring is symmetric, spin fluctuations will be isotropic.

Figure 2 (a) and (b) show the integrated intensities I of [111] satellites with increasing field and temperature, respectively. At $B < B_c$ (the helical state), the intensity of [111] satellites increases with increasing field. In this region, the magnetic field enhances the spin diffraction along [110]. On the other hand, at $B_c < B < B_f$ (the conical state), the intensity is suppressed by increasing field. In conical region, a cone axis turns to [110] direction and the spin diffraction is suppressed. With increasing temperature it decreases monotonically up to T = 25 K. We have observed the additional peak around T = 26.5 K. This intensity peak may be connected to the anomaly of AC susceptibility near T_C [3], which is so-called "A-phase".

The present obtained results are consistent with the previous report [1]. Never the less, MnSi should be measured under high pressure up to P = 1.7 GPa where the metamagnetic transition disappears. This is very interesting study as collapse of Mn moment by the pressure will be directly observed by the neutron small-angle diffraction measurements.

References

1) Y. Ishikawa, K. Tajima, D. Bloch and M. Roth, Solid State Commum. 19 (1976) 525.
2) C. Pfleiderer, G. J. McMullan, S. R. Julian and G. G. Lonzarich, Phy. Rev. B 55 (1997) 8330.
3) C. Thessieu, C. Pfleiderer, A. N. Stepanov and J. Flouquet, J. Phys.: Condens. Matter 9 (1997) 6677.
4) M. Yamada, T. Goto and T. Kanomata, J. Alloys and Compounds (2003). *in press.*
5) T. Goto, K. Fukamichi and H. Yamada, Physca B 300 (2001) 167.

2.4.15

Neutron Diffraction Study on the Antiferroquadrupolar Order of DyB_2C_2 under the Magnetic Field

H. Yamauchi, S. Katano[1], M. Matsuda[1], K. Ohoyama, K. Indoh, H. Onodera and Y. Yamaguchi

Institute for Materials Research, Tohoku University, Sendai, Miyagi 980-8577
[1]Advanced Science Research Center, Japan Atomic Energy Research Institute, Tokai, Ibaraki 319-1195

Generally speaking, a rare earth ion has an incomplete 4f shell, and an atomic magnetic moment and a quadrupolar moment arises from the 4f electrons. The quadrupolar moment is associated asphericity of the 4f electron distribution as same as the orbital magnetic moment, and strongly couples with the spin moment by strong LS interaction.

There are two kinds of couplings between quadrupolar moments. These are ferroquadrupolar(FQ) and antiferroquadrupolar(AFQ) coupling. FQ coupling is a parallel coupling of the electron distribution, and there is no discrepancy with the magnetic interaction. In the other hand AFQ coupling means rectangular configuration of the electron distribution, and it is completely inconsistent with any magnetic interaction. Therefore we can expect novel phenomena in the situation coexisting AFQ and magnetic interactions.

Tetragonal RB_2C_2 compounds are known as in which AFQ interaction is very strong. For example, AFQ ordering temperature of DyB_2C_2 is 24.7K about one order higher than other type of AFQ ordering compounds [1]. The magnetic unit cell below the Neel temperature, 15.3K, is two times large compared with the chemical one along the c-axis, and two rare earth layers are in it perpendicular to the c-axis. The magnetic moments lie in the c-plane, and the direction oscillates as 0-70-0-70 degrees along the c-axis. This structure is considered to come from competing of AFQ and antiferromagnetic(AFM) interactions.

In the present report we mention about the observation of AFQ ordering by neutron diffraction, and we pick up the phase change depending on the temperature and magnetic field applied

parallel to [110] direction of DyB_2C_2 crystal.

Magnetic phase diagram of DyB_2C_2 is shown [1] with the magnetic field applied parallel to [110]. This phase diagram was obtained by magnetization and specific heat measurements using stationary and pulsed high magnetic field. There are four phases in the diagram. The phase I is paramagnetic and paraquadrupolar state, and the phase III is AFM and AFQ ordered state concluded from the unique magnetic structure. The phase II is thought to be AFQ ordered state, and we have examined it by observing induced magnetic moments using neutron diffraction.

Temperature dependence of integrated intensity of (0,0,1/2) reflection under magnetic field of 4 and 8T is shown in Fig.1. Result under 8T is a simple curve showing a second order transition at T_Q. On the other hand, result under 4T is somewhat complex, and it is thought to show a new phase transition in the phase II which has been suggested by Dr. Indoh [2]. The change of the intensity is consistent to the magnetic structure model obtained by the magnetization measurements.

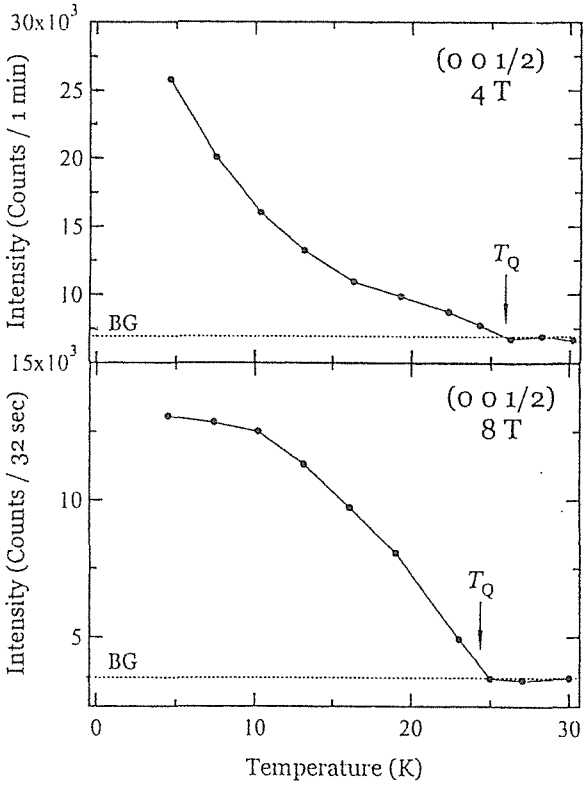

Figure 1. Temperature dependence of integrated intensity of (0,0,1/2) reflection under magnetic field of 4T (upper) and 8T (lower).

References

[1] H.Yamauchi *et al.*: J. Phys. Soc. Jpn. **68** (1999) 2057.

[2] K. Indoh, Doctor Thesis (Tohoku Univ., 2003)

2.5 Structural Physics

2.5.1

Small Angle Neutron Scattering from Superionic Conducting Glasses

H. TAKAHASHI, T. OGIHARA, T. SAKUMA[1], Y. ISHII[2] and J. SUZUKI[2]

Faculty of Engineering, Ibaraki University, Hitachi 316-8511
[1]Faculty of Science, Ibaraki University, Mito, 310-8512
[2]Advanced Science Research Center, JAERI, Tokai, Ibaraki 319-1195

In the previous study, new FSDP was observed in $10AgI\text{-}3Ag_2O\text{-}2V_2O_5$ glass from the elastic neutron scattering experiment[1]. The medium range structure for superionic conducting glasses is of interest in connection with the origin of the FSDP in low-Q region.

Small-angle neutron scattering experiments were performed by the SANS-J at JRR-3. The incident neutron wavelength of 0.650 nm is employed. The scattering data was recorded in the range $0.04 \leq Q \leq 0.3$ nm^{-1} at room temperature. Obtained data was corrected from the background and then normalized using standard sample.

Figure 1 shows the SANS profiles for $nAgI\text{-}Ag_2O\text{-}V_2O_5$ glasses (hereafter referred to as n-3-2, n=0, 2, 5, 12 and 15). It is observed by X-ray diffraction that 15-3-2 glass include precipitated β-AgI crystal. SANS profile for 15-3-2 is clearly different from those for samples within glass forming region. Sub-figure (a) indicates the composition dependence of relative intensity at q=0.1 nm^{-1}. The intensity decreases with AgI concentration within glass forming region and then increases at AgI-precipitated composition. It is well known that the host glass network has the density fluctuation. The density fluctuation occurs from the interstitial void, which is built up by cross-linked or folded VO_4 polymeric chains. Doped-AgI is incorporated into the interstitial void. As a result, apparent density fluctuation is considered to reduce with AgI content. It is considered that the reduction of density fluctuation with AgI concentration leads to the decrease of SANS intensity. On the other hand, the increase of SANS intensity beyond the glass forming range would result from the formation of the crystalline phase. The normalized intensity divided by the SANS intensity for AgI-free glass is shown in the sub-figure (b). The normalized intensity for 15-3-2 glass increases above 0.1 nm^{-1}. It is natural to connect this behavior with crystallization process. Similar trend, however, seems to appear at 5-3-2 glass. In order to clarify the medium range order accompanied by crystallization, it is necessary to investigate the SANS study for the composition at around glass forming limit in the higher q range.

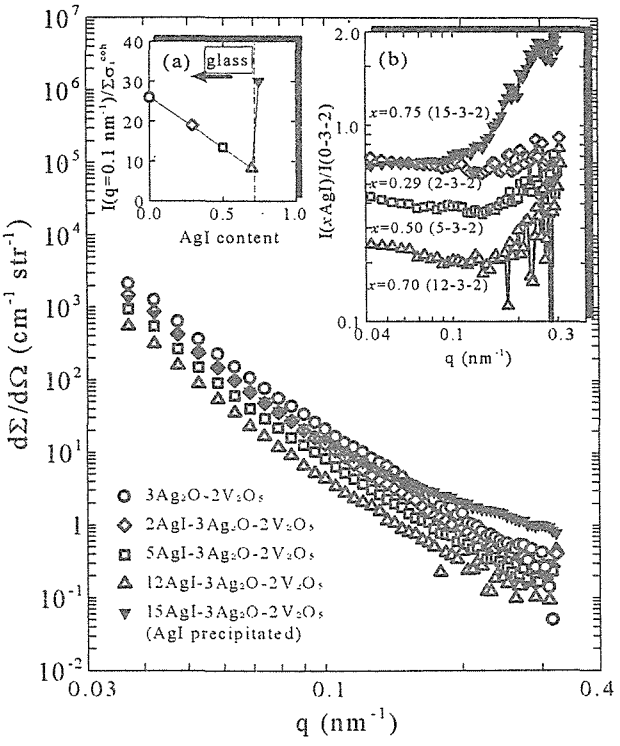

Figure 1: SANS profiles for several AgI concentration of silver vanadate glasses.

References

1) H. Takahashi, N. Rikitake, T. Sakuma and Y. Ishii : J. Non-Cryst. Solids, to be published.

2.5.2

Neutron diffraction and X-ray absorption study of silver-lead oxide $Ag_5Pb_2O_6$ synthesized from fused nitrates

K. YOSHII, H. ABE[1], M. MIZUMAKI[2], A. NAKAMURA[3], Y. SHIMOJO[3], Y. ISHII[3], Y. MORII[3], K. KATO[2], T. URUGA[2]

Synchrotron Radiation Research Center, Japan Atomic Energy Research Institute (JAERI), Mikazuki, Sayo-gun, Hyogo, 679-5148
[1]National Institute for Materials Science, Tsukuba, Ibaraki 304-0047
[2]Japan Synchrotron Radiation Research Institute, Mikazuki, Sayo-gun, Hyogo, 679-5198
[3]Advanced Science Research Center, JAERI, Tokai, Ibaraki, 319-1195

A silver-lead oxide $Ag_5Pb_2O_6$ shows metallic conductivity below room temperature.[1)] The crystal structure of this material is a trigonal type of $P\text{-}31m$, which has a two-dimensional Ag layer and a Pb_2O_6 network. The origin of the metallic conductivity has been discussed from the two different viewpoints. Jansen *et al.* proposed a valence formula of $Ag^{1+}{}_5Pb^{4+}{}_2O^{2-}{}_6(e^-)$, which means that a free excessive electron per unit formula leads to the conductivity.[1)] On the other hand, a tight-binding calculation suggested that the valence formula could be expressed as $[Ag_5]^{4+}Pb^{4+}{}_2O^{2-}{}_6$.[2)] The Fermi energy lies in a half-filled band consisting mostly of silver-*s* orbitals.

This material has been synthesized by a solid-state reaction under high-pressure oxygen. Recently, we reported that single crystals of this material can be grown in the fused mixture of nitrates at an ambient pressure.[3)] The formation of $Ag_5Pb_2O_6$ was observed from X-ray diffraction. In the present study, neutron diffraction and X-ray absorption measurements were carried out to obtain further information on the structural details and the valence state of each ion. Neutron diffraction experiments were conducted with a high resolution powder diffractometer (HRPD) at the JRR-3 reactor. X-ray absorption measurements were carried out using synchrotron radiation at the BL01B1 beamline of SPring-8.

Figure 1 shows the neutron diffraction patterns at room temperature. It was found that the experimental pattern could be fitted to the $P\text{-}31m$ structure by the Rietveld analysis (RIETAN-2000) with an almost stoichiometric oxygen content. The structural parameters such as bond lengths were well close to those reported previously.[1)] Thus, $Ag_5Pb_2O_6$ is actually synthesized by the present method. From a preliminary analysis, almost the same structural parameters have been obtained from the X-ray absorption data. The absorption measurements showed also that the valence of Ag is nearly +1, while that of Pb stands between +3 and +4. This result implies that atomic orbitals of Pb play an important role in the conductivity.

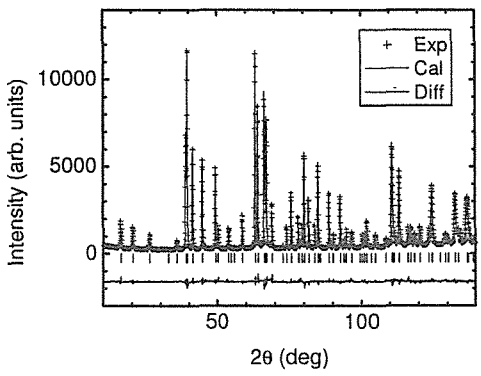

Figure 1: Neutron powder diffraction patterns of $Ag_5Pb_2O_6$ at room temperature.

References

1) M. Jansen *et al.*: L. Less-Common Met. **161** (1990) 17.
2) T. D. Brennan and J. K. Burdett: Inorg. Chem. **33** (1994) 4794.
3) H. Abe *et al.*: J. Cryst. Growth **241** (2002) 347.

2.5.3

Correlation among thermal displacements of atoms in crystalline AgCl

M. ARAI, A. THAZIN, Y. FUJISHIMA, T. SAKUMA, H. TAKAHASHI[1] and Y. ISHII[2]

Faculty of Science, Ibaraki University, Mito, Ibaraki 310-8512
[1]Faculty of Engineering, Ibaraki University, Hitachi, Ibaraki 316-8511
[2]Advanced Science Research Center, JAERI, Tokai, Ibaraki 319-1195

The diffuse scattering in solid electrolytes has been investigated by X-ray and neutron diffraction measurement[1, 2]. In case of the large thermal atomic vibration, the diffuse scattering intensities become large and show oscillatory form. The oscillatory diffuse scattering is explained by correlation effects between the thermal displacements of atoms.

Neutron scattering measurements were carried out for a powder AgCl from 10 K to 260 K in a cryostat using HRPD at JRR-3 in JAERI. The powder sample was contained in a vanadium container with 10 mm in diameter. The incident neutron wave length of 1.823 Å was used. Neutron diffraction data were collected for 1 d at 0.05° intervals over the 2θ range of 20° to 150°. Several sharp Bragg lines and a large oscillatory diffuse scattering were observed at 260 K. However the oscillatory characteristic in the diffuse scattering at 10 K is not clear. The values of thermal parameter at 260 K are larger than those at 6 K. The diffuse scattering intensity depends on thermal vibration parameter.

The observed powder diffraction intensities of AgCl at 260K are shown by broken line in Fig. 1. Solid line shows the calculated diffuse scattering intensities. Observed diffuse scattering has an oscillatory form and the peaks appear in the position of $2\theta \sim 35$, 60 and 100°. Diffuse scattering intensities calculated by the correlation effect between the thermal displacements of atoms showed similar oscillatory form, and the peaks appeared in the same positions as those of observed data.

The peaks of $2\theta \sim 60$ and 100° are based on thermal correlation between the first nearest neighboring atoms (Ag-Cl). The main contribution to the oscillatory diffuse scattering is from the correlation among the displacements of first nearest neighboring atoms. The peak of $2\theta \sim 35°$ is the influence of the correlation effect between the second nearest neighboring atoms (Ag-Ag, Cl-Cl). The value of correlation between the first nearest neighboring atoms is about 0.8 and the correlation between the second nearest neighboring atoms about 0.5. If the interatomic distances become greater than that of the third nearest neighboring atom, the values of correlation become less than 0.1, and most influences on diffuse scattering are not observed. The value of thermal correlation decreases rapidly with the interatomic distance.

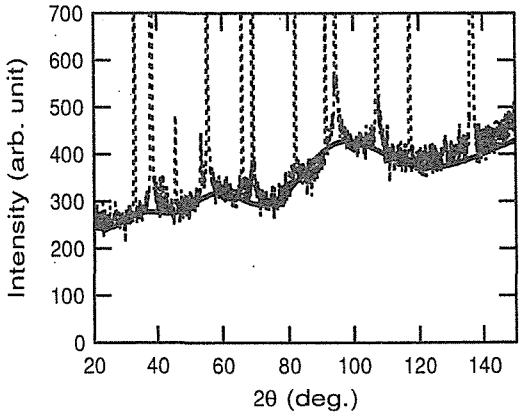

Figure 1: Observed neutron powder diffraction intensity (broken line) and calculated diffuse scattering intensity (solid line) for AgCl at 260 K.

References

1) T. Sakuma: J. Phys. Soc. Jpn. **42** (1993) 4150.
2) T. Sakuma, Y. Nakamura, M. Hirota, M. Arai and Y. Ishii: J. Phys. Chem. Solids **60** (1999) 1503.

2.5.4 Temperature dependence of diffuse scattering from crystalline Ge

M. ARAI, A. THAZIN, Y. FUJISHIMA, T. SAKUMA, H. TAKAHASHI[1] and Y. ISHII[2]

Faculty of Science, Ibaraki University, Mito, Ibaraki 310-8512
[1]Faculty of Engineering, Ibaraki University, Hitachi, Ibaraki 316-8511
[2]Advanced Science Research Center, JAERI, Tokai, Ibaraki 319-1195

Correlation effects between the thermal displacements of atoms play an important role in the superionic conductors. In addition to superionic conductors an oscillatory diffuse scattering was observed in semiconductor GaAs[1)]. In order to investigate the detailed thermal correlation among atoms at distances above second nearest neighboring atoms, diffuse neutron background intensity of Ge has been measured from 6 K to 673 K using a neutron diffractometer HRPD installed at JRR-3 in JAERI. A powder sample of Ge in a vanadium container with 10 mm in diameter was used. The incident neutron wave length of 1.83 Å was used. Neutron diffraction data were collected for 1 d over the 2θ range of 20° to 115°. Figure 1 shows the results of the measurement of Ge at 6, 290 and 673 K. Several sharp Bragg lines and a large diffuse scattering were observed except at 6 K. The oscillatory diffuse scattering from Ge crystals was confirmed by the measurement at high temperatures. The maximum intensity of the Bragg line is about 60,000. The first and second peak of the oscillatory diffuse scattering appear at 2θ~55° and 110° in Fig. 1, respectively. It is also found that small peaks of the oscillatory diffuse scattering appear at 2θ~30°, 60° and 90° at 673 K.

Numerical calculations of the diffuse background have been made based on diamond type structure including the correlation between the thermal displacements of atoms[2)]. The positions of the first and second peak in diffuse scattering of Ge in Fig. 1 at 673 K are related to the reciprocal of the distance between first nearest neighboring atoms; the distance in Ge is about 2.46 Å. The diffuse scattering intensity changes as $\sin(Qr)/Qr$. The main contribution to the oscillatory diffuse scattering was from the correlation among the displacements of first nearest neighboring atoms. The value of the thermal correlation between these Ge atoms is about 0.7.

Expected contributions from second nearest neighboring atoms in crystalline Ge to the diffuse scattering were calculated. The observed oscillatory diffuse scattering at 2θ~30°, 60° and 90° corresponded to the contribution from the correlation between the thermal displacements of the second nearest neighboring atoms. The value of the thermal correlation between these Ge atoms is less than that between first nearest neighboring atoms.

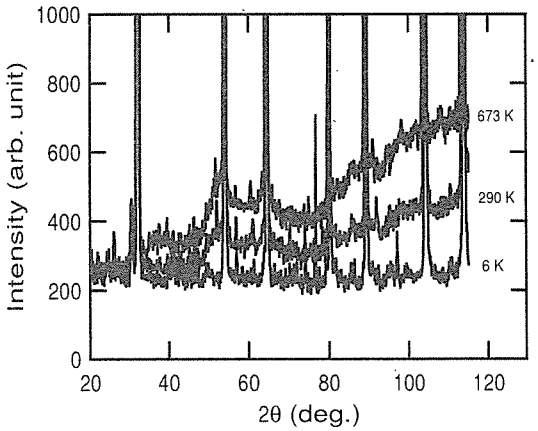

Figure 1: Observed neutron powder diffraction intensity for Ge at 6, 290 and 673 K.

References

1) M. Arai, K. Ohki, M. Mutou, T. Sakuma, H. Takahashi and Y. Ishii: J. Phys. Soc. Jpn. **70** (2001) 250.
2) T. Sakuma: J. Phys. Soc. Jpn. **42** (1993) 4150.

2.5.5 Structural Phase Transition for Ternary Iridium Oxide Pr_3IrO_7

H. Nishimine, M. Wakeshima, Y. Hinatsu, Y. Ishii[1]

Division of Chemistry, Graduate School of Science, Hokkaido University, Sapporo 060-0810
[1]Japan Atomic Energy Research Institute, Tokai-mura, Ibaraki 319-1195

Figure 1 shows the temperature dependence of specific heats for a ternary iridium oxide Pr_3IrO_7. A first order phase transition is observed at around 260 K in the $C-T$ curve.. We have considered that this anomalies was due to a strucural phase transition. The crystal structure of the high-temperature phase was determined to be an orthorhombic La_3NbO_7-type structure with space group *Cmcm* through powder X-ray diffraction measurement at room temperature.

In order to elucidate the crystal structure of the low-temperature phase, powder neutron diffraction patterns for Pr_3IrO_7 were collected at 250 K and room temperature (RT) using a High Resolution Powder Diffractometer (HRPD) in the JRR - 3M reactor with a neutron wave length (λ = 1.82268 Å). The refinements for diffraction patterns were performed by the Rietveld method.

Both of the neutron diffraction patterns were refined with space group *Cmcm*. Figure 2 shows the diffraction patterns at RT. The refinement for RT data is successful and the lattice constants and the atomic positions are in good agreement with those for XRD data (R_{wp} = 6.66 %, R_I = 2.74 %, a = 10.9782(13) Å, b = 7.4389(9) Å, c = 7.5361(9) Å). The refined structral parameters are listed in Table 1. In the diffraction pattern at 250K, however, some additional Bragg reflections which could not be fitted with *Cmcm* appear. The results for neurton diffraction measurements provide the evidence that the structural phase transition occurs at the temperature that the thermal anomaly is observed. We tried to determine the structure of the low-temperature phase. Unfortunately, we could not obtain the valuable information on its structure because the number of extra reflections is limited and their intensity is very weak as well as XRD data.

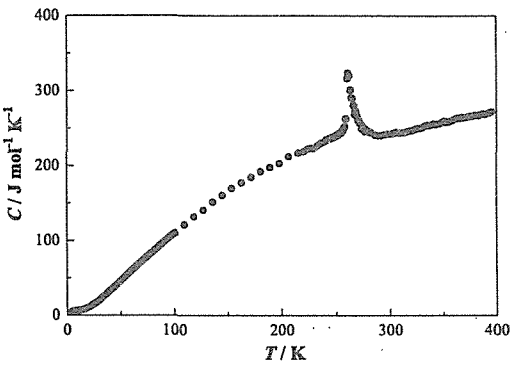

Figure 1: Temperature dependence of specific heats for Pr_3IrO_7.

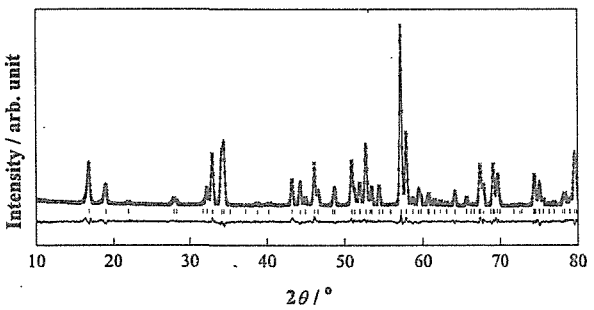

Figure 2: Powder neutron diffraction profiles for Pr_3IrO_7 at room temperature.

Table 1 Positional parameters for Pr_3IrO_7 at room temperature.

Atom	x	y	z	B(Å^2)
Pr(1)	0	0	0	0.93(8)
Pr(2)	0.2222(2)	0.3083(3)	0	0.66(6)
Ir	0	1/2	0	0.47(4)
O(1)	0.1256(1)	0.3171(2)	0.9582(2)	1.08(4)
O(2)	0.1308(2)	0.0289(3)	1/4	0.56(5)
O(3)	0	0.4098(4)	1/4	0.41(6)

2.5.6

Crystal Structure and Physical Properties of Pseudo-One-Dimensional Calcium Iridate $Ca_5Ir_3O_{12}$

M. Wakeshima, Y. Hinatsu, Y. Ishii[1]

Division of Chemistry, Graduate School of Science, Hokkaido University, Sapporo 060-0810
[1]Japan Atomic Energy Research Institute, Tokai-mura, Ibaraki 319-1195

The crystal structure of ternary oxide $Ca_5Ir_3O_{12}$ consists of infinite one-dimensional chains of the edge-sharing IrO_6 octahedra as shown in Fig. 1. This compound showed a weak ferromagnetic transition at 7.5 K through the magnetic susceptibility and specific heat measurements. Figure 2 shows the temperature dependence of the specific heats of $Ca_5Ir_3O_{12}$. In addition to the anomaly due to the magnetic ordering at 7.5 K, another λ-type anomaly which is not due to the magnetic ordering is observed at 105 K.

In order to elucidate the anomaly at 105 K, powder neutron diffraction patterns for $Ca_5Ir_3O_{12}$ were collected at 90 and 120 K using a High Resolution Powder Diffractometer (HRPD) in the JRR - 3M reactor with a neutron wave length ($\lambda = 1.82268$ Å). The refinements for diffraction patterns were performed by the Rietveld method.

The neutron diffraction profiles of $Ca_5Ir_3O_{12}$ at 90 and 120 K could be indexed in a hexagonal unit cell with space group of $P\bar{6}2m$. No difference between two diffraction profiles was observed and the Rietveld analyses of these diffraction data were performed by applying the same space group ($a = 9.3472(5)$Å, $c = 3.1710(1)$Å at 90 K, $a = 9.3490(5)$Å, $c = 3.1713(1)$Å at 120 K). The refined crystallographic parameters are listed in Table 1. The positional parameters, calculated bond lengths and bond angles at 90 and 120 K agree within the experimental error. If the anomaly at 105 K is due to only the local translation without transformations of the unit cell, such as a rotation of the IrO_6 octahedron, it is difficult to detect such as a change in the crystal structure by the powder diffraction technique because of the overlap of the reflection intensities.

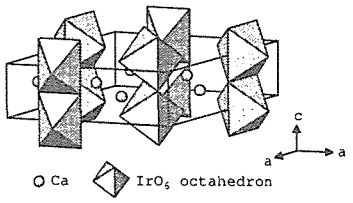

Figure 1: Schematic crystal structure of $Ca_5Ir_3O_{12}$.

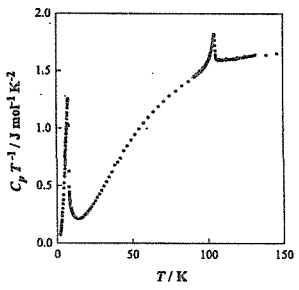

Figure 2: Temperature dependence of specific heats for $Ca_5Ir_3O_{12}$.

Table 1 Positional parameters for $Ca_5Ir_3O_{12}$ at 90 and 120 K.

Atom	x	y	z	B(Å^2)
90 K				
Ca(1)	1/3	2/3	1/2	0.18(17)
Ca(2)	0.7127(8)	0	1/2	0.18
Ir	0.3330(3)	0	0	0.43(8)
O(1)	0.2006(6)	0	1/2	0.59(8)
O(2)	0.4617(7)	0	1/2	0.59
O(3)	0.4460(5)	0.2407(4)	0	0.59
120 K				
Ca(1)	1/3	2/3	1/2	0.20(17)
Ca(2)	0.7131(9)	0	1/2	0.20
Ir	0.3334(3)	0	0	0.35(8)
O(1)	0.2008(6)	0	1/2	0.74(8)
O(2)	0.4620(6)	0	1/2	0.74
O(3)	0.4459(5)	0.2407(4)	0	0.74

2.5.7 Crystal Structure of Perovskite $Ba_3Tb_2WO_9$

S. OYAMA, Y. DOI, Y. HINATSU and Y. ISHII[1]

Division of Chemistry, Graduate School of Science, Hokkaido University, Sapporo 060-0810
[1]Advanced Science Research Center, JAERI, Tokai, Ibaraki 319-1195

Quaternary oxides $Ba_3Ln_2WO_9$ (Ln = lanthanides) have a perovskite-type (ABO_3) structure. The Ln and W ions adopt a disordered arrangement in the B sites. The lattice parameters increase monotonically with the Ln^{3+} ionic radius. However, lattice parameters for $Ba_3Tb_2WO_9$ deviate greatly from this tendency. In addition, only this compound shows a reflection at $2\theta \sim 18°$ in the x-ray diffraction pattern, which indicates the B-site ordering.

In order to determine the detailed crystal structure for $Ba_3Tb_2WO_9$, powder neutron diffraction pattern was measured at room temperature using a High Resolution Powder Diffractometer (HRPD) at the JRR-3M reactor with a neutron incident wave length (λ = 1.82301 Å).

Figure 1 shows the observed and calculated diffraction patterns. The crystal structure was refined by applying the space group $P2_1/n$ (a =6.0059(4) Å, b = 6.0134(3) Å, c = 8.4931(7) Å, and β = 90.173(9)°). The structural parameters are listed in Table 1. The result of Rietveld analysis indicates that $Ba_3Tb_2WO_9$ is a 1:1 ordered compound, i.e., one of the B sites is fully occupied by Tb, whereas the other contains 2/3W and 1/3Tb with a random distribution. The crystal structure of $Ba_3Tb_2WO_9$ is illustrated in Fig.2. The Tb and W ions are alternatively arranged between Tb and (1/3Tb + 2/3W), and that this has a rock salt sublattice. Therefore, this compound should be described as $Ba_2Tb(Tb_{1/3}WO_{2/3})O_6$.

Table 1: Structural parameters for $Ba_3Tb_2WO_9$.

Atom	Site	g	x	y	z
Ba	4e	1.0	0.520	0.503	0.247
Tb(1)	2d	1.0	0	1/2	0
Tb(2)	2c	0.333	1/2	0	0
W	2c	0.667	1/2	0	0
O(1)	4e	1.0	0.235	0.233	-0.022
O(2)	4e	1.0	0.241	0.777	-0.018
O(3)	4e	1.0	0.479	-0.004	0.231

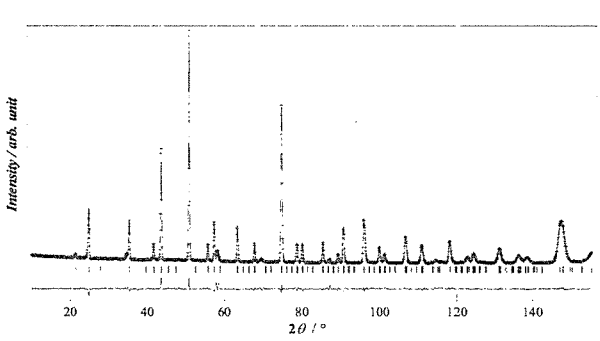

Figure 1: Powder neutron diffraction pattern of $Ba_3Tb_2WO_9$ at room temperature.

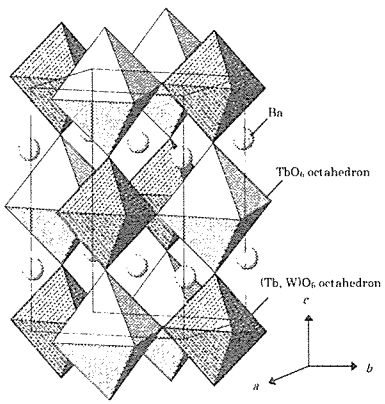

Figure 2: The crystal structure of $Ba_3Tb_2WO_9$.

2.5.8 Lattice dynamics of tetragonal $PbTiO_3$

I. TOMENO, Y. ISHII[1] and Y. TSUNODA[2]

Faculty of Education and Human Studies, Akita University, Akita 010-8502
[1]Neutron Science Research Center, JAERI, Tokai, Ibaraki 319-1195
[2]School of Science and Engineering, Waseda University, Shinjuku-ku, Tokyo 169-8555

$PbTiO_3$ undergoes only a single phase transition from a cubic paraelectric to tetragonal ferroelectric phase at T_C=763 K. The donation of 10 % Ti atoms to $Pb(Zn_{1/3}Nb_{2/3})O_3$ gives rise to a huge piezoelectric effect. Thus $PbTiO_3$ is the mother material of the relaxor $Pb(Zn_{1/3}Nb_{2/3})O_3$.

Figure 1 depicts the phonon dispersion relations along the [110] direction at room temperature. The bars refer to the FWHM obtained from Gaussian fits to the constant-Q or constant-E scans. The dashed lines are sound velocities determined by Brillouin scattering measurements. [1] The slope for each TA phonon branch around the Γ point is in good agreement with the sound velocity data. [1] The high-frequency phonon at Γ correspond to the A_1 TO mode, and the low-frequency phonon corresponds to the E TO mode. These results are consistent with the dielectric constant relation $\epsilon_{11} > \epsilon_{33}$ at room temperature, [1] in view of the Lyddane-Sacks-Teller relation. The zone-center TO phonon frequencies are in good agreement with the data determined by Raman scattering experiments. [2] The FWHM for the Σ_1 TO phonon around the zone center is extremely broader than that for the Σ_2 TO phonon. Similar tendency has been pointed out by the Raman scattering measurements. [2] The A_1 TO phonon behaves as the well-defined soft mode near T_C. [3] The origin of the broad width for the A_1 TO mode is still controversial. [4] We are planning an inelastic-neutron-scattering study at high temperatures.

References

1) Z. Li, M.Grimsditch, C.M.Foster and S.-K. Chan : Ferroelectrics **141** (1992) 313.
2) C.M.Foster, Z. Li, M.Grimsditch, S.-K. Chan and D.J. Lam : Phys.Rev. B **48** (1993) 10160.
3) G. Shirane, J. D. Axe, J. Harada and J. P. Remeika : Phys. Rev. B **2** (1970) 155.
4) S. M. Cho, H. M. Jang and T.-Y. Kim : Phys. Rev. B **64** (2001) 014103.

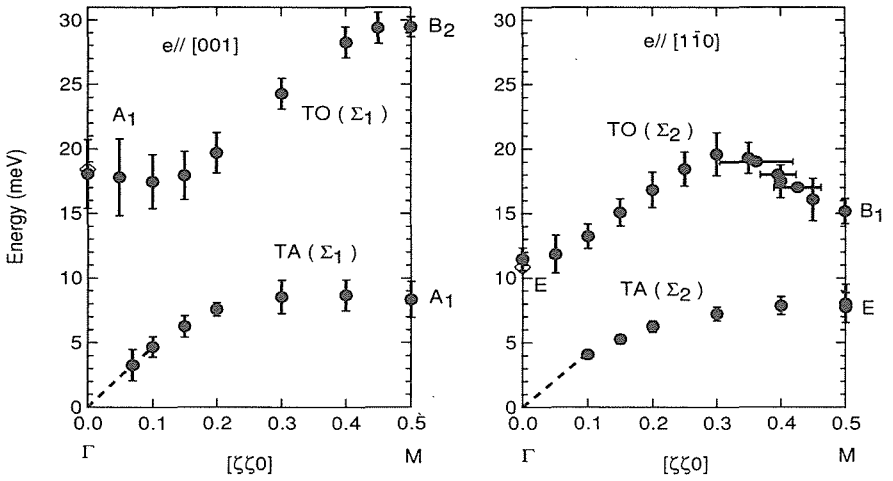

Figure 1: Phonon dispersion relations for $PbTiO_3$.

2.5.9

Direct Extraction of Hydrogen Atoms in the Crystal Structure Analysis of Synthetic Polymers by Utilizing 2-Dimensional Neutron Imaging Plate System

K.TASHIRO, N.NIIMURA[1,2], I.TANAKA[1] and S.FUJIWARA[1]

Graduate School of Science, Osaka University, Osaka 560-0043
[1]Advanced Science Research Center, JAERI, Tokai, Ibaraki 319-1195
[2]Faculty of Engineering, Ibaraki University, Hitachi, Ibaraki 316-8511

In order to clarify the relation between structure and mechanical property of polymer crystals in a quantitative manner, we need to know the exact atomic positions in the crystal lattices, in particular the positions of hydrogen atoms. Unfortunately, however, there had been almost no trial to reveal the hydrogen atom positions as exactly as possible for the synthetic polymer materials because of poor x-ray diffraction data in general compared with the cases of low-molecular-weight compounds. In the previous paper[1)] we succeeded in extract the hydrogen atoms by calculating the Fo-Fc Fourier map based on the X-ray imaging-plate system. But we may expect to obtain the hydrogen atom positions in more exact and direct manner by taking the 2-dimensional neutron diffraction patterns of the deuterated polymer materials through the neutron imaging plate system.[2)] This is a report about the first success of direct extraction of hydrogen atoms of synthetic polymer crystals by measuring the 2-dimensional neutron fiber diagrams.

Figure1 shows the 2-dimensional neutron fiber diagrams taken for the uniaxially-oriented samples of fully-deuterated (D) and totally-hydrogeneous (H) polyethylenes, which were measured by using a JAERI BIX-3 system. In this figure are also shown the neutron fiber diagrams predicted for D and H polyethylene crystals (see Fig. 2), which give good correspondence with the actually observed patterns. By evaluating the inte-

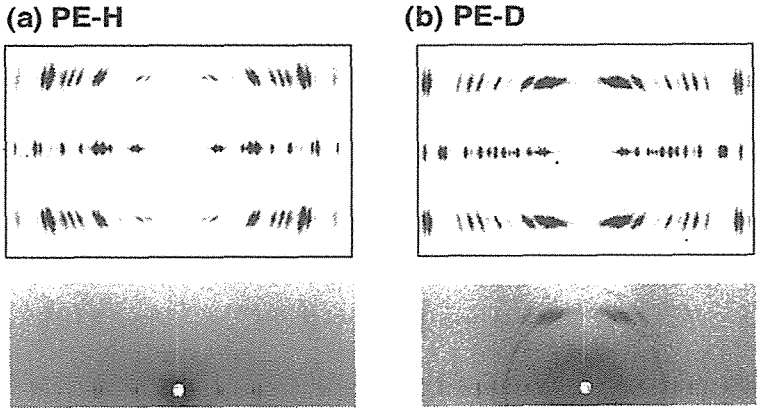

Figure 1: Neutron fiber diagrams of uniaxially-oriented (a) H and (b) D polyethylene samples.

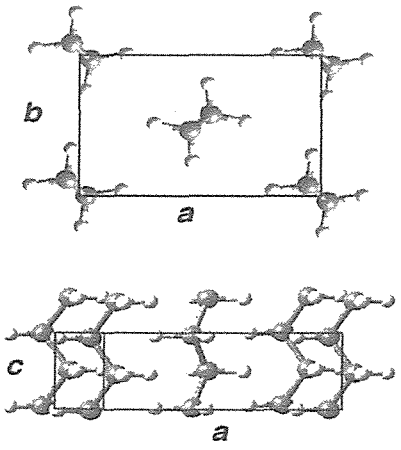

Figure 2: Crystal structure of orthorhombic polyethylene.

grated intensities of the observed reflections, the Fourier map was calculated for the D sample. Different from the X-ray structure analysis, where only the carbon atoms were found as shown in Fig. 3 (b), the neutron fiber diagram of the D sample allowed us to extract the hydrogen atoms quite clearly and directly as seen in Fig. 3 (a). We are now refining the crystal structure by using the thus extracted hydrogen (and carbon) atom positions.

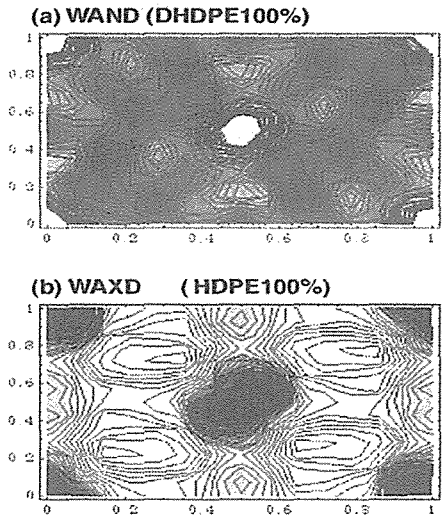

Figure 3: Fourier maps calculated from (a) WAND data of deuterated polyethylene and (b) WAXD data of normal polyethylene. Refer to Fig. 2.

Figure 4 shows the neutron equatorial diffraction patterns measured for a series of random copolymers between D and H ethylene monomeric units. With a change in the relative content of the deuterated component, the diffraction pattern changed systematically. This systematic change can be reproduced reasonably and quantitatively by assuming statistically random arrangement of the D and H units in the crystal lattice. This is consistent with the infrared spectral data showing a systematic change in the band splitting width due to the vibrational correlation between the adjacent chain stems.[3)]

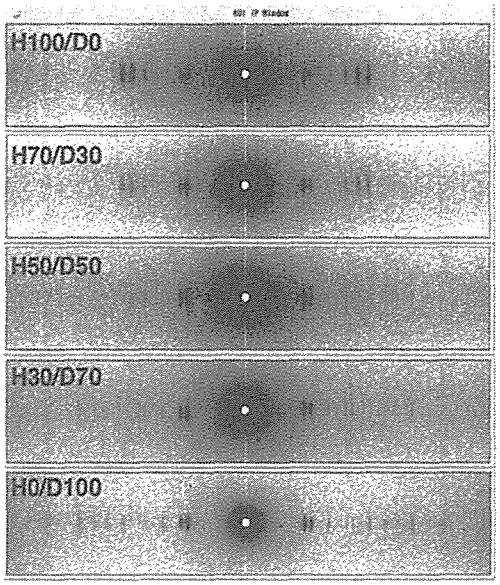

Figure 4: Neutron fiber diagrams (equatorial line) measured for a series of uniaxially-oriented D/H random ethylene copolymers .

References

1) K. Tashiro, H. Asanaga, K. Ishino, R. Tazaki, and M. Kobayashi, J. Polym. Sci.: Part B: Polym. Phys. **35** (1997) 1667.
2) N. Niimura, Y. Karasawa, I. Tanaka, J. Miyahara, K. Takahashi, H. Saito, S. Koizumi, and M. Hidaka, Nucl. Instrum. Meth. Phys. Res. A. **349** (1994) 521.
3) K. Tashiro, M. Sato, Y. Cho and M. Kobayashi, Polym. Prepr. Jpn. **48** (1999) 3574.

2.5.10 Modulated Structure of the Composite Crystal $(Ca_{0.80}Y_{0.20})_{0.82}CuO_2$

Y. MIYAZAKI, Y. ISHII[1], Y. MORII[1] and T. KAJITANI

Department of Applied Physics, Tohoku University, Sendai 980-8579
[1]Advanced Science Research Center, JAERI, Tokai, Ibaraki 319-1195

Quasi one-dimensional (1D) cuprate $(Ca_{1-x}Y_x)_{0.82}CuO_2$ [1,2] has recently attracted much attention owing to its unique magnetic properties. The crystal structure, on the other hand, has not yet been satisfactorily determined except for the terminal compounds. In this report, we present the crystal structure of the compound with $x = 0.20$ on the basis of a four-dimensional superspace group approach using powder neutron diffraction data.

Neutron powder diffraction (ND) data were collected at 293 K by means of HRPD diffractometer installed at the JRR-3M reactor in JAERI. The ND data were analyzed using a Rietveld refinement program PREMOS 91 [3] designed for modulated structure analyses. The superspace group of $F2/m(1+\alpha\ 0\ \gamma)0s$ was adopted.

Figure 1 shows the observed, calculated and difference profiles for the ND data. Short vertical lines below the patterns indicate the peak positions of main (upper) and satellite (lower) reflections for the two subsystems. A satisfactorily good fit was achieved and the final R_{WP} factor was 12.8 %.

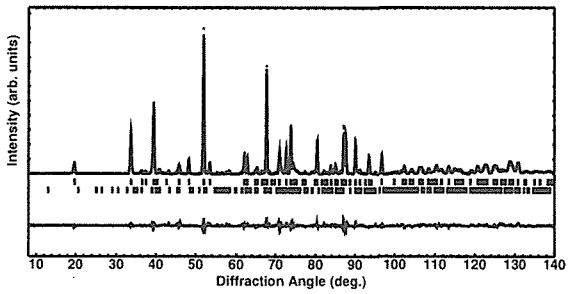

Figure 1: Observed, calculated and difference patterns of the powder neutron diffraction data for $(Ca_{0.80}Y_{0.20})_{0.82}CuO_2$ measured at 293 K.

Figure 2 shows the refined modulated structure viewed in perspective from the a-axis. The compound consists of mutually interpenetrating $[Ca_{0.80}Y_{0.20}]$ subsystem and edge-shared 1D $[CuO_2]$ chains, being incommensurate parallel to the a-axis. Lattice parameters were refined to be $a_1 = 2.8165(2)$ Å, $b = 6.2595(2)$ Å, $c = 10.5603(5)$ Å and $\beta = 90.06(1)°$. One can recognize markedly waved rows of the CuO_2 ribbons. The Cu atom sites are found to fluctuate larger than that of $x = 0.435$ sample but much smaller than that of $x = 0$ sample.

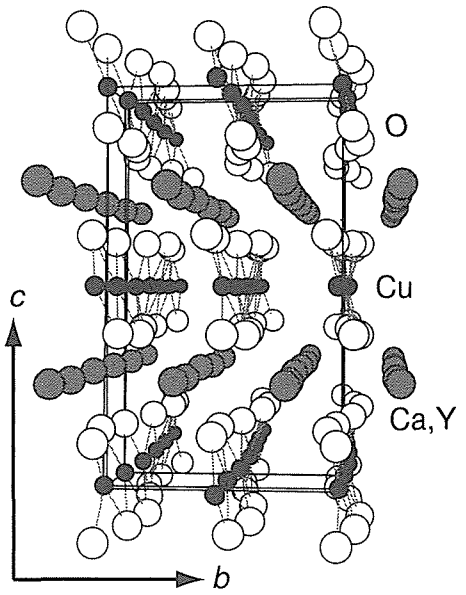

Figure 2: The refined fundamental structure of $(Ca_{0.80}Y_{0.20})_{0.82}CuO_2$ projected in perspective from the a-axis.

References

1) A. Hayashi *et al.*: Phys. Rev. B **58** (1998) 2678.
2) Y. Miyazaki *et al.*: Chem. Eur. J. **5** (1999) 2265.
3) A. Yamamoto: Acta Crystallogr. A **49** (1993) 831.

2.5.11

Modulated Structure of the Composite Crystal $[Ca_2(Co_{0.65}Cu_{0.35})_2O_4]_{0.63}CoO_2$

Y. MIYAZAKI, Y. MIURA, M. ONODA[1], Y. ISHII[2], Y. ONO, Y. MORII[2] and T. KAJITANI

Department of Applied Physics, Tohoku University, Sendai 980-8579
[1]Advanced Materials Laboratory, NIMS, Tsukuba, Ibaraki 305-0044
[2]Advanced Science Research Center, JAERI, Tokai, Ibaraki 319-1195

Misfit-layered cobalt oxides have recently attracted much attention as potential candidates for thermoelectric (TE) materials. We have discovered a new layered compound in the Ca-Co-Cu-O system and the compound also exhibits excellent TE properties. In this report, we present the structure analysis of the compound on the basis of a four-dimensional superspace group approach using powder neutron diffraction data.

Neutron powder diffraction (ND) data were collected at 293 K by means of HRPD diffractometer installed at the JRR-3M reactor in JAERI. The ND data were analyzed using a Rietveld refinement program PREMOS 91 [1)] designed for modulated structure analyses. The superspace group of $C2/m(1\ p\ 0)s0$ was adopted on the basis of the observed systematic absences.

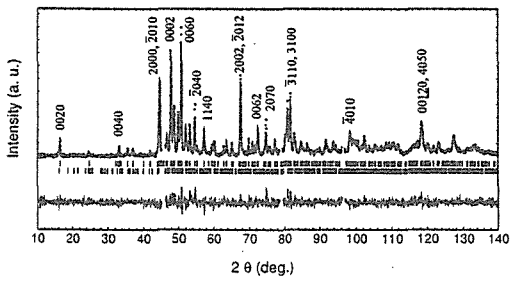

Figure 1: Observed, calculated and difference patterns of the powder neutron diffraction data for $[Ca_2(Co_{0.65}Cu_{0.35})_2O_4]_{0.63}CoO_2$ measured at 293 K.

Figure 1 shows the observed, calculated and difference profiles for the ND data. Short vertical lines below the patterns indicate the peak positions of main (upper) and satellite (lower) reflections for the two subsystems. A satisfactorily good fit was achieved and the final R_{WP} factor was 8.1 %. The structure formula was expressed as $[Ca_2(Co_{0.65}Cu_{0.35})_2O_4]_{0.63}CoO_2$.

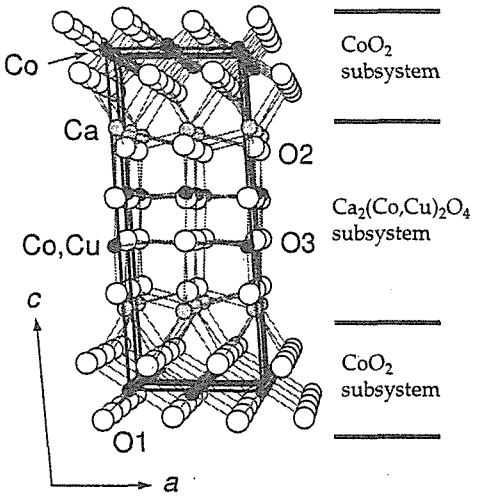

Figure 2: The refined fundamental structure of $[Ca_2(Co_{0.65}Cu_{0.35})_2O_4]_{0.63}CoO_2$ projected in perspective from the b-axis.

Figure 2 shows the fundamental structure viewed in perspective from the b-axis. The structure consists of a CoO_2 sheet (subsystem 1) and an ordered four-layered NaCl-type $Ca_2(Co_{0.65}Cu_{0.35})_2O_4$ block (subsystem 2), stacked parallel to the c-axis. The CoO_2 sheet is composed of edge-shared CoO_6 octahedra forming a triangular lattice as seen in the CdI_2-type structure. Lattice parameters were refined to be $a = 4.8212(4)$ Å, $b_1 = 2.8103(3)$ Å, $b_2 = 4.4915(3)$ Å, $c = 12.7671(8)$ Å and $\beta = 93.93(1)°$. The Cu^{2+} ions appear to play an important role to stabilize such a four-atom thick subsystem in this compound.

References

1) A. Yamamoto: Acta Crystallogr. A **49** (1993) 831.

2.5.12 Determination of the Structure of a Molecular Ice that Forms within a Molecular Cage

M. YOSHIZAWA, T. KUSUKAWA, M. KAWANO, M. FUJITA, T. OHHARA[1], I. TANAKA[1], K. KURIHARA[1] and N. NIIMURA[1]

Dept. of Applied Chemistry, The University of Tokyo and CREST, JST, Tokyo 113-8656
[1]Advanced Science Research Center, JAERI, Tokai, Ibaraki 319-1195

Self-assembly of molecules is an essential feature of natural process controlled by weak interactions between molecules, and recently becomes an important synthetic methodology in organic and inorganic chemistry.[1)2)] In nature, one of the simplest but indispensable self-assemblies can be found in water clusters that form by hydrogen bonding interactions.[2)] Though there have been extensive studies on bulk water by experimental and theoretical approaches, the microscopic phenomena of small water clusters ($(H_2O)_n$, $n =\sim 10$) remain poorly understood because of their dynamic nature and low stability.[3)4)] Among them, we are interested in the character of water that is its preferential orientation in the hydration shell of non-polar solutes by hydrophobic interactions. We expect that if an isolated hydrophobic cavity is provided in an aqueous medium, the formation of discrete water networks can be found in the cavity. Accordingly, we have recently found the formation of a cluster of ten water molecules, $(H_2O)_{10}$, in a hydrophobic cavity of the self-assembled coordination cage (**1**).[5)] In the crystal structure of **1** with the $(H_2O)_{10}$ cluster, water oxygens can be located displaying adamantanoid framework (a static fundamental unit of ice Ic; **2**) but water hydrogen's are missing. The determination of hydrogen positions are, however, particularly important to understand how the cavity recognizes the cluster. Thus, in the present study, we examine neutron diffraction analysis for the complex to clarify the structure of the water cluster and the host-guest interaction.

A single crystal neutron diffraction measurement of the cage complex **1** with H_2O molecules was examined by BIX-4 diffractometer sited on the JRR-3 reactor at JAERI. The crystal size was 3.5x3.5x2.0 mm^3. 325 oscillation images ($\Delta\omega = 0.6°$) were obtained by 13 days measurement. As a result of data processing, the cell parameters were $a = 30.884(3), b = 30.884(3), c = 29.831(4)$, the space group was $P4_32_12$, and the number of unique reflections was 2456. The structure analysis is now progress.

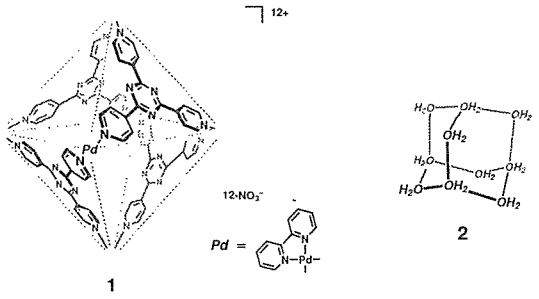

Figure 1: The self assembled coordination cage with water cluster.

References

1) Lehn J. -M. *Supramolecular Chemistry: Concept and Perspectives* (VCH, Weinheim, 1995).
2) Ball P. *H_2O: A Biography of Water* (Weidenfeld Nicolson, London 1999).
3) Ludwig R. *Angew. Chem. Int. Ed.* **40**, 1808-1827 (2001).
4) (a) Barhour L. J., Orr G. W. Atwood J. L. *Nature* **393**, 671-673 (1998). (b) Muller A., Fedin V. P., Kuhlmann C., Bogge H. Schmidtmann M. A. *Chem. Commun.* 927-928 (1999). (c) Wyndham B. B., Scott W., Gordon-Wylie George R. C., Kenneth D. J., John T. W., Urs. G., Terrence, J. C. *J. Am. Chem. Soc.* **121**, 3551-3552 (1999).
5) Fujita, M., Oguro, D., Miyazawa, M., Oka, H., Yamaguchi, K. Ogura, K. *Nature* **378**, 469-471 (1995).

2.6 Materials Science and Industrial Applications

2.6.1

Crystal Structure Study on Defective Silicalite by Neutron Diffraction

T. Suzuki, M. Inui, K. Sugita and Y. Ishii[1]

Basic Chemicals Research Lab., Sumitomo Chemical Co., Ltd., Sobiraki, Niihama, 792-5821
[1]ASRC, Japan Atomic Energy Research Institute, Tokai, Ibaraki 319-1195

Zeolites are used in the industry as catalysts. Performance of catalysts is strongly related to the crystal structure and the concentration of point defects in the zeolite crystal, because the point defects in the crystal often behave as active sites for reaction. Artioli *et al.*[1)] determined the crystal structure of silicalite by neutron diffraction experiments. However, information for concentration of the defect is insufficient. Therefore we study the crystal structure and defect concentration of silicalite with neutron diffraction measurements.

Silicalite powder samples were stirred in D_2O water at 353 K for H-D exchange. IR measurement of this sample was carried out for checking the H-D exchange. After this checking the fully deuterated sample was dehydrated at 673 K under He-gas flow. The sample was sealed in a special vanadium tube without air exposure. The neutron powder diffraction pattern of the deuterated silicalite sample was observed with the High-Resolution Powder Diffractometer (HRPD) installed at the JRR-3 in JAERI.

Measurements were carried out at low temperature of 3.5 K in order to minimize the diffraction effect due to thermal vibration of atoms. Data were collected between 5° and 155° in diffraction angle with an equal step of 0.05°. The diffraction data were refined by Rietveld method using the RIETAN-2000 software program.

Rietveld refinement of deuterated silicalite is shown in Fig.1. Lattice parameters were refined to be a=19.8342(8)Å, b=20.1031(8)Å, c=13.3658(5)Å and β = 90.952(2)°. The determination of Si T-site occupancy was very difficult because monoclinic phase has too many parameters.

References

1) G. Artioli, C. Lamberti and G. L. Marra: Acta Cryst. **B56** (2000) 2-10.

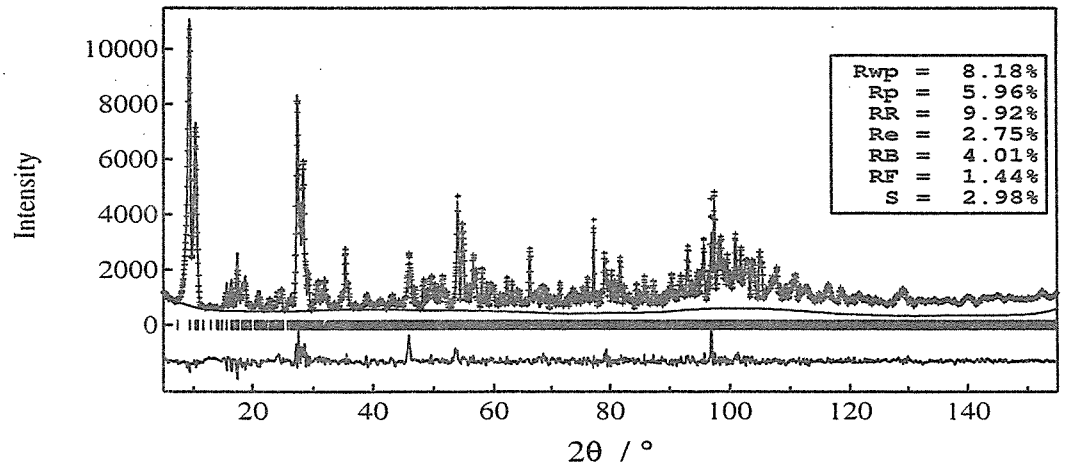

Figure 1: After refinements of deuterated silicalite measured at 3.5 K.

2.6.2 Deuterium Migration Mechanism in Chiral Thiolactam Formation by Neutron Diffraction Analysis

T. HOSOYA, H. UEKUSA, Y. OHASHI, T. OHHARA,[1] I. TANAKA[2] and N. NIIMURA[2]

Department of Chemistry and Materials Science, Tokyo Institute of Tech., Tokyo 152-8550
[1]Institute of Materials Structure Science, HEARO (KEK), Tsukuba, Ibaraki 305-0801
[2]Advanced Science Research Center, JAERI, Tokai, Ibaraki 319-1195

The molecule of *N,N*-dibenzyl-1-cyclohexenecarbothioamide, **1a**, was photoisomerized to 1-benzyl-4-phenyl-2-thioxoazetidine-3-spirocyclohexane, **2a**, in high optical yield.[1)] From the crystal structure analyses of the reactant and product crystals by X-rays, the mechanism of the asymmetric induction was proposed.

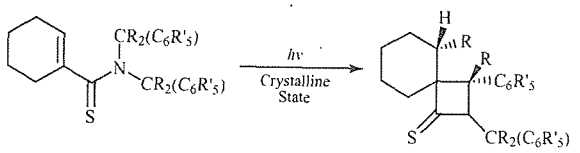

1a: R=R'=H
1b: R=D, R'=H
1c: R=R'=D

2a: R=R'=H
2b: R=D, R'=H
2c: R=R'=D

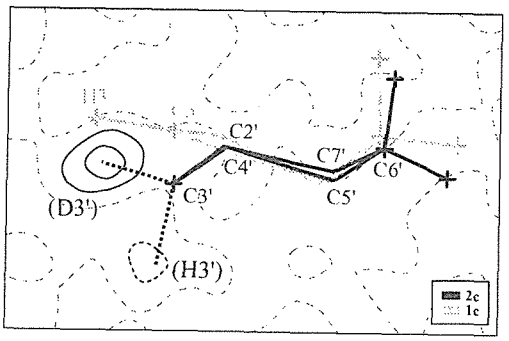

Figure 1: Difference Fourier map projected on the plane composed of H3-C3-C3'. All the atoms except H3' and D3' were included in the F_c calculation.[4)] Solid and dotted/dashed contours indicate positive and negative ones, respectively.

Recently we succeeded in isomerizing **1a** to **2a** with retention of the single crystal form after many trials.[2)] A crystal was irradiated with a xenon lamp for 330 h and then the structure analyzed by X-rays indicated 65.7 % of **1a** was converted to **2a** within the crystal. This disordered structure made clear how the benzyl carbon of **1a** makes a bond with the a carbon of the cyclohexene ring and why only one enantiomer of **2a** is produced from the chiral crystal. However, the question whether the β-carbon of the cyclohexene ring abstracts the hydrogen atom within a molecule or from the neighboring molecule has not been made clear.

To analyze the hydrogen migration mechanism in the crystal, four α-hydrogen atoms of the two benzyl groups of compound **1a**, were replaced with the deuterium atoms, **1b**. If the crystal was irradiated with a xenon lamp, the photo isomerization occurred with retention of the single crystal form to produce **1b**. This work reports the deuterium-migration mechanism in the photo isomerization by neutron diffraction technique.

In this study, other hydrogen atoms of these two benzyl groups of **1b** was replaced with deuterium atoms, **1c**, in order to reduce the background intensity caused by incoherent scattering and the large neutron absorption by hydrogen atoms. A large crystal of **1c** was divied to some pieces, and these were irradiated for 20 days at 263 K with a xenon lamp through a Y-44 sharp-cut filter (HOYA).[3)] A small crystal was quarried out from the center of one of the crystals. From its crystal structure analysis by X-rays, approximately 28 % of **1c** were photoisomerized to **2c**, and absolute configuration of a chiral methine carbone was determined.

Another crystal of **1c** after irradiation, $4.5 \times 1.5 \times 1.4\,\mathrm{mm}^3$ was mounted on the BIX-III (1G) neutron imaging plate diffractometer set up at the JRR-3M reactor in JAERI. The neutron diffraction data were collected for 4 days at 290 K, and peak integration by *MAC*

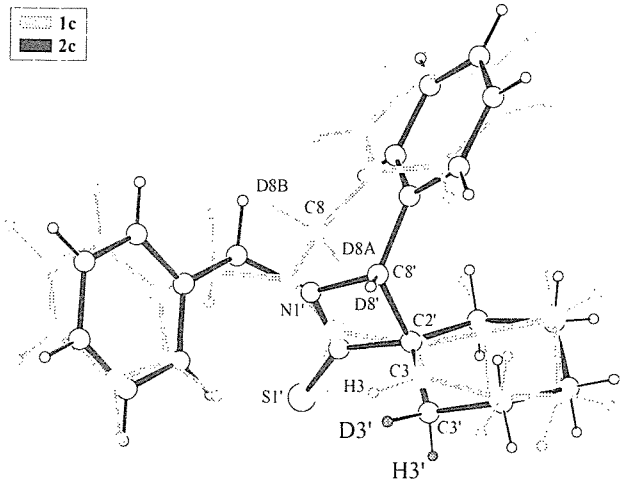

Figure 2: Molecular structure of **1c** & **2c** (disordered). The deuterium atom bonded to C3' was occupied to equatorial site of cyclohexane ring moiety.

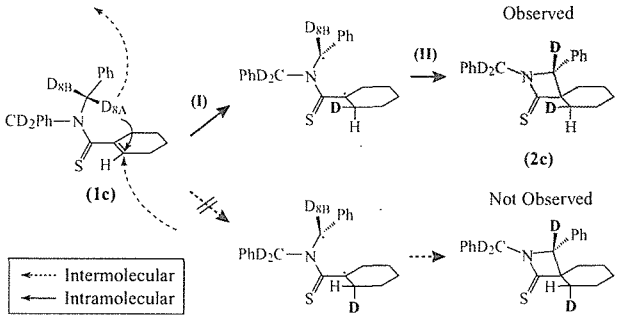

Figure 3: Reaction mechanism of **1c**: The first (I) and second (II) reaction steps indicate the intra- or intermolecular deuterium migration leaving a benzyl radical and the benzyl carbon radical makes the thiolactam ring, respectively.

DENZO created a *SHELX*-format *hkl* file. The crystallographic data and experimental details are summarized in Table **1**.

The difference Fourier map around C3 is shown in Fig. **1**. The positive peak at H3 indicates that a part of the H3 atom is moved to the negative peak at H3'. The positive peak at D3' can be assigned to the position of the transferred deuterium atom. This indicates that the positions of deuterium and hydrogen atoms are equatorial and axial, respectively, shown in Fig. **2**. This result clearly suggests that the photoreaction proceeds via the intramolecular deuterium migration as shown in Fig. **3**. The β-carbon of the cyclohexene, C3, abstracts an intra-molecular deuterium atom, D8A, involving homolytic bond cleavage. If

Table 1: Crystal data and experimental details.

[Crystal Data]	
Empirical formula	$C_{21}H_9D_{14}NS$
Temperature /K	290
Wavelength /Å	1.51
Crystal system, space group	Monoclinic, $P2_1$
a /Å	8.911(1)
b /Å	10.472(2)
c /Å	10.335(1)
β /°	102.526(6)
V /Å^3	941.5(2)
Z	2
Calculated density /Mg m^{-3}	1.183
Diffractometer	BIX-III
Crystal size /mm	4.50×1.50×1.40
[Data Collection]	
θ range / °	14.63–57.48
Limiting indices	$0 \le h \le 9$
	$0 \le k \le 11$
	$-11 \le l \le 11$
Reflections collected / unique	1270 / 1270
Completeness to θ /%	87.0
[Refinement]	
Refinement on	F^2
Data / restraints / parameters	1270 / 15 / 356
Goodness-of-fit on F^2	1.709
R_1 ($F^2 > 2\sigma(F^2)$), wR_2	0.1316, 0.3247
R_1 (all data), wR_2	0.1358, 0.3289
$\Delta\rho_{max}$, $\Delta\rho_{min}$ /eÅ^{-3}	0.073, -0.066

the deuterium atom comes from the neighbouring molecule, the transferred deuterium, D8A'(=D3'), should occupy the axial position. The benzyl carbon radical would be generated after the deuterium abstraction. Then, the produced benzyl carbon radical moves to form the β-thiolactam ring with keeping its conformation, considering from the observation by X-rays.

References

1) M. Sakamoto, M. Takahashi, K. Kamiya, K. Yamaguchi, T. Fujita, and S. Watanabe: *J. Am. Chem. Soc.*, **118**, 10664 (1996).
2) T. Hosoya, T. Ohhara, H. Uekusa, and Y. Ohashi: *Bull. Chem. Soc. Jpn.*, **75**, 2147 (2002).
3) This Y-44 filter shuts out the light whose wavelength is shorter than 440 nm.
4) The X-ray analysis of **2a** indicates that the positions of H3' and D3' are almost on the plane of H3-C3-C3'.

2.6.3 Development of A Method for Determining Residual Stress Using Diffraction Ring Detected with Neutron Image Plate

T.SASAKI[1], N.MINAKAWA[2], Y.MORII[2], N.NIIMURA[2] and Y.HIROSE[1]

[1]Department of Materials Science and Engineering, Kanazawa University, Kanazawa, Ishikawa 920-1192

[2]Advanced Science Research Center, JAERI, Tokai, Ibaraki 319-1195

A neutron image plate (NIP) was used to determine tensile stress in a steel specimen. The thickness of the specimen was 5 mm. Debye-Scherrer rings of the 211 back-reflection neutron beams were obtained under the exposure time of 5 hours, and spatial resolution of 100μm. As the mean residual stress over the thickness of the sample must be zero, it can not give rise distinguished change in the behavior of the radius. From a numerical simulation on the formation of the composed neutron diffraction profiles under the same conditions as the experiment, it was found that the diffracted beams from inside the material can cause a change in the radius as seen in the experiment even if for stress free state. Namely, the diffraction radius can be changed due to both the stress state and the thickness (or geometry) of the material, whereas the thickness of the material has generally no effects on the diffraction profiles for X-ray image plate experiment without a steep stress gradient case and so on. The stress determination was then carried out to the NIP image data using the cosα method, which was developed by Tanaka *et al.* Figure1 shows the stresses obtained as a function of the applied stresses which were converted from strains detected with the strain gauges on the specimen.

The open circles in the figure indicate values obtained from the cosα method, which shows a proportional behavior as well almost constant intervals against the applied stresses. The closed circles indicate the result obtained from the correction, in which the original NIP data were subtracted by those at stress free state and then the cosα method was used. It can be seen in the figure that the corrected data agree with the applied stresses (solid line). This means that the cosα method, which is adequate only to the X-ray experiment, is also effective to the neutron experiment. The reason of the result can be explained that the behaivior of the angular peak in the composed neutron profile on the NIP is almost the same as that of the diffracted beam on the most surface of the sample, because such beams act as the cosα method as same as X-ray beams. However, it should be noted that the present result will be obtained only in the case of samples with no stress gradients. As examples of this type of use of a NIP for the stress measurement, a mean stress evaluation in a layer joined to the other materials such as the SHS method, or phase stresses in composite materials. But the goal of the authors' study is the development of a method for determining depth profiles of residual stresses in the materials over the thickness in a nondestructive way.

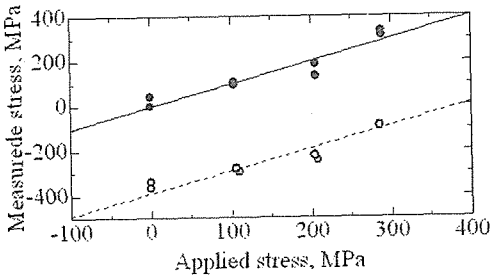

Figure 1: Stresses obtained from raw data (○) as well as from corrected data (●) using the cosα method as a function of applied stress.

2.6.4 Study of Residual Stress for Carbon/Carbon Composite by Neutron Scattering

S. BABA, M. ISHIHARA, N. MINAKAWA[1] and J. SUZUKI[1]

Department of Advanced Nuclear Heat Technology, JAERI, Oarai, Ibaragi 311-1394
[1]Department of Advanced Science Research Center, JAERI, Tokai, Ibaragi 319-1195

1. INTRODUCTION

The carbon fiber reinforced carbon matrix composite (c/c composite) is thought to be one of advanced heat resistant material in the nuclear engineering field. However, a lot of cracks are observed in manufacturing process of the ring type c/c composite due to the delamination between the fiber and the matrix by the residual stress. This is because of the different shrinkage between the fiber and the matrix during carbonization and graphitization heat treatment. Therefore, we investigated the residual stress in the ring type c/c composite aiming at the improvement of the manufacturing process. In this study, we measured the distributed residual stress in the ring type specimen using the neutron scattering experimental facility in the Japan Research Reactor No.3 Modified (JRR-3M) of Japan Atomic Energy Research Institute (JAERI).

2. EXPERIMENTAL PROCEDURE

2.1. Specimen preparation

The c/c composite material, CX-270G (made by TOYO TANSO Co.Ltd.,) was prepared as following process. The 6K plane weaves, 6000 PAN-based fiber in a fiber bundle with phenol resin coating, were molded by a so-called the vacuum bag method. After that, performing the hardening by heat treatment, carbon fiber reinforced plastic (CFRP) was made. The CFRP was heat treated over 800 ℃ under inert gas atmosphere to achieve carbonization and then heat treated finally about 2800 ℃ under unoxidation atmosphere to achieve graphitization. To product cylindrical shaped c/c composite specimen, the cylindrical shaped prepreg made of flat cloths was heat treated and harden to get the CFRP. After this process, the same treatment as above was conducted. Two kinds of isotropic graphites (IG-110, ISO-88) were prepared so as to obtain basic data on the c/c composite. Figure 1 shows the ring type c/c composite with 100mm outer diameter and 5mm thickness.

2.2. Apparatus

(1) High Resolution Powder Diffractometer, HRPD

The HRPD is a device to analyze the crystal structures as well as magnetic structures of the powder sample and also polycrystalline sample. We measured the standard lattice parameter of strain-free materials using the HRPD. In the experiment, to secure high resolution in a wide range, we set small divergence angle in the horizontal direction of the first and third collimators, and set large scattering angle of the monochrometer. Furthermore, to achieve high efficiency of measurement, we used a quasicurve type monochrometer to converge the neutron in the vertical direction at the sample position, and also used 64 sets of neutron detectors at every 2.5 degree of the scattering angle.

(2) Diffractometer for the residual stress analysis, RESA

The single crystal for monochromization of RESA has achieved the wavelength of 0.13~0.3nm by adopting a level vertical lightgathering type silicon crystal, Si(311), and also vertical vent light-gathering type pyrolytic graphite crystal, PG(002). The goniometers can move in one direction Z, three directions X, Y,

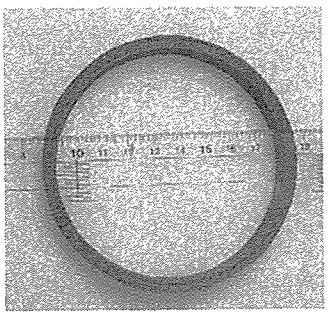

Figure 1: Ring type c/c composite specimen.

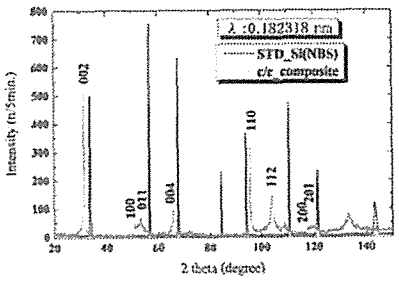

Figure 2: Powder diffraction patern of c/c composite and silicon(NBS).

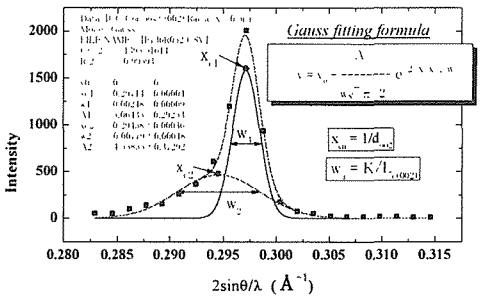

Figure 3: Gauss fitting formula of 002 layer spacing and crystallite, Lc for c/c composite.

Z, and five directions χ, ϕ, X, Y, Z. Furthermore, the diffraction angle can be measured under in-situ loading condition by the tension tester of the RESA apparatus.

3. RESULTS AND DISCUSSIONS

3.1. Measurement of layer spacing of strain-free sample

The powder sample of the c/c composite was prepared using an iron file. The calibration of incidence wave-length was carried out by a standard sample, silicon of National Bureau Standard, (silicon (NBS)). Measured in-tensity of the c/c composite powder and the silicon (NBS) samples is shown in Fig.2. From the measurement, we determined the wavelength of HRPD as λ =0.182318 nm. Then the strain-free diffracting plane, d002, is determined to be 0.33542 nm from 002 diffraction angle obtained by Gauss approximation of the measured diffraction peak for the powder sample of the c/c composite. To determine the d002, we used the diffraction neutron intensity vs. 2sinq/l plot corresponding to a reciprocal lattice layer spacing, 2sinq/l=1/d002. From the 1/d002 corresponding to a diffraction peak, we can determine the d002 value directly. The measured d002 diffraction intensity of the c/c composite sample showed the peak with the shoulder on the low angle side as shown in Fig.3. In the c/c composite, there are well-graphitized matrix part and not well-graphitized carbon fiber part just as a turbostratic structure.[1,2] The intensity peak in Fig.3 appears respectively at higher position with narrow width for well-graphitized parts and at lower position with wide width for not well-graphitized parts. This is thought to be a reason why the shoulder appeared. Average crystallite height in 002 plane, Lc, was determined by the half-width, Wn, as shown in Fig.3.

3.2. Residual stress in ring type c/c composite

The neutron radiation diffracts in accordance with the diffraction condition of Bragg's law as given in equation (1) like the X-ray diffraction fundamentally,

$$n\ \lambda\ = 2d\sin\ \theta\ \ (1)$$

where, n is the dimensional number, λ neutron wave-length, d lattice distance and θ diffraction angle. As for the lattice distance of a crystal, a diffraction angle changes by the applied stress. By differentiation of the equation (1), we rewrite the strain as

$$\varepsilon\ = \Delta\ d/d = (d\text{-}d0)/d0 = \text{-cot}\ \theta\ 0\ \Delta\ \theta\ ,\ (2)$$

where d0 is the layer spacing and θ 0 the diffraction angle of strain-free condition. Accordingly, the stress σ is estimated by equation (3) based on the Hooke's law, if E and ν are respectively the diffraction elastic constant and Poisson's ratio for the specific diffraction plane.

$$\sigma\ = E\ \varepsilon\ /\ \nu\ \ (3)$$

The diffraction lines in the radius direction of the ring type c/c composite were measured of the interval of 0.5mm from outside to inside surface. The diffraction angle for 002 was measured for 4minutes at 0.2 degrees of stepping interval. As shown in Fig.4, the residual stress/strain decreased from inner to outer surface of the ring type c/c composite. Here, we should note that the obtained stress/strain within about 0.5mm from the inner surface express not true value, because in this region a part the neutron beam volume misses from the gauge volume.

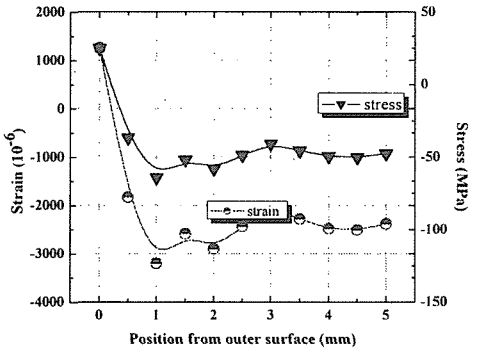

Figure 4: Residual stress and strain of ring type c/c composite.

4. CONCLUSIONS

The residual stress distribution in the c/c composite was studied aiming at the improvement of the manufacturing process using the neutron diffraction method. As a result of this study, it is the compressive stress, and that the macroscopic residual stress/strain is absorbed mainly microstructural change such as pore shape change.

References

1) T. Tamotsu, S. Baba and M. Eto, Changes of Tensile Property and X-Ray parameter for Carbon Fiber after
2) M. Eto and T. Oku : J. Nucl. Mater **54** (1974) 245-253.

2.6.5 Crystal structures of γ-Na_xCoO_2 (x=0.67, 0.71, 0.73 and 0.75)

Y. ONO, N.KATO, Y.ISHII[1], Y.MIYAZAKI and T.KAJITANI

Department of Applied Physics, Tohoku University, Sendai 980-8579
[1]Advanced Science Research Center, JAERI, Tokai, Ibaraki 319-1195

Recent discovery of potential oxide thermoelectric (TE) materials has attracted much attention for their high performance and chemical stability at high temperatures[1-4]. The layered cobaltite, γ-Na_xCoO_2($0.60 \leq x \leq 0.75$), is the most promising p-type TE-materials with dimensionless figure of merit, $ZT = S^2T/\rho\kappa$ =1.2 at T=800 K[5], where S, ρ and κ are Seebeck coefficient, electric resistivity and thermal conductivity, respectively. This ZT value sutisfies the criterion for practical applications. In this study, structure parameters of four samples with different x are refined by Rietveld analysis of powder neutron diffraction data.

Polycrystalline samples of γ-Na_xCoO_2 (x=0.67, 0.71, 0.73 and 0.75) were prepared by a solid state reaction. The mixture of Na_2CO_3 (99.5%) and Co_3O_4(99.9%) powders was pressed into pellets and calcined in air at 1073 K and sintered at 1123 K for 12 h in air with an intermediate grinding. Na and Co contents in the samples were determined by inductively coupled plasma (ICP) analysis. Neutron diffraction measurements were carried out at room temperature using HRPD (λ =1.82318 Å). The measured intensities were analyzed by a program RIETAN2000[6], assuming the space symmetry $P6_3/mmc$ (No.194). Total Na content was constrained to be equal to the ICP results during the analysis.

Figure 1 shows observed, calculated and difference neutron diffraction profiles of γ-$Na_{0.67}CoO_2$. There is good agreement between the observed and calculated intensities in all data sets (R_{wp}=4.5-7.4% and R_I=2.6-2.8%). Little changes are noticed in the crystal structure, except for Na contents at Na1 and Na2 sites[7]. As shown in Fig.2, the Na ions are unequally distributed at Na1 and Na2 sites despite of similar oxygen coordination to both sites. This discrepancy is possibly ascribed to the different coordinations of Co ions to the Na sites.

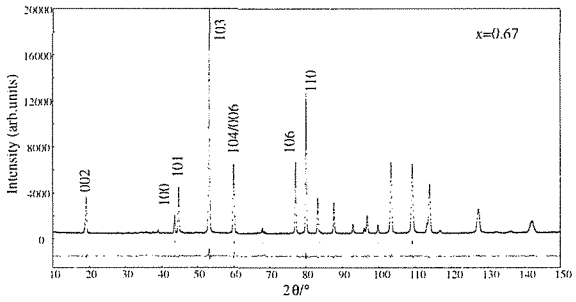

Figure 1: Observed, calculated and difference neutron diffraction profiles of γ-$Na_{0.67}CoO_2$.

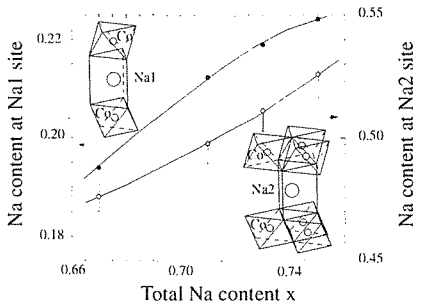

Figure 2: Na contents at Na1 and Na2 sites.

References

1) I. Terasaki *et al.*: Phys. Rev. **B56** (1997) R12685.
2) M. Yasukawa and N. Murayama : Mater. Sci. Eng. **B54** (1998) 64.
3) R. Funahashi *et al.*: Jpn. J. Appl. Phys. **39** (2000) 1127.
4) Y. Miyazaki *et al.*: Jpn. J. Appl. Phys. **40** (2001) L531.
5) K. Fujita: Jpn. J. Appl. Phys. **40** (2001) 4644.
6) F. Izumi and T. Ikeda: J. Crystllogr. Soc. Jpn. **42** (2000) 516.
7) Y.Ono *et al.*: J. Jpn. Soc. Powder and Powder Metallurgy. **50** (2003) 469.

2.6.6

Diffraction angle error investigation of the sample surface measurement by the small neutron beam

N. Minakawa, A. Moriai, Y. Morii

Advanced Science Research Center, JAERI, Tokai, Ibaraki 319-1195

In order that to evaluate the soundness of material or processed goods, safety, and a life, an internal spacing of lattice planes is measured from the material surface, and it determines for a strain and a stress distribution. Near the surface, it measures the spacing of lattice planes more than a forecast then. Therefore, using the carbon steel sample of the non-strain condition which heat-treated, we reproduced this phenomenon.

We used SM400 carbon steel with heat-treated suitable vertical 50 mm, a length 100 mm, and a thickness of 10mm for the measurement sample. By the beforehand neutron diffraction measurement, a crystal structure is BCC and it determined for a lattice constant being 0.28682nm. The slit of 1 mm width and 15 mm height was used for the measurement at the incidence and scattering side, using the neutron wavelength of 0.20963nm. Mostly, the diffraction angle used the 200 reflections, which is 90 degrees, and measured the measurement diffraction lattice planes by the reflection method and the transmission method. The measurement position was used as 0.5mm step near the surface, and the inside was measured at 1mm step. The distribution of a forecast intensity with a method of measurement is shown in Fig. 1.

The result, which measured by the reflection method and the transmission method, is shown in Fig. 2 and Fig. 3. The absorption coefficient of SM400 was μ = 1.17 as a result of measurement, and maximum diffraction intensity thickness t_{Imax} was 0.584mm from the next equation.

$$t_{Imax} = 1 / \mu \sec \theta$$

The maximum intensity position, which can be found from the integrated intensity distribution curve of Fig. 3, is equivalent to calculation value. Therefore, it can be said that a sample mount position is exact.

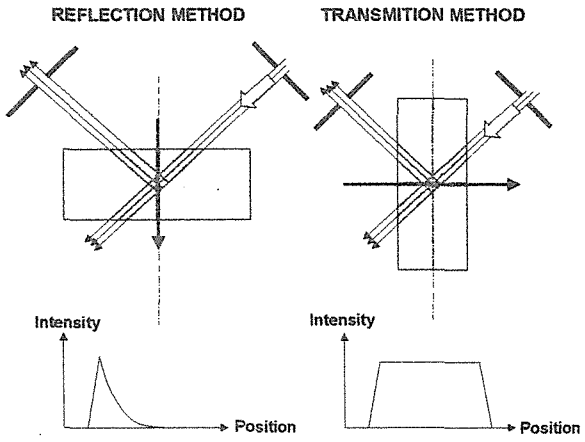

Figure 1: Measurement method of sample.

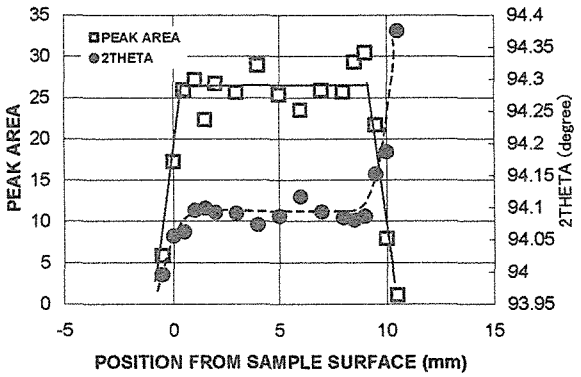

Figure 2: Distribution of 2Theta and intensity by the reflection method.

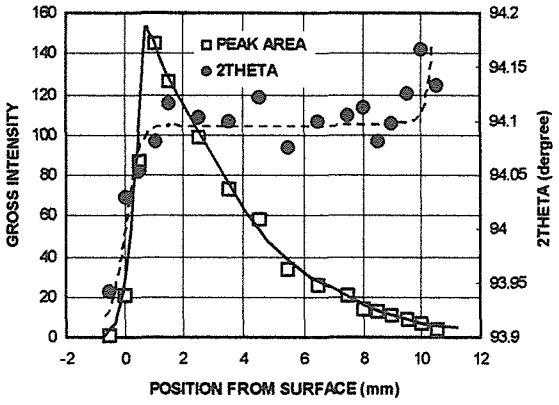

Figure 3: Distribution of 2Theta and intensity by the transmission method.

Originally, the diffraction angle distribution of Fig.2 and Fig. 3 has the desirable same angle from the surface of sample to back, but an angle becomes high exponentially also from this measurement result, or the diffraction angle near the surface becomes low, and the result as expected was obtained.

In order that the neutron guide tube is using super mirror of the 2Q, the divergence angle to a monochromator crystal is 0.36 degrees equivalent to a critical angle. The locking curve FWHM of the monochromator crystal was about 0.2 degrees, and in order that the bending stress was applied in the horizontal plane to the crystal, the divergence angle of a monochromatic neutron beam was 0.3 degrees as a result of measuring by the photograph method. The beam divergence angle by the diffraction is determined with the distance between sample and detector, and the size of collimator and slit. The position of a sample and the condition of the diffraction by the divergence angle are shown in Fig. 4.

An incidence beam passes the center of the sample table. The diffraction angle outputted to data is a true rotation angle of a sample table center. The neutron diffraction near the sample surface becomes strong the diffraction by the divergence angle. Therefore, we understood that it was different from the diffraction angle of an inside of sample part. Moreover, the bending stress is loaded to the monochromator crystal for the control of crystal mosaic spread. Therefore, when a crystal bends, it has a wavelength distribution in a horizontal plane. These conditions overlap near the surface, and in order that the diffraction is performed, the complicated correction method is needed and it is under investigation now.

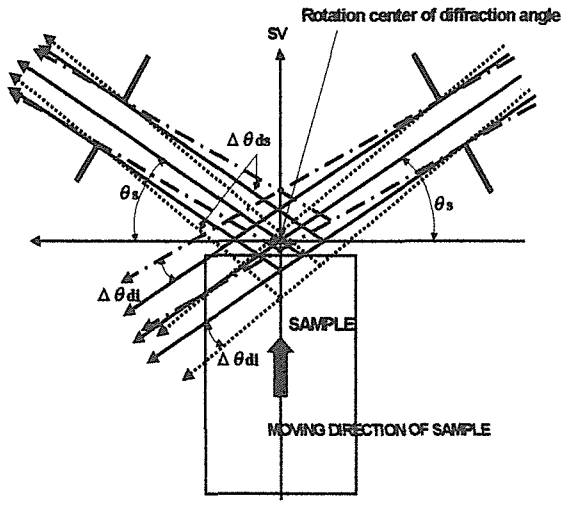

Figure 4: Neutron diffraction by the divergence beam.

2.6.7

The comparison measurement of the strain gauge method and the neutron diffraction methods by the automobile aluminum engine

N. Minakawa[1], A. Moriai[1], Y. Morii[1], K. Goto[2], S. Nishii[2],
S. Yamada[2], H. Hosoda[2], A. Nomura[2], and T. Hamamoto[2]

[1]Advanced Science Research Center, JAERI, Tokai,Ibaraki 319-1195
[2]The 4th Development Center, Toyota Motor Corp

The automobiles engine is loading continuously the thermal stress with severe repetition impact stress. Inside of automobile engine, the intensity that can bear the stress is maintained, safeness and soundness are guaranteed, and we utilize. When we imagine, in a future automotive society, it will become an important assignment to guarantee safeness scientifically. Therefore, becoming an important technique after this for the purpose of residual stress measurement at the inside of engine by the neutron diffraction method is expected.

Now, the stress measurement for the inside of engine has the cutting strain method by the strain gauge. Therefore, this fiscal year compared and measured the surface strain measurement by the strain gauge, and the neutron diffraction method. Measurement equipment used the neutron diffractometer for residual stress analysis (RESA) installed in the experimental hall of neutron guide tube in JRR-3. The rosette type strain gauge with a diameter of 5mm was used for the strain gauge method. The measurement sample cut from an aluminum engine and used a small block with 21.5 mm width, 15.7 mm height, and 11.5 mm depth. The strain gauge was affixed on the small block, and strain was measured by the strain gauge method and the neutron diffraction method. After that, moreover, sample was cut to a small block by the electrical discharge machining, and strain was measured by the both methods, and we searched for about change of strain value. The cut aluminum engine block is shown in Fig. 1.

The measurement method by the neutron

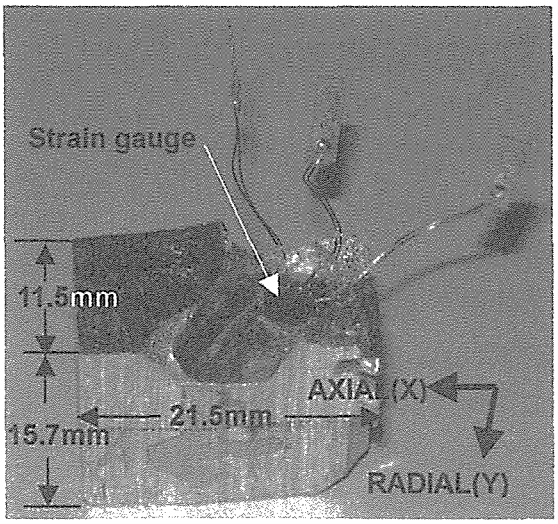

Figure 1: The cut aluminum engine block.

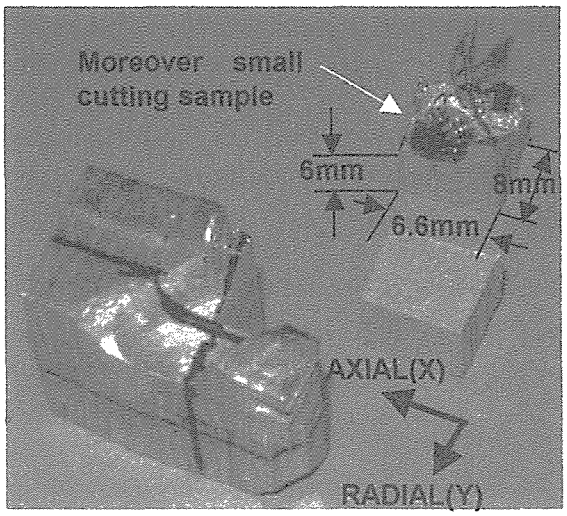

Figure 2: The engine block cut moreover smaller by the electrical discharge machining.

diffraction made a beam size 1 mm height, 2 mm width and measured that bottom of the gauge and downward direction at the 1 mm step. The measurement mirror index used (311), and neutron wavelength is 0.20891nm. The incidence neutron flux of a measurement beam size was 3.3 x 10^3 (n/2mm^2/30sec) = 1.1 x 10^3 (n/2mm^2/sec), measurement time was wanted. Therefore, 7.5 hours was used in order that to measure one diffraction (311) pattern. By electrical discharge machining, the engine block cut moreover small is shown in Fig. 2. A measurement sample position is shown in Fig. 3. and a measurement result is shown in Table 1.

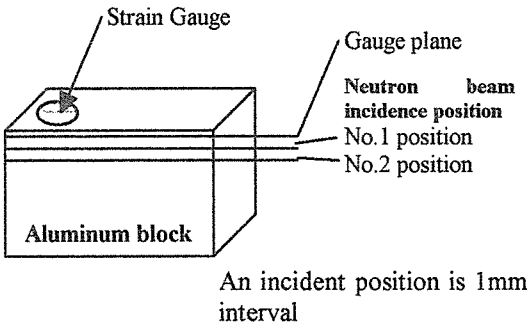

Figure 3: Measurement sample position.

By the strain gauge method, it measures the surface strain of the affixed position. By the neutron diffraction method, it measures the average strain in a gauge volume. The figure of a gauge volume in this measurement with consideration to the divergence angle is shown in Fig. 4.

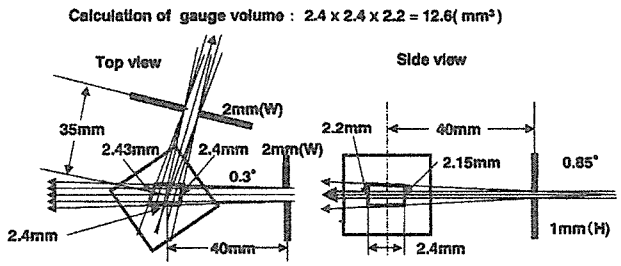

Figure 4: The gauge volume in this measurement with consideration to the divergence angle.

The difference before and behind cutting of the AXIAL direction by the strain gauge is 128 (micro strain), the RADIAL direction is 51 (micro strain) and these are very small strain change. That is, on the surface, it can be said that the strain is opened for the surface by cutting. At the result of the strain measurement by the neutron diffraction, it was 543 (micro strain) in the AXIAL (X) direction and 495 (micro strain) in the RADIAL (Y) direction. Although this result is not an extremely big strain, either, it can be said that it was about change by the open strain by cutting. Moreover, the AXIAL (X) direction was –1233 (micro strain) and the RADIAL (Y) direction was –276 (micro strain) of the strain of a gauge to 1mm lower part. By cutting a small block, the compression strain was generated. Even though it was the block smaller cut from this result, it understands that a residual strain cannot be opened perfect.

Table 1 : Measurement result of strain

DIRECTION	POSITION	BEFORE CUT	AFTER CUT	A-B *
AXIAL	strain gauge	-255	-127	128
AXIAL	No.1	265	760	495
AXIAL	No.2	1180	-53	-1233
RADIAL	strain gauge	-340	-289	51
RADIAL	No.1	652	1153	501
RADIAL	No.2	898	578	-319

* A : After cutting B : Before cutting

2.6.8

Residual stress measurement of peened material by neutron diffraction method

S. OKIDO, T.MACHIDA[1], M. HAYASHI[2],
Y. MORII, N. MINAKAWA and A. MORIAI[3]

[1]Mechanical Engineering Research Laboratory, Hitachi, Ltd., Hitachi, Ibaraki 317-8511
[2]Power and Industrial Systems, Hitachi, Ltd., Hitachi Ibaraki 317-8511
[3]Advanced Science Research Center, JAERI, Tokai, Ibaraki 319-1195

Shot peening deforms and hardens a metal surface plastically with particles of metal or glass. As a result, compressive residual stress appears and the surface properties are improved. The region of compressive residual stress by shot peening is less than a few-mm depth. The neutron diffraction method is inferior to X-ray diffraction method when the residual stress near the surface is measured. So the accuracy of residual stress near surface of the peened materials measured by neutron diffraction was discussed comparing with that measured by X-ray diffraction.

The material used in this research wwa peened stainless steel Type-304. The lattice strain was measured by using RESA. The 111 diffraction of γ-Fe in type-304 steel was used in the measurement of strain. The wavelength, λ was 0.20995 nm. Cadmium masks were inserted in both the incoming beam and the diffracted beam to define a sampling volume of 0.3x0.3x8 mm^3.

The residual stress measurement at the surface make the peak angle of diffraction profile shift from veritable peak angle, causing a bias of neutron irradiation. So, peak angles obtained from diffraction profiles at surface of stress free specimen are shown in Fig.1. A peak shifts appeared at the surface less than 0.7 mm depth. This result shows that the peak angle correction is required measuring at the surface less than 0.7 mm depth.

The results of surface residual stress obtained from before and after peened specimen are shown in Fig. 2. The results of measured by x-ray diffraction method added to Fig.2 to discuss the accuracy of those of neutron diffraction method. These residual stresses measured by neutron diffraction method at the surface less than 0.7 mm depth is corrected with results of Fig.1. The peening effects produce a difference between before and after peening residual stress less than 0.5 mm depth. The residual stress over 0.5 mm depth was not affected by the shot peening. Moreover, the residual stresses as obtained by neutron diffraction almost agreed with those by x-ray diffraction. These results show that peak profile correction make the neutron diffraction method possible application of measuring the surface residual stress.

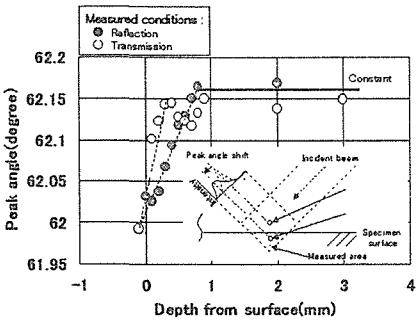

Figure 1: Change of diffraction profile obtained from stress free material surface.

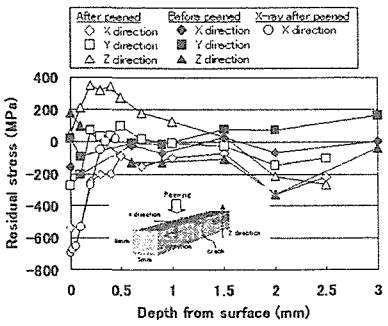

Figure 2: Residual stress distributions vicinity of crack before and after peening.

2.6.9 Residual Stress in the Induction Hardened S45C Round Bar

K. INOUE, M. SUGIMOTO, H. MAEDA, T. HORIKAWA, T. TSUJIKAMI,
N. MINAKAWA[1], A. MORIAI[1] and F. IKUTA[2]

Faculty of Science and Technology, Ryukoku University, Seta, Otsu 520-2194
[1]Advanced Science Research Center, JAERI, Tokai, Ibaraki 319-1195
[2]Heating Machine Division, Neturen Co., Tanuma, Hiratsuka 254-0013

The residual stress of an induction hardened S45C round bar was estimated from the resitual strain measured by neutron diffraction experiment with RESA at JRR-3. The obtained stress was compared with the results calculated by the finite element method, FEM.

The diameter of the round bar was 20 mm and the length was 60 mm. The surface of the bar was treated by induction heating of 50kHz for 8.5 s. The temperature of the surface was increased up to 950 °C and was cooled down to 26.9 °C with the water. It is expected that the martensitic phase occurs near the surface, whereas the inner region is not hardened and is in the coexistent state of ferrite and pearlite.

We prepared the sliced specimen cut from the round bar along the direction of the hight including the center of the bar. It was etched with 5% nital for 10s, after mirror finishing by buffing. The photograph of the hardened sliced specimen is swown in Fig.1. In Fig.1 we are able to distinguish the martensitic region near the surface from the coexitent region of pearlite and ferrite. The SEM images at each positon on the radius of central sectional plane, which was observed using this sliced specimen, are shown in Fig.2 for hardened bar and in Fig.3 for non-hardened bar. In Fig.2, we see that the fraction of the martensitic phase increases as we get near the surface.

The stress free lattice spacing, d_0, Young's modulus and Poisson ratio at each position are necessary to estimate the stress at each position of the sample. We have measured the (110) latttice spacing at each position of the surface of the sliced sample to obtain d_0. The diffraction was observed for the virtical

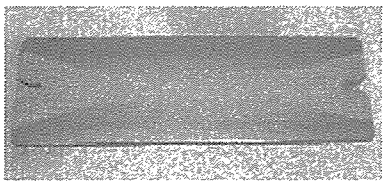

Figure 1: Photograph of the sliced specimen cut from the hardened round bar.

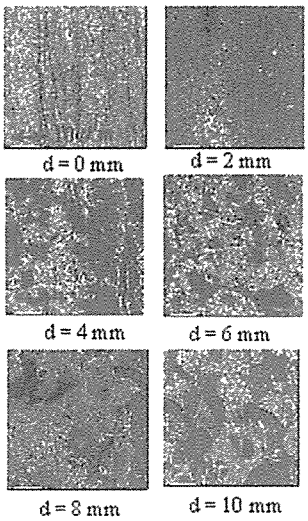

Figure 2: SEM images of the induction hardened S45C round bar at each positionon on the radius of central sectional plane. The letter, d, means the distance from the surface.

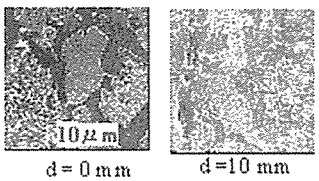

Figure 3: SEM images of the non heat treated S45C round bar at the surface and the center on the radius of central sectional plane. The letter, d, means the distance from the surface.

direction of the surface, because the stress is released in the virtical direction at the surface. The peak position of the 110 reflection was different due to each position of the specimen. The stress free lattice spacing, d_0, at each position was estimated and are shown in Fig. 4.

Young's modulous and Poisson ratio of the martensite single phase and of the pearlite single phase were estimated from the 110 reflection of each single state test piece under tensile condition. The experimantal results are shown in the previous report.[1] Young's modulous and Poisson ratio at each posion where the martensite and ferrite are coexistent were determined by averaging the experimentally obtained two values over the volume fraction of each phase. The volume fraction of the martensite at each position of the bar was estimated by simulation.[2]

As a result, the residual stress for three directions at each position on the radius of the central sectional plane of inducton hardened bar is shown in Fig.5. The residual stress calculated by FEM is shown in Fig.6. We see that coincidence between the stress obtained by neutron diffraction and that estimated by FEM is extremely good. They are also coincident with the stress measured by X-ray at the surface, as shown in Fig.6 where the measured values are also plotted.

We conlude that this success in determing the residual stress when the martensite and the ferrite are coexistent is owing to the precise determination of the stress free lattice spacing, d_0, for coexitent situation of two phase.

References

1) K. Inoue, T. Horikawa, N.Minakawa, A. Moriai *et al*: JAERI-Review 2003-019 (2003) 336.
2) F. Ikuta and T. Horino: Netsu-Syori **42** (2002) 359. (in Japanese)

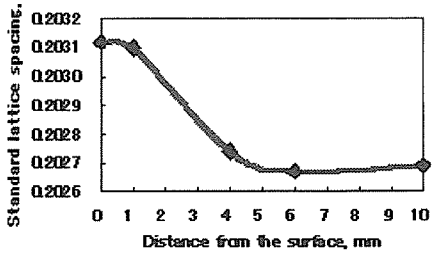

Figure 4: Stress free lattice spacing, d_0, at each position on the radius of the central sectional plane.

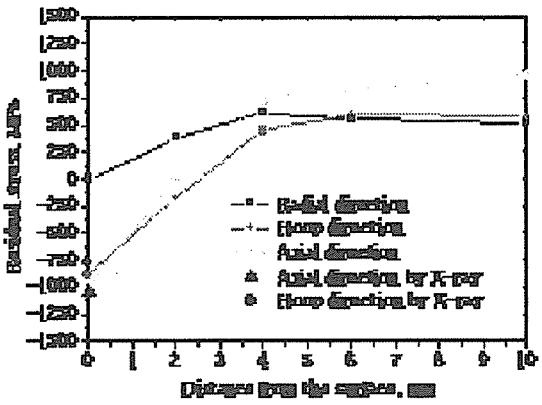

Figure 5: Residual stress at each position on the radius of central sectional plane of inductioned hardened round S45C bar, obtained by RESA.

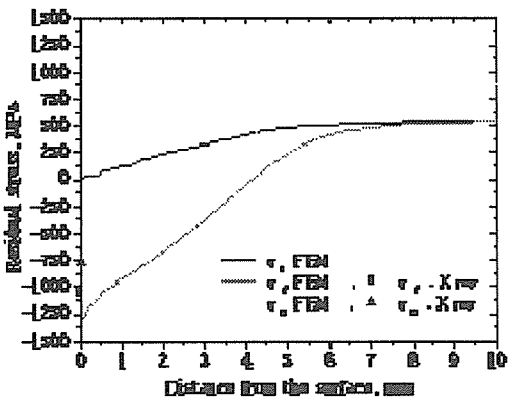

Figure 6: Residual stress at each position on the radius of central sectional plane of onduction hardened bar, calculated by FEM. At the surface measured values by X-ray are also plotted.

2.6.10

Anisotropy in Residual Phase Stresses in a Pearlitic Steel Subjected to Tensile Deformation

T. Suzuki, Y.Tomota[1], A. Moriai[2], N. Minakawa[2] and Y. Morii[2]

Research Center for Superplasticity, Faculty of Engineering, Ibaraki University, Hitachi, Ibaraki, 316-8511

1. Department of Materials Science, Faculty of Engineering, Ibaraki University, Hitachi, Ibaraki, 316-8511
2. Advanced Science Research Center, Japan Atomic Energy Research Institute, Tokai, Ibaraki, 319-1195

The strength of a drawn pearlite steel wire along the drawing direction is higher than that along the transverse one but the reason is unclear[1]. Two possible reasons, i.e., texture and residual phase stress, were examined in this study. Tensile deformation was employed because the drawing was complicated in plastic manner. The results obtained are compared with the results for the drawn wires obtained previously.

A hypereutectoid steel with the chemical compositions of 0.85C, 0.24Si, 0.82Mn, 0.011P, 0.01S, 0.02Al and 0.05Cr in mass% was hot-rolled and patented through an industrial process to produce fully pearlitic structure (specimen P1). They were drawn by 75% in area reduction (P2) and aged at 698 K for 0.6 ks (P4): Zn-plating simulated heat. The details in sample preparation were reported in ref. 2.

The texture of P1(ϕ 11mm) was evaluated by 110 pole figure obtained by X-ray diffraction with the Schulz reflection method using nickel-filtered Cu K_α radiation. Because the specimen diameter of P2 and P4 is small (ϕ 5 mm), their textures were measured by neutron diffraction. The measurements were conducted using the Neutron Diffractometer for Residual Stress Analysis (RESA) at Japan Atomic Energy Research Institute (JAERI).

Tensile tests were carried out at 300 K using a gear type tester with an initial strain rate of 6.7×10^{-4} s^{-1}. Figure 1 (a) shows shape and dimensions of tensile specimen. After the tensile tests, specimens for the measurement of residual strains were prepared by cutting from their parallel part; uniformly elongated part. The residual strain measurements were conducted by a conventional θ -2 θ method with neutron diffraction by using RESA at JAERI. Lattice plane spacing of (110) ferrite was measured, where a specimen was rotated by 0, 22.5, 45, 67.5 and 90° with respect to the tensile direction as illustrated in Fig. 1 (b). Peak positions of the diffraction profiles were determined by curve fitting with a Gaussian function.

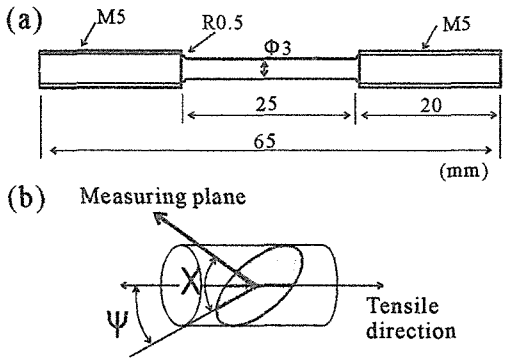

Figure 1: Shape and dimensions of a tensile specimen (a) and geometrical arrangements for texture and residual strain measurements (b).

The microstructure observations reveal that the pearlite colonies in P4 are elongated along the drawing direction and their lamellar spacing becomes smaller in comparison with P1. In a 110 pole figure of the ferrite matrix in P1 obtained by the X-ray diffraction, no areas of high pole density could be found, indicating very weak texture. The pole figure for P4 is shown in Fig. 2 which is quite similar for P2. As seen, a maximum intensity of

6.8 times of the average density exhibiting the 110 fiber texture. The texture was formed by the drawing process (P2) and was hardly affected by the annealing at 698 K (P4).

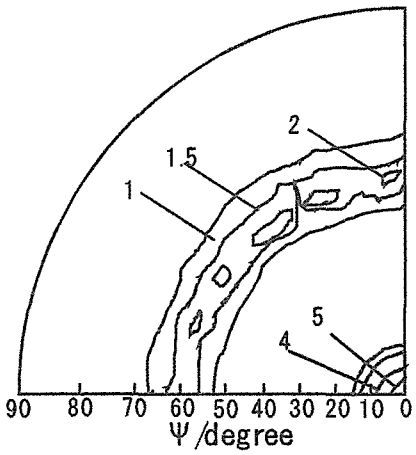

Figure 2: 110 pole figure obtained by neutron diffraction for P4.

Figure 3 shows lattice plane strains of P1 and P4 after tensile deformation. The residual strain of P1 simply increases from compression to tension with increasing of the measuring angle from 0 to 90° . This is quite acceptable from the view point of phase stress generation between hard and soft phase in a two-phase material. On the other hand, in the lattice plane strains of P4 (b), the overall trend is from compression to tension with increasing of the measuring angle, but the residual strain at 90° is lower than that at 67.5°. This is the same trend observed in the drawn wire that shows strength anisotropy. This unusual results stem from the texture.

Comparing the features of P1, P2 and P4 before testing, the texture is similar for P2 and P4 while the residual phase stress is similar for P1 and P4. When tensile deformation is applied to P1 and P4, different phase stresses are yielded. The stresses for P4 subjected to tensile deformation resemble that for P2. The strength anisotropy is found only in P2 not in P1 and P4[3]. Hence, it is concluded that the strength anisotropy stems from the features of residual phase stress not from the texture. It should, however, be noted the texture brings the different residual stress distribution after plastic deformation. This can be explained from the influence of texture on the plastic flow in individual grains. Such discussion will be given in ref. 3.

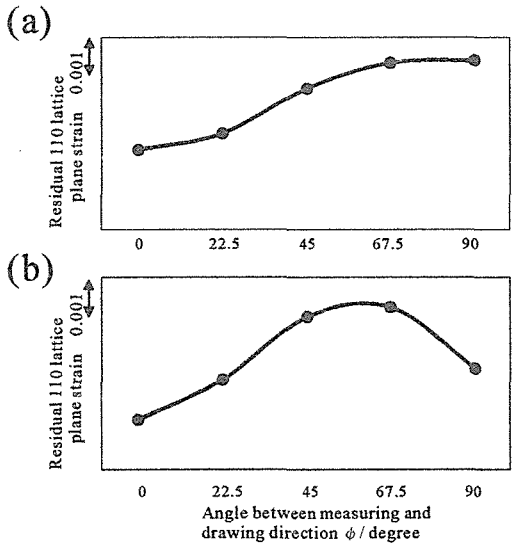

Figure 3: Residual elastic strains in the ferrite matrix of P1 (a) and P4 (b) after tensile tests.

REFERENCES

1. T. Fujita, Y. Yamada and T. Yamada: Tetsu-to-Hagane **59** (1973) S255.
2. Y. Tomota, P. Lukas, D. Neov, S. Harjo and Y. R. Abe: Acta mater. **51** (2003) p.805.
3. T. Suzuki, Y. Tomota, A. Moriai, N. Minakawa and Y. Morii, ATEM.03, Nagoya, (2003), Sept., JSME-MMD.

2.6.11 Strengthening Mechanism of a Heavily Drawn Pearlite Wire with 4 GPa - *In situ* Neutron Diffraction under Tensile Loading-

Y. Tomota, A. Kanie[1], Y. Shiota[1], T. Suzuki[2] , A. Moriai[3], N. Minakawa[3] and Y. Morii[3]

Department of Materials Science, Faculty of Engineering, Ibaraki University, Hitachi, Ibaraki, 316-8511

1. Graduate student of Ibaraki University, Hitachi, Ibaraki, 316-8511
2. Research Center for Superplasticity, Ibaraki University, Hitachi, Ibaraki, 316-8511
3. Advanced Science Research Center, Japan Atomic Energy Research Institute, Tokai, Ibaraki, 319-1195

Much attention has been paid on the micro structure of a heavily drawn pearlitte wire because it shows ultra high strength; the champion strength. The microstructure of pearlite consisting of ferrite and cementite changes drastically by sever plastic deformation; cementite plate in lamellae dissolved in to the ferrite matrix and hence strengthening mechanism to exhibit more than 4 GPa is unclear. Thus, many workers have been investigated the microstructural evolution during sever deformation by Mossbauer spectroscopy, AP-FIM, TEM etc. Although the structural feature has been revealed to some degree, but the strengthening mechanism is quite difficult to study. Neutron diffraction is a powerful tool to investigate the strength of such a wire. Thus, *in situ* neutron diffraction during tensile loading was performed.

The chemical compositions of a steel used are listed in Table 1. The hot-rolled bars were patented and then drawn through an industrial process at Sumitomo metal industry Ltd. They were drawn to wires with several diameters as shown in Table 2.

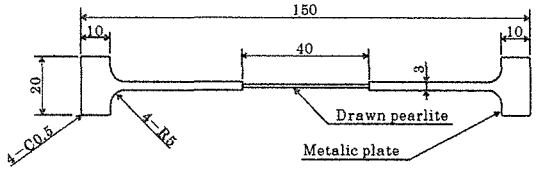

Figure 1: Shape and dimensions of specimen holder.

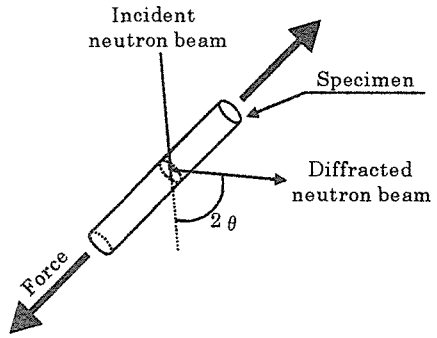

Figure 2: *In situ* neutron diffraction experiment for a wire under tensile loading.

To hold a wire, a special holding jig was prepared as shown in Fig. 1; a wire was bonded by two steel plates. Figure 2 shows the testing condition of *in situ* neutron diffraction. Even for a wire with 0.2 mm in diameter, it becomes possible to obtain a (110) diffraction profile with sufficient intensity to determine the center of the peak by

Table 1: Chemical compositions of a pearlitic steel

C	Si	Mn	P	S	Cr	Al	N
0.88	0.16	0.51	0.009	0.005	0.03	0.001	0.0029

Table 2: Specimens prepared by drawing

Diameter(mm)	ϕ1.5	ϕ0.72	ϕ0.43	ϕ0.27	ϕ0.20
Decrease rate of section(%)	0	77.0	91.8	96.8	98.2
Drawn strain	0	1.5	2.5	3.4	4.0

exactly adjusting the tensile direction because the strong 110 fiber texture was evolved in the wire. Even in such a condition, the gauge volume was so small for the 0.2 mm wire ($0.47mm^3$) that the measuring time of 5.4 ks was needed to obtain an individual diffraction profile. The peak positions were determined by Gaussian curve fitting.

Figure 3 shows the (110) lattice plane strain as a function of the tensile stress, in which the data previously obtained for a patented pearlite steel [1] were also plotted. As has been made clear in ref. 1, the high strength of a pearlite steel, presumably up to 2 GPa is attributed to the stress partitioning between ferrite and cementite; work hardening due to phase stress. The cementite plate is estimated to bear more than 5 GPa and then the steel can achieve 2 GPa. Hence, as can be seen in Fig. 3, the lattice plane strain in the ferrite matrix stops to increase at approximately 0.004. Here, the volume fraction of cementite is about 0.14. A heavily drawn pearlite exhibits more than 5 GPa and then a question has risen why so strong and what is the strengthening mechanism. Figure 3 answers that the ferrite matrix itself is strengthened. As seen in the figure, the lattice plane strain goes up to 0.018; the elastic strain of 1.8% is extremely large value for steel. The residual strains for (110) in the drawing direction was - 0.0034 in compression so that the net tensile strain for (110) spacing is about 0.015, still extremely large. Another point to be noted here is the curve observed in Fig. 3. The curve obtained deviates from the linear relation after the strain of 0.011 or the external load of 2.5GPa. Nonlinear elastic relation seemed to be verified at extremely high stress actually.

The strength of 3.4 GPa in Fig. 3 is achieved for the ferrite in which the cementite plates were dissolved. Because the maximum strength for pure or low carbon steel subjected to sever deformation is less than 2 GPa at the similar deformation and 3 GPa at true strain of 10 (extremely sever deforamtion)[2], the present high strength is attributed to carbon atoms. It is, however, the dissolution mechanism and the location of carbon atoms after the dissolution are not made clear.

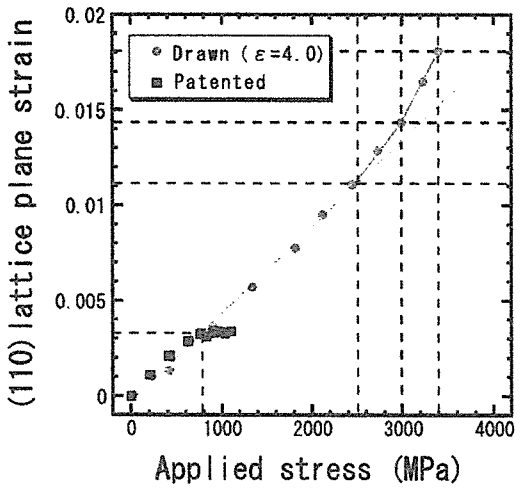

Figure 3: Lattice plane strain determined from (110) diffraction as a function of the external stress.

REFERENCES

1. Y. Tomota, P. Lukas, D. Neov, S. Harjo and Y. R. Abe: Acta mater. **51** (2003) 805.
2. H.Tashiro, Ph. D thesis, (1992) Tohoku Univesity.

2.6.12 Residual Grain Stress and Ultra-High Strength of a Heavily Drawn Ferrite Steel

Y. Tomota, M. Uno[1], T. Suzuki[2], A. Moriai[3], N. Minakawa[3] and Y. Morii[3]

Department of Materials Science, Faculty of Engineering, Ibaraki University, Hitachi, Ibaraki, 316-8511

1. Graduate student of Ibaraki University, Hitachi, Ibaraki, 316-8511
2. Research Center for Superplasticity, Ibaraki University, Hitachi, Ibaraki, 316-8511
3. Advanced Science Research Center, Japan Atomic Energy Research Institute, Tokai, Ibaraki, 319-1195

The utra-fine gained materials or nano crystals have recently been studied by many workers [1-3]. Some of them are made through very sever plastic deformation including ball milling, ECAP, ARB etc. The concept of continuous recrysatlization has been proposed. It is possible to give an extremely sever deformation to a mateiral by drawing, but little report has been made. The pearlite wire subjected to extremely sever deformation is another topic in hot discussion because the cementite dissolution takes place during deformation. The dissolution was first recognized in drawing and it is engineeringly important as a production of tire-code wire with higher than 4GPa. It is helpful to study ferrite wire and pearlite wire to compare their behavior under sever deformation and the mechanical properties of the deformed specimens. Therefore, the microstructural evolution and tensile behavior of drawn ferrte wires were studied.

The chemical compositions of a steel used are 0.008C, 0.01Si, 0.13Mn, 0.012P, 0.004S, 0.01Ni, 0.02Cr, 0.01Cu in mass%. The hot-rolled bars with 5.5 mm in diameter were drawn to several wires with diameters of 2.0, 0.73, 0.38 and 0.20 mm, true strains of 2.0, 4.0, 5.3, and 6.6, respectively, at the Kamaishi factory of Nippon Steel Co.

The Vickers hardness was plotted as a function of true strain in Fig. 1. The hardness increases with increasing of true strain. Stress-strain curves obtained by tensile test were

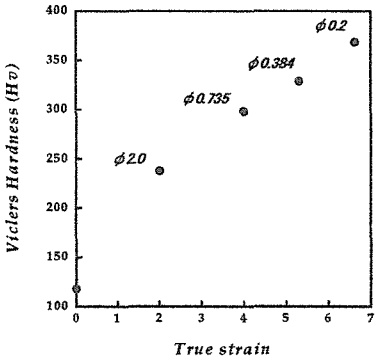

Figure 1: Hardness as a function of true strain given by the drawing.

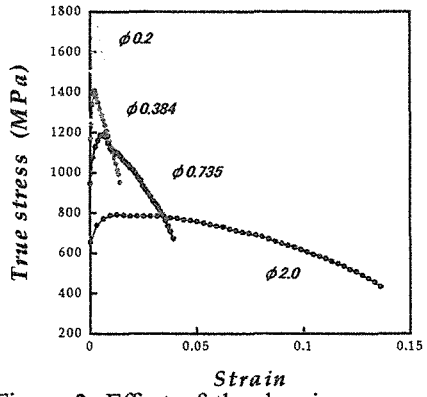

Figure 2: Effect of the drawing on nominal stress-strain curves of wires at room temperature.

shown in Fig. 2. As seen, strength increases but uniform elongation decreases with true strain. This is consistent with the stress-strain behavior observed in ultra-fine grained ferritic steels produced through mechanical milling and sintering, ECAP or ARB.

The lattice plane spacing was measured by neutron diffraction using RESA. Figure 3 shows

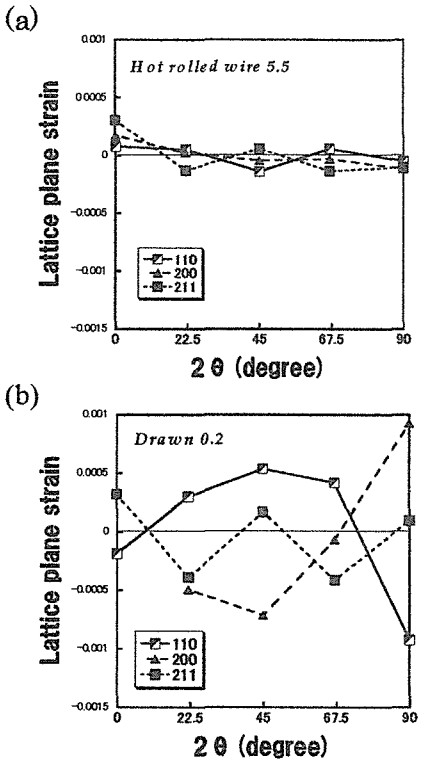

Figure 3: Residual lattice plane strains as a function of the angle with respect to the drawing direction.

the lattice plane strains of specimens measured in various directions for (110), (200) and (211). In hot-rolled samples (a), the dependence of the observing angle and (hkl) plane seems to be within an experimental error, i.e., no residual stress. However, the influence of the observing angle and (hkl) plane employed are obviously found in drawn wires with 0.2 mm in diameter (b). Such dependence is very similar to that found in a pearlite steel. It is hence made clear that the lattice plane strains, i.e., residual stresses, are remained after the drawing in a ferritic steel as well as a pealitic steel. This is a kind of classical concept of Heyn stress, that is, grain stress.

The residual stress was relieved by annealing. Figure 4 shows the influence of annealing temperature on lattice plane strain (annealing time: 3.6 ks). The residual stress was relaxed by recovery and/or recrystalization. Figure 5 shows the effect of annealing temperature on hardness. It is reported that only the grain growth occurs in an ultra-heavily deformed specimen because the continuous recrystallization took place during the deformation. The hardness behavior of the heavily drawn wires are similar to that of such grain growth.

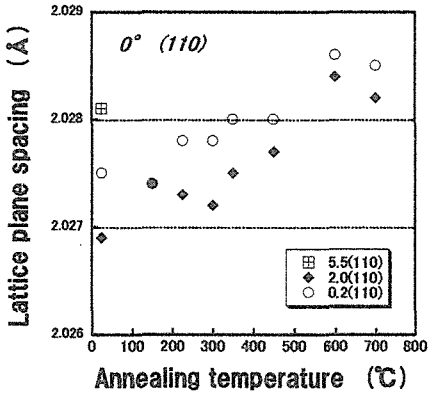

Figure 4: Stress relaxation behavior with annealing.

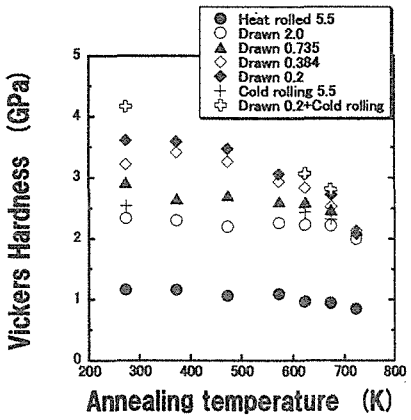

Figure 5: Influence of annealing on hardness.

The *in situ* neutron diffraction during tensile deformation was also performed using RESA. It is found the lattice plane stain of 0.007 was measured when 1.4 GPa was applied to a 0.2 mm wire. The present samples are therefore very suitable to study the ultra-fine grained specimens.

REFERENCES

1. K. S. Kumar, S. Suresh, M. F. Chisholm, J. A. Horton and P. Wang: Acta mater. **51** (2003) 387.
2. D. Jia, K. T. Ramesh and E. Ma: Acta mater. **51** (2003) 3495.
3. For example, S. Takaki: Materia (Japan) **41** (2002) 418.

2.6.13 HRPD study on FeCo-Zr-O soft magnetic films

M. OHNUMA, J. SUZUKI[1] and Y. ISHII[1]

National Institute for Metals, Tsukuba, Ibaraki 305-0047
[1]Advanced Science Research Center, JAERI, Tokai, Ibaraki 319-1195

Magnetic materials for application in recording heads are required to have a high saturation magnetization, high magnetic permeability at high frequencies and low coercivity. Xiong et al.[1)] reported that $(Fe_{0.65}Co_{0.35})_{99}99O_1$ sputtered film shows high saturation magnetic induction (B_s=2.45 T) and low coercivity (H_c=400 A/m) after annealing at 470 °C for 1 hour, while the as deposited films show large coercivity over than 8000 A/m. The peak width in profiles corresponding to bcc-Fe(Co) phase becomes sharp by annealing indicating the internal stress are released by annealing. Although the stress relief can decrease the coercivity, the obtained coercivity value is still smaller than the one for bcc-FeCo phase. One possibility which can explain the decreasing coarcivity is the existence of ordered FeCo phase whose anisotropy constant is known to be small. Neutron diffraction is the only technique that can detect ordered FeCo phase because scattering length of Fe and Co is almost same for XRD but they are different for ND. For clarifying the existence of ordered FeCo phase, we measured neutron diffraction patterns of sputtered $(Fe_{0.65}Co_{0.35})_{99}99O_1$ film. The samples are made by sputtering on polyimide films with 8 micron thick. The films with 100 mg (total weight with polyimide films) for as deposited and 50 mg for annealed samples are put into V holder. Figure 1 shows a profiles for as Deposited films. a simulated profile for CsCl type ordered FeCo phase are also shown in the lower part. Although the (100) peak is not visible because of low S/N, a peak corresponding to (111) peak appears at 66 degree indicating the existence of ordered phase even in as deposited film. The (111) peak become relatively clearer after annealing suggesting small increment of volume fraction of ordered phase. A series of fundamental peaks become sharp by annealing, which is same with the result of XRD measurements, indicating the stress relief. Therefore, we can conclude that decreasing of coacivity is due to both the stress relief and increment of volume fraction of ordered phase. The former is seems to be dominant because the ordered phase is already formed in as-deposited condition. As a summary we confirm the existence of ordered FeCo phase which can explain the low coercivity of $(Fe_{0.65}Co_{0.35})_{99}99O_1$ film.

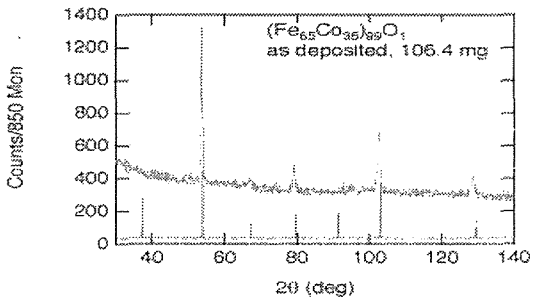

Figure 1: Neutron Diffraction pattern of as-deposited film.

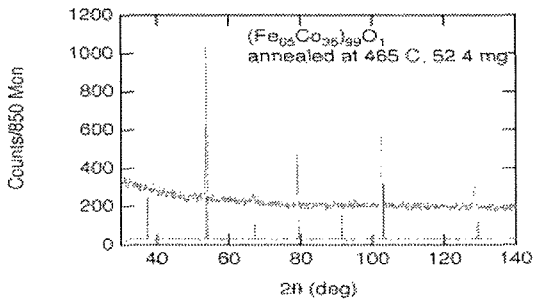

Figure 2: Neutron Diffraction pattern of annealed film.

References

1) X.Y. Xiong, M. Ohnuma, T. Ohkubo, D.H. Ping, K. Hono, S. Ohnuma, H. Fujimori, and T. Masumoto: J. Magn. Magn. Mat., in print.

2.6.14 Inside Residual Stress Measurement of Quenched Steel by Neutron Diffraction Method

R.Mukai[1],D.Y.Ju[1],N.Minakawa[2],Y.Morii[2],and A.Moriai[2]

[1]Department of Material Science and Engineering, Saitama Institute of Tech, Okabe, Saitama 369-0293
[2]Advanced Science Research Center, JAERI, Tokai, Ibaraki 319-1195

The measurement of residual stress by the neutron diffraction method has difficulty in case of the material being thermochemical treated such as quenching, etc. As the factor, it is necessary to measure the non-distortion diffraction lattice spacing d_0[1]. Since the lattice spacing is variable depend on the composition and microstructure, d_0 is not uniform in the heat treated material in which various phase transformations were generated. In addition, since it changes also with fraction of the microstructure, the microstructure distribution must be sufficiently grasped in order to measure the residual stress with multiple microstructures.

This study measures residual stress in the cylinder steel with phase transformation after quenching using the equipment RESA (Residual Stress Analysis Equipment) installed at the JRR-3M of JAERI. Moreover, from metallo-thermo-mechanical theory, coupled simulation by finite element method is carried out, and the residual stress considering phase transformation is predicted. Then, the experiment results and calculated values are compared and examined.

The measurement principle is completely equal to diffraction method by the X-ray only one different point is it could get the internal distribution of three-dimensional stresses. By agreeing on the scattered neutron in striking the neutron on the material, the phase produces the resistant diffracted ray when next Bragg's the diffraction condition is satisfied.

$$\lambda = 2d \cdot sin\theta \qquad (1)$$

Here, λ is a neutron wavelength, d is the lattice spacing and θ is diffraction angle. Strain ϵ is required for by the following formula from lattice spacing d required from degree of angle of diffraction.

$$e = \frac{d - d_0}{d_0} = -cot\theta_0 \cdot \Delta\theta \qquad (2)$$

Here, d_0 and θ_0 are the lattice spacing and diffraction angle for non-distortion state. The peak position of the diffraction profile approximates the diffraction profile by Gaussian distribution, and it is determined by the center line.

In the neutron diffraction method, stress is required by the measurement of total strains in space, since the stress is not obtained only by measuring the uniaxial strain. For the analysis in cylinder coordinate system, from equation (2), the stress is required from the measured strains, when distortion ϵ_R of radius direction, distortion ϵ_H of hoop direction and distortion ϵ_A of axial direction were measured, in the following equations. Stress σ_R of radius direction is given by equations (3).

$$\sigma_R = \frac{E}{(1+\nu)(1-2\nu)}\{\epsilon_R(1-\nu) + \nu(\epsilon_H + \epsilon_A)\} \qquad (3)$$

Stress σ_H of hoop direction, stress σ_A of axial direction are also similar.

When calculating stress from the direction distortions using equation (3), Young's modular E and the Poisson's ratio ν are needed. There was the diffraction plane dependence in these, and in this study, the (110) plane was measured.

In residual stress measurement by the neutron diffraction method, it is necessary to measure d_0 lattice spacing of the non-distortion state. The material used ϕ 3 × 20mm cylinder of carbon steel S45C on the d_0 measurement test piece. And, in order to investigate the change of d_0 by quenching condition, four kinds of pieces of a quenching examination, normal, air-cooling, oil quenching, and water quenching, were used. In addition, the beam slit width is 20mm × 20mm.

The diffraction profile obtained in the measurement is shown in Fig.1. In the case of quenching, from this profile we could obviously see, the peak is shifting to low-angle side, and turns lower and wider simultaneously. This is regarded as the reason of the martensite phase transformation occurred by quenching. The measured results of θ_0 and d_0 for S45C in the neutron diffraction measurement is shown in Table.1. From these results, it is proven that considering the microstructure distribution is important for residual stress measurement in the quenching material.

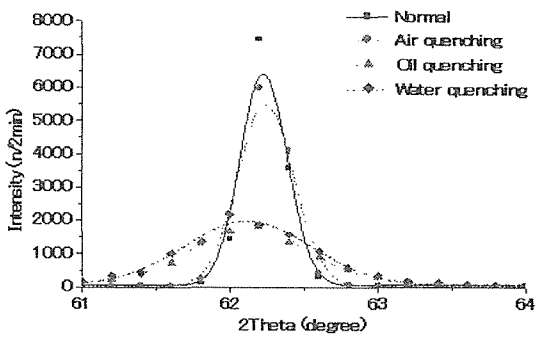

Figure 1: Diffraction profile.

Table 1: Physical properties value of (110) plane.

Measurement conditions and result Quenching condition	Wavelength λ (Å)	Non-distortion diffraction angle θ_0(deg)	Non-distortion diffraction lattice spacing d_0	Young's modular E(GPa)	Poisson's ratio ν
Normal	2.097210882	62.23787	2.028914	242.3	0.278
Air cooling	2.097210882	62.24275	2.028828	231.8	0.259
Oil quenching	2.096931247	62.12606	2.031986	222.6	0.236
Water quenching	2.097210882	62.10950	2.032745	217.8	0.221

The change of lattice spacing was measured by the neutron diffraction method, while tensile test was carried out. This time, a Young's modulus in the (110) direction is required, because to carry out the residual stress measurement of the cylinder was the (110) plane. And, Poisson's ratio was obtained from (110) and shrinkage percentage of the rectangular direction. Quenching condition and beam slit width of the measurement test piece are similar to the d_0 measurement. The measurement result is shown in Table.1. From the result, both Young's modulus and Poisson's ratio have lowered, as the cooling speed is rapider. The martensitic phase mainly produces this, and it is proven that the strength increases.

A cylinder test piece (Fig.2) was used as the specimen to the residual stress water quenching. Measurement points are the 6 points of 0,3,5,7,8.5,9.4mm from the center of the 30mm height. In addition, simulation using heat treatment analysis program COSMAP is also carried out in order to predict the microstructure distribution with the residual stress. Analytical model by the simulation used two-dimensional half model, which made central axis the symmetry. All node numbers are 2541, and all number of element are 2400. Condition of constraint fixed all nodes, which there was taking all nodes as X direction in central axis at the 30mm height in the Y direction. And, 3 edges except for the central axis were handled and were set as heat transfer boundary condition. Then, martensite distribution by simulation is Fig.3.

From the proportion of the martensite phase calculated by simulation analysis, d_0 E and ν were decided at the every measurement point. It is shown in residual stress measurement result Fig.4 of (110) direction by the neutron diffraction method of cylinder test piece. In the central part, from neutron diffraction measurement result, tensile stress is measured direction of 3 axes. However, with approaching on the surface, it becomes compressive stress in the axial direction. These are typical residual stress in the quenching material. From these results, it seems to improve the accuracy of residual stress measurement by the neutron diffraction method, if the distribution of the microstructure is grasped in detail.

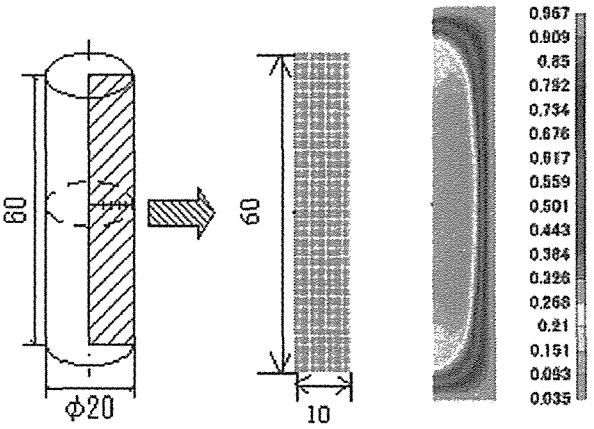

Figure 2: Measurement test piece and analysis model (unit mm).

Figure 3: Martensite distribution by simulation.

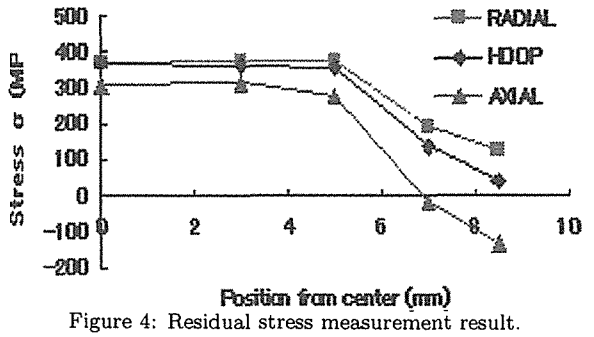

Figure 4: Residual stress measurement result.

In this study, d_0, E and ν by the difference between volume fraction of martensite phase were measured with the test piece after various quenching processes using neutron diffraction method. It was possible to clarify the relationship between microstructure and residual stress in the neutron diffraction method by introducing those values into residual stress measurement inside the material, and comparing with the simulation analysis result.

References

1) T. Saito, N. Minakawa, Y. Morii, T. Sasaki and Y. Hirose: J. Soc. Mat. Sci. Japan Vol. 50, No. 7, (2001) p.702

2.6.15

Compatibility study of SS316 with Pb-Bi by neutron diffraction method

K. Kikuchi, N. Minakawa, A. Moriai and Y. Morii

Advanced Science Research Center, Japan Atomic Energy Research Institute, Tokai, Ibaraki, 319-1195

Lead bismuth target has been studied as a spallation neutron source of accelerator-driven nuclear transmutation system, ADS. The ADS aims at managing long-lived high-level waste as minor actinides, MA, and long-lived FP in order to reduce the burden of waste disposal. Proton beams injected from accelerator react with spallation target produce neutrons and transmute the waste in the fuel. In this system lead bismuth is used as target material and reactor coolant. Advantage for usage of lead-bismuth is that a melting temperature of the lead-bismuth alloy is quite low, 125°C, in the ratio of 45 Pb/55 Bi (wt%) and small neutron absorption enables the lead-bismuth a candidate for coolant in sub-critical reactor. Material issue of the system is corrosion. In order to know corrosion of the material, flowing lead-bismuth experiment was done under the condition of 450°C maximum temperature and 50°C temperature difference during 3000 hrs. Figure 1 showed neutron radiography image (JRR-3) of tube cut from the circulating loop. After drain out Pb-Bi from the loop it still existed in the circulating tube. Figure 2 showed cross section of the tube. It showed that corrosion depth of SS316 was 0.1 mm. Tested tube was 12 mm in diameter and 2 mm in thickness. Our interest is to know the substantial depth of mass transfer by diffusion from flowing Pb-Bi to SS316 tube thickness. Figure 3 and 4 showed the result of neutron diffraction experiment of tube after and before flowing test. X-axis means the position from the outer surface of the tube. So x=2 indicates the inner surface of the tube. After the test Pb-Bi remained in the tube. Measured length is extended to 2.5mm. Bismuth and Pb oxides were formed in the adhered area. They consist of different type of oxides. We looked at only the 2-theta fitted assuming the Gaussian distribution and the peak area for SS316 (200). The results showed that SS316 (200) was disturbed by Pb-Bi in the range of x=1.5 to 2 mm roughly. So corrosion depth after 3000 hrs operations was 0.1 mm but the tube was affected by 0.5mm length in the lattice arrangement.

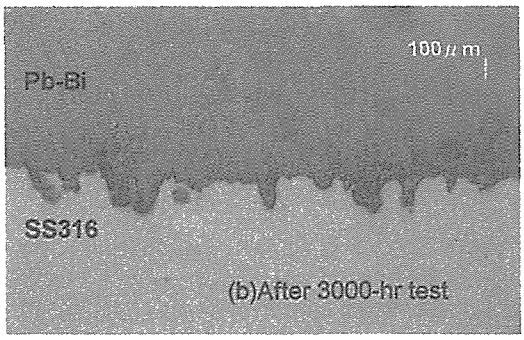

Figure 1: Cross-section of circulating lead bismuth loop.

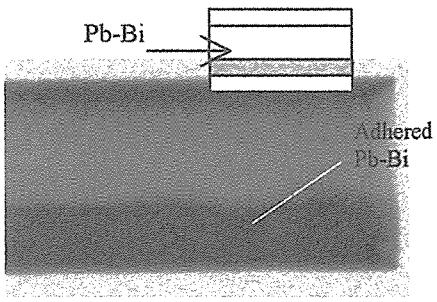

Figure 2: Neutron radiography image (JRR-3) of tube cut from the circulating loop.

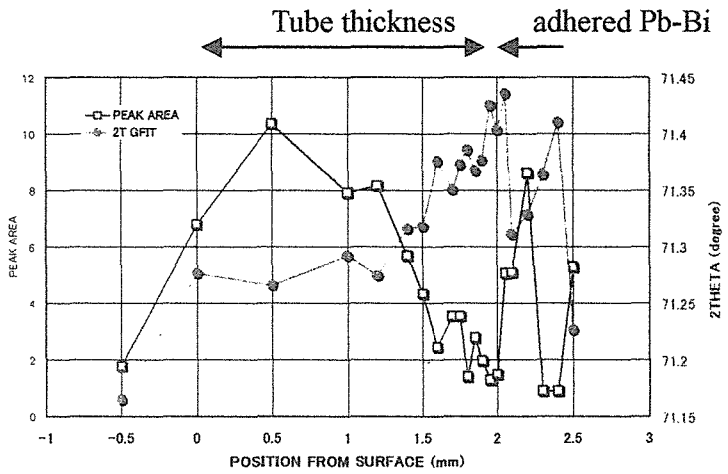

Figure 3: Two theta and peak area distribution of Pb-Bi adhered SS316 (200) after the flowing test.

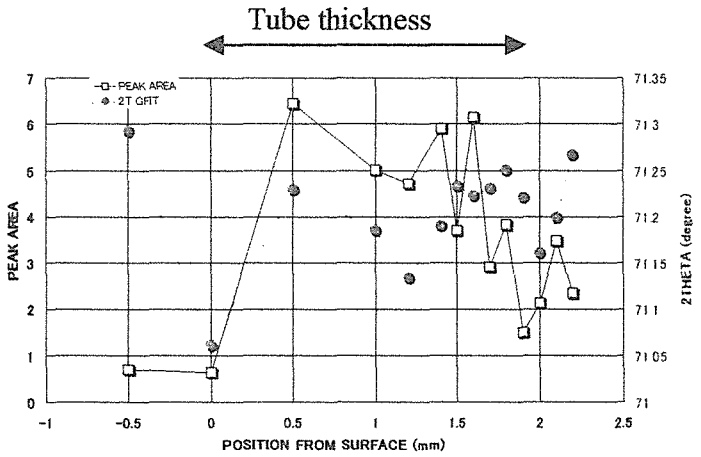

Figure 4: Two theta and peak area of SS316 (200) tube before the flowing test.

2.6.16 Neutron Diffraction Measurement of Residual Strain of Partial Penetration Welds for ITER Vacuum Vessel

M. NAKAHIRA, A. MORIAI[1] and N. MINAKAWA[1]

Department of ITER Project, JAERI, Naka, Ibaraki 311-0193
[1]Advanced Science Research Center, JAERI, Tokai, Ibaraki 319-1195

The vacuum vessel (VV) of ITER is a double-walled "doughnut" structure made of stainless steel SS316L with D-shaped cross section. The development of the partial penetration welding by through-wall electron beam welding (EBW) is carried out for the T joint of the outer shell (40-60mm plates) and the rib, because it has advantage from distortion and cost points of view. In this study, neutron diffraction measurement of residual strain of this new welding had been carried out in order to investigate an applicability of the welding to the VV. The configuration of weld and the measurement positions of residual strain are shown in Fig. 1. RESA (Neutron Diffractometer for -REsidual Stress Analysis) in the JRR-3 is used for the measurement. The results in last year showed that the wider slit area was required to obtain sufficient neutron intensity within practical exposure time, because the test piece was thick. The slit of 2 × 15 mm was used this time (3 × 3 mm was used at last time). The neutron intensity was obtained in the toroidal direction. The test condition and results are shown in Table 1 and Fig. 2, respectively. D-space is the lattice length and the unit is Å. The exposure time of each step is 5 min. The result shows that the area of weld metal which leis in 3.5 to 8.5 mm from sample surface has larger lattice length. It can be considered that the tension stress remains in toroidal direction at weld metal. Other two directions are under measuring with more exposure time, because path length of neutron is much longer than the toroidal direction measurement. The result will be obtained in next fiscal year.

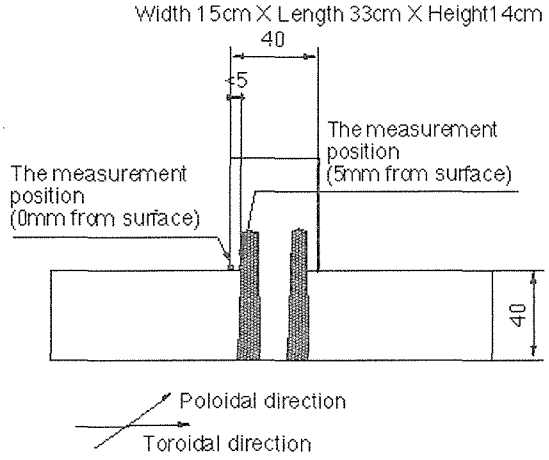

Figure 1: The configuration of weld specimens and the measurement positions.

Table 1: Test conditions

Structure	Wave length (Å)	Slit(mm)
FCC (220)	2.09632	2W × 15H

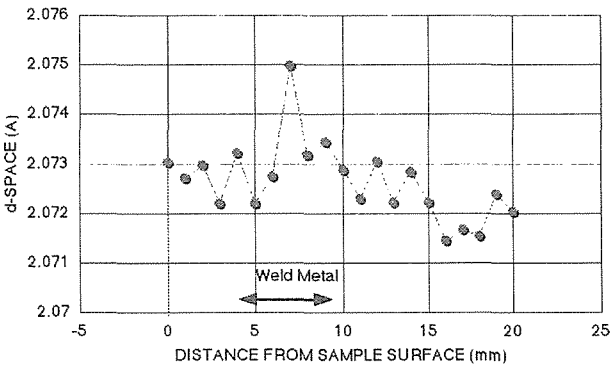

Figure 2: Obtained lattice length.

2.6.17 Phase Transformation in Smooth Specimen and at Notch Root in Shape Memory Alloy TiNi

Y. AKINIWA, H. KIMURA, K. TANAKA, N. MINAKAWA[1] and Y. MORII[1]

Department of Mechanical Engineering, Nagoya University, Nagoya 464-8306
[1]Advanced Science Research Center, JAERI, Tokai, Ibaraki 319-1195

1. Intruduction

The equiatomic TiNi alloy is an intermetallic compound that shows not only excellent resistance against corrosion and wear but also shape memory effect with large recovery strain and superelasticity. Though TiNi has been used for pipe couplings and the frames of glasses utilizing the shape memory effect and superelastic property [1], the practical application is limited because the fatigue properties of TiNi has not been fully clarified. In addition to the conventional use, TiNi has attracted attention as an actuator of intelligent structure in recent years and the fatigue reliability over long-term use has been recognized as an important subject in the utilization [2]. In order to evaluate the fatigue properties, it is necessary to understand the martensitic transformation behavior under applied loads, especially at stress concentration area.

In this study, stress-induced martensitic transformation was investigated in shape memory TiNi, hereinafter denoted as FML4, and superelastic TiNi, FML6. The smooth specimen and notched specimen were utilized for the measurement by neutron diffraction patterns in order to clarify the overall martensitic transformation and the local transformation around the notch root.

2. Materials and measurement

Shape memory TiNi, FML4, was heated to 450 degrees Celsius in order to introduce shape memory effect at room temperature. Superelastic TiNi, FML6, was heated to 750 degrees Celsius to introduce superelastic property at room temperature. Because the martensitic transformation start temperature of FML4 is 21 degrees Celsius, it is composed of austenitic and martensitic phases at room temperature of approximately 20 degrees Celsius without loading. On the other hand, the martensitic transformation start temperature of FML6 is -60 degrees Celsius. Therefore, it is fully austenitic at the room temperature without loading.

Smooth specimens with the dimension of 10 x 70 x 2 mm^3 were prepared. Single-edge-notched specimens with the same dimension containing a notch of 1 mm at the center were also prepared. The specimens were shaped by electrical discharge machining followed by electrolytic polishing.

The neutron facility of JAERI (RESA) was used for the neutron diffraction measurement. The wave length of the beam was 0.21009 nm with the preset time of 1800 sec. The diffraction planes of (110) in austenite and (022) in martensite were employed for the measurement.

3. Martensitic Transformation in Smooth Specimen

The phase transition was investigated by neutron diffraction measurement under the applied stress of 5, 50, 100, 200, 350, 550MPa and 5 MPa during unloading in a smooth specimen. The results of the diffraction intensity from austenitic (110) and martensitic (022) phases in FML4 are presented in Fig.1 and Fig.2, respectively. Under the stress level of 100 MPa, only austenitic phase was observed. At the stress level of 100 MPa, the existence of both the austenitic and martensitic phases were confirmed. Above the stress level of 100 MPa, the austenitic phase disappeared and martensitic phase remained even after unloading.

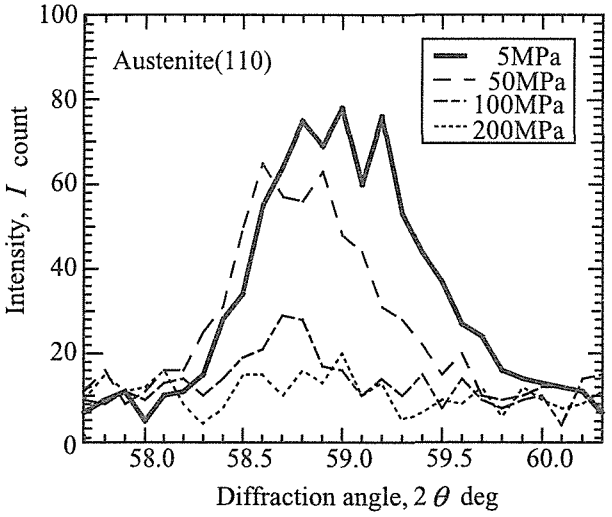

Figure 1: Results of neutron diffraction in FML4 (Austenite)

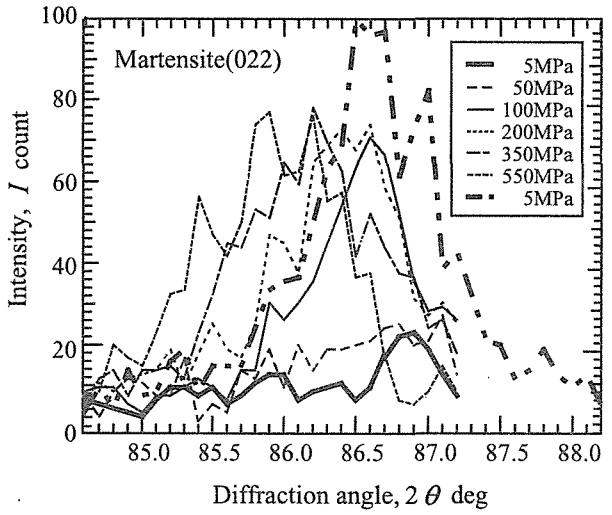

Figure 2: Results of neutron diffraction in FML4 (Martensite)

4. Martensitic Transformation at Notch Root

The distribution of martensitic phase at notch root was also investigated. Load of 33 N was applied on the specimen with the sectional dimension of 6 x 3 mm^2 under 4-point bending with the outer span of 60 and inner span of 20 mm. The width of the incident beam was 0.3 mm with the preset time of 1800 sec. The diffraction profiles at 14 measurement points marked by x in Fig.3 were obtained. The contour of the stress-induced martensitic phase was determined as depicted in the figure. The result shows that the stress-induced martensitic phase stretched about 0.5 mm from the notch root to the direction of the notch. It was found to stretch further in the perpendicular direction. Based on this result, the stress induced martensitic phase at a crack tip, which is indispensable to understand the fatigue crack propagation behavior in those materials, can also be expected to be measured in the same manner.

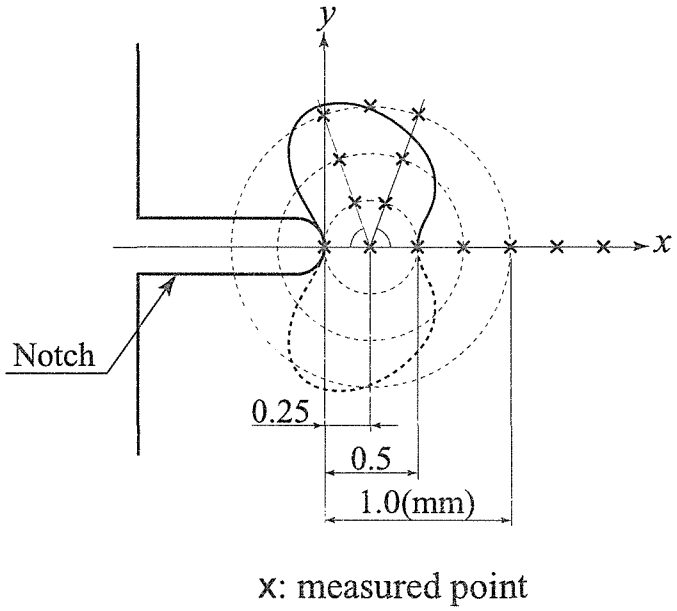

Figure 3: Martensitic phase at notch root

5. Conclusion

(1) The phase transition from austenite to martensite was observed at the stress level of 100 MPa. The existence of the residual martensitic phase was confirmed in the shape memory TiNi.

(2) The distribution of martensitic phase at notch root was measured. It was found to stretch further in the direction perpendicular to the notch. The measurement by neutron diffraction was found to be effective to determine the distribution of stress-induced martensitic phase at a crack tip by enabling the measurement at a small local area.

References

1) H.Sakamoto: Trans. Jpn. Inst. Met. **24** (1983) p. 665.

2) H. Tobushi: J. of JSTP **35-403** (1994) p. 910.

2.7 Instrumentation and Methods

2.7.1

2-dimensional Characteristics of $SrBPO_5:Eu^{2+}$ Photostimulable Phosphor

K.SAKASAI, M.KATAGIRI, K.TOH, H.TAKAHASHI[1], M.NAKAZAWA[1], and Y.KONDO[2]

Neutron Science Research Center, JAERI, Tokai, Ibaraki 319-1195
[1]Dept. of Quantum Engineering and System Science, University of Tokyo, Tokyo, 113-8656
[2]Dept. of Applied Physics, Tohoku University, Sendai 980-8579

The neutron imaging plate (NIP) has made a great success in the field of neutron scattering study but the NIP is sensitive to not only neutron but also gamma ray. Therefore, it is difficult to discriminate neutron signal from gamma ray one when the NIP is read out. To overcome the problem, the authors have been studying a $SrBPO_5:Eu^{2+}$ material as a new neutron storage phosphor consisting of light materials.

The $SrBPO_5:Eu^{2+}$ powder sample was prepared by firing raw materials ($SrCO_3$, H_3BO_3, $(NH_4)_2HPO_3$, and $EuCl_3 \cdot 6H_2O$) in a muffle furnace in a nitrogen atmosphereat 600°C for 2 hours and at 800°C for 2 hours. A disk-like sample with a diameter of 12 mm and a thickness of 1mm was prepared for 2D image measurement. This sample was made by the Spark Plasma Sintering (SPS) method. In the SPS method, the $Sr^{10}BPO_5:Eu^{2+}$ (2%) powder was set in a carbon vessel and then fired for 10 minutes at 800°C. The powder sample was pressed with a stress of 5 kN in a vacuum atmosphere throughout the firing.

After the sample was irradiated with a collimated neutron beam with a diameter of 1.5 mm, its surface was scanned with focused laser light by using an X-Y stage controller. The neutron flux and neutron irradiation time were 3.1 x 10^4 n/cm^2/s and 30 minutes, respectively. The scanning was carried out every 0.25 mm on the sample surface. The results are shown in Fig.1. The beam intensity image can be clearly obtained. Fig.2 shows the edge spread function measured with the sample, where half of the surface (left side) was irradiated with neutrons. Although Lorentzian line spread function (LSF) is usually applied to photographic film, the imaging plate detector's LSF was reported to have a strong similarity to Gaussian[1)]. Therefore the authors fitted the data in Fig.2 by ESF of a Gaussian LSF and estimated the spatial resolution to be about 0.4 mm when FWHM of LSF is defined as the spatial resolution.

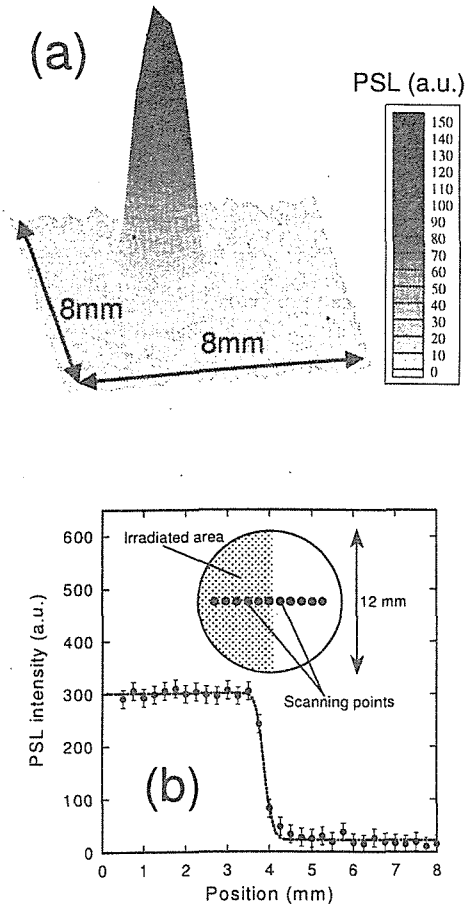

Figure 1: (a) A collimated neutron beam image obtained with the sample. The beam size was 1.5 mmϕ. (b)The measured the edge spread function.

References

1) Jens Hofmann and Christian Rausch : Nucl. Instrum. Methods **A355** (1995) 494.

2.7.2 An Elastically Bent Si Monochromator to Share the Whole Beam Neutron Size Tandem Among Three Diffractometers

I. TANAKA[1], M. REFAI-MUSLIH[2],
K. KURIHARA[1] and N. NIIMURA[1,3]

[1]Neutron Science Research Center, JAERI, Tokai, Ibaraki 319-1195
[2]National Nuclear Energy Agency, BATAN, Indonesia
[3]Faculty of Engineering, Ibaraki Univ., Hitachi, Ibaraki 316-8511

Neutron is a very rare and powerful probe for structure determination and dynamics observation of materials in an atomic resolution. Because the number of relatively-higher-flux neutron sources and the beam ports are so limited compared to that of other probes, it is important to use them efficiently. From this standpoint, it is well known that beams with tall height cross-section at the guide halls have been shared by several instruments but each instrument is allocated a particular beam height width not to decrease the beam intensity in the spectrum which may be absorbed or scattered by upstream instruments. On the other hand, at 1G port in the reactor hall in JRR-3, there are three instruments. Two of them are diffractometers for biological macromolecules; BIX-4 [1], BIX-3 [2], and One of them is a high resolution powder diffractometer; HRPD (from upstream). They share whole height and width beam cross section by Elastically Bent Perfect Silicon (EBP-Si) monochromators [3] one another. EBP-Si is one of the most useful monochromators, which realizes higher transmission compared to PG in wider spectrum with focusing effect and so on.

When EPB-Si monochromators are set at the 1G beam port so that they cover the whole cross section; 45mm in width and 80mm in height at the BIX-3 monochromator position, not a small absorption was observed by HRPD monitor counter under various conditions of BIX-4 and BIX-3 monochromators (Fig.1). BIX-4 had Si(111) monochromator with 10mm in thickness, curvature R$\sim$4.1m (300 μ strain) and 49° in $2\theta_M$ (λ=2.60$\AA$).

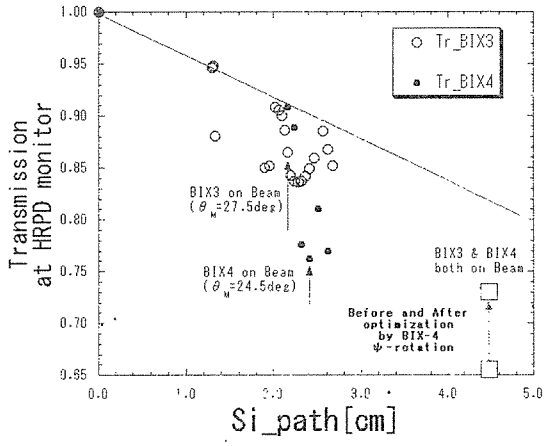

Figure 1: Neutron transmission of BIX-4 and BIX-3 at HRPD monitor count at 1G port at JRR-3. Horizontal is the total thickness of EBP-Si monochromators corresponding to ω angles. Vertical axis is normalized transmission. Open circle: BIX-3 monochromator ω-scan without BIX-4's (down). Closed circle: BIX-4 ω-scan without BIX-3's (down). Solid line are absorption curve when absorption coefficient μ is twice of the table value (0.02 cm^{-1}). Open square: Normal transmission with BIX-3 and BIX-4 are on beam.

BIX-3 had Si(111) with 10mm in thickness, R$\sim$3.4m (400 μ strain) and 55° in $2\theta_M$ (λ =2.90$\AA$), and HRPD had hot-pressed Ge(331) with 89° in $2\theta_M$ (λ =1.82$\AA$). The monochromator Si plates were cut from ingots, purchased from Shin-Etsu-Kagaku Co. Ltd., Japan, whose conductivities were not determined, and the surfaces were treated by chemical etch so that the larger surface was 250mm in width and 20 to 40mm in height. 4 plates of 2.5mm in thickness were stacked.

To measure the R dependence of EBP-Si monochromator, transmission/absorption of EBP-Si for certain neutron wavelength

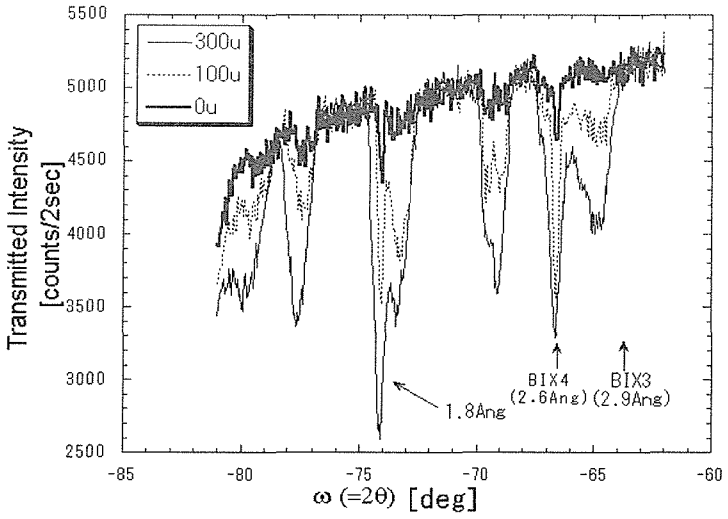

Figure 2: 1.82Å neutron transmission curvature dependence of EBP-Si(111) 10mm thickness at TAS-2. Horizontal axis is ω angle of EBP-Si sample. 0u, 100u and 300u corresponds to the curvature in strain gauge (μ strain); R$\sim\infty$, 12m, 4.1m, respectively. Arrows and numbers (wavelengths) correspond symmetric Bragg conditions of ω angle at TAS-2 for all instruments at the 1G port, respectively.

(1.82Å) for each R was examined (Fig.2). The EBP-Si(111) sample dimension was 250 x 40 x 10 (4 plates stacked in thickness) mm and Si(111) plane was 250 x 40mm^2. The stronger the curvature of EBP-Si became, the deeper the absorption dips became. It is thought that these absorption-dips were caused by asymmetric reflections of sample EBP-Si monochromator crystal. The absorption was at most 30% for all ω rotation of sample crystal except the exact symmetric Bragg condition of the sample. Then the EBP-Si sample was rotated and scanned around ψ axis (perpendicular to the plane of Si(111)) at the BIX-4 ω angle (Bragg condition). Significant difference of transmission was observed (Fig.3). This fact was quickly expected to improve the transmission at the 1G port.

When the BIX-4 monochromator was rotated around ψ axis by 1.5°, the transmission of 1.82Å neutrons of BIX-4 and BIX-3 was improved from 66% to 73% at HRPD monitor counter just like square plots in Fig. 1.

Computer simulation was also tried to explain and predict something valuable to design monochromators to share neutron beam at higher level.

In this way, with relatively minimum loss of neutrons in the downstream instrument(s), beam sharing with more instruments was established by EBP-Si monochromators. Though there are still some problems in shorter wavelengths, but this beam sharing procedure will stimulate the higher level utilization of neutron beam.

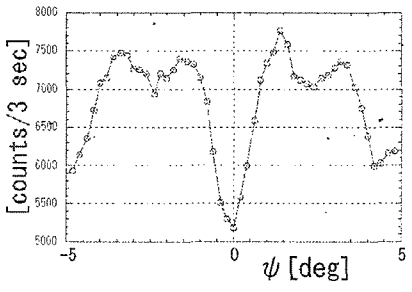

Figure 3: ψ-scan profile under BIX-4 monochromator Bragg condition at TAS-2.

References

1) K. Kurihara *et al.*: J. Synchrotron Rad. (2003) *submitted.*
2) I. Tanaka, K. Kurihara, T. Chatake and N. Niimura: J. Appl. Cryst. **35** (2002) 34.
3) I. Tanaka, N. Niimura and P. Mikula: J. Appl. Cryst. **32** (1999) 525.

2.7.3 Neutron Beam Enhancement with a HOPG Pre-Crystal

H.TOMIMITSU, Y.HASEGAWA[1] and K.AIZAWA[2]

Advanced Science Research Center, JAERI, Tokai, Ibaraki 319-1195
[1]Atominstitut, Austria University, Wien, Austria A-1020
[2]Center for Proton Accelerator Facilities, JAERI, Tokai, Ibaraki 319-1195

In the research on the development and application of the neutron interferometry[1,2], we often feel the insufficiency of the neutron beam intensity. Therefore, we are trying to realize a convenient and practical method to enhance the neutron flux.

Neutron experiment was carried out at the PNO apparatus in the JRR-3 of JAERI. With the double monochromator system of the highly oriented pyrolytic graphite (HOPG) with the mosaic spread of 0.4 deg., the collimation being of 30min. We measured the intensity I_o diffracted by the Si plate with 220 reflection put directly in the incident beam without any pre-crystal, and the intensity I_p diffracted in the diffraction beam from the pre-crystal, and compared $I_p/\ I_o$ with unity. We also observed their FWHMs. In every case, with the original $10*10mm^2$ beam, the $3*3mm^2$ slit was used as the incidence slit for the following Si plate.

As the pre-crystal, we tryed the asymmetric reflection of a silicon perfect crystal, and also the asymmetric reflection of imperfect single crystals, such as Cu-based alloys, Ni-based super alloy, in addition to the HOPG.

After all, we found a simple but useful effect with a flat HOPG pre-crystal in the symmetric arrangement, beam enhancement by around 3 times with 2Åwavelength[3], Fig.1. We studied further on the nature of the effect, and got the results as follows.

(1) Both surfaces of a HOPG plate showed the similar result, by around 3-times enhancement and with improved FWHM by around one third with 2Åwavelength. These seem to suggest that the beam-enhancement is not due to the macroscopic deformation of the HOPG plate, such as concave.

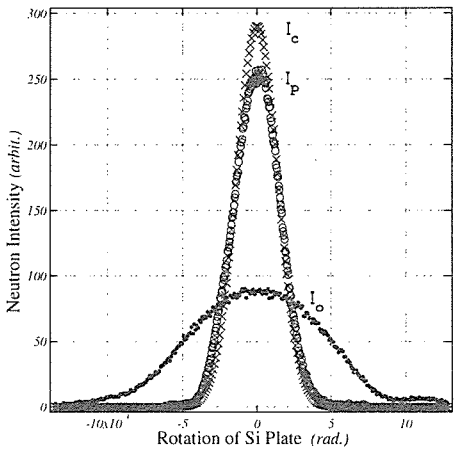

Figure 1: Comparison of the rocking curves of a Si 220 reflection without the pre-crystal (I_o, closed circle) and with a HOPG pre-crystal (I_p, open circle). I_c, crosses, represent the calculated curve, see Text.

(2) We tried, on the other hand, the double or triple thicknesses of the HOPG plate, namely, we measured on the attached two or three HOPG plates, observing the similar rocking curve with that by a single HOPG plate.

(3) In order to ensure the effects mentioned above, we tested on various HOPG plates with each thicknesses, as summarized in the Table 1. All of them were made by the same company as the best grade products, "ZYA" class with mosaicity of 0.4deg., but at the quite different time and with different sizes, especially the thicknesses is quite different. All the HOPGs tested, with the thickness ranging from 1.2 mm to 1.8 mm, showed the similar effect, suggesting that this beam-enhancement is not special nor accidental but general and due to intrinsic nature of the HOPG plates.

Table 1: Summary of results on the peak intensity ratio and on the FWHM ratio by various HOPGs, on both surface, with their thicknesses.

HOPG Pre-Crystal	thickness	Peak Ratio	FWHM ratio
(No pre-crystal)		1.00	1.00
M1-surface	1.8 *mm*	2.40	0.38
back face		2.45	0.33
M2-surface	1.8	1.84	0.35
back face		1.86	0.35
M3-surface	1.8	3.49	0.32
back face		2.96	0.35
T415-surface	1.6	3.43	0.34
back face		3.45	0.33
T4665-surface	1.6	3.22	0.35
back face		2.81	0.35
N1606-surface	1.2	3.21	0.31
back face		3.28	0.32

(4) For all cases above, the observed rocking curves were clearly fitted with the simple Gauss-functions. This strongly suggests that the pre-crystal make the incident-beam-divergence narrower at once with a single cause, rather than multiple causes.

(5) Once, we tested instantly this beam-enhancement effect on a LLL-type interferometer in order to ensure whether we can really utilize the effect or not. We could clearly recognize the beam intensity being kept more than twice, and furthermore the oscillation was clearly seen in the profile with pre-crystal.

(6) The phenomenon of the beam enhancement by a HOPG pre-crystal, mentioned above, seems that another factor in the HOPG reflection, *i.e.* the very sharp distribution of the lattice spacing deviation[4,5], condenses or focuses the original beam divergence into the main direction within around one third, and consequently enhances the peak value by around three times, as compared in Fig.1[6]. In the figure, I_c is the calculated curve with the assumption of the reflectivity of the HOPG equals to unity, I_p being around 85% of I_c with the actual reflectivity.

As the conclusion, a HOPG pre-crystal in symmetric arrangement enhance the neutron flux for the following Si reflection, more than 3 times with 2Åwavelength. This effect can be generally utilized in the so-called precise neutron optics, such as the double LL-type neutron interferometry, for example. The origin of this effect seemed to be explained phenomenologically with the idea of the very sharp distribution of the deviation of the lattice parameter in the HOPG itself.

We are studying this effect on the relation with the wavelengths and with the reflecting planes, and, especially, if the effect can be applied in the case of "imperfect" crystals.

References

1) H.Tomimitsu, Y.Hasegawa and K.Aizawa: *Proc. Int. Conf. Present Status and Future Aspects of Neutron Interferometry*, NSL News Letter 2002-1, ISSP, Univ. Tokyo, 2002, pp.3-6.
2) H.Tomimitsu, Y.Hasegawa and K.Aizawa: JAERI-Report **2002-028** (2002), 124.
3) H.Tomimitsu, Y.Hasegawa and K.Aizawa: Physics Letters **A274** (2000), 175.
4) A.W.Moore, M.Popovici, A.D.Stoica: Physica **B276-278** (2000), 858.
5) T.Keller, K.Habicht: Appl. Physics **A74** (2002), s127.
6) H.Tomimitsu, Y.Hasegawa and K.Aizawa: Physics Letters **A309** (2003), 175.

2.7.4 Performance of the renewed polarization analysis option on TAS-1

M. NAKAMURA, M. TAKEDA, Y. SHIMOJO and K. KAKURAI

Advanced Science Research Center, JAERI, Tokai, Ibaraki 319-1195, Japan

Our research group is currently making efforts to install the CRYOgenic Polarization Analysis Device (CRYOPAD) on thermal neutron triple axis spectrometer TAS-1 at JRR-3M reactor in collaboration with French neutron scattering scientists†. We will be able to carry out the zero-field spherical neutron polarimetry (SNP) by using the CRYOPAD[1].

However, a great improvement of the incident polarized neutron flux is indispensable for utilizing the advantage of SNP. We are currently upgrading the polarization analysis option on TAS-1 spectrometer. Recently, the installation of new Heusler monochromator was completed, and here we report the first neutron test of its performance. A new doubly focusing Heusler monochromator has 140 mm wide and 100 mm height with horizontal focussing mechanism. The vertical focussing is optimized and fixed at E_i=30.5 meV. When installing the new Heusler monochromator on TAS-1, we carefully covered all its non-crystal parts, especially the magnetic york, with B_4C rubber and Cd sheet in order to suppress the back ground.

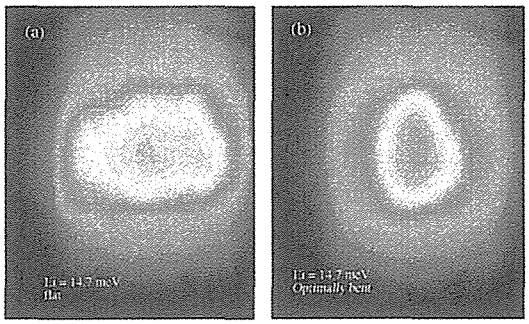

Figure 1: Polarized neutron beam distribution at sample position measured by neutron imaging plate; (a) horizontal bent is zero, that is "flat", and (b) horizontal bent is optimized. Incident neutron energy was 14.7 meV.

We measured the polarized neutron beam distribution at sample position using the neutron imaging plate as given in Fig. 1. It is confirmed that the beam focussing works well as we expected. Figure 2(a) gives the direct comparison of the intensity from the (113) nuclear Bragg peak of Al_2O_3 polycrystal between the old set-up and the new one. The comparison of magnetic scattering intensity is also given in Fig. 2(b), whose intensities are from the para-

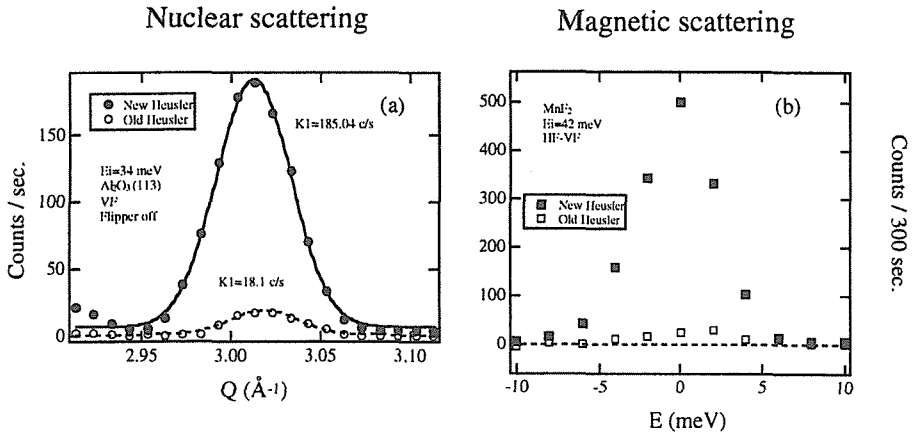

Figure 2: Comparison of the scattered intensity between old set-up and new set-up (a) for coherent nuclear scattering from Al_2O_3 and (b) for paramagnetic scattering from MnF_2.

magnetic scattering of MnF_2. The relation between neutron polarization $\vec{P}$ and scattering vector $\vec{\kappa}$ gives significant information for polarization analysis of magnetic scattering[2]. We refer the experimental geometry $\vec{P} \parallel \vec{\kappa}$ as HF geometry, and $\vec{P} \perp \vec{\kappa}$ as VF geometry. For the spin flip (SF) scattering only the nuclear spin scattering and paramagnetic scattering (NS) contribute. The experiment in HF geometry gives

$$\left(\frac{d\sigma}{d\Omega}\right)_{HF:SF} = \left(\frac{d\sigma}{d\Omega}\right)_{para} + \frac{2}{3}\left(\frac{d\sigma}{d\Omega}\right)_{NS} \quad (1)$$

whereas, in VF geometry

$$\left(\frac{d\sigma}{d\Omega}\right)_{VF:SF} = \frac{1}{2}\left(\frac{d\sigma}{d\Omega}\right)_{para} + \frac{2}{3}\left(\frac{d\sigma}{d\Omega}\right)_{NS}. \quad (2)$$

Therefore, we can obtain the pure magnetic scattering by subtracting $I_{HF:SF} - I_{VF:SF}$, as shown in Fig. 2(b).

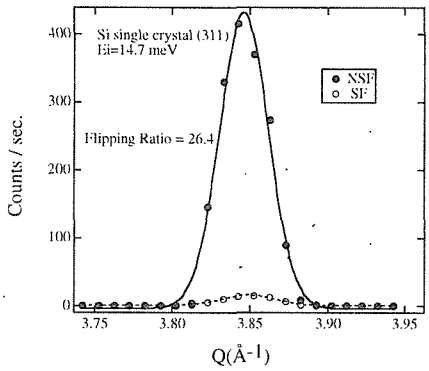

Figure 3: Polarization analysis of the coherent nuclear scattering from Si single crystal.

In addition, the polarization efficiency was estimated from the coherent nuclear scattering of Si single crystal as given in Fig. 3. We confirm that the flipping ratio is 26.4, which means that polarizing efficiency is more than 90%.

By installing the new Heusler monochromator, the data collection rate in the polarization analysis option of TAS-1 increases by a factor 5–15 without decreasing the polarization efficiency as compared to the old setup as demonstrated in Fig. 4. We should

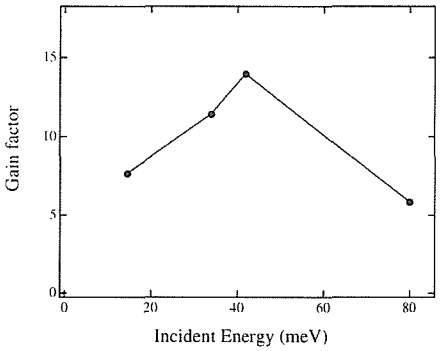

Figure 4: Estimated gain factors by installing the new Heusler monochromator.

note that the analyzer used in these measurements is unchanged, which will be upgraded in the coming fiscal year. New Heusler analyzer is expected to further increase the data collection rate by a factor 4. We have already started the polarization analysis experiments for quantum spin dimer systems, $TlCuCl_3$ and $SrCu_2(BO_3)_2$, using greatly improved polarized neutron beam flux.

References

1) F. Tasset *et al.* : Physica B **267-268** (1999) 69.

2) R. M. Moon *et al.* : Phys. Rev. **181** (1969) 920.

† Dr. F. Tasset (ILL), Dr. E. Leliévre-Berna (ILL) and Dr. L. P. Regnault (CEA-Grenoble)

2.7.5 Development of optical devices for cold neutrons

H. M. Shimizu[1], T. Adachi[1], T. Oku[1], K. Ikeda[1], H. Sato[1], Y. Takizawa[1], K. Morimoto[1], S. Morita[1], H. Ohmori[1], K. Sakai[1,2], F. Tokanai[3], K. Sasaki[4], Y. Kiyanagi[4] and J. Suzuki[5]

[1]RIKEN, Wako, Saitama 351-0198
[2]Department of Physics, Tokyo Institute of Technology, Ohokayama, Meguro 152-8551
[3]Department of Physics, Yamagata University, Yamagata 990-8560
[4]Atomic Science and Nuclear Engineering, Hokkaido University, Sapporo, Hokkaido 060-8628
[5]Advanced Science Research Center, JAERI, Tokai, Ibaraki 319-1195

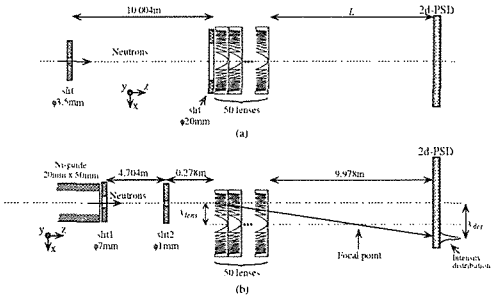

Figure 1: Experimental setups for lens characterization.

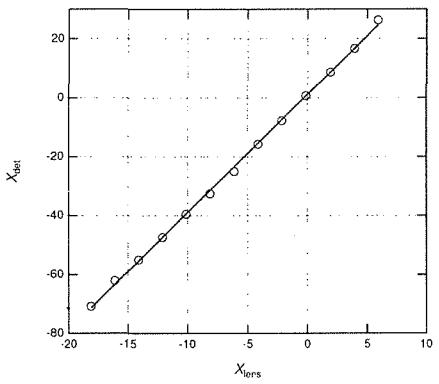

Figure 2: Measurement of the focal performance. The circles represent the observed data. The line is the result to fit with the observed data by least square method. The slope of this line is 4.0 at 1.6 nm. The focal length of 1.6 nm is 2.5 m.

We have developed more penetrative lens in large aperture (45 mm in diameter). Typical application of neutron focusing lens is Focusing geometry Small Angle Neutron Scattering (F-SANS) instruments [1]. Neutron beam can penetrate all aperture area of Fresnel-type lens very well. Considerable gain will be expected compared to Pinhole geometry Small Angle Neutron Scattering (P-SANS).
We have fabricated lens elements made of MgF_2 single crystals which provide an effective scattering potential-energy difference of $(131\text{-}0.00018i)$ neV with respect to vacuum. Each element was made from a 1 mm in thickness and 50 mm in diameter optically polished disk, ground to a Fresnel shape using the electrolytic inprocess dressing (ELID) grinding technique [2]. The detailed design was described before [3]. The root-mean-square roughness (in μm) of the two faces of a lens element is approximately 0.01 (polished side) and 0.2 (ground side). A set of lens elements is composed of 50 disks.
The microstructure in a MgF_2 single crystal was measured by small-angle neutron scattering using the SANS-J instrument at the JRR-3M reactor of JAERI. Little small-angle scattering and high transmission of 0.998 ± 0.001 for 0.8 nm neutrons were observed. The results were described elsewhere [4].
The performance of the compound lens was investigated using a cold neutron beam from the SANS-J instrument at the JRR-3M reactor of JAERI. The experimental setup is shown schematically in Fig. 1. A collimated neutron beam entered the lens, and the transmitted and refracted intensities were measured by a two-dimensional position sensitive detector (PSD) located at 10 m downstream from the center of the lens. The PSD has 128 $\times$ 128 position channels over a 640-mm in diameter sensitive area. The position resolution of the PSD was specified to be 5 mm.
The transmission was measured with the setup in Fig. 1(a). The observed transmission of the lens is 0.829 for 1.14 nm neutrons. The expected transmission calculated from the measurement of a plate sample is 0.954 for 1.14 nm neutrons. The measured transmission is less than the expected.

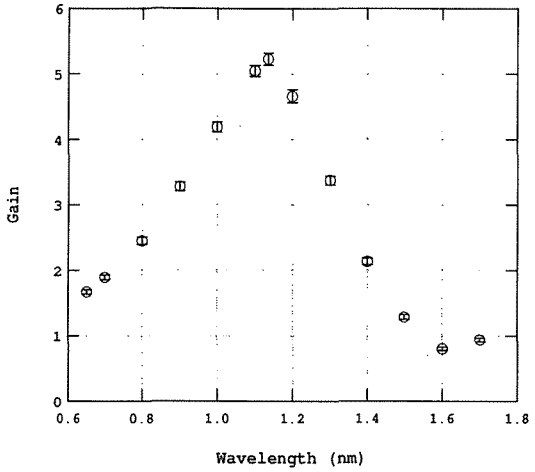

Figure 3: Ratio of peak intensity of focusing beam to plain beam at various wavelength on the 10 m distance (L) between lens and PSD. Experimental setup of measurement is as shown in Fig. 1(a). Neutron counts on the detector is integrated in the area same as the first pinhole which is 3.5 mm in diameter after fitted to two-dimensional Gaussian function. The gain becomes the maximum at 1.14 nm in L=10 m.

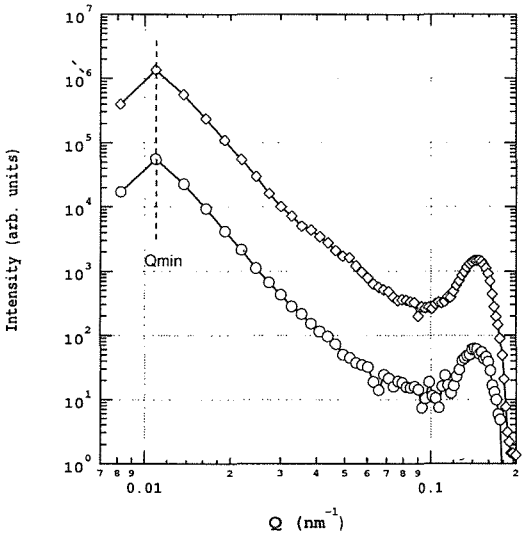

Figure 4: Typical measurement of small-angle scattering. The circles and the rhombuses represent the observed data of P-SANS and F-SANS, respectively. The intensity is relatively normalized. The factor between curves shows gain of the instrument configuration. The gain in the condition of this beam-line is more than ten times.

In order to investigate the lens characteristics carefully, a neutron beam collimated by a 1 mm in diameter pinhole was used. The setup of this experiment is shown in Fig. 1(b). The two-dimensional neutron images ware observed by PSD at 10 m downstream position from the lens. The peak of the distribution were determined to fit the Gaussian to the observed data. Figure 2 shows result of the measurement of the focal performance. The slope of this line indicates L/f, where L means distance between lens and PSD and f means focal length. The focal length of this lens is 2.5 m at 1.6 nm neutrons.

To measure the gain by focusing of the neutrons, a neutron beam collimated by a pinhole of 20 mm in diameter in front of the lens and a pinhole of 3.5 mm in diameter at 10 m upstream position of the lens were used. The setup of this experiment is shown in Fig. 1(a). Figure 3 shows the ratio of peak intensity of focusing beam to plain beam at various wavelength on the 10 m distance (L) between lens and PSD. The gain becomes the maximum at 1.14 nm in L=10 m.

We obtained considerable, more than 5 times, gain of beam intensity using focusing lens. However, the gain is too less than 33 times simply calculated by the ratio of the area because a divergence of the beam coming into the first pinhole is not enough large.

Typical small-angle scattering measurements were performed, and we compared focusing method, F-SANS, with conventional method, P-SANS. The condition of pinholes was selected as being able to measure same minimum momentum transfer. The intensity ratio F-SANS to P-SANS was more than ten. That value is the gain by beam focusing using lens. If a divergence of the beam coming into the first pinhole is enough large, more gain would be observed. In order to get better performance, we need investigate details of the noise from lens further.

References

1) S.-M. Choi, J. G. Barker, C. J. Glinka, Y. T. Cheng and P. L. Gammel, *J. Appl. Cryst.*, **33** (2000) 793.
2) H. Ohmori, *Int. J. Japan Soc. Prec. Eng.* **26** (1992) 273.
3) T. Oku, S. Morita, S. Moriyasu, Y. Yamagata, H. Ohmori, Y. Takizawa, H. M. Shimizu, T. Hirota, Y. Kiyanagi and J. Suzuki, *Nucl. Instrum. Methods A* **462** (2001) 435.
4) T. Adachi, T. Oku, S. Morita, H. Ohmori, Y. Takizawa, H. M. Shimizu, J. Suzuki, C.-K. Loong, K. C. Littrell and R. Goyette, *Appl. Phys. A* **74** (2002) S180.

2.7.6 Development of an Electrostatic Levitation Furnace for Neutron Scattering Experiments of High Temperature Liquids

T. MASAKI, T. ISHIKAWA, P.-F. PARADIS, H. AOKI, T. AOYAMA, Y. ARAI, Y. ISHII[1] and S. YODA

National Space Development Agency of Japan, 2-1-1, Sengen, Tsukuba, Ibaraki 305-8505
[1] Advanced Science Research Center, JAERI, Tokai, Ibaraki 319-1195

In recent years, considerable attention has focused on the containerless techniques for the experimental research of high temperature melts or deeply undercooling liquids, especially for structure analysis by neutron or X-ray scattering.[1)] Recently, NASDA has developed an electrostatic levitation furnace for microgravity experiments in the international space station as well as for ground-based experiments. Since this technique is attractive for neutron scattering experiments, NASDA and JAERI have developed a dedicated electrostatic levitation furnace (ESL) for neutron scattering experiments of extremely high temperature melts and deeply undercooling liquids. Last year, the ESL was developed and its technical capability was investigated with the neutron scattering measurements of levitated sintered alumina at room temperature. The sample could be kept levitated continuously for more than 11 hours. In this "cold" experiment, the diffraction peaks of alumina were clearly observed without any other peaks coming from the background. The details are described in ref. 2.

This year, the verification of ESL operation with high temperature melts was performed. The facility configuration was identical as last year's except for sample heating. In order to heat the levitated sample, a CO_2 laser was added to the facility. The heating laser heated the sample the top of the vacuum chamber through a ZnSe optical window. Zirconium was selected as the test material for the "hot" experiment because its low vapour pressure makes it suitable for long duration experiments. The "hot" experiment was very successful, with the continuous levitation of a molten zirconium sample for eight hours. Fig. 1 shows the levitated liquid zirconium at 2500 K. It can be seen that the levitation method provides a nearly spherical sample for which the data correction, in particular the correction of absorption, could be easily performed on the diffraction data analysis. Since the sample size was rather small (ca. 2 mm diameter), the scattering intensity acquired from the levitated sample was not sufficient within the duration of levitation of this experiment. In the near future, experiments of much longer duration are planned to obtain the scattering data.

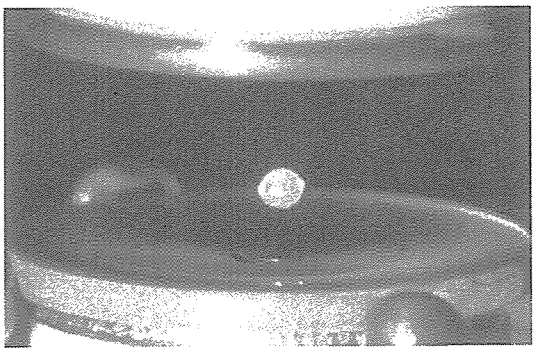

Figure 1: Levitated liquid Zr at 2500 K.
The bright sphere is the levitated sample. The upper and lower disks are electrodes for controlling electrostatic field.

References

1) T. Schenk, D. Holland-Moritz, V. Simonet, R. Bellissent, and D.M. Herlach : Phys. Rev. Lett. **89** (2002) 075507.
2) H.Aoki, P.-F. Paradis, T. Ishikawa, T. Aoyama, T. Masaki, S. Yoda, Y. Ishii, and T. Itami : Rev. Sci. Instr. **74** (2003) 1147.

2.7.7 Neutron Stress Measurement of Composite and Film Materials

T. HANABUSA, K. KUSAKA, M. NISHIDA[1], N. MINAKAWA[2] and A. MORIAI[2]

Department of Mechanical Engineering, Tokushima University, Tokushima 770-8506
[1]Kobe City College of Technology, Gakuenhigashi-machi, Nishi-ku, Kobe 651-2194
[2]JAERI, Tokai, Ibaraki 319-1195

1 Internal Stress Measurement in Tungsten Fiber Reinforced Copper Composite

1.1 Introduction

Since there is commonly a large difference in the coefficient of thermal expansion between a matrix and a fiber, a microscopic stress state develops in a composite material. In this study, thermal residual stresses and thermal stresses in sub-zero temperature region in the tungsten fibers and in the copper matrix were measured by the neutron diffraction method.

1.2 Experimental procedure

The specimen used in this investigation is a tungsten-fiber (100 μm in diameter) reinforced copper composite. Tungsten fibers had a 110 texture along their longitudinal direction. A cross section of the specimen is shown in Fig.1. The volume fraction of the tungsten fiber is about 10 %. This specimen was annealed at 973 K for 2 hours before stress measurement. The wave length of a neutron beam was 0.20978 nm. The stress-free lattice spacings of each $\{hkl\}$ were measured from a bundle of tungsten-fibers annealed at 973 K, set up on a rotating sample attachment.

In this study, the ordinary triaxial measurement method by using Hooke's equation and the $\sin^2\psi$ were employed for stress evaluation.

1.3 Results of neutron stress measurement

The results of the stress measurement are shown in Table 1. The stress for 200 and

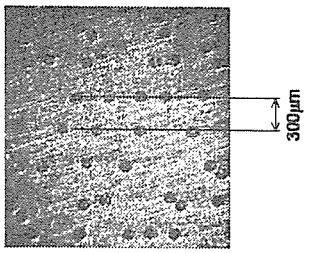

Figure 1: A cross section of W-fiber reinforced Cu composite.

211 diffractions could not be evaluated by the triaxial measurement method because the diffraction peak from the tungsten fiber did not appear at $\psi = 0^\circ$. On the other hand, the $\sin^2\psi$ method could be adopted for each plane of 110, 200 and 211. The residual stresses in the tungsten fibers were compressive in three orthogonal directions. The residual stress evaluated from the $\sin^2\psi$ method using neutron diffraction is the difference of two principal stresses, $\sigma_{11} - \sigma_{33}$. It seems from the results that there is a small difference between the stresses in the interior and those in the surface.

A thermal stress was tried to measure in a temperature region below the room temperature to 50 K. The stress free lattice spacing is necessary for evaluating the triaxial stress state. The 110 diffraction of the tungsten fiber and the 111 diffraction of the copper were used for the thermal stress measurement. The thermal stresses both in the fiber and the matrix behaved non-linearly against the temperature. Since there is no systematic change in the thermal stress behavior, it is considered that the interface between the fiber and the matrix slipped each other in a sub-zero temperature region.

Table 1: Results of neutron stress measurement.

Triaxial measurement method (MPa)				$\sin^2\psi$ method (MPa)
hkl	σ_{11}	σ_{22}	σ_{33}	$\sigma_{11}-\sigma_{33}$
100	-467	-219	-150	-268
200	-	-	-	-215
211	-	-	-	-209

2 Residual Stresses Measurement in CrN and Cr Films

2.1 Introduction

CrN films are considered to be useful for a piston ring and a connecting rod in engines because of very hard and durable properties. A thick film over than 10 μm is needed for utilizing it in the automobile industry. Residual stresses always develop in the films, because the film and the substrate differ in an atomic distance, thermal expansion coefficients.

In this study, an arc-ion plating (AIP) system was employed to prepare films. Residual stresses in these films were investigated by neutron and X-ray diffraction.

2.2 Experimental procedure

CrN and Cr films and CrN films with Cr interlayer were deposited on a SUS304 substrate by arc-ion plating under the conditions shown in Table 2. The residual stresses in the CrN and Cr films and CrN film with Cr interlayer were measured by neutron diffraction at RESA in JAERI. The wavelength was 0.2098 nm and the incident slit size was 10 mm in width and 15 mm in height. The CrN film and the Cr film had a random orientation and 100 texture, respectively. Therefore, the residual stress in the CrN film was measured by $\sin^2\psi$ method with 220 diffraction, and that in Cr film was measured by two-tilt method with 200 diffraction. The residual stresses in these films were also measured by X-ray diffraction. The characteristic X-rays were CrKα (λ =0.2098 nm) and the incident slit size was 2×4 mm^2.

2.3 Results and discussion

Table 3 shows the results of residual stress measurement in the Cr and CrN film and CrN film with Cr interlayer. A large compressive stress was observed in all films. In the case of thick single-layered CrN film, compressive stress measured by neutron diffraction was smaller than that by X-ray diffraction. In the case of single-layered Cr thin film, compressive stress was almost equal to that by X-ray diffraction. In the case of CrN film with Cr interlayer, compressive stress measured by neutron diffraction was different from that by X-ray diffraction. The reason of the different results between neutron and X-ray diffractions is not clear. One reason would come from the different measurement conditions such as irradiated area size and used diffraction.

Table 2: Conditions of film preparation.

Film	CrN		Cr		CrN/Cr	
I_A (A)	100	200	100	200	100	200
V_B (V)	-300		-300		-300	
Ts (K)	573		573		573	
t ,(μm)	9-10	18-20	4	8	7	

Table 3: Results of residual stress measurement.

Method		Neutron		X-ray	
Film	I_A (A)	σ_N (GPa)		σ_X (GPa)	
CrN	100	-2.2		-2.7	
	200	-1.3		-1.5	
Cr	100	-1.3		-1.3	
	200	-1.6		-1.4	
CrN/Cr	100	CrN	-2.5	CrN	-3.0
		Cr	-0.7	Cr	-1.4
	200	CrN	-3.4	CrN	-1.9
		Cr	-4.8	Cr	-

2.7.8 High-Pressure Apparatus for Magnetic Neutron Diffraction beyond 3 GPa at Low Temperature

T. OSAKABE, M. KOHGI[1], D. KAWANA[1], A. HANNAN[1], K. SOYAMA and H. KITAZAWA[2]

Advanced Science Research Center, JAERI, Tokai, Ibaraki 319-1195
[1]Department of Physics, Tokyo Metropolitan University, Hachioji, Tokyo 192-0397
[2]National Institute for Materials Science, Tsukuba, Ibaraki 305-0047

On the transport and magnetic properties of 3d, 4f, and 5f electron systems, interesting phenomena, such as the magnetic phase transition, insulator-metal transition, and superconductivity, appear by pressurization up to about 10 GPa. Therefore, if neutron scattering experiments can be performed at low temperature, putting pressure to the range of about 10 GPa, it can make a great contribution to the research of the magnetism of these systems. However, the highest attainment pressure in almost all magnetic neutron scattering experiments has stopped at about 3 GPa generated by piston-cylinder-type high-pressure cells. In this paper we report recent development of the high-pressure apparatus for magnetic neutron diffraction experiments beyond 3 GPa in JAERI.

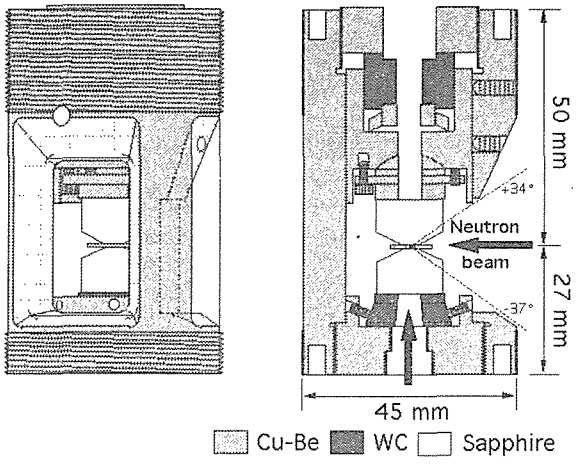

Figure 1: Schematic drawings of the sapphire-anvil high-pressure cell.

The most suitable method for generating pressure beyond 3 GPa is using anvil technique. Figure 1 shows the schematic drawing of the newly developed anvil-type high-pressure cell. The main parts of the cell are made of non-magnetic Cu-Be alloy. The cell is so compact that it is easily attached in a standard cryostat or superconducting magnet. The cell has three large windows for the neutrn beam, which have the horizontal and vertical opening angles of about 90 degrees and about 80 degrees. We adopted a pair of sapphire (single crystal of Al_2O_3) anvils because sapphire is a hard material (Knoop hardness: ~2000) and hardly absorbs neutrons. We also use the moissanite (single crystal of SiC) anvils [1)] or Ti-doped sapphire anvils, which are harder (Knoop hardness: ~3000) than the sapphire anvils. The mechanism for angular adjustment and centering of the anvils follows that of usual diamond anvil cells. A gasket sandwiched between the anvils is made of Cu-0.3% P alloy, aluminum alloy (7075T6) or Cu-Zn alloy. The thickness and diameter of the gasket is 0.3-0.4 mm and 5-6 mm. A hole with a diameter of 0.7mm is made in the center of the gasket. A single crystal sample and small splinterd rubys are put into the hole together with a pressure-transmitting medium. We usually use the 4:1 deuterated methanol-ethanol solution, some kinds of oil (Daphne oil 7373, Silicon oil KF96-50cs, Fomblin oil Y140/13) or Fluorinert FC70-77 mixture as the pressure-transmitting medium. The pressure is measured by the standard ruby-fluorescence method. The highest attainment pressure by the sapphire anvil cell (SAC, hereafter) depends on the combination of the anvil shape especially the smooth-

ness of the culet edge, the material of the gasket and the kind of pressure-transmitting medium. Maximum pressure generated by the SAC with 2.5 mm anvil tip and Cu-P gasket is about 6 GPa at present. Figure 2 shows the temperature dependence of (1, -2, 0) and (1/2, -2, 0) magnetic Bragg intensities of CeSb in the SAC at 4.6 GPa [2,3]. The peaks correspond to the type-I and type-IA antifferomagnetic orders of 2 μ_B magnetic moments of Ce ions. The sample size is about 0.5×0.4×0.1 mm^3. In spite of the tiny sample, the S/N ratio was nearly the same as that of the standard piston-cylinder cell. This was achieved both by covering almost all parts of the SAC with Cd sheets and by optimizing the condition of the spectrometer so as to increase the incident neutron flux. From this result, it is expected that, when magnetic moments are 1 μ_B or more, the magnetic signal is observed.

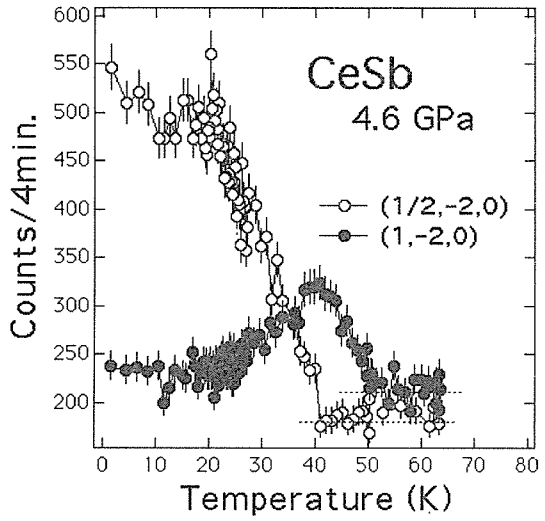

Figure 2: Temperature dependence of the magnetic Bragg intensities of CeSb in the SAC at 4.6 GPa.

The best method for compensating weak magnetic signals from a tiny sample in SAC is focusing the incident neutron beam on a sample position. The most likely successful method for the focusing is mirror reflection. We are now developing the focusing device with a lot of curved supermirrors according to the proposal of D.F.R.Mildner [4]. The inset of Fig. 3 shows the schematic drawing of the device. The shape of the cross section of each supermirror is a circle arc. The extension of the end of each mirror meets at a focal point (sample position). Neutrons are repeatedly reflected with the same angle by the inner side of the circle and arrive at the sample position. Figure 3 shows results of Monte Carlo ray-tracing simulation for a triple-axis neutron spectrometer TAS-1. The closed circles indicate the neutron intensity distribution at the sample position. This is the case of placing the device of 450 mm length that has 16 supermirrors with Q of 3.0 in the space of 600 mm between the 2nd collimator and the sample. Here, Q is the critical wave number of the total reflection of the mirror relative to that of natural nickel. The open circles indicate the distribution for the general experiment condition without the device. It is clear that the considerable gain of about 7 is obtained using the device. Therefore, it is expected that the device is very effective not only in the high-pressure experiments but also in the neutron inelastic scattering experiments with very weak signals.

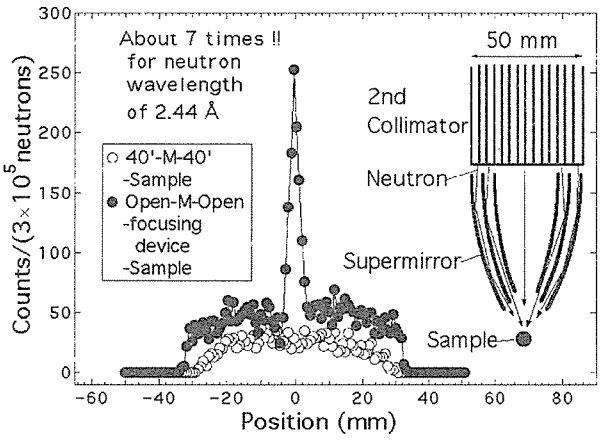

Figure 3: Calculated distribution of the neutron intensities.

References

1) Ji-an Xu, Ho-kwang Mao: SCIENCE, **290** (2000) 783.
2) T. Osakabe, A. Hannan, N. Tachi, M. Kohgi, H. Kitazawa: Appl. Phys. A**74** (2002) 799.
3) T. Osakabe, A. Hannan, D. Kawana, M. Kohgi, H. Kitazawa: Acta Physica Polonica B**34** (2003) 1469-1472.
4) D.F.R. Mildner: Nucl. Instr. And Meth. A**299** (1990) 416.

2.7.9 Development of Neutron Detector by Using a Novel Metallic High-T_c Superconductor MgB_2

T. ISHIDA, K. TAKAHASHI, T. YOTSUYA[1], K. SATOH[1], A. SAITO[2], A. KAWAKAMI[2], H. SHIMAKAGE[2], Z. WANG[2], S. OKAYASU[3], K. HOJYOU[3], M. KATAGIRI[3], Y. MORII[3], AND N. NIIMURA[3]

Department of Physics and Electronics, Osaka Prefecture University, Sakai, Osaka, 599-8531
[1] Technology Research Institute of Osaka Prefecture 2-7-1 Ayumino, Izumi, Osaka 594-1157
[2] Kansai Advanced Research Center, Communications Research Laboratory, 588-2, Iwaoka-cho, Nishi-ku, Kobe, Hyogo 651-2429
[3] Japan Atomic Energy Research Institute, Tokai, Naka, Ibaraki 319-1195

[Introduction]

It is difficult to detect neutrons compared to charged particles. Neutrons are useful to investigate properties of the various substances. For example, the protein structure has been successfully determined by the diffraction experiment by using an imaging plate[2)]. A BF_3 counter is widely used to detect neutrons. However, this counter requires a high voltage of 2000 V and is large in size to achieve a reasonable detection efficiency.

A novel metallic superconductor MgB_2 has a high-T_c of 40 K[1)]. The ^{10}B has a huge cross section for the nuclear reaction of $^{10}B(n,\alpha)^7Li$. It reaches 3800 barns for thermal neutrons. We propose to develop a MgB_2 thin film detector with the aid of the nanofabrication technique of the electron beam lithography.

[Experiments and Results]

The MgB_2 thin films were prepared on an Al_2O_3 substrate (R-plane) by a multiple-target sputtering method[3)]. This process is advantageous to make high quality devices because it requires neither a post-annealing process nor a high substrate temperature T_s. We fabricated six meandering pattern units on this film by using an electron beam lithograpy. Figure 1 is the drawing and the microscope photograph of the patterning. Since the range of α particles in the MgB_2 is on the order of 1μm, we chose the line width as 1μm. The nuclear reaction $^{10}B(n,\alpha)^7Li$ rate R_a of this MgB_2 film with neutrons is estimated as

$$R_a = \sigma I n \mathrm{d}x, \qquad (1)$$

where σ is the cross section, $I \simeq 1 \times 10^7$ cm^{-2}s^{-1} is the beam intensity, $n = 1.38 \times 10^{22}$ cm^{-3} is the number of ^{10}B nuclides per volume, and $\mathrm{d}x = 200$ nm is the thickness of the MgB_2 film. The cross section σ of our experiment is estimated 1.3×10^4 barns for the wave length of 6 Å. The neutrons intensity I of JRR−3M is about 1×10^7 cm^{-2}s^{-1}. We estimated R_a is 3.5×10^4 cm^{-2}s^{-1}. The total surface area of the one meandering patterns is $\sim 4.7 \times 10^{-3}$cm^2. Finally, we estimate that the nuclear reaction $^{10}B(n,\alpha)^7Li$ rate is 167 events per second.

Figure 2 is the $R-T$ curves of the two meandering patterns. The #1 patterning unit shows that $T_c^{onset} \simeq 14.8$K and $\Delta T = 0.6$K. The electric resistance in normal state is almost consistent with the value estimated from Ref. 3. We set a sample temperature in the transition regime.

Figure 3 is the schematic diagram of our detection system. The photographs in the left side are a sample holder of a 4-K refrigerator and a MgB_2 thin film. When neutrons react with ^{10}B in MgB_2, the reaction energy causes a partial destruction of superconductivity and a change in the resistivity. The slight variation of the voltage is amplified by a preamplifer and a linear amplifer. We searched a pulse signal caused by the nuclear reaction by a fast digital oscilloscope. The photographs in the

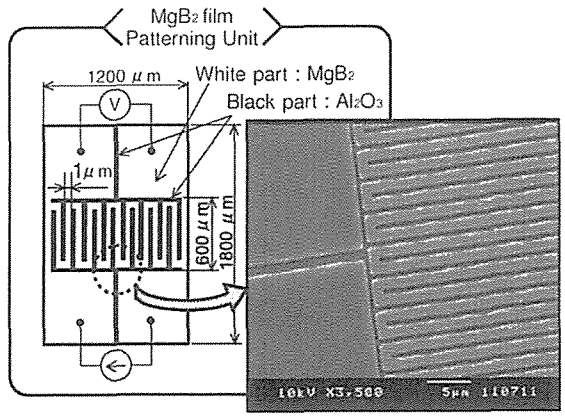

Figure 1: The shematic drawing (the MgB_2 films is the white part while substrate (Al_2O_3) is the black part) and the photograph of MgB_2 patterning unit. We measured electric resistance of meandering pattern by using the four terminal method.

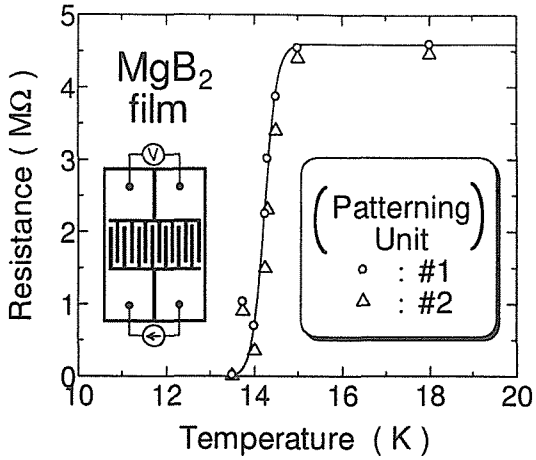

Figure 2: The $R-T$ curve of MgB_2 patterning unit. We can find T_c^{onset} is 14.8K. We performed the neutron irradiation experiment by maintaining the temperature at the trasition edge of the $R-T$ curve.

right side of Figure 3 show the examples of such pulse signals. However, we are not sure whether this comes from the nuclear reaction or from external noise signals.

[Conclusion]

We succeeded in fabricating the $1\mu m$ meandering patterns on MgB_2 thin film. This patterns showed a sharp resistive transition, which is suitable for neutrons detector. It is inclusive that the pulse signal observed by the digital oscilloscope is from the ^{10}B nuclear reactions. Further studies are necessary to complete the development of a novel neutron detector as one of the nanotechnology virtual laboratories of the JST-CREST projects.

The present work is partially supported by the REIMEI Research Resources of Japan Atomic Energy Research Institute.

References

1) J. Nagamatsu *et al.*, Nature **410** (2001) 63.
2) N. Niimura *et al.*, Nature Structural Biology, 4 (1997) 909-914.
3) A. Saito *et al.*, Supercond. Sci. Technol. **15** (2002) 1-5.

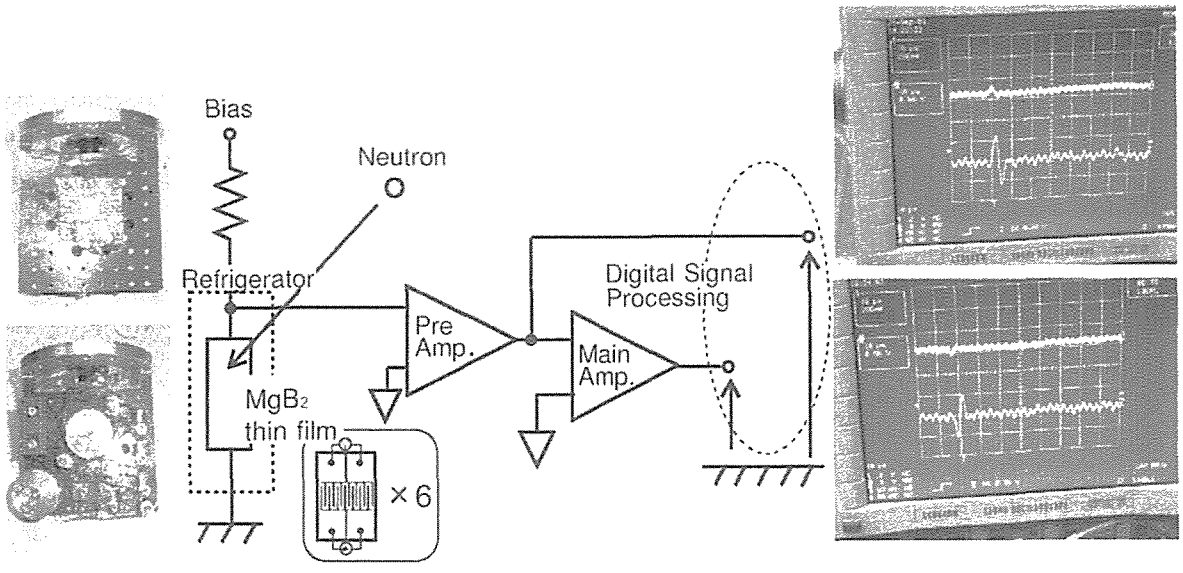

Figure 3: The schematic diagram of our neutron detection system. The left photographs are for the sample holder in 4K-refrigerator. A slight change in voltage due to the nuclear reaction of $^{10}B(n,\alpha)^7Li$ is amplified by a preamplifier and a linear amplifier. This signal is analyzed by a digital signal oscilloscope.

Appendix A

Program Committee for Neutron Beam Utilization in the JFY 2002
of the Advisory Council for JAERI'S Research Facilities

(Chairman)	Yasuhiko	Fujii	Professor, The Institute for Solid State Physics, The University of Tokyo
(Vice-Chairman)	Mitsuru	Ebihara	Professor, Graduate School of Science, Tokyo Metropolitan University
	Kazuyoshi	Yamada	Professor, Institute for Chemical Research, Kyoto University
	Susumu	Ikeda	Professor, High Energy Accelera for Research Organization
	Masafumi	Kohgi	Professor, Graduate School of Science, Tokyo Metropolitan University
	Takeji	Hashimoto	Professor, Graduate School of Engineering, Kyoto University
	Mamoru	Sato	Professor, Graduate School of Integrated Science, Yokohama City University
	Makoto	Hayashi	Head, Div Power Laboratory, Hitachi Ltd.
	Yoichi	Sakai	Professor, Chemical Class, Daido Institute of Technology
	Masayoshi	Tamaki	Assistant Professor, Department of Nuclear Engineering, Nagoya University
	Hideki	Yoshizawa	Professor, The Institute for Solid State Physics, The University of Tokyo
	Toshiji	Kanaya	Professor, Institute for Chemical Research, Kyoto University
	Kazuma	Hirota	Assistant Professor, Graduate School of Science, Tohoku University
	Nobuo	Niimura	Principal Scientist, Advanced Science Research Center
	Takemasa	Shibata	Deputy Director, Advanced Science Research Center
	Kazuhisa	Kakurai	Principal Scientist, Advanced Science Research Center
	Yukio	Oyama	Deputy Director, Center for Neutron Science
	Kazuo	Watanabe	Principal Scientist, Department of Environmental Sciences
	Masaki	Katagiri	Principal Scientist, Advanced Science Research Center
	Yoshirou	Funayama	General Manager, Department of Research Reactor
(Secretary)	Yukio	Morii	Principal Scientist, Advanced Science Research Center
	Hisashi	Sagawa	General Manager, Department of Research Reactor
(Observer)	Hiromasa	Watanabe	Head, Office of Planning
	Masahito	Matsubayashi	Senior Scientist, Center for Neutron Science
	Chushiro	Yonezawa	Senior Scientist, Department of Environmental Sciences
	Naohiko	Hori	Chief, Department of Research Reactor

Appendix B

Themes of Cooperative Research Projects with Universities in the JFY 2002

1.	The First Challenge to Refined Structural Analysis of Synthetic Polymer Crystals by Neutron Imaging Plate System	K. Tashiro	Osaka Univ.
2.	Crystal Structures of Polymers (Crystal Structure of Cellulose)	Y. Takahashi	Osaka Univ.
3.	Missing Number		
4.	Spin Correlations in 3D Spin Frustration System $CdFe_2O_4$ under High Pressure	Y. Tsunoda	Waseda Univ.
5.	Spin Dynamics of Hole-doped $Nd_{2-x}Ca_xBaNiO_5$	J. Akimitsu	Aoyama Gakuin Univ.
6.	Disorder in Superionic Conductors	T. Sakuma	Ibaraki Univ.
7.	Characterization of Water Cluster $(H_2O)_{10}$ with in a Self-assembled Coordination Cage	M. Fujita	Tokyo Univ.
8.	Studies on Reactive Block Copolymer Systems	T. Hashimoto	Kyoto Univ.
9.	Phonon Dispersion Relation in $PbTiO_3$	Y. Tsunoda	Waseda Univ.
10.	Magnetic Structure of DyAg and DyCu under Magnetic Field	T. Kakeshita	Osaka Univ.
11.	Neutron Line Crystal Structure Analysis of Nitric Oxide-binding Protein Cytochrome c'	T. Kohzuma	Ibaraki Univ.
12.	Exotic Magnetic Phases of Ce-compound-strongly-correlated-electron-systems	M. Kohgi	Tokyo Metropolitan Univ.
13.	Construction of Air-Water Interface Neutron Reflelctometer with Two-dimensional Imaging Plate	H. Matsuoka	Kyoto Univ.
14.	Chemical Reactions in Microdomains Formed by Block Polymers	M. Annaka	Chiba Univ.
15.	Relationship between Fluctuations and Superconductivity in the Electron-doped Superconductor $Pr_{1-x}LaCe_xCuO_{4+y}$	K. Yamada	Kyoto Univ.
16.	Magnetic Excitation Spectra of the T *-type High-T_c Superconductor	M. Sato	Nagoya Univ.
17.	Magnetic Structure of $Cr_{1-x}Te$ and Related Systems	M. Sato	Nagoya Univ.
18.	Evaluation of Residual Stress and Materials Properties under loading in Structural Materials	Y. Akiniwa	Nagoya Univ.
19.	Neutron Diffraction Study on the Thermal Stress of Heat Treated Materials	K. Inoue	Ryukoku Univ.
20.	Antiferroquadrupolar Ordering in RB_2C_2 System	Y. Yamaguchi	Tohoku Univ.
21.	Measurement of Internal Stresses in Laminated Coating Files	T. Hanabusa	Tokushima Univ.

Appendix B

Themes of Cooperative Research Projects with Universities in the JFY 2002

1.	The First Challenge to Refined Structural Analysis of Synthetic Polymer Crystals by Neutron Imaging Plate System	K. Tashiro	Osaka Univ.
2.	Crystal Structures of Polymers (Crystal Structure of Cellulose)	Y. Takahashi	Osaka Univ.
3.	Missing Number		
4.	Spin Correlations in 3D Spin Frustration System $CdFe_2O_4$ under High Pressure	Y. Tsunoda	Waseda Univ.
5.	Spin Dynamics of Hole-doped $Nd_{2-x}Ca_xBaNiO_5$	J. Akimitsu	Aoyama Gakuin Univ.
6.	Disorder in Superionic Conductors	T. Sakuma	Ibaraki Univ.
7.	Characterization of Water Cluster $(H_2O)_{10}$ with in a Self-assembled Coordination Cage	M. Fujita	Tokyo Univ.
8.	Studies on Reactive Block Copolymer Systems	T. Hashimoto	Kyoto Univ.
9.	Phonon Dispersion Relation in $PbTiO_3$	Y. Tsunoda	Waseda Univ.
10.	Magnetic Structure of DyAg and DyCu under Magnetic Field	T. Kakeshita	Osaka Univ.
11.	Neutron Line Crystal Structure Analysis of Nitric Oxide-binding Protein Cytochrome c'	T. Kohzuma	Ibaraki Univ.
12.	Exotic Magnetic Phases of Ce-compound-strongly-correlated-electron-systems	M. Kohgi	Tokyo Metropolitan Univ.
13.	Construction of Air-Water Interface Neutron Reflelctometer with Two-dimensional Imaging Plate	H. Matsuoka	Kyoto Univ.
14.	Chemical Reactions in Microdomains Formed by Block Polymers	M. Annaka	Chiba Univ.
15.	Relationship between Fluctuations and Superconductivity in the Electron-doped Superconductor $Pr_{1-x}LaCe_xCuO_{4+y}$	K. Yamada	Kyoto Univ.
16.	Magnetic Excitation Spectra of the T *-type High-T_c Superconductor	M. Sato	Nagoya Univ.
17.	Magnetic Structure of $Cr_{1-x}Te$ and Related Systems	M. Sato	Nagoya Univ.
18.	Evaluation of Residual Stress and Materials Properties under loading in Structural Materials	Y. Akiniwa	Nagoya Univ.
19.	Neutron Diffraction Study on the Thermal Stress of Heat Treated Materials	K. Inoue	Ryukoku Univ.
20.	Antiferroquadrupolar Ordering in RB_2C_2 System	Y. Yamaguchi	Tohoku Univ.
21.	Measurement of Internal Stresses in Laminated Coating Files	T. Hanabusa	Tokushima Univ.

22.	Elementally Excitations in the Quantum Spin System $TlCuCl_3$ and Related Compounds	H. Tanaka	Tokyo Inst. of Tech.
23.	A High Resolution Neutron Structure Analysis of FMN-binding Protein	Y. Morimoto	Himeji Inst. of Tech.
24.	Magnetic and Chemical Structures of SemiMagnetic Conductors	T. Kajitani	Tohoku Univ.
25.	Relation between Nano-scale Structural Distortions and Meta-magnetic Transition in $Sr_3Ru_2O_7$	Y. Uwatoko	The Univ. of Tokyo
26.	Study of Magnetic Excitations in the Ni-doped Superconducting Cuprate LSCO	Y. Endoh	Tohoku Univ.
27.	Magnetic Structure of γ-Mn and β-Mn Alloys	T. Hori	Shibaura Inst. of Tech.
28.	Functional Mechanism of Proteins Based on Their Hydrogen-atom Positions	K. Fukuyama	Osaka Univ.
29.	Magnetic Structure of Perovskite-Related Oxides Containing Lanthanide and Platinum Group Elements	Y. Hinatsu	Hokkaido Univ.
30.	Magnetic Excitations in Uranium Compound $U_3Pd_{20}Si_6$ of Exhibiting Localized Magnetism	M. Kohgi	Tokyo Metropolitan Univ.
31.	Development of the Method for Determining Residual Stress using Whole Part of Neutron Debye-scherrerPattem Detected with Neutron Image Plate	T. Sasaki	Kanazawa Univ.
32.	Relationship between Dynamic Heterogeneities and Concentration Fluctuations in Miscible Polymer Blends 2	M. Naoki	Gunma Univ.
33.	Hydrogen Transfer in Photoisomerization of Vitamine B12 Model Compounds	Y. Ohashi	Tokyo Inst. of Tech.

Appendix C

Themes of Cooperative Research Projects with Private Enterprises and National Laboratories in the JFY 2002

1.	Residual Stress Measurement of Constructions by Neutron Diffraction	T. Machida	Hitachi Ltd.
2.	Refractive Optics and Detector for Cold Neutron Beam	H. M. Shimizu	RIKEN
3.	Study of Liquid Structures in the High Temperature/under Cooling State Due to Electrostatic Levitation Furnace	S. Yoda	NASDA
4.	Study on the Relation between Unusual Formation of High-ordered Protein Structures and Abnormal Apoptosis	S. Naito	KEK
5.	Neutron Powder Diffraction Study of Defective High-Silica MFI Zeolite	T. Suzuki	Sumitomo Chemical Co. Ltd.
6.	Development of the Residual Strain Measurement Technique of Automobile Engine Parts by the Neutron Diffraction Method	T. Hamamoto	Toyota Co. Ltd.
7.	In Situ Observation of Structure Deformation of Polymer by Small-angle Neutron Scattering	T. Kasahara	Sumitomo Chemical Co. Ltd.

Appendix D

Publication List in the Period of the JFY 2002

1. Neutron Powder Diffraction Studied as a Function of Temperature of Structure II Hydrate Formed from a Methane + Ethane Gas Mixture
   C. J. Rawn, A. J. Rondinone, B. C. Chakoumakos, S. T. Marshall, L. A. Stern, S. Circone, S. H. Kirby, C. Y. Jones, B. H. Toby, Y. Ishii
   Proceedings of Fourth International Conference on Gas Hydrates Vol. **2** (2002) 595-598

2. Neutron Diffraction Study of Structure I and Structure II Trimethylene Oxide Clathrate Deuterate
   A. J. Rondinone, B. C. Chakoumakos, C. J. Rawn, Y. Ishii
   Proceedings of Fourth International Conference on Gas Hydrates Vol. **2** (2002) 625-629

3. The Use of Rigid Body Constraints in Rietveld Refinements of Neutron Diffraction Data of Clathrate Hydrates
   B. C. Chakoumakos, C. J. Rawn, A. J. Rondinone, S. L. Marshall, L. A. Stern, S. Circone, S. H. Kirby, C. Y. Jones, B. H. Toby, Y. Ishii
   Proceedings of Fourth International Conference on Gas Hydrates Vol. **2** (2002) 655-658

4. Anomalous Spin Density Distribution in CeB_6
   M. Saitou, H. Takagisi, T. Yokoo, J. Akimitsu, N. Okada, E. Nishibori, M. Takada, M. Sakata, M. Nishi, K. Kakurai, A. Kunii
   J. Phys. Soc. Jpn **71** No.**10** (2002) 2369-2372

5. Neutron Diffraction Study of Antiferromagnetic Order in UGa_3 under Pressure
   M. Nakamura, Y. Koike, N. Metoki, K. Kakurai, Y. Haga, G. H. Lander, D. Aoki, Y. Onuki
   J. Phys. Chem. Sol. **63** (2002) 1193-1196

6. Neutron Scattering Experiment on $U_3Pd_{20}Si_6$ I : Crystal and Magnetic Structures
   N. Tateiwa, N. Metoki, Y. Koike, K. Oikawa, N. Kimura, H. Aoki, T. Komatsubara
   Physica B **312-313** (2002) 891-893

7. Neutron Scattering Experiment on $U_3Pd_{20}Si_6$ II : Crystalline Electric Field and Spin Wave Excitations
   N. Tateiwa, N. Metoki, Y. Koike, N. Kimura, H. Aoki, T. Komatsubara
   Physica B **312-313** (2002) 894-896

8. Magnetic Structure, Phase Diagram, and a New Type of Spin-Flop Transition Dominated by Higher Order Interaction in a Localized *5f* System $U_3Pd_{20}Si_6$
Y. Koike, N. Metoki, Y. Haga, K. A. McEwen, M. Kohgi, R. Yamamoto, N. Aso, N. Tateiwa, T. Komatsubara, N. Kimura, H. Aoki
Phys. Rev. Lett. Vol.**89** 7 (2002) 077202 1-4

9. Spin Wave Excitations in Single Crystalline $U_3Pd_{20}Si_6$
N. Aso, N. Metoki, M. Kohgi, K. A. McEwen, Y. Koike, Y. Haga, N. Tateiwa, N. Kimura, H. Aoki, T. Komatsubara, Y. Morii
Physica B **312-313** (2002) 897-898

10. Magnetic and Fermi Surface Properties of $UNiGa_5$
Y. Tokiwa, Y. Haga, N. Metoki, S. Ikeda, R. Settai, Y. Onuki
Physica B **312-313** (2002) 294-296

11. Detailed Magnetic Structure of the Coupled Edge-sharing CuO_2 Chains in $Ca_2Y_2Cu_5O_{10}$
M. Matsuda, K. Kakurai, H. Yamaguchi, T. Ito, C. H. Lee, K. Oka
Appl. Phys. **A 74** [Suppl.] (2002) S637-S639

12. Liquid-He-Free 10T Superconducting Magnet for Neutron Scattering
S. Katano, N. Minakawa, N. Metoki, T. Osakabe, J. Suzuki, Y. Koike, Y. Ishii
Appl. Phys. **A 74** [Suppl.] (2002) S270-S272

13. Is Gel a Solid or a Liquid? It Sees 2nd Page Nature by Neutron Scattering
S. Koizumi
Kobunshi **51** (2002) 957 (Japanese)

14. Development of New-type Cobalt Oxide Thermoelectric Materials
T. Kajitani, Y. Ono Y. Miyazaki, Y. Morii
21st International Conference on Thermoelectronics Proc. (2002) 195-198

15. Single Crystal Growth and Structural and Magnetic Properties of the Uranium Ternary Intermetallic Compound UCr_2Si_2
T. D. Matsuda, N. Metoki, Y. Haga, S. Ikeda, T. Okubo, K. Sugiyama, N. Nakamura, K. Kindo, K. Kaneko, A. Nakamura, E. Yamamoto, Y. Onuki
J. Phys. Soc. Jpn. **72** (2002) 122-130

16. Magnetic Properties of $UNiGa_5$ and $UPtGa_5$
Y. Tokiwa, Y. Haga, N. Metoki, A. Nakamura, Y. Ishii, Y. Onuki
J. Nuclear Sci. Tec. Suppl. **3** (2002) 210-213

17. Hydrogen and Deuterium in Myoglobin as Seen by a Neutron Structure Determination at 1.5Å Resolution
A. Ostermann, I. Tanaka, N. Engler, N. Niimura, F. G. Parak
Biophysical Chem. **95** (2002) 183-193

18. Preface " Hydrogen and Hydration" Sensitive Structural Biology
N. Niimura
Biophysical Chem. **95** (2002) 181

19. Optimization of Neutron Imaging Plate
Y. K. Haga, K. Neriishi, K. Takahashi, N. Niimura
Nucl. Instrum. Methods Phys. Res. **A 487** (2002) 504-510

20. An Insight into the Pathway of the Amyloid Fibril Formation of Hen Egg White Lysozyme Obtained from a Small-angle X-ray and Neutron Scattering Study
Y. Yonczawa, S. Tanaka, T. Kubota, K. Wakabayashi, K. Yutani & S. Fujiwara
Journal of Molecular Biology

21. Foreword 「Water」
N. Niimura
Seibutsubutsuri **224** (2002) 261 (Japanese)

22. Research of the Gel Phase Transition by Neutron Scattering
N. Niimura, S. Koizumi
Gel and a Life (T. Tanaka Anthology) Tokyo Univ. Publication (2002) 116 (Japanese)

23. Direct Observation of Deuterium Migration in Crystalline-State Reaction by Single Crystal Neutron Diffraction IV. "Hula-Twist" Rotation of a Long Alkyl Radical Produced by Photoirradiation
T. Ohhara, S. Ikeda, H. Imura, H. Uekusa, Y. Ohashi, I. Tanaka, N. Niimura
J. Am. Chem. Soc. **124** (2002) 14736-14740

24. A Neutron Crystallographic Analysis of a Rubredoxin Mutant
T. Chatake, K. Kurihara, I. Tanaka, M. W. W. Adams, F. E. JenneyJr, I. Tsyba, R. Bau, N. Niimura
Applied Physics A **74** [Suppl.] (2002) 1280-1282

25. Neutron Scattering Study of Dipolar Spin Ice $Ho_2Sn_2O_7$: Frustrated Pyrochlore Magnet
H. Kadowaki, Y. Ishii, K. Matsuhira, Y. Hinatsu
Phys. Rev. B **65** (2002) 144421 1-8

26. Crystal Structures and Magnetic Properties of Cobalt Chalcogenides $BaLa_2Co(S_{1-x}\ Se_x)_5$ $(0.0 \leq x \leq 0.4)$
M. Wakeshima, Y. Hinatsu, Y. Ishii, Y. Shimojo, Y. Morii
J. Mater. Chem. **12** (2002) 631-634

27. Crystal Distortion and Magnetic Structure of γ -MnPd Alloys
T. Hori, Y. Tsuchiya, Y. Ishii, K. Hojou
Mater. Transactions vol. **43** No.3 (2002) 436-438

28. Crystal Structure, Electric and Magnetic Properties of Layered Cobaltite β -Na_xCoO_2
Y. Ono, R. Ishikawa, Y. Miyazaki, Y. Ishii, Y. Morii, T. Kajitani
J. Sol. State Chem. **166** (2002) 177-181

29. Crystal Distortion and Magnetic Structure of γ -MnPt Alloys
T. Hori, Y. Tsuchiya, H. Shiraishi, Y. Ishii, K. Hojou
Appl. Phys. A **74** Suppl. (2002) S743-745

30. Modulated Structure of the Thermoelectric Compound $[Ca_2CoO_3]_{0.62}\ CoO_2$
Y. Miyazaki, M. Onoda, T. Oku, M. Kikuchi, Y. Ishii, Y. Ono, Y. Morii, T. Kajitani
J. Phys. Soc. Jpn. **71** (2002) 491-497

31. Magnetic and Calorimetric Studies on Ordered Perovskite Ba_2ErRuO_6
Y. Izumiyama, Y. Doi, M. Wakeshima, Y. Hinatsu, A. Nakamura, Y. Ishii
J. Sol. Sta. Chem. **169** (2002) 125-130

32. Low-energy Excitation in $CsPbX_3$ (X=Cl, Br)
T. Sakuma, M. Mutou, K. Ohki, M. Arai, H. Takahashi, Y. Ishii
Sol. Sta. Ionics **154-155** (2002) 237-242

33. Jahn-teller Distortion and Cluster-glass Like Behavior in $La_{0.875}Ca_{0.125}\ MnO_3$
S. Begum, Y. Ono, Y. Tomioka, Y. Tokura, Y. Ishii, Y. Morii, T. Kajitani
J. Phys. and Chem. of Soc. **63** (2002) 939-942

34. Oscillatory Diffuse Neutron Scattering from β-AgI
A. Thazin, M. Arai, T. Sakuma, Y. Ishii
Sol. Sta. Ionics (Trends in the new millennium) (2002) 777-784

35. Structures and Magnetic Properties of Ternary Lithium Oxides $LiRO_2$ (R=Rare Earths)
Y. Hashimoto, M. Wakeshima, K. Matsuhira, Y. Hinatsu, Y. Ishii
Chem. Mater. **14** (2002) 3245-3251

36. Magnetic and Calorimetric Studies on Ordered Perovskite Ba_2ErRuO_6
Y. Izumiyama, Y. Doi, M. Wakeshima, Y. Hinatsu, A. Nakamura, Y. Ishii
J. Sol. Sta. Chem. **169** (2002) 125-130

37. Inelastic Neutron Scattering Experiment on Dzyaloshinski-moriya Interaction in $SrCu_2(BO_3)_2$
K. Kakurai, N. Aso, K. Nukui, M. Nishi, H. Kageyama, H. Ueda, H. Kadowaki, O. Cepas
Proc. French-Japanese Symposium on
"Quantum Properties of Low-Dimensional Antiferromagnets" (2002) 102-108

38. Dominance of Excitation Continuum in the Longitudinal Spectrum of Weakly Coupled Heisenberg S=1/2 Chains
A. Zheludev, K. Kakurai, T. Matsuda, K. Utinokura, K. Nakajima
Phys. Rev. Lett. **89** No.14 (2002) 197205-1~4

39. Magnetic Structure and the Hall Resistivity of $Ca_{1-x}Zn_xCr_2Se_4$
S. Iikubo, Y. Yasui, K. Oda, Y. Ohno, Y. Kobayashi, M. Sato, K. Kakurai
J. Phys. Soc. Jpn. **71** No.11 (2002) 2792-2799

40. Magnetic Field Effects and Magnetic Anisotropy in Lightly Doped $La_{2-x}Sr_xCuO_4$
M. Matsuda, M. Fujita, K. Yamada, R. J. Birgeneau, Y. Endoh, G. Shirane
Physical Review B **66** (2002) 174508 1-6

41. Absense of Magnetic-field Effect on Static Magnetic Order in Electron-doped Superconductor $Nd_{1.86}Ce_{0.14}CuO_4$
M. Matsuda, S. Katano, T. Uefuji, M. Fujita, K. Yamada
Physical Review B **66** (2002) 172509 1-4

42. Magnetic Excitations in the Edge-sharing CuO_2 Chains
M. Matsuda
Single Crystal Neutron Spectroscopy Proceedings (ILL report) (2002)

43. Magnetic Excitations in the Quantum Spin System NH_4CuCl_3
A. Oosawa, T. Ono, K. Kakurai, H. Tanaka
Single Crystal Neutron Spectroscopy Proceedings (ILL report) (2002)

44. Single Crystal Growth and Structural and Magnetic Properties of the Uranium Ternary Intermetallic Compound UCr_2Si_2
T. D. Matsuda, N. Metoki, Y. Haga, S. Ikeda, T. Okubo, K. Sugiyama, N. Nakamura, K. Kindo, K. Kaneko, A. Nakamura, E. Yamamoto, Y. Onuki
J. Phys. Soc. Jpn. **72** (2002) 122-130

45. Neutron Structural Biology and X-rays Complementarity
N. Niimura, T. Chatake
The Japanese Society for Neutron Science (2003) (Japanese)

46. Hydration in proteins observed by high-resolution neutron crystallography.
T. Chatake, A. Ostermann, K. Kurihara, Fritz G. Parak, N. Niimura
Journal Proteins **50** (2003) 516-523

47. High Resolution Neutron Protein Crystallography Hydrogen and Hydration in Proteins
N. Niimura, T. Chatake, A. Ostermann, K. Kurihara, I. Tanaka
Journal Z. Kristallogr **218** (2003) 96-107

48. Development of an Electrostatic Levitator for Neutron Diffraction Structure Analysis
T. Itami, S. Munejiri, T. Masaki, H. Aoki, Y. Ishii, T. Kamiyama, Y. Senda, F. Shimojo, K. Hoshino
Rev. of Scientific Instruments **74** No.2 (2003) 1147-1149

49. Structure of Liquid Sn over a Wide Temperature Range from Neutron Scattering Experiments and First-principles Molecular Dynamics Simulation: A Comparison to Liquid Pb
T. Itami, S. Munejiri, T. Masaki, H. Aoki, Y. Ishii, T. Kamiyama, Y. Senda, F. Shimojo, K. Hoshino
Phys. Rev. B **67** (2003) 064201 1-12

Appendix E

FOREIGN NATIONAL VISIT in JAERI of the 2002

NAME	DAYS
Francis J. E. Tasset	Mar. 12-21, 2002
Bryan Chakoumakos	May. 14-18, 2002
Adam J. Rondinone	May. 14-18, 2002
Gerald H. Lander	May. 20-Jun. 1, 2002
Birgit Schroeder-Smeibidl	Sep. 5, 2002
Hiroshi Takahashi	Oct. 21-23, 2002
Jung dae Ji	Oct. 21-23, 2002
Jae Hyun Park	Oct. 21-23, 2002
Keith A. McEwen	Oct. 30-Nov. 17, 2002
Andreas Lindbaum	Nov. 9-16, 2002
Je-Guen Park	Nov. 10-14, 2002
Ji-Young So	Nov. 10-18, 2002
Franck Wastin	Nov. 11-15, 2002
Silke Buehler-Paschen	Nov. 11-15, 2002
Gerald H. Lander	Nov. 11-16, 2002
Nicholas Bernhoeft	Nov. 13-25, 2002
Thomas M. Holden	Nov. 25-Dec. 4, 2002
Whang, Joo ho	Dec. 11-13, 2002
Kim, Young Jin	Dec. 11-13, 2002
Lee, Chang Hee	Dec. 11-13, 2002
Patrick Kingsley MANG	Feb. 13-14, 2003
Bau Robert	Feb. 16-24, 2003
Arunan Nadarajah	Mar. 5-14, 2003
Douglas Tobias	Mar. 9-15, 2003
Mikeska, Hans-Jürgen	Mar. 14, 2003
Andreas Ostermann	Mar. 22-29, 2003

This is a blank page.

国際単位系（SI）と換算表

表1　SI基本単位および補助単位

量	名称	記号
長さ	メートル	m
質量	キログラム	kg
時間	秒	s
電流	アンペア	A
熱力学温度	ケルビン	K
物質量	モル	mol
光度	カンデラ	cd
平面角	ラジアン	rad
立体角	ステラジアン	sr

表2　SIと併用される単位

名称	記号
分，時，日	min，h，d
度，分，秒	°，′，″
リットル	l，L
トン	t
電子ボルト	eV
原子質量単位	u

1 eV=1.60218×10^{-19}J

1 u=1.66054×10^{-27}kg

表3　固有の名称をもつSI組立単位

量	名称	記号	他のSI単位による表現
周波数	ヘルツ	Hz	s^{-1}
力	ニュートン	N	$m\cdot kg/s^2$
圧力，応力	パスカル	Pa	N/m^2
エネルギー,仕事,熱量	ジュール	J	N·m
工率，放射束	ワット	W	J/s
電気量，電荷	クーロン	C	A·s
電位，電圧，起電力	ボルト	V	W/A
静電容量	ファラド	F	C/V
電気抵抗	オーム	Ω	V/A
コンダクタンス	ジーメンス	S	A/V
磁束	ウェーバ	Wb	V·s
磁束密度	テスラ	T	Wb/m^2
インダクタンス	ヘンリー	H	Wb/A
セルシウス温度	セルシウス度	℃	
光束	ルーメン	lm	cd·sr
照度	ルクス	lx	lm/m^2
放射能	ベクレル	Bq	s^{-1}
吸収線量	グレイ	Gy	J/kg
線量等量	シーベルト	Sv	J/kg

表4　SIと共に暫定的に維持される単位

名称	記号
オングストローム	Å
バーン	b
バール	bar
ガル	Gal
キュリー	Ci
レントゲン	R
ラド	rad
レム	rem

1 Å=0.1nm=10^{-10}m

1 b=100fm^2=$10^{-28}m^2$

1 bar=0.1MPa=10^5Pa

1 Gal=1cm/s^2=$10^{-2}m/s^2$

1 Ci=3.7×10^{10}Bq

1 R=2.58×10^{-4}C/kg

1 rad=1cGy=10^{-2}Gy

1 rem=1cSv=10^{-2}Sv

表5　SI接頭語

倍数	接頭語	記号
10^{18}	エクサ	E
10^{15}	ペタ	P
10^{12}	テラ	T
10^9	ギガ	G
10^6	メガ	M
10^3	キロ	k
10^2	ヘクト	h
10^1	デカ	da
10^{-1}	デシ	d
10^{-2}	センチ	c
10^{-3}	ミリ	m
10^{-6}	マイクロ	μ
10^{-9}	ナノ	n
10^{-12}	ピコ	p
10^{-15}	フェムト	f
10^{-18}	アト	a

（注）

1．表1－5は「国際単位系」第5版，国際度量衡局 1985年刊行による。ただし，1 eVおよび1 uの値はCODATAの1986年推奨値によった。

2．表4には海里，ノット，アール，ヘクタールも含まれているが日常の単位なのでここでは省略した。

3．barは，JISでは流体の圧力を表わす場合に限り表2のカテゴリーに分類されている。

4．EC閣僚理事会指令ではbar，barnおよび「血圧の単位」mmHgを表2のカテゴリーに入れている。

換算表

力	N(=10^5dyn)	kgf	lbf
	1	0.101972	0.224809
	9.80665	1	2.20462
	4.44822	0.453592	1

粘度　1 Pa·s(N·s/m^2)=10P(ポアズ)(g/(cm·s))

動粘度　1m^2/s=10^4St(ストークス)(cm^2/s)

圧力	MPa(=10bar)	kgf/cm^2	atm	mmHg(Torr)	lbf/in^2(psi)
	1	10.1972	9.86923	7.50062×10^3	145.038
	0.0980665	1	0.967841	735.559	14.2233
	0.101325	1.03323	1	760	14.6959
	1.33322×10^{-4}	1.35951×10^{-3}	1.31579×10^{-3}	1	1.93368×10^{-2}
	6.89476×10^{-3}	7.03070×10^{-2}	6.80460×10^{-2}	51.7149	1

エネルギー・仕事・熱量	J(=10^7 erg)	kgf·m	kW·h	cal(計量法)	Btu	ft·lbf	eV
	1	0.101972	2.77778×10^{-7}	0.238889	9.47813×10^{-4}	0.737562	6.24150×10^{18}
	9.80665	1	2.72407×10^{-6}	2.34270	9.29487×10^{-3}	7.23301	6.12082×10^{19}
	3.6×10^6	3.67098×10^5	1	8.59999×10^5	3412.13	2.65522×10^6	2.24694×10^{25}
	4.18605	0.426858	1.16279×10^{-6}	1	3.96759×10^{-3}	3.08747	2.61272×10^{19}
	1055.06	107.586	2.93072×10^{-4}	252.042	1	778.172	6.58515×10^{21}
	1.35582	0.138255	3.76616×10^{-7}	0.323890	1.28506×10^{-3}	1	8.46233×10^{18}
	1.60218×10^{-19}	1.63377×10^{-20}	4.45050×10^{-26}	3.82743×10^{-20}	1.51857×10^{-22}	1.18171×10^{-19}	1

1 cal= 4.18605J（計量法）

= 4.184J（熱化学）

= 4.1855J（15℃）

= 4.1868J（国際蒸気表）

仕事率　1 PS(仏馬力)

= 75 kgf·m/s

= 735.499W

放射能	Bq	Ci
	1	2.70270×10^{-11}
	3.7×10^{10}	1

吸収線量	Gy	rad
	1	100
	0.01	1

照射線量	C/kg	R
	1	3876
	2.58×10^{-4}	1

線量当量	Sv	rem
	1	100
	0.01	1

（86年12月26日現在）

Progress Report on Neutron Scattering Research (April 1,2002-March 31, 2003)